Kerr Electro-Optic Tomography for Determination of Nonuniform Electric Field Distributions in Dielectrics

by

Afşin Üstündağ

B.S., Electical and Electronics Engineering, Boğaziçi Üniversitesi (1992)

B.S., Physics, Boğaziçi Üniversitesi (1992)

M.S., Electrical Engineering, Worcester Polytechnic Institute (1994)

Submitted to the Department of Electrical Engineering and Computer Science in Partial Fulfillment of the Requirements for the Degree of

Doctor of Philosophy in Electrical Engineering and Computer Science

at the

Massachusetts Institute of Technology

June 1999

Signature of Author .....
Department of Electrical Engineering and Computer Science
May 4, 1999

Certified by .....
Markus Zahn
Professor of Electrical Engineering
Thesis Supervisor

Accepted by .....
Arthur C. Smith
Chairman, Committee on Graduate Students
Department of Electrical Engineering and Computer Science

Dedicated to my parents

Betül and Bekir Üstündağ

Kerr Electro-Optic Tomography for Determination of Nonuniform Electric Field Distributions in Dielectrics

by

Afşin Üstündağ

Submitted to the Department of Electrical Engineering and Computer Science on May 4, 1999 in Partial Fulfillment of the Requirements for the Degree of Doctor of Philosophy in Electrical Engineering and Computer Science

ABSTRACT

The electrical breakdown strength of insulating materials is the limiting factor for greater efficiencies in AC, DC and pulse power apparatus and systems. To improve high voltage designs and prevent failures it is necessary to understand the physics of charge injection and transport and electrical breakdown phenomena. Kerr electro-optic measurements utilize the applied electric field induced anisotropy in refractive index. The anisotropy affects light propagation through the dielectric so that light intensity measurements provide information on electric field distributions which cannot be calculated from knowledge of the geometry alone due to unknown space charge distributions. Most past Kerr electro-optic measurements have been limited to cases where the electric field direction and magnitude are constants along the light path allowing simple relationships between measured light intensity and electric field.

This thesis analyzes the more general case when the applied electric field magnitude and direction vary along the light path. An approximate slow spatial variation form of Maxwell equations is obtained as the governing equations of light propagation in Kerr media and extensively analyzed. It is shown that from each light intensity measurement it is possible to obtain three characteristic parameters when the medium is highly birefringent and the electrode geometry has no symmetry, and two characteristic parameters when the medium is weakly birefringent and/or the geometry is axisymmetric. The characteristic parameters are related to the applied electric field for which new generalized Kerr electro-optic measurement techniques were developed. Three classes of algorithms for the inverse problem of reconstructing electric field distributions from Kerr electro-optic data are investigated. We developed a finite element method based reconstruction algorithm which is applicable to arbitrary three-dimensional geometries when the medium is weakly birefringent. For axisymmetric media the onion peeling algorithm of radially discretized concentric circular regions is developed and successfully applied to reconstruct the applied electric field. Finally, algebraic reconstruction techniques which have been developed in Japan in a research parallel to this one are studied and compared to our algorithms.

Thesis Supervisor: Markus Zahn

Title: Professor of Electrical Engineering

ACKNOWLEDGMENTS

I would like to express my great appreciation to my advisor Professor Markus Zahn for his academic, financial and personal support throughout this project. He proof-read this text several times. He was very patient and understanding and without his help this thesis could never have been completed.

I would also like to express my gratitude to Professor George Verghese, Professor Cardinal Warde, and Professor Peter L. Levin for serving on my committee. Their suggestions and questions were invaluable during the development of this thesis. Special thanks to Professor Levin who started it all by bringing me to the US for my graduate studies.

My officemates in the High Voltage Research Laboratory, Yanqing Du, Tza-Jing Gung, Robert J. Lyons, Alexander V. Mamishev and Darrell Schlicker were always helpful. They together with other members of the Laboratory for Electromagnetic and Electronic Systems made my environment rich and enjoyable.

I would like to thank Ansoft Corp. for providing the electromagnetic software package Maxwell, and to thank the MIT Department of Electrical Engineering and Computer Science for awarding me the Winton Hayes, Edwin S. Webster and Grass Instrument Co. fellowships. In addition, I also want to acknowledge the support by the National Science Foundation under Grant No. ECS9220638 which funded the early part of this research program.

Finally I would like to thank my parents Betül and Bekir Üstündağ, my grandparents Hatice and İlhami Algan, my aunt İclal Güler, and my uncles Erkan and late Bülent Algan for raising me and giving me unconditional support and love. This thesis belongs to them as much as it belongs to me. Special thanks goes to my sister Dilara Üstündağ who has always been there for me.

Contents

List of Figures

List of Tables

Chapter 1

Introduction

1.1 Space Charge Effects In Insulating Dielectrics

In high voltage apparatus, electric field phenomena within insulating dielectrics are governed by the electroquasistatic form of Maxwell's equations

$$\vec{\nabla} \times \vec{E}(\vec{r}) = 0 \tag{1.1}$$

$$\epsilon_s \vec{\nabla} \cdot \vec{E}(\vec{r}) = \rho(\vec{r}) \tag{1.2}$$

where $\vec{E}$ is the electric field, ρ is the volume charge density, ϵ_s is the low frequency dielectric permittivity and $\vec{r}$ is the position vector. Due to (1.1) the electric field is said to be irrotational and can be represented as the negative gradient of the electric scalar potential ϕ

$$\vec{E} = -\vec{\nabla}\phi(\vec{r}) \tag{1.3}$$

Equations (1.1)-(1.3) show that the electric potential is governed by Poisson's equation

$$\nabla^2 \phi(\vec{r}) = -\frac{\rho(\vec{r})}{\epsilon_s} \tag{1.4}$$

Equations (1.1) and (1.2) follow from Maxwell equations (see Section 2.2) when the dielectric is isotropic and homogeneous. If the electric field is constant in time (1.1) is an exact relation. Even when the electric field is time dependent (1.1) remains valid in the electroquasistatic limit in which the electromagnetic wave propagation time within the apparatus is much faster than the time constants of electric field variation [1].

This work is relevant to both transient and steady state phenomena and when the charge density is time dependent but with time constants for charge injection and transport long enough to make the electroquasistatic limit valid. The time dependence in (1.4) is often not explicitly shown. It should be understood that at each instant in time (1.4) is valid with the instantaneous ρ.

The current density $\vec{J}$ is the other important field quantity for the description of electric field phenomena in insulating dielectrics and related to the charge density by the charge conservation law

$$\vec{\nabla} \cdot \vec{J}(\vec{r}) + \frac{\partial \rho(\vec{r})}{\partial t} = 0 \tag{1.5}$$

In many engineering applications charge transport phenomena is adequately modeled by Ohm's law

$$\vec{J} = \sigma \vec{E} \tag{1.6}$$

If σ is spatially uniform, substituting (1.2) and (1.6) in (1.5) yields a first order differential equation in time

$$\frac{\partial \rho(\vec{r}, t)}{\partial t} + \frac{\sigma}{\epsilon_s} \rho(\vec{r}, t) = 0 \tag{1.7}$$

whose solution is

$$\rho(\vec{r}, t) = \rho(\vec{r}, 0) \exp -t/\tau \tag{1.8}$$

Here $\tau = \epsilon_s/\sigma$ is the charge dielectric relaxation time constant. Equation (1.8) shows that in the absence of charge generation mechanisms any initial volume charge distribution relaxes to zero.

However real dielectrics in a high voltage environment often do not obey Ohm's law so that drift, diffusion and convective currents can result in non-zero space charge distributions. Various mechanisms introduce volume charge into insulating dielectrics. One very important mechanism is charge injection from high voltage stressed electrodes where the injected charge can be negative or positive depending on the polarity of the charge injecting electrode. For liquid dielectrics the entrainment by fluid motion of the mobile part of the electrical double layer that forms between dissimilar materials is another mechanism. Still another mechanism is the dissocation of molecules, ionic

contaminants or additives within the dielectrics. Charge generation mechanisms are opposed by relaxation and recombination.

By definition, an ideal insulating dielectric cannot sustain a steady conduction current [2]. There are no perfect insulators, however for most engineering insulating dielectrics σ is very small so that effects of conduction currents that cause heating and energy dissipation are tolerable for a wide range of electric field magnitudes. However there does exist a maximum electric field magnitude called the electric breakdown strength to which an insulating dielectric can withstand. Once the electric field magnitude exceeds the breakdown strength, dielectrics lose their insulating characteristics and a large amount of current begins to flow causing excessive heating, burn-out and eventual failure of the apparatus.

The electrical breakdown strength of insulating materials is the limiting factor in AC and DC power generation and transmission and for larger energies in pulsed power applications such as lasers, inertial confinement fusion, charged particle beam devices and directed energy devices [3]. Space and efficiency concerns requires the maximum electric field magnitude in high voltage apparatus to be as high as possible while safety and reliability limits the maximum electric field magnitude to be lower than the electrical breakdown strength of insulating dielectrics at all times. Thus optimum designs require accurate knowledge of the electric field distribution.

If the space charge distribution is known at all times then (1.4) can be solved by traditional numerical methods. The solution can then be used in engineering designs to assure that the electric field magnitude does not exceed safe limits. Unfortunately, the physical laws that govern space charge injection and transport are not fully known. The parameters in models are very sensitive to such factors as temperature, additives, contaminants and electrode materials. Furthermore the parameters change over time as the properties of aged dielectrics in high voltage apparatus differ from those of new dielectrics. Thus in the absence of experimental data, ρ in (1.4) can not be modeled adequately.

In the absence of knowledge of the space charge distribution, engineering designs often take the insulating materials to be uncharged so that the electric field distribution can be found by solving Laplace's equation for which ρ is identically zero. Such designs can not predict where the electric field magnitude may exceed safe maximums in the presence of space charge. Indeed some catastrophic failures in high voltage apparatus are attributed to unexpected buildup of volume and surface charge. Even when space charge effects do not cause breakdown, they affect the performance of high voltage

equipment by distorting the electric field.

Consequently, to improve designs and prevent failures it is of great interest to understand or at least empirically model the physics of charge injection and transport and electrical breakdown phenomena in various dielectrics and to study the effects of different dielectric and electrode materials, and contaminants and additives. This challenge requires accurate determination of space charge and electric field distributions in experiments. Kerr electro-optic measurements provide a convenient noninvasive methodology for this purpose.

1.2 Kerr Electro-Optic Measurements

1.2.1 The Kerr Electro-Optic Effect

In general, dielectrics are isotropic due to random orientation of the molecules. When the dielectric medium is stressed by a high electric field, the field direction becomes preferred for molecular dipoles and the dielectric medium becomes birefringent so that incident linearly or circularly polarized light propagating through the medium becomes elliptically polarized. This applied electric field induced birefringence is known as the Kerr effect.

The fundamental relation of this thesis relates the birefringence to the magnitude of the applied electric field in dielectrics which exhibit the Kerr effect [3, 4]

$$\Delta n = n_{\parallel_0} - n_{\perp_0} = \lambda B E^2 \tag{1.9}$$

Here $n_{\parallel_0}$ and $n_{\perp_0}$ are the refractive indices for light polarized in the direction of the applied field and in the direction perpendicular to the field respectively; λ is the free space wavelength of the light; B is the Kerr constant; and E is the magnitude of the applied electric field.

In the dielectric literature (1.9) is often replaced by

$$\Delta n \approx n_{\parallel} - n_{\perp} \approx \lambda B E_T^2 \tag{1.10}$$

where E_T is the magnitude of $\vec{E}_T$, the component of the applied electric field transverse to the light propagation direction; and $n_{\parallel}$ and $n_{\perp}$ are respectively the refractive indices for light polarized in the direction of $\vec{E}_T$ and in the direction perpendicular to $\vec{E}_T$ and the light propagation direction. Equation (1.10) is an approximate form of (1.9) which

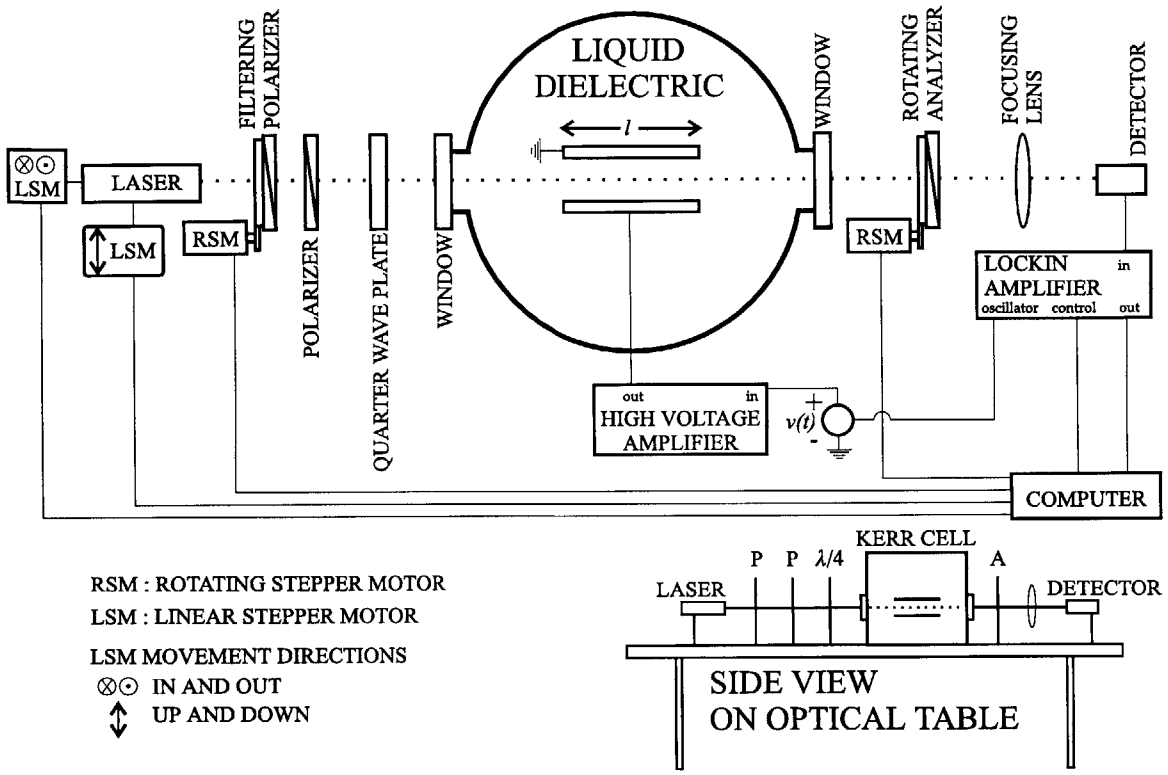

Figure 1.1: A basic Kerr electro-optic measurement set-up. The main chamber is filled with a liquid dielectric and houses an electrode system (here parallel plate electrodes) whose electric field and space charge distributions are under investigation. An advanced set-up also includes filtration, vacuum and temperature control systems to control and monitor the dielectric state.

is valid when the birefringence is small

$$\Delta n \ll 1 \tag{1.11}$$

Derivation of (1.10) from (1.9) is provided in Chapter 2. The transverse component $\vec{E}_T$ and the directions associated with the subscripts $\|_0$, $\perp_0$, $\|$ and $\perp$ are also detailed in Chapter 2 (see Figure 2.1).

1.2.2 Principles Of The Measurements

A typical Kerr electro-optic measurement set-up is shown in Figure 1.1 for parallel plate electrodes. The electric field is applied through the high voltage amplifier. Neglecting electrode end effects the applied electric field is spatially uniform and perpendicular to the propagation direction of light within the electrode length of l. Since the applied

electric field is perpendicular to the light propagation direction $\vec{E}_T = \vec{E}$ and (1.9) and (1.10) are identical. Upon entering the electrode region the light electric field decomposes into components in the direction of the applied electric field and perpendicular to it. As implied by (1.9) these two components travel with slightly different speed and at the end of the electrode region an optical phase shift is introduced

$$\Phi = \int_{s=0}^{l} \frac{2\pi}{\lambda} \Delta n \, ds = 2\pi B E^2 l \tag{1.12}$$

where s is the position coordinate along the light path. Thus if Φ is measured, the electric field magnitude follows as

$$E = \sqrt{\frac{\Phi}{2\pi B l}} \tag{1.13}$$

The low intensity light has virtually no effect on the applied electric field distribution hence the method is noninvasive. Optical measurements offer near-perfect electrical isolation between the measured field and the measuring instrumentation, avoids interference errors and makes extensive shielding and insulation requirements unnecessary [5].

The optical elements (polarizers and quarter wave plates) are used to measure the phase shift introduced by the stressed dielectric and constitute what is known as an optical polariscope system. For the particular system in Figure 1.1, when the polarizer transmission and quarterwave plate slow axes are 45° to each other the output intensity I is given as

$$\frac{I}{I_0} = \frac{1 + \sin\Phi \sin 2(\varphi - \theta_a)}{2} \tag{1.14}$$

Here φ is the direction of the applied electric field and θ_a is the direction of the analyzer transmission axis both with respect to some fixed reference direction perpendicular to the light propagation direction. I_0 is the light intensity just after the filtering polarizer which is introduced to control the light intensity so that the photo-detector is not saturated. It is clear from (1.14) that output light intensity measurements can be used to measure both the magnitude and the direction of the electric field by rotating the analyzer (thus changing θ_a).

1.2.3 Kerr Media

In this thesis we define Kerr media to be electrically stressed transparent dielectrics which obey (1.9). The classification of a Kerr medium (homogeneous vs. inhomogeneous for example) will refer to the permittivity and/or refractive index tensor of the medium. The effect is generally strongest in polar dielectric liquids.

The method is limited to transparent dielectrics. However most liquid dielectrics, in particular the most common high voltage insulant transformer oil, are in this category making the method very attractive. Liquid dielectrics which were investigated in the past using the Kerr electro-optic effect include transformer oil [6–11], highly purified water and water/ethylene glycol mixtures [12–14], and nitrobenzene [15–17]. The effect can also be used for gases (SF_6) [3] and solids (polymethylmethacrylate) [18, 19].

1.2.4 Measurement Techniques

There are two general measurement schemes as shown in Figure 1.2. Earlier measurements typically used the two dimensional scheme in which the laser beam is expanded using an optical beam expander to cover the entire area of interest and the output light beam is photographed. Depending on the polariscope system the output intensity expressions differ but invariably contain sine and/or cosine terms that depend on Φ and the electric field direction as in (1.14). As the one or two dimensional electric field magnitude and/or direction change in the plane perpendicular to the light path, a fringe pattern of light maxima and minima result.

In Figure 1.3 we illustrate 5 such computed patterns for different charge injection processes. This is a rounded edge parallel plate electrode with gap of 1 cm and length l of 10 cm (into the page). The medium is nitrobenzene for which $B = 3 \times 10^{-12}$ m/V^2 and the applied voltage V is 30 kV. The polariscope system is a crossed polarizer circular polariscope for which the output intensity is

$$\frac{I}{I_0} = \sin^2 \frac{\Phi}{2} \tag{1.15}$$

and does not depend on the direction of the electric field. A crossed polarizer circular polariscope is obtained by having the transmission axes of the two polarizers perpendicular and adding a second quarter wave plate to the system shown in Figure 1.1 between the medium and the analyzer with slow axis at 45° to the analyzer transmission axis and perpendicular (90°) to the first quarter wave plate slow axis.

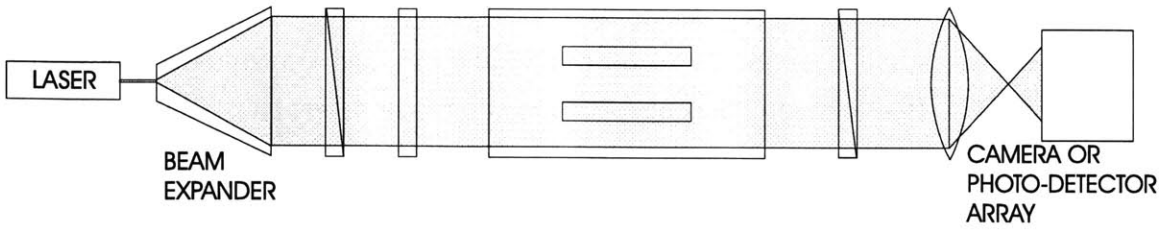

(a) Two Dimensional Measuring Scheme

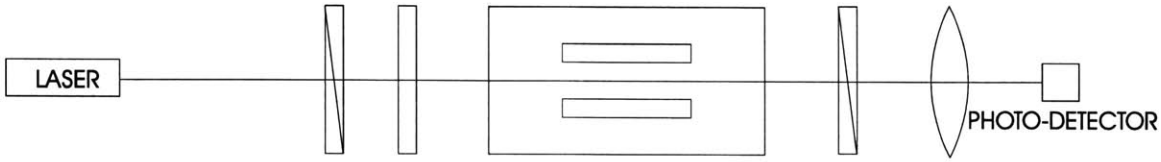

(b) Point Measuring Scheme

Figure 1.2: Kerr electro-optic measurement schemes. On the top the beam is expanded and covers the entire area of interest. On the bottom each measurement yields data on a single point. Two dimensional data is gathered by mechanically moving the laser.

The calculated patterns shown are for no charge injection (Laplacian field), positive charge injection, negative charge injection, bipolar homocharge injection, and bipolar heterocharge injection. For positive and negative charge injection we assume the charge density to be spatially uniform ($\rho = \epsilon_s V/d^2$) within the electrodes and for bipolar charge injections we assume that the charge densities are symmetrically linear ($\rho_{\text{peak}} = \epsilon_s V/d^2$). Here $d = 1$ cm is the gap distance. Although (1.15) is not a one to one function the values of Φ can still be determined. Far from the electrodes where the electric field goes to zero, Φ is also zero and each light maximum corresponds to some odd integer times π for Φ and each minimum corresponds to an even integer times π for Φ such that

$$\Phi = n\pi \quad n = 1, 2, \cdots \tag{1.16}$$

and n can be determined by counting the number of prior maxima and minima between the outer dark region.

In the two dimensional scheme using the fringe patterns, it is possible to measure Φ accurately. Based on the fringe patterns both qualitative and quantitative conclusions are possible. For example if there are more closely spaced fringes near an electrode as

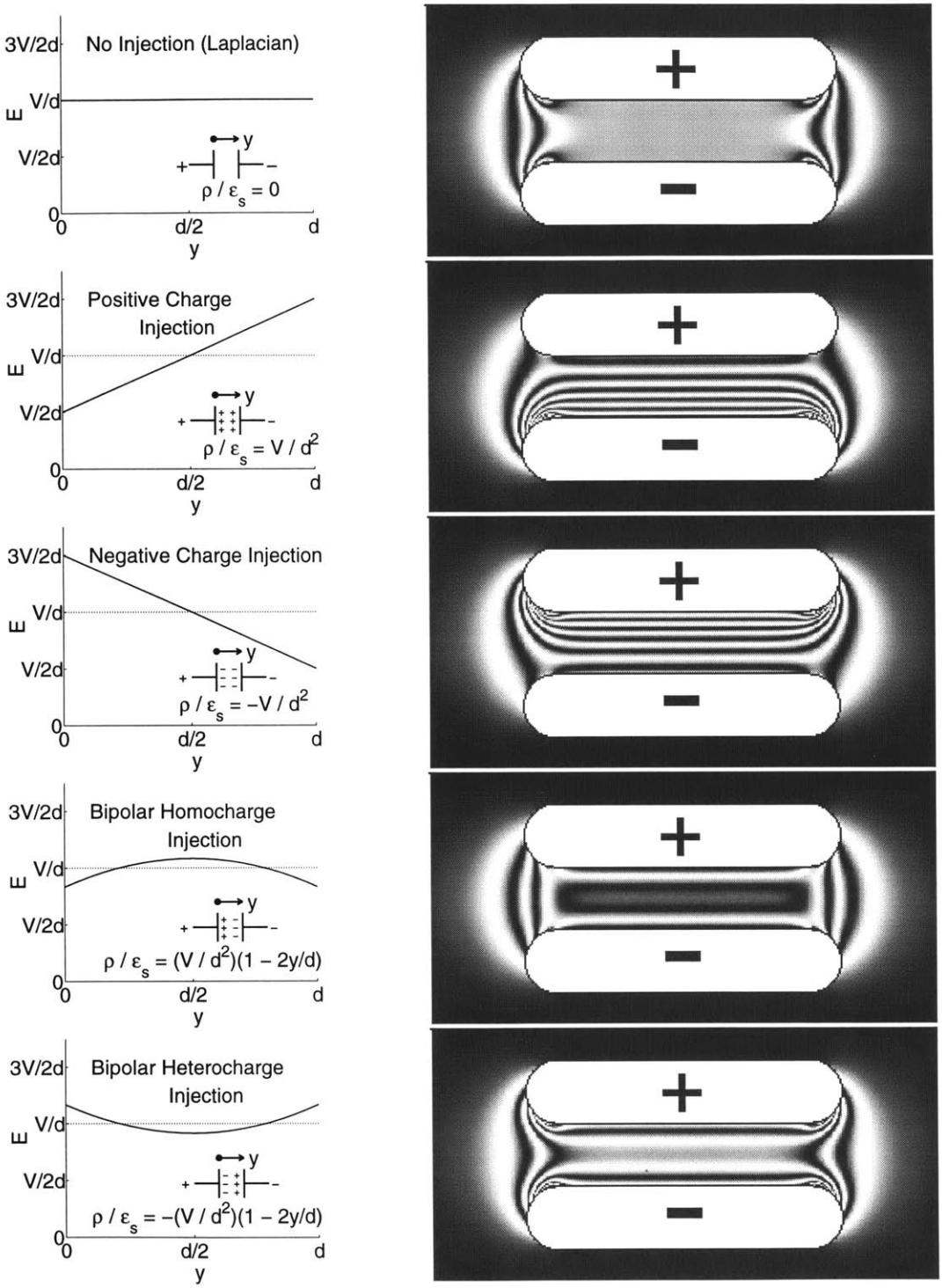

Figure 1.3: Calculated crossed polarizer circular polariscope intensity patterns using parallel plate electrodes with gap $d = 1$ cm for various charge injection processes. The dielectric medium is nitrobenzene ($B \approx 3 \times 10^{-12}\text{m/V}^2$), the applied voltage V is 30 kV and the electrode length l is 10 cm.

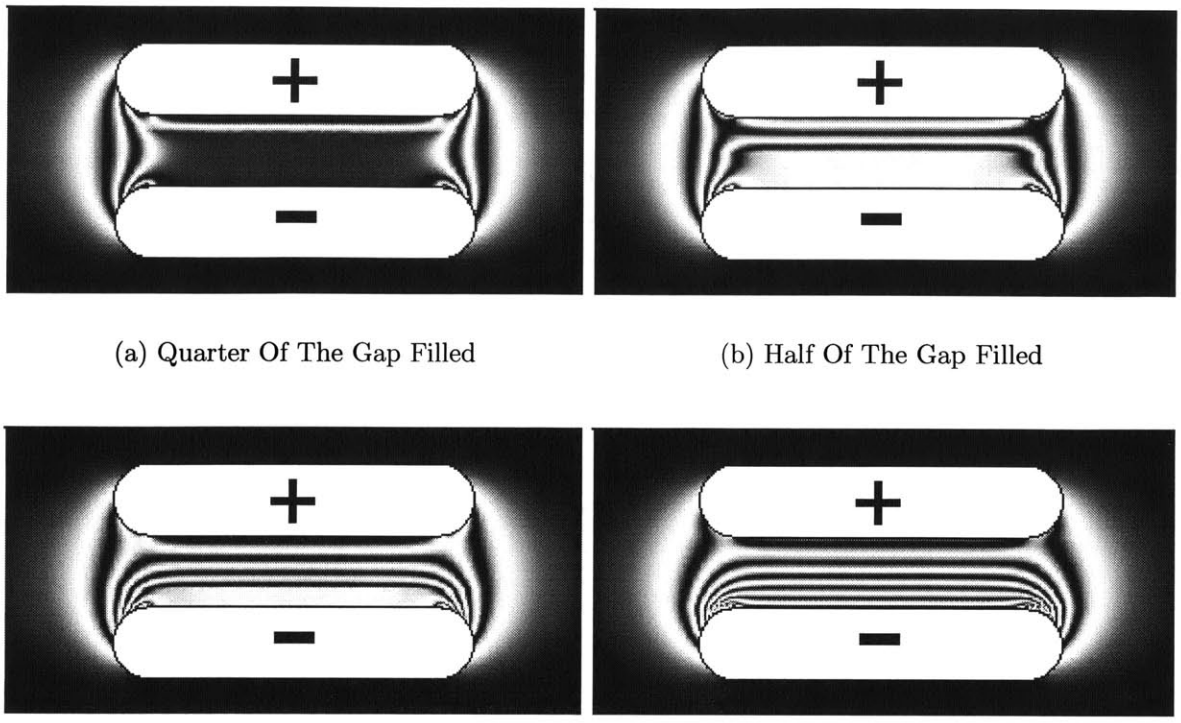

(a) Quarter Of The Gap Filled

(b) Half Of The Gap Filled

(c) Three Quarters Of The Gap Filled

(d) Whole Gap Filled

Figure 1.4: Illustration of time evolution of injected positive charge from the positive electrode with negligible recombination and/or relaxation.

in the 2nd and 3rd figures in Figure 1.3 then it may be concluded that the electric field is strongest at the electrode with polarity opposite to that of the positive or negative unipolar charge injection and that the charge is injected from the electrode where the field is weakest. This technique has the added advantage that the time evolution of charge can be recorded by high speed photography, up to 5000 frames per second in reference [3]. In Figure 1.4 we illustrate computational snapshots of propagating positive charge injection as the charge fills a quarter, a half, three fourths and all of the gap. The geometry and material parameters are identical to those in Figure 1.3.

Photographic data however is useful only when the Kerr constant B is high enough so that optical fringe patterns are available. If the Kerr constant is small so that Φ never exceeds $\pi/2$, it is not possible to observe fringes. For this reason earlier measurements were limited to high Kerr constant materials such as nitrobenzene and water (with meter long electrodes) for which $B \approx 3 \times 10^{-12}$ m/V^2 and $B \approx 3.0 \times 10^{-14}$ m/V^2 respectively.

The second scheme for Kerr electro-optic measurements uses an unexpanded laser beam. For good spatial resolution it is advantageous to use a beam with as small a radius as possible. After light propagates through the medium the output intensity is measured by a photo-detector. The most common insulant transformer oil has a Kerr constant on the order of 10^{-15} m/V^2. For reasonable applied voltages and electrode gaps and lengths the phase shift is less than 0.1 radians, making it difficult to measure such small dc signals from the photo-detector.

The sensitivity of Kerr electro-optic measurements is increased by the use of an ac modulation method where an ac quasistatic electric field is superposed onto a dc field [8, 9, 20–22]. For parallel plate electrodes the total electric field is then given as

$$E = E_{dc} + E_{ac} \cos \omega t \tag{1.17}$$

Substituting (1.17) in (1.12) yields

$$\Phi = 2\pi Bl \left[E_{dc}^2 + \frac{E_{ac}^2}{2} + \frac{E_{ac}^2}{2} \cos 2\omega t + 2E_{dc}E_{ac} \cos \omega t \right] \tag{1.18}$$

Thus the optical phase shift has dc, fundamental frequency and double frequency components. When the electrode system illustrated in Figure 1.1 is used and the analyzer angle is set at $\pi/4$ radians to the electric field direction the output intensity reduces to

$$\frac{I_f}{I_0} \approx \frac{1 + \Phi}{2} \tag{1.19}$$

since Φ is small. Substituting (1.18) in (1.19) yields dc, fundamental frequency and double frequency components for the intensity. The dc component is essentially equal to $I_0/2$

$$I_{dc} = I_0 \left[\frac{1}{2} + \pi Bl E_{dc}^2 + \pi Bl \frac{E_{ac}^2}{2} \right] \approx \frac{I_0}{2} \tag{1.20}$$

since B is so small that the electric field dependent terms are much less than 1/2. The ratios of the fundamental and double frequency components to I_{dc} are then given as

$$\frac{I_\omega}{I_{dc}} = 4\pi Bl E_{dc} E_{ac} \tag{1.21}$$

$$\frac{I_{2\omega}}{I_{dc}} = \pi Bl E_{ac}^2 \tag{1.22}$$

Both I_ω/I_{dc} and $I_{2\omega}/I_{dc}$ can be measured very accurately using a lock-in amplifier which can then be used to find E_{dc} and E_{ac}.

Ac modulation increases the sensitivity of the Kerr electro-optic measurements dramatically and it becomes possible to conduct research on small Kerr constant media and in particular transformer oil using Kerr electro-optic measurements. One other advantage of the method is that the ac field is not affected by space charge since typical charge mobilities are small enough that the space charge cannot follow the ac field for sufficiently high frequencies (typically frequencies on the order of 100 Hz suffice). Thus E_{ac} can be found analytically or numerically from solutions to Laplace's equation and I_{2w} may be used to calibrate the measurements for increased accuracy in measuring E_{dc}.

1.2.5 Nonuniform Electric Field Distributions

On the ground planes of electrode systems such as point/plane electrodes (Appendix A) and sphere/plane electrodes (Appendix B), the electric field direction is constant but the magnitude $E(x, y)$ varies as a function of position where we choose the xy-plane to coincide with the ground plane. For a light path on the ground plane the applied electric field direction is perpendicular to the path and using (1.9) the optical phase shift Φ can be expressed as

$$\Phi(p,\theta) = \int_{s_{\text{in}}}^{s_{\text{out}}} \frac{2\pi}{\lambda}\Delta n\, ds = 2\pi B \int_{s_{\text{in}}}^{s_{\text{out}}} E^2(x,y)ds \tag{1.23}$$

$$= 2\pi B \int_{s_{\text{in}}}^{s_{\text{out}}} E^2(p\cos\theta - s\sin\theta, p\sin\theta + s\cos\theta)ds \tag{1.24}$$

Here p and θ describe the light path in the xy-plane; p is the distance between the origin and the path, and θ is the angle between the normal to the path and the x-axis (see Figure 9.1). s_{in} and s_{out} are the entrance and the exit points of the light ray into the inter-electrode region.

Equation (1.23) shows that a single optical phase shift measurement does not provide much information on the spatial distribution of electric field magnitude. The next question is if it is possible to approximately determine $E(x, y)$ from a set of optical phase shift measurements and the answer is affirmative. In fact reconstruction of a planar function from its line integrals is of interest in a variety of scientific disciplines and is known as tomography. For scalar functions many well established methods exist

and we describe some of them in Chapter 7 and Chapter 9. Thus for special cases where electric field magnitude varies but the direction is constant along the light path Kerr electro-optic measurements can still be used to measure the electric field.

However when both the magnitude and the direction of the electric field vary along the light path optically measuring the electric field distribution is not straight forward. Since the electric field direction is not constant along the light path it is not possible to integrate (1.9) to find the optical phase shift. Thus it is necessary to develop the theory that relates the Kerr electro-optic measurements to the applied electric field. If this is achieved then the next step is the development of algorithms which can reconstruct the electric field distribution from a set of Kerr electro-optic intensity measurements. These constitute the objectives of this thesis.

1.3 Objectives Of The Thesis

This work is part of a continuing effort to measure electric field distributions using the Kerr electro-optic effect [6,12–15,19,23–27]. The past experimental work has been limited to cases where the electric field magnitude and direction have been constant along the light path such as two long concentric or parallel cylinders [3,12,15] or parallel plate electrodes [3,13].

In those cases using high Kerr constant dielectrics the electric field magnitude and direction is directly available from intensity measurements as demonstrated in (1.14). However, to study charge injection and breakdown phenomena very high electric fields are necessary ($\approx 10^7$ V/m) with long electrode lengths and for these geometries large electric field magnitudes can be obtained only with very high voltages (typically more than 100 kV). Furthermore, in these geometries the breakdown and charge injection processes occur randomly in space often due to small unavoidable imperfections on otherwise smooth electrodes. The randomness of this surface makes it impossible to localize the charge injection and breakdown and the problem is complicated because the electric field direction also changes along the light path. To create large electric fields for charge injection at known location and at reasonable voltages a point electrode is often used in high voltage research where again the electric field direction changes along the light path. The ultimate goal of this research is to use the Kerr electro-optic measurement for typical arrangements in high voltage apparatus for which the geometries are mostly three dimensional. Hence it is of interest here to extend Kerr electro-optic measurements to cases where the applied electric field direction changes

along the light path.

The primary objective of this thesis is the mathematical modeling of the inverse formulation of using Kerr electro-optic measurements of light intensity along many light paths to determine the arbitrary three dimensional electric field direction and magnitude everywhere between electrodes. The inverse problem of measuring nonuniform electric field distributions in space from the Kerr electro-optical measurements will be referred to as Kerr electro-optic tomography. In this thesis we attempt to extend, improve and apply methods of medical tomography and photoelasticity to Kerr electro-optic tomography. Kerr electro-optic measurements are nonlinearly related to the vector components of the applied electric field. Examples of vector tomography and nonlinear tomography are rare in the literature and this work is expected to provide a case study for other disciplines as well.

1.4 Outline Of The Thesis

The thesis begins with the introduction chapter which gives a background of Kerr electro-optic measurements and states the scope of the thesis. The remainder of the thesis is divided into two main parts.

In Part I we develop the forward theory of Kerr electro-optic measurements. The development begins in Chapter 2 with macroscopic and molecular descriptions of the Kerr electro-optic effect and the derivation of a reduced form of Maxwell equations which govern light propagation in electrically stressed dielectrics which exhibit the Kerr effect. Chapter 3 introduces the matricant which describes the evolution of the polarization while light is propagating through the anisotropic dielectric. In Chapter 4 the matricant theory leads to the definition of characteristic parameters which are proven to be the only independent measurables in a Kerr electro-optic measurement. This chapter also develops the relations between the electric field distribution and the characteristic parameters. Part I is concluded with Chapter 5 which describes how various optical polariscope systems can be used to measure the characteristic parameters and compares optical intensity patterns of two dimensional and axisymmetric geometries.

Part II is devoted to the inverse problem of reconstructing the electric field and space charge from the Kerr electro-optic light intensity measurements. We use synthetic Kerr electro-optic data based on the theory in Part I. When possible we use synthetic data that is indicative of the actual data which are being taken for the ex-

perimental thesis work on Kerr electro-optic measurements which has been continuing parallel to this one at MIT [28]. The onion peeling method is the first reconstruction algorithm in Part II and described in Chapter 6. Chapter 7 is devoted to the adaptation of algebraic reconstruction techniques (ART) of scalar tomography to Kerr electro-optic measurements. Chapter 8 develops a finite element method based reconstruction algorithm. We conclude Part II with a review of transform methods of scalar and vector tomography and a discussion of how they might be extended to Kerr electro-optic measurements in future research. The thesis finishes with conclusions and the suggestions for future research, and the appendices. Figure 1.5 summarizes the content of the thesis.

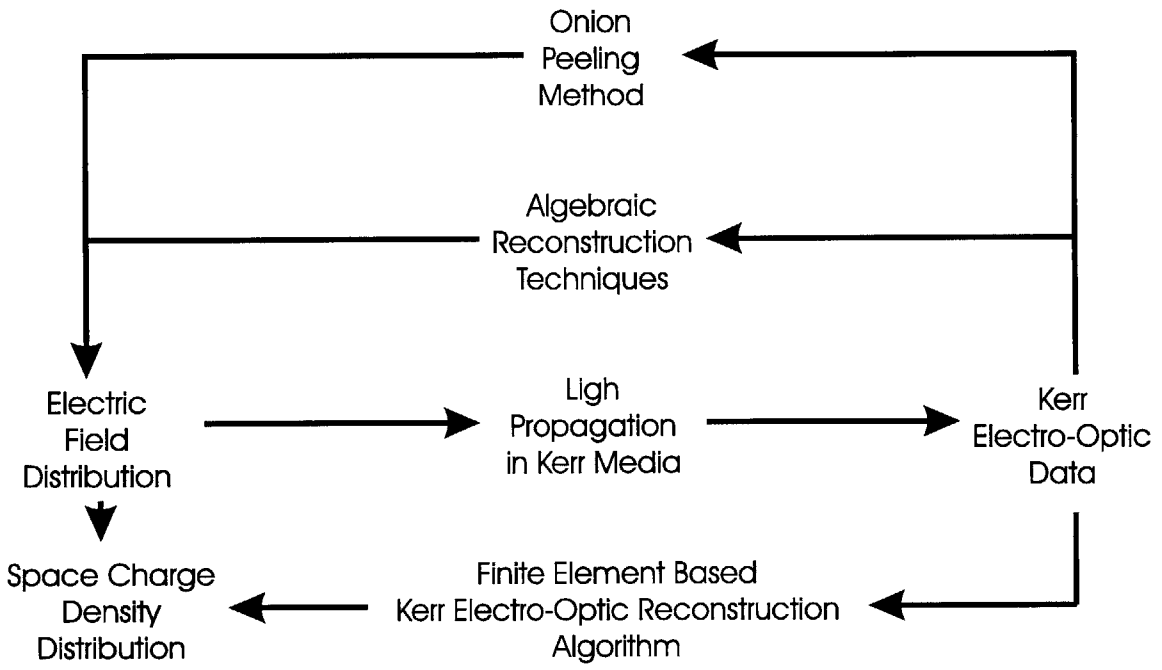

Figure 1.5: The summary of the content of the thesis. In Part I light propagation in Kerr media is developed and Kerr electro-optic measurements are related to applied electric field distributions in dielectrics. Part II introduces three algorithms which reconstruct applied electric field or space charge density distributions from Kerr electro-optic data.

Part I

The Forward Problem

Chapter 2

Light Propagation In Kerr Media

2.1 Introduction

In Chapter 1 we discussed electric field phenomena in insulating dielectrics and introduce the principles of Kerr electro-optic measurements. Kerr media are defined to be transparent insulating dielectrics which become birefringent in the presence of an applied electric field and for which this birefringence depends quadratically on the applied electric field magnitude.

Maxwell's equations are the basis for both quasistatic electric field phenomena and light propagation in insulating dielectrics. This otherwise distinctly treated phenomena are coupled in Kerr electro-optic measurements through the electric constitutive laws of electric field induced anisotropy in the refractive indices. This chapter begins with a statement of Maxwell's equations and the dielectric constitutive laws. The Kerr electro-optic effect is detailed both from macroscopic and microscopic view points. It is shown that for light propagation, Kerr media can be treated as a uniaxial crystal. Light propagation in homogeneous uniaxial media is reviewed and generalized to inhomogeneous media. The final results of this chapter are approximated forms of Maxwell's equations which are easier to analyze and constitute the governing equations for light propagation in inhomogeneous Kerr media in this work.

2.2 Maxwell's Equations

2.2.1 Basics

As most phenomena involving electromagnetism, Maxwell's equations are the very basis of this work. There are numerous introductory books on the subject [29–31]. Here we merely state them for reference and to underline approximations used in this work.

Maxwell equations are usually expressed as

$$\vec{\nabla} \times \vec{\mathcal{E}}(\vec{r},t) = -\frac{\partial \vec{\mathcal{B}}(\vec{r},t)}{\partial t} \tag{2.1a}$$

$$\vec{\nabla} \times \vec{\mathcal{H}}(\vec{r},t) = \frac{\partial \vec{\mathcal{D}}(\vec{r},t)}{\partial t} + \vec{J}(\vec{r},t) \tag{2.1b}$$

$$\vec{\nabla} \cdot \vec{\mathcal{D}}(\vec{r},t) = \rho(\vec{r},t) \tag{2.1c}$$

$$\vec{\nabla} \cdot \vec{\mathcal{B}}(\vec{r},t) = 0 \tag{2.1d}$$

where $\vec{\mathcal{E}}$, $\vec{\mathcal{D}}$, $\vec{\mathcal{H}}$ and $\vec{\mathcal{B}}$ are respectively electric field, electric displacement field, magnetic field and magnetic flux density; $\vec{r}$ and t denote the position vector and time. We use calligraphic letters to maintain generality since $\vec{\mathcal{E}}$, $\vec{\mathcal{D}}$, $\vec{\mathcal{H}}$ and $\vec{\mathcal{B}}$ may refer to quasistatic field quantities of high voltage environments which we denote by $\vec{E}$, $\vec{D}$, $\vec{H}$ and $\vec{B}$, to optical field quantities which we denote by $\vec{e}$, $\vec{d}$, $\vec{h}$ and $\vec{b}$, or to the sum of quasistatic and optical field quantities as they are both present in Kerr electro-optic measurements. No such distinction is necessary for the electric current $\vec{J}$ and the charge density ρ since they are the sources of quasistatic fields only and identically vanish for optical fields as there are no light sources within Kerr media. Note that $\vec{J}$ and ρ are related by the charge conservation law (1.5) which follow from (2.1b) and (2.1c).

Equation (2.1) relates electromagnetic field quantities. Material interactions with electromagnetic fields are described by the constitutive laws which interrelate $\vec{\mathcal{E}}$, $\vec{\mathcal{D}}$, $\vec{\mathcal{H}}$ and $\vec{\mathcal{B}}$. This work is limited to nonmagnetic materials for which $\vec{\mathcal{H}}$ and $\vec{\mathcal{B}}$ are related by

$$\vec{\mathcal{B}}(\vec{r},t) = \mu_0 \vec{\mathcal{H}}(\vec{r},t) \tag{2.2}$$

where $\mu_0 = 4\pi \times 10^{-7}$ henries/meter is the magnetic permeability of free space. The second and most important constitutive law used in this work relates the displacement

and electric fields

$$\vec{\mathcal{D}}(\vec{r},t) = \epsilon_0 \vec{\mathcal{E}}(\vec{r},t) + \vec{\mathcal{P}}(\vec{r},t) \tag{2.3}$$

where $\vec{\mathcal{P}}$ is called the polarization density and $\epsilon_0 \approx 1/36\pi \times 10^{-9}$ Farad/meter is the free space permittivity. $\vec{\mathcal{P}}$ describes the effects of microscopic (and sometimes macroscopic) dipoles that form in the material as a response to $\vec{\mathcal{E}}$ [30].

Materials for which $\vec{\mathcal{P}}$ is in the same direction as $\vec{\mathcal{E}}$ are called electrically isotropic and for which the components of $\vec{\mathcal{P}}$ are linearly dependent on the components of $\vec{\mathcal{E}}$ are called linear. For isotropic linear materials

$$\vec{\mathcal{P}} = \epsilon_0 \chi(\omega) \vec{\mathcal{E}} \tag{2.4}$$

where χ is the suspectibility and ω is the frequency of the electric field. Here we assume that the electric field has a single frequency component or that the frequency dependence of χ is negligible within the bandwidth of $\vec{\mathcal{E}}$. Otherwise (2.4) must be expressed as a sum of the individual frequency components of $\vec{\mathcal{E}}$. Substituting (2.4) into (2.3) yields

$$\vec{\mathcal{D}}(\vec{r},t) = \epsilon(\omega)\, \vec{\mathcal{E}}(\vec{r},t) \tag{2.5}$$

where $\epsilon(\omega) = \epsilon_0[1 + \chi(\omega)]$ is the dielectric permittivity.

For quasistatic fields Kerr media are linear, isotropic and the frequency dependence of ϵ is negligible for relevant frequencies. We denote this low frequency value of dielectric permittivity by ϵ_s where s stands for static. Thus

$$\vec{D}(\vec{r},t) = \epsilon_s\, \vec{E}(\vec{r},t) \tag{2.6}$$

where $\vec{D}$ and $\vec{E}$ denote quasistatic displacement and electric fields respectively.

When there is no applied quasistatic field Kerr media are linear and isotropic for optical fields as well. The frequency bandwidth of the light used in Kerr electro-optic measurements is small and the frequency dependence of ϵ can be neglected

$$\vec{d}(\vec{r},t) = \epsilon\, \vec{e}(\vec{r},t) \tag{2.7}$$

Here $\vec{d}$ and $\vec{e}$ denote optical displacement and electric fields respectively. In the rest of

this work ϵ refers to optical isotropic permittivity.

In the presence of an applied quasistatic field optical isotropy is no longer valid since a strong quasistatic field introduces a preferred direction and the Kerr medium becomes anisotropic. Much of the rest of this chapter describes this anisotropy and its effect on light propagation.

2.2.2 Nonlinear Electric Constitutive Law

Materials which are not isotropic are called anisotropic and which are not linear are called nonlinear. Equation (2.4) is generalized to anisotropic but linear materials by allowing the suspectibility to become a second rank tensor

$$\vec{\mathcal{P}} = \epsilon_0 \bar{\bar{\chi}}(\omega) \cdot \vec{\mathcal{E}} \tag{2.8}$$

where ω is the frequency of the electric field. Here we assume that $\vec{\mathcal{E}}$ has a single frequency component or the bandwidth around ω is negligible. Otherwise (2.8) must be written as a sum for individual frequency components. For linear anisotropic materials the permittivity generalizes to the permittivity tensor $\bar{\bar{\epsilon}} = \epsilon_0 \left[\bar{\bar{I}} + \bar{\bar{\chi}}\right]$ where $\bar{\bar{I}}$ is the second rank identity tensor.

In electromagnetism, nonlinearities are often handled by expressing $\vec{\mathcal{P}}$ as a Taylor series expansion in $\vec{\mathcal{E}}$

$$\vec{\mathcal{P}} = \epsilon_0 \bar{\bar{\chi}}(\omega) \cdot \vec{\mathcal{E}} + \epsilon_0 \bar{\bar{\bar{\chi}}}(\omega) : \vec{\mathcal{E}}\,\vec{\mathcal{E}} + + \epsilon_0 \bar{\bar{\bar{\bar{\chi}}}}(\omega) \vdots \vec{\mathcal{E}}\,\vec{\mathcal{E}}\,\vec{\mathcal{E}} + \ldots \tag{2.9}$$

where

$$\epsilon_0 \left[\bar{\bar{\chi}}\right]_{ij} = \left.\frac{\partial \mathcal{P}_i}{\partial \mathcal{E}_j}\right|_{\vec{\mathcal{E}}=\vec{0}} \qquad \epsilon_0 \left[\bar{\bar{\bar{\chi}}}\right]_{ijk} = \left.\frac{\partial^2 \mathcal{P}_i}{2!\,\partial \mathcal{E}_j \partial \mathcal{E}_k}\right|_{\vec{\mathcal{E}}=\vec{0}} \qquad \epsilon_0 \left[\bar{\bar{\bar{\bar{\chi}}}}\right]_{ijkl} = \left.\frac{\partial^3 \mathcal{P}_i}{3!\,\partial \mathcal{E}_j \partial \mathcal{E}_k \partial \mathcal{E}_l}\right|_{\vec{\mathcal{E}}=\vec{0}} \tag{2.10}$$

and i, j, k, l = 1, 2, 3 refer to the components in a Cartesian reference frame. Equation (2.9) uses the dyad notation where $\vec{\mathcal{E}}\,\vec{\mathcal{E}}$ is a second order tensor with components

$$\left[\vec{\mathcal{E}}\,\vec{\mathcal{E}}\right]_{ij} = \mathcal{E}_i \mathcal{E}_j \tag{2.11}$$

and $\vec{\mathcal{E}}\,\vec{\mathcal{E}}\,\vec{\mathcal{E}}$ and $\vec{\mathcal{E}}\,\vec{\mathcal{E}}\,\vec{\mathcal{E}}\,\vec{\mathcal{E}}$ are similarly defined third and fourth rank tensors with components $\left[\vec{\mathcal{E}}\,\vec{\mathcal{E}}\,\vec{\mathcal{E}}\right]_{ijk} = \mathcal{E}_i \mathcal{E}_j \mathcal{E}_k$ and $\left[\vec{\mathcal{E}}\,\vec{\mathcal{E}}\,\vec{\mathcal{E}}\,\vec{\mathcal{E}}\right]_{ijkl} = \mathcal{E}_i \mathcal{E}_j \mathcal{E}_k \mathcal{E}_l$. The symbols : and $\vdots$ in (2.9)

respectively denote sums on two and three indices. Inclusion of Taylor series' coefficients 2! and 3! in the susceptibilities in (2.10) rather than in (2.9) is customary and terms beyond those shown in (2.9) are rarely used in practice [32].

In the expansion of (2.9) it is assumed that the polarization density vanishes when $\vec{\mathcal{E}} = \vec{0}$. This is true for most dielectrics and in particular Kerr media. For large electric field magnitudes the polarization density may approximately become independent of the electric field. For this nonlinear saturation phenomena a Taylor series expansion around the saturation electric field is more appropriate than (2.9). For fields and materials relevant to this thesis saturation related nonlinearities are not important even for breakdown electric fields. Thus saturation related phenomena is not in the scope of this thesis.

When media exhibit symmetries, certain components of suspectibility tensors vanish and others turn out to be identical. As an example, for isotropic materials suspectibility tensors reduce to constants. Another example is media with inversion symmetry for which reversing the sign $\vec{\mathcal{E}}$ also reverses the sign of $\vec{\mathcal{P}}$. For such media $\overline{\overline{\chi}}$ and any higher order suspectibility tensor multiplying even powers of electric field components in (2.9) vanish. Inversion symmetry is important in this work as it explains why the Kerr electro-optic birefringence depends on the second power of the electric field magnitude (Section 2.5) as opposed to Pockels effect birefringence in asymmetric crystals which depends on the first power of the electric field.

2.3 Isotropic Light Propagation

2.3.1 Linear Media

In the absence of the applied electric field, Kerr media are isotropic and linear. This section discusses light propagation in linear isotropic media and underlines various approximations used in this work. We use lower case letters $\vec{e}$, $\vec{d}$, $\vec{h}$ and $\vec{b}$ to denote the field quantities of light and $\epsilon = n^2\epsilon_0$ to denote the optical permittivity constant in non-magnetic media where n is the isotropic refractive index. There are no light sources within Kerr media and thus for light propagation the space charge density and current density vanish.

In uniform linear isotropic source-free media, taking the curl of (2.1a) and using

(2.1b) with the identity

$$\vec{\nabla} \times \vec{\nabla} \times \vec{e}(\vec{r},t) = \vec{\nabla}\vec{\nabla} \cdot \vec{e}(\vec{r},t) - \vec{\nabla}^2 \vec{e}(\vec{r},t) \tag{2.12}$$

Maxwell's equations (2.1) and the constitutive laws (2.2) and (2.7) yield

$$\vec{\nabla}^2 \vec{e}\ (\vec{r},t) = \mu_0 \epsilon \frac{\partial^2 \vec{e}\ (\vec{r},t)}{\partial t^2} \tag{2.13a}$$

$$\vec{\nabla} \cdot \vec{e}\ (\vec{r},t) = 0 \tag{2.13b}$$

Here (2.13a) is the wave equation and (2.13) governs the wave solutions of Maxwell's equations or electromagnetic waves and in particular light in a uniform linear isotropic medium.

The sinusoidal steady state solutions to Maxwell's equations are called monochromatic waves. The sinusoidal steady state solutions are most conveniently expressed by the time dependence $\exp(i\omega t)$ and *time independent* complex amplitudes $\vec{e}$, $\vec{d}$, $\vec{h}$ and $\vec{b}$ which are related to the real time fields by

$$\vec{e}(\vec{r},t) = \mathfrak{Re}\left\{\vec{e}(\vec{r})e^{i\omega t}\right\} \qquad \vec{d}(\vec{r},t) = \mathfrak{Re}\left\{\vec{d}(\vec{r})e^{i\omega t}\right\} \tag{2.14}$$

$$\vec{h}(\vec{r},t) = \mathfrak{Re}\left\{\vec{h}(\vec{r})e^{i\omega t}\right\} \qquad \vec{b}(\vec{r},t) = \mathfrak{Re}\left\{\vec{b}(\vec{r})e^{i\omega t}\right\} \tag{2.15}$$

where $i = \sqrt{-1}$, $\mathfrak{Re}$ denotes the real part of the complex argument, and ω is the radian frequency.

Most electromagnetic wave phenomena is investigated in terms of monochromatic waves. The analysis can then be extended to arbitrary time domain phenomena utilizing Fourier analysis [31]. The frequency bandwidth of the laser light used in Kerr electro-optic measurements is so narrow that no such analysis is needed in this work.

We proceed assuming solutions of the form

$$\vec{e}\,(\vec{r}) = \vec{e}\exp(-i\vec{k} \cdot \vec{r}) \tag{2.16}$$

in (2.13). Here $\vec{k}$ is the position independent wavevector and the conditions for (2.16) to be a solution to (2.13) are found by substitution

$$k^2 = \mu_0 \epsilon \omega^2 \tag{2.17}$$

$$\vec{k} \cdot \vec{e} = 0 \tag{2.18}$$

The solutions of the form given in (2.16) are known as transverse plane waves. They describe waves traveling in the direction of $\vec{k}$ and whose wave fronts are uniform in the plane perpendicular to $\vec{k}$. The propagation direction $\vec{k}$ and its magnitude k are respectively called the wavevector and wavenumber. Equation (2.17) relates the magnitude of the wavevector to the frequency, magnetic permeability and permittivity and is known as the dispersion relation. Equation (2.18) shows that the plane wave electric field vector can only have components in the direction transverse to the propagation direction in isotropic media.

Plane waves are widely used to understand the characteristics of light propagation. However no light source and in particular lasers do not output plane waves as that would require an infinite aperture width. In fact lasers output a Gaussian beam whose wave front is nonuniform in the directions perpendicular to $\vec{k}$.

Once there is a nonuniformity in the initial wave front, this nonuniformity changes as light propagates. In particular, propagation of Gaussian beams in isotropic media is well understood and leads to the result that the beam expands as it propagates. This diffraction effect is negligible for small propagation distances much less than $\pi a^2/\lambda$ where a is the radius of the optical beam and λ is the optical wavelength [30]. Then the beam can be treated as a plane wave. For a 0.5 mm radius light beam of wavelength 600 nm $\pi a^2/\lambda$ is around 1 meter.

For two dimensional Kerr electro-optic measurements the beam radius is typically expanded to $\approx$ 10 mm and the light path is on the order of 10 cm and thus diffraction effects can be safely neglected for the typical light wavelength of 600 nm. For point measurements the initial light beam radius is on the order of 1 mm and for typical propagation distances on the order of 10 cm the beam expands less than 1.1 times of its original size. In this work this slight diffraction effect is neglected in the development and light propagation equations are developed exclusively with plane waves.

2.3.2 Absorption And Complex Permittivity

The constitutive law of (2.5) with real suspectibilities implies that the optical electric field and the optical polarization density are in phase. This means that any change in the electric field instantaneously changes the polarization density. The molecular origins of polarization are briefly reviewed in Section 2.5. We here note that not all underlying processes of polarization can follow the optical frequencies and the response of the medium can not be approximated to be instantaneous. In fact some processes

are so slow that they can be neglected for optical frequencies. For others however, inverse relaxation time constants are on the order of optical frequencies. For sinusoidal steady state solutions this causes phase differences between the electric field and the polarization density which results in complex permittivity.

If the permittivity is complex (2.17) shows that the wave vector is also complex. It then follows from (2.16) that the light attenuates as it propagates. For light propagation equations developed in this chapter this absorption is neglected completely, as the transparency of the Kerr medium implies that the absorption is small. Secondly, the polarization dependence of absorption is not expected to be significant for Kerr media. This implies that absorption can be modeled for birefringence measurements by a common multiplier to the polarization components and this does not effect the theory developed in this work.

2.3.3 Nonlinear Optics

In the nonlinear constitutive law of (2.9) the susceptibilities are functions of the frequency for optical electric fields. Furthermore when $\vec{\mathcal{E}}$ is composed of multiple frequency components, due to the nonlinear terms in (2.9) the polarization density contains additional frequency components that are not present in the electric field. As an illustration consider an optically nonlinear medium without inversion symmetry and an electric field with two frequency components

$$\begin{aligned}\vec{\mathcal{E}}(t) &= \mathfrak{Re}\left\{\vec{e}_1 \exp(i\omega_1 t) + \vec{e}_2 \exp(i\omega_2 t)\right\} \\ &= \frac{1}{2}\left\{\vec{e}_1 \exp[i\omega_1 t] + \vec{e}_1^{\,*} \exp[-i\omega_1 t] + \vec{e}_2 \exp[i\omega_2 t] + \vec{e}_2^{\,*} \exp[-i\omega_2 t]\right\} \end{aligned} \tag{2.19}$$

where we did not show any position dependence as it is not relevant to this discussion. Each term in (2.9) consists of multiple frequency components which can be expressed as

$$\begin{aligned}\vec{\mathcal{P}}(t) = \epsilon_0 \mathfrak{Re}\Bigg\{ & \bar{\bar{\chi}}(\omega_1)\cdot\vec{e}_1 \exp[i\omega_1 t] + \bar{\bar{\chi}}(\omega_2)\cdot\vec{e}_2 \exp[i\omega_2 t] + \frac{1}{2}\bar{\bar{\bar{\chi}}}(0) : \left[\vec{e}_1\vec{e}_1^{\,*} + \vec{e}_2\vec{e}_2^{\,*}\right] \\ & + \frac{1}{2}\bar{\bar{\bar{\chi}}}(2\omega_1) : \vec{e}_1\vec{e}_1 \exp[i2\omega_1 t] + \frac{1}{2}\bar{\bar{\bar{\chi}}}(2\omega_2) : \vec{e}_2\vec{e}_2 \exp[i2\omega_2 t] \\ & + \bar{\bar{\bar{\chi}}}(\omega_1+\omega_2) : \vec{e}_1\vec{e}_2 \exp[i(\omega_1+\omega_2)t] + \bar{\bar{\bar{\chi}}}(\omega_1-\omega_2) : \vec{e}_1\vec{e}_2^{\,*} \exp[i(\omega_1-\omega_2)t] \\ & + \frac{1}{4}\bar{\bar{\bar{\chi}}}(3\omega_1) \vdots \vec{e}_1\vec{e}_1\vec{e}_1 \exp[i3\omega_1 t] + \frac{1}{4}\bar{\bar{\bar{\chi}}}(3\omega_2) \vdots \vec{e}_2\vec{e}_2\vec{e}_2 \exp[i3\omega_2 t]\end{aligned}$$

$$+\frac{1}{4}\overset{\equiv}{\overset{\equiv}{\chi}}(\omega_1)\vdots\Big[3\vec{e}_1\vec{e}_1\vec{e}_1^{*}+6\vec{e}_1\vec{e}_2\vec{e}_2^{*}\Big]\exp[i\omega_1 t]+\frac{1}{4}\overset{\equiv}{\overset{\equiv}{\chi}}(\omega_2)\vdots\Big[3\vec{e}_2\vec{e}_2\vec{e}_2^{*}+6\vec{e}_1\vec{e}_1^{*}\vec{e}_2\Big]\exp[i\omega_2 t]$$
$$+\frac{3}{4}\overset{\equiv}{\overset{\equiv}{\chi}}(2\omega_1+\omega_2)\vdots\vec{e}_1\vec{e}_1\vec{e}_2\exp[j(2\omega_1+\omega_2)]+\frac{3}{4}\overset{\equiv}{\overset{\equiv}{\chi}}(2\omega_2+\omega_1)\vdots\vec{e}_1\vec{e}_2\vec{e}_2\exp[i(2\omega_2+\omega_1)t]$$
$$+\frac{3}{4}\overset{\equiv}{\overset{\equiv}{\chi}}(2\omega_1-\omega_2)\vdots\vec{e}_1\vec{e}_1\vec{e}_2^{*}\exp[i(2\omega_1-\omega_2)t]+\frac{3}{4}\overset{\equiv}{\overset{\equiv}{\chi}}(2\omega_2-\omega_1)\vdots\vec{e}_1^{*}\vec{e}_2\vec{e}_2\exp[i(2\omega_2-\omega_1)t]$$
$$+\cdots\Bigg\} \quad (2.20)$$

Equation (2.20) shows that beside the fundamental frequencies ω_1 and ω_2, the polarization density has frequency components at $2\omega_1$, $2\omega_2$, $\omega_1-\omega_2$, $\omega_1+\omega_2$, etc.

Particularly relevant to this work is when there is a single frequency component of the electric field $\omega=\omega_1=\omega_2$. Using $\vec{e}_1=\vec{e}$ and $\vec{e}_2=\vec{0}$ (2.20) reduces to

$$\vec{\mathcal{P}}(t)=\epsilon_0\mathfrak{Re}\Bigg\{\bar{\bar{\chi}}(\omega)\cdot\vec{e}\exp[i\omega t]+\frac{3}{4}\overset{\equiv}{\overset{\equiv}{\chi}}(\omega)\vdots\vec{e}\,\vec{e}\,\vec{e}^{*}\exp[i\omega t]+\frac{1}{2}\overset{\equiv}{\overset{\equiv}{\chi}}(0):\vec{e}\,\vec{e}^{*}$$
$$+\frac{1}{2}\overset{\equiv}{\overset{\equiv}{\chi}}(2\omega):\vec{e}\,\vec{e}\exp[i2\omega t]+\frac{1}{4}\overset{\equiv}{\overset{\equiv}{\chi}}(3\omega)\vdots\vec{e}\,\vec{e}\,\vec{e}\exp[i3\omega t]+\cdots\Bigg\} \quad (2.21)$$

The first term is the usual linear polarization and the second term leads to the optical Kerr effect which is described in the next paragraph. The third term in (2.21) is a dc field. Optical creation of a dc field is called rectification. The $\exp(i2\omega t)$ term causes the so called second harmonic generation. The $\exp(i3\omega t)$ term has little practical significance.

When the media is isotropic, changing the sign of $\vec{e}$ must cause a change of sign in $\vec{\mathcal{P}}$ (inversion symmetry) and thus the dc and double frequency terms are not present. Neglecting the triple frequency term and noting that suspectibility tensors reduce to constants due to isotropy, the polarization density has only the fundamental frequency term which reduces to

$$\vec{p}=\epsilon_0\Big[\chi(\omega)+\chi^{(3)}(\omega)\,|\vec{e}|^2\Big]\vec{e} \quad (2.22)$$

where for isotropic media $\overset{\equiv}{\overset{\equiv}{\chi}}(\omega)=\chi^{(3)}(\omega)\overset{\equiv}{\overset{\equiv}{I}}$ and $\bar{\bar{\chi}}(\omega)=\chi(\omega)\bar{\bar{I}}$. Thus the effective suspectibility is dependent on the intensity of the light. This effect is known as the optical Kerr effect. It causes self-focusing which inhibits the expansion of light beams.

Although we do not use any results due to nonlinear optics in this work, this section is included because it underlines the difference between the Kerr electro-optic effect

and optical Kerr effect. Equation (2.22) shows that the intensity of the light in Kerr electro-optic measurements must be chosen small enough or the effects due to the optical Kerr effect must be considered. This is also true for other nonlinear optical effects such as double harmonic generation. Finally the derivation of (2.20) clarifies the description of electro-optic effects which are similarly explained in Section 2.5.

2.4 Light-Frame, E-Frame and E_T-frame

Here we introduce three reference frames which are necessary to simplify the description of the Kerr electro-optic effect and the derivation of the governing equations of light propagation in Kerr media which constitute the remainder of this chapter.

2.4.1 Light-Frame

The light-frame is fixed to the propagation direction of light which we denote with the unit vector $\hat{s}$. We choose $\hat{s}$ to be the third coordinate direction of the light-frame. The other two directions transverse to the propagation direction are necessary to form a right handed coordinate frame and are denoted by $\hat{m}$ as the first coordinate direction and $\hat{p}$ as the second coordinate direction. When light propagates parallel to the optical table, $\hat{m}$ (or $\hat{p}$) is often chosen to be the direction perpendicular to the optical table. The respective coordinates are m, p and s and the respective components of a vector $\vec{v}$ are denoted by v_m, v_p and v_s.

The light frame is fundamental and often serves as the fixed frame for light propagation phenomena both in general and in the Kerr electro-optic literature. In this work however a distinction is necessary as in Part II we discuss the reconstruction of the applied electric field from intensity measurements obtained from light propagating in different directions.

2.4.2 E-Frame

The E-frame is fixed to the direction of the applied electric field and is useful for the optical constitutive law for Kerr media as the permittivity tensor is diagonal in this frame (Section 2.5.2). We choose the direction of the applied electric field to be the third coordinate direction of the E-frame which is denoted by $\hat{i}_{\|_0}$. The other two directions necessary to form a right handed coordinate frame are denoted by $\hat{i}_{\perp_0^1}$ and

$\hat{i}_{\perp_0^2}$. To simplify future development $\hat{i}_{\perp_0^1}$ is chosen to be the unit vector perpendicular to the electric field in the plane formed by the electric field and the propagation direction of the light. The E-frame is only used in Sections 2.5 and 2.6 and we use the subscripts 0 for $\perp$ and $\|$ for E-frame to reserve the subscript free versions for the E_T-frame of Section 2.4.3 which is more fundamental in this work. The E-frame is illustrated in Figure 2.1 in terms of the light-frame. We use $v_{\perp_\circ^2}$, $v_{\perp_\circ^1}$ and $v_{\|_\circ}$ to identify the components of a vector $\vec{v}$ in the E-frame.

$$\vec{v} = v_{\perp_\circ^1}\hat{i}_{\perp_0^1} + v_{\perp_\circ^2}\hat{i}_{\perp_0^2} + v_{\|_\circ}\hat{i}_{\|_0} \tag{2.23}$$

2.4.3 E_T-Frame

The component of the applied electric field transverse to the propagation direction of light is denoted by $\vec{E}_T$ as shown in Figure 2.1. In this work $\vec{E}_T$ is more fundamental than the applied electric field $\vec{E}$ itself. It is shown in Section 2.6.1 that the electric field induced birefringence effects to a very good approximation depend only on $\vec{E}_T$. Thus the E_T-frame which is fixed to $\vec{E}_T$ is particularly useful. The direction of $\vec{E}_T$ in the *mp*-plane is denoted by $\hat{i}_\|$ and constitutes the first coordinate direction of the E_T-frame. The third coordinate direction of the E_T-frame is the light propagation direction $\hat{s}$. The second coordinate direction in the *mp*-plane is found from $\hat{i}_\|$ and $\hat{s}$ to complete the right handed coordinate frame and denoted by $\hat{i}_\perp$. These components of a vector $\vec{v}$ in the E_T-frame are denoted by $v_\|$, $v_\perp$ and v_s.

The angle between $\hat{i}_\|$ and $\hat{m}$ is denoted by φ. For spatially varying applied electric fields φ changes with s as light propagates thus the E_T-frame rotates with respect to the light-frame. For this reason, in the literature frames similar to the E_T-frame are sometimes called rotating frames.

The theory of Kerr electro-optic measurements can be built using either the E_T-frame or light-frame alone. However certain relationships are easier to derive in one frame than the other and using both frames allows sanity checks which often prove to be useful in the development of this work. Throughout this thesis we use both the light-frame and the E_T-frame extensively.

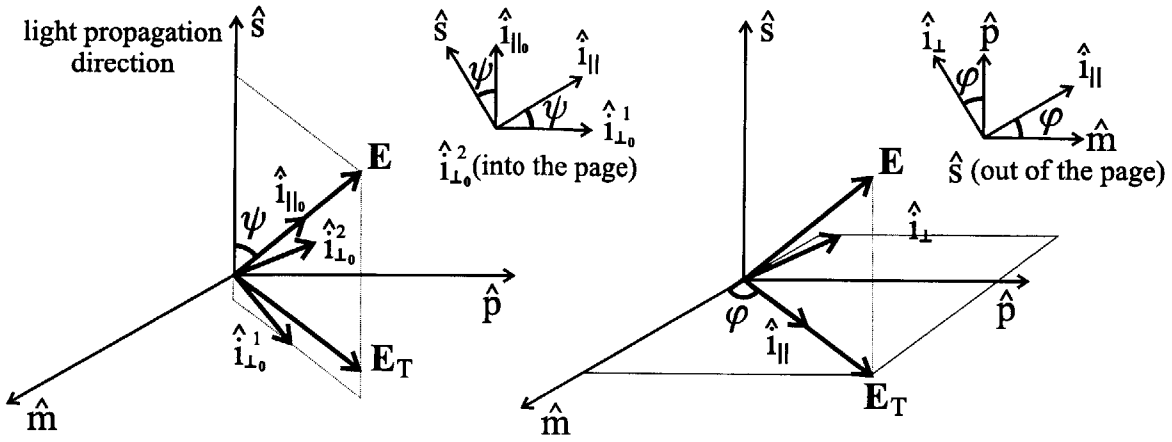

Figure 2.1: The illustrations of the unit vectors of the E-frame and E_T-frame in terms of the light-frame. $\vec{E}_T$ is the transverse component of the applied electric field $\vec{E}$ with respect to the light propagation direction $\hat{s}$; φ is the angle between the transverse field $\vec{E}_T$ and the m-axis and ψ is the angle between the electric field $\vec{E}$ and the propagation direction of the light along the $\hat{s}$ axis.

2.5 The Kerr Electro-Optic Effect

2.5.1 Electro-Optic Effects

Electro-optic effects refer to cases where an externally applied quasistatic electric field modifies the optical susceptibility tensor of a transparent medium changing the characteristics of the light. Macroscopic description of electro-optic effects can be based on the nonlinear constitutive law in (2.20). The real total electric field $\vec{\mathcal{E}}$ is composed of the quasistatic field $\vec{E}$ and the real part of the complex light electric field $\vec{e}$ which respectively replace $\vec{e}_1$ and $\vec{e}_2$ in (2.19)

$$\vec{\mathcal{E}}(t) = \vec{E}(t) + \frac{1}{2}\vec{e}\exp(i\omega t) + \frac{1}{2}\vec{e}^{*}\exp(-i\omega t) \tag{2.24}$$

Resulting multiple frequency polarization density $\vec{\mathcal{P}}$ can be found by substituting $\omega_1 = 0$ and $\omega_2 = \omega$ in (2.20). $\vec{\mathcal{P}}$ has quasistatic components, components at the fundamental frequency ω and higher order components in integer multiples of ω.

For most applications of the electro-optic effect, including this work, the light electric field is small and introduces only a small perturbation on top of the quasistatic field. The linear quasistatic constitutive law remains the same. As the light electric field is small, nonlinear phenomena of second or higher order in the optical electric

field such as the optical Kerr effect and second harmonic generation are negligible. The (complex) optical polarization density then contains fundamental frequency terms which are linear in the optical electric field

$$\vec{p} = \epsilon_0 \bar{\bar{\chi}}(\omega) \cdot \vec{e} + \underbrace{2\epsilon_0 \bar{\bar{\bar{\chi}}}(\omega) : \vec{E}\,\vec{e}}_{\text{Pockels' Effect}} + \underbrace{3\epsilon_0 \bar{\bar{\bar{\bar{\chi}}}}(\omega) \vdots \vec{E}\vec{E}\,\vec{e}}_{\text{Kerr Effect}} + \cdots \tag{2.25}$$

Equation (2.25) describes electro-optic effects where the optical polarization density depends on the quasistatic electric field. The terms linear and quadratic in the quasistatic electric field are respectively called Pockels' and Kerr electro-optic effects. Terms higher than quadratic in the quasistatic field have no practical significance.

When present Pockels' effect is often much stronger than the Kerr effect. For media that exhibit inversion symmetry however, the Pockels' effect vanishes as the reversal of sign in the *total* electric field must cause a reversal of sign in the *total* polarization density component. Thus the Pockels' effect is mostly important in solids that have an asymmetric crystal structure. The Pockels' effect is typically utilized in light modulators [30]. For gases, liquids and isotropic solids the Kerr effect is the predominant electro-optic effect.

2.5.2 Macroscopic Description Of The Kerr Effect

Kerr media are isotropic in the absence of the applied electric field. Thus $\bar{\bar{\chi}}$ in (2.25) reduces to an optical susceptibility constant χ. The Pockels' effect term identically vanishes due to inversion symmetry. As Kerr media are isotropic in the absence of electric field, the applied electric field direction constitutes the only preferred direction and the perpendicular directions are degenerate. Thus it is intuitively clear that most components of $\bar{\bar{\bar{\bar{\chi}}}}$ in (2.25) should be identical and (2.25) assumes a simple form for Kerr media. This form is most easily realized in the E-frame.

We begin with the component form of (2.25) in the E-frame

$$p_i = \epsilon_0 \chi e_i + 3\epsilon_0 \sum_{j,k,l} \left[\bar{\bar{\bar{\bar{\chi}}}}\right]_{iklj} E_k E_l e_j \quad i,\, j,\, k,\, l = \perp_\circ^2,\, \perp_\circ^1,\, \|_\circ \tag{2.26}$$

Since $E_{\perp_\circ^2} = E_{\perp_\circ^1} = 0$ and $|E_{\|_\circ}|$ is equal to E the magnitude of $\vec{E}$, equation (2.26) reduces to

$$p_i = \epsilon_0 \chi e_i + 3\epsilon_0 E^2 \sum_j \left[\bar{\bar{\bar{\bar{\chi}}}}\right]_{i\|_\circ\|_\circ j} e_j \quad i,\, j = \perp_\circ^1,\, \perp_\circ^2,\, \|_\circ \tag{2.27}$$

An optical field along the applied electric field must not yield an optical polarization density component in the plane perpendicular to the electric field direction since all directions in this plane are degenerate. Furthermore any rotation around the electric field must leave $\overline{\overline{\overline{\chi}}}$ unmodified. It follows that the only nonzero components of $\overline{\overline{\overline{\chi}}}$ are $\chi^{(3)}_{\perp_o^2 \parallel_o \parallel_o \perp_o^2}$, $\chi^{(3)}_{\perp_o^1 \parallel_o \parallel_o \perp_o^1}$ and $\chi^{(3)}_{\parallel_o \parallel_o \parallel_o \parallel_o}$ where we used the superscript (3) to differentiate the components of $\overline{\overline{\overline{\chi}}}$ from the optical susceptibility constant χ. Furthermore again, due to degeneracy in the plane perpendicular to the electric field $\chi^{(3)}_{\perp_o^2 \parallel_o \parallel_o \perp_o^2} = \chi^{(3)}_{\perp_o^1 \parallel_o \parallel_o \perp_o^1}$. Thus for Kerr media (2.25) reduces to

$$\vec{p} = \epsilon_0 \overline{\overline{\chi}}_m \cdot \vec{e} \tag{2.28}$$

where $\overline{\overline{\chi}}_m$ is a second rank tensor which is diagonal in the E-frame

$$[\overline{\overline{\chi}}_m] = \begin{bmatrix} \chi + 3\chi^{(3)}_{\perp_o \parallel_o \parallel_o \perp_o} E^2 & 0 & 0 \\ 0 & \chi + 3\chi^{(3)}_{\perp_o \parallel_o \parallel_o \perp_o} E^2 & 0 \\ 0 & 0 & \chi + 3\chi^{(3)}_{\parallel_o \parallel_o \parallel_o \parallel_o} E^2 \end{bmatrix} \tag{2.29}$$

The permittivity tensor corresponding to (2.29) is also diagonal in the E-frame with components $\epsilon_{\parallel_o}$ and $\epsilon_{\perp_o}$. It follows from $\overline{\overline{\epsilon}} = \epsilon_0 \left[\overline{\overline{I}} + \overline{\overline{\chi}}_m\right]$ and (2.29) that

$$\Delta\epsilon \equiv \epsilon_{\parallel_o} - \epsilon_{\perp_o} = 2\lambda B \sqrt{\epsilon_0 \epsilon} E^2 \tag{2.30}$$

where $2\lambda B\sqrt{\epsilon_0\epsilon} = 4\epsilon_0(\chi^{(3)}_{\parallel_o \parallel_o \parallel_o \parallel_o} - \chi^{(3)}_{\perp_o \parallel_o \parallel_o \perp_o})$. Clearly without any physical arguments and/or experiments it is not possible to predict the magnitude of B. However within the framework of optics the nonlinearities and the anisotropic effects of the applied electric field are expected to be small

$$\frac{|\epsilon_{\parallel_0} - \epsilon_{\perp_0}|}{\epsilon_0}, \frac{|\epsilon_{\parallel_0} - \epsilon|}{\epsilon_0}, \frac{|\epsilon - \epsilon_{\perp_0}|}{\epsilon_0} \ll 1 \tag{2.31}$$

Using (2.31), (2.30) can be expressed in terms of the refractive index

$$\Delta n = n_{\parallel_o} - n_{\perp_o} = \frac{1}{\sqrt{\epsilon_0}} \left(\sqrt{\epsilon_{\parallel_o}} - \sqrt{\epsilon_{\perp_o}}\right) = \frac{\Delta\epsilon}{2\sqrt{\epsilon_0\epsilon}} + O\left[\left(\frac{\Delta\epsilon}{\epsilon_0}\right)^2\right] \tag{2.32}$$

$$\approx \lambda B E^2 \tag{2.33}$$

which is identical to (1.9).

2.5.3 The Microscopic Description and The Kerr Constant

We consider (1.9) (or (2.33)) to be a macroscopic relationship which follows from the nonlinear electric constitutive law as described in Section 2.5.2 and build the theory of Kerr electro-optic measurements solely upon it. Although the microscopic origins of the Kerr effect are not explicitly used in the rest of the thesis, here we provide a brief discussion to give a physical background and to underline some microscopic results which are important to the Kerr electro-optic measurement theory.

Internal Electric Field

The microscopic description of the Kerr electro-optic effect is a part of the electric polarization theory of dielectrics. This description requires modeling the influences of the applied electric field on individual molecules and molecular interactions in the presence of the applied electric field. Much of the modeling complexity in electric polarization theory is due to molecular interactions and is often handled by using the so called internal electric field which is defined as the total electric field at the position of the particle minus the field due to the particle itself [33]. The influences on individual molecules are then described in terms of the internal field and various models are used to express the internal electric field in terms of the applied electric field.

The earliest model for the internal electric field uses the electric field inside a spherical cavity in a otherwise homogeneous medium under the influence of a constant applied electric field. This field can be found by solving Laplace's equation for the scalar electric potential with electric field boundary conditions [2, 33]

$$\vec{E}_I = \frac{\epsilon_s + 2\epsilon_0}{3\epsilon_0}\vec{E} \tag{2.34}$$

where we use $\vec{E}_I$ to denote the internal electric. Equation (2.34) is called the Lorentz equation. Although (2.34) is written for the quasistatic electric field we assume it is valid for optical fields as well if the radius of the spherical cavity is much less than a wavelength. More advanced treatment of the internal field is beyond the scope of this thesis.

The Dipole Moment

Central to the electric polarization theory is the dipole moment $\vec{\mu}$ of a molecule which is a measure of the relative displacement of positive and negative charges. For an atomic

model of a point charge nucleus surrounded by an electron cloud the dipole moment of a molecule is

$$\vec{\mu} = q(\vec{r}_+ - \vec{r}_-) \tag{2.35}$$

where q is the sum of positive (or equal amount of negative) charges of the nuclei of individual atoms in the molecule and $\vec{r}_+$ and $\vec{r}_-$ are the centers of charge of the nuclei and the electron cloud respectively. The dipole moment generalizes to other atomic models and in particular can be defined in terms of wave functions in quantum mechanics.

Most nonsymmetric molecules have permanent dipole moments. The molecules with relatively high permanent dipole moment magnitudes are said to be polar. We denote the permanent dipole moment by $\vec{\mu}_p$.

Polarization Components

When an electric field is applied to a dielectric medium it affects the relative positions of negative and positive charges through the Coulomb force and polarizes the molecule; the dipole moments of individual molecules are modified. The quasistatic and optical macroscopic polarization densities $\vec{P}$ and $\vec{p}$ have the dimensions of dipole moment per unit volume and are measures of these changes averaged over all molecules in a macroscopic volume.

There are three fundamental mechanisms that an applied electric can polarize a molecule

1. Electronic Polarization
2. Atomic Polarization
3. Orientation Polarization

Electronic polarization is due to the shift in electrons' relative positions to the positive charges. The displacements of the atoms of a molecule relative to each other give rise to the atomic polarization. The internal electric field strength is typically much smaller than the intermolecular fields and the dipole moment change of an individual molecule under the influence of the field can be linearized to yield

$$\vec{\mu}_{i_s} = \bar{\bar{\alpha}} \cdot \vec{E}_I \tag{2.36}$$

$$\vec{\mu}_{i_o} = \bar{\bar{\beta}} \cdot \vec{e}_I \tag{2.37}$$

where $\vec{\mu}_{i_s}$ and $\vec{\mu}_{i_o}$ are the quasistatic and optical induced dipole moments, $\bar{\bar{\alpha}}$ and $\bar{\bar{\beta}}$ are quasistatic and optical polarizabilities and $\vec{E}_I$ and $\vec{e}_I$ are quasistatic and optical internal electric fields.

In the absence of the applied electric field each molecule is randomly oriented and each direction for permanent dipole moments are equally likely. On the macroscopic scale the total dipole moment averages out leaving zero net polarization density. When an applied electric field is present there is an aligning torque on the dipoles which is opposed by the thermal agitation. A statistical average yields a net orientation polarization.

The relaxation time constants of the polarization effects are not the same. The electronic polarization is the fastest and can be assumed instantaneous for optical and quasistatic fields. The atomic polarization is relatively slower and its inverse relaxation time constant can be on the order of the optical frequencies causing absorption. Compared to electronic and atomic polarization, orientation polarization is sluggish and does not effect optical polarization.

Statistical Average Of Dipole Moments

In the presence of an external field, the potential energy of molecules vary with the orientation due to permanent and induced dipoles. The orientation of a molecule is best described in terms of a coordinate system fixed to the molecule and the Euler angles $\boldsymbol{\theta}_\mathbf{m} = (\theta_m, \varphi_m, \psi_m)$ which describe the orientation of the molecular system as shown in Figure 2.2. The molecular system is typically chosen such that the quasistatic and/or optical polarizabilities are diagonal. The orientation potential energy w is typically much smaller than the thermal energy so that the relative number of particles pointing between a direction $\boldsymbol{\theta}_\mathbf{m}$ and $\boldsymbol{\theta}_\mathbf{m} + d\boldsymbol{\theta}_\mathbf{m}$ is given by the Boltzmann distribution law

$$\frac{dN(\boldsymbol{\theta}_\mathbf{m})}{N} = \frac{1}{Z} \exp\left[-w(\boldsymbol{\theta}_\mathbf{m})/kT\right] \sin\theta_m \, d\theta_m \, d\varphi_m \, d\psi_m \tag{2.38}$$

where Z is the normalization factor

$$Z = \int_{\psi_m=0}^{2\pi} \int_{\varphi_m=0}^{2\pi} \int_{\theta_m=0}^{\pi} \exp\left[-w(\boldsymbol{\theta}_\mathbf{m})/kT\right] \sin\theta_m \, d\theta_m \, d\varphi_m \, d\psi_m \tag{2.39}$$

k is the Boltzman constant and T is the absolute temperature.

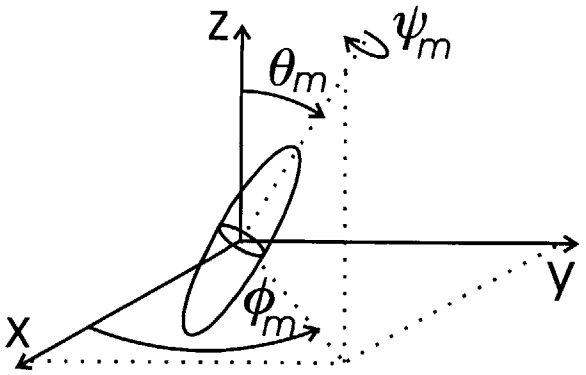

Figure 2.2: The Euler angles that describe the position of a molecule with respect to the fixed cartesian frame [34]. Here the molecule is represented by an ellipsoid.

Under the influence of a quasistatic applied electric field the total dipole moment of an individual molecule is the sum of the permanent and induced dipole moments

$$\vec{\mu}_s = \vec{\mu_p} + \vec{\mu}_{i_s} = \vec{\mu_p} + \bar{\bar{\alpha}} \cdot \vec{E}_I \tag{2.40}$$

and the orientation potential energy of such a molecule is given as

$$w = -\vec{\mu_p} \cdot \vec{E}_I - \frac{1}{2}\vec{E}_I \cdot \bar{\bar{\alpha}} \cdot \vec{E}_I \tag{2.41}$$

Here the first term is due to the torque on the permanent dipole moment by the applied field and the second term is similar to the well-known spring potential energy and follows from (2.36). Clearly (2.41) depends on the molecular orientation with respect to the applied electric field. The statistical average of dipole moments follows from (2.38)

$$< \vec{\mu}_s >= \frac{1}{Z} \int_{\psi_m=0}^{2\pi} \int_{\varphi_m=0}^{2\pi} \int_{\theta_m=0}^{\pi} \vec{\mu}_s(\boldsymbol{\theta}_\mathbf{m}) \exp\left[-w(\boldsymbol{\theta}_\mathbf{m})/kT\right] \sin\theta_m \, d\theta_m \, d\varphi_m \, d\psi_m \tag{2.42}$$

where $\vec{\mu}_s$ and w are respectively given in (2.40) and (2.41) and the average is taken over all possible molecular orientations.

For isotropic materials stressed by an applied electric field the only preferred direction is that of the applied electric field. Thus the statistical average of any component of the dipole moment perpendicular to the applied electric field is zero. Even with this simplification analytical evaluation of (2.42) is in general not possible. However since $w(\boldsymbol{\theta}_\mathbf{m}) \ll kT$ the exponential terms in the numerator and denominator (Z) of (2.42)

can be Taylor series expanded in E_I for which the linear term can be found as

$$< \vec{\mu}_s >= \left[\overline{\alpha} + \frac{\mu_p^2}{3kT}\right] \vec{E}_I \tag{2.43}$$

Here $\overline{\alpha}$ is the average quasistatic polarizability and (2.43) relates the statistical average of the dipole moments to the quasistatic (internal) electric field and molecular parameters.

For optical fields orientation of molecules cannot follow the optical electric field frequency and the permanent dipole moments do not contribute to the polarization. Thus the permanent dipole term in (2.43) drops out yielding

$$< \vec{\mu}_o >= \overline{\beta}\, \vec{e}_I \tag{2.44}$$

where $\overline{\beta}$ is the average optical polarizability, $\vec{\mu}_o$ is the optical dipole moment and we used lower case $\vec{e}_I$ to differentiate the optical internal electric field from that of the quasistatic field $\vec{E}_I$.

Permittivity In Terms Of Dipole Moments

Using the Lorentz internal field in (2.34) and (2.43) we obtain

$$(\epsilon_s - \epsilon_0)\vec{E} = \vec{P} = N < \vec{\mu}_s >= N \left[\overline{\alpha} + \frac{\mu_p^2}{3kT}\right] \vec{E}_I \tag{2.45}$$

$$= \frac{\epsilon_s + 2\epsilon_0}{3\epsilon_0} N \left[\overline{\alpha} + \frac{\mu_p^2}{3kT}\right] \vec{E} \tag{2.46}$$

which reduces to

$$\frac{\epsilon_s - \epsilon_0}{\epsilon_s + 2\epsilon_0} = \frac{N}{3\epsilon_0} \left[\overline{\alpha} + \frac{\mu_p^2}{3kT}\right] \tag{2.47}$$

Here N is the particle density. Equation (2.47) is the well known Clausius-Mossotti equation and expresses the dielectric constant ϵ_s in terms of molecular quantities.

The Clausius-Mossotti equation can also be used for optical fields by neglecting the permanent dipole term

$$\frac{\epsilon - \epsilon_0}{\epsilon + 2\epsilon_0} = \frac{N\overline{\beta}}{3\epsilon_0} \tag{2.48}$$

Statistical Average Of Dipole Moments For Kerr Media

We assume that in the presence of the quasistatic field and the weak intensity optical field, the orientational potential energy of the molecule is completely determined by the quasistatic electric field. Then the quasistatic component of the statistical average of the dipole moments remains the same leaving (2.43) unchanged. For optical frequency components the medium becomes anisotropic and the average dipole moment depends on the direction of the optical field. If the optical field is in the same direction as the quasistatic applied electric field then the average dipole moment is given as

$$< \mu_{||_o} >= \frac{e_I}{Z} \int_{\psi_m=0}^{2\pi} \int_{\varphi_m=0}^{2\pi} \int_{\theta_m=0}^{\pi} \hat{E} \cdot \bar{\bar{\beta}}(\boldsymbol{\theta}_\mathbf{m}) \cdot \hat{E} \exp\left[-w(\boldsymbol{\theta}_\mathbf{m})/kT\right] \sin\theta_m \, d\theta_m \, d\varphi_m \, d\psi_m \tag{2.49}$$

where $\mu_{||_o}$ is the component of the optical permanent dipole along the applied electric field and $\hat{E}$ is the unit vector along the applied electric field. Equation (2.49) can again be Taylor expanded in E_I with the first and second terms yielding

$$< \mu_{||_o} >= \left[\overline{\beta} + \frac{k_m}{45} E_I^2\right] e_I \tag{2.50}$$

where

$$k_m = \frac{b_1}{kT} + \frac{b_2}{(kT)^2} \tag{2.51}$$

with

$$b_1 = (\beta_1 - \beta_2)(\alpha_1 - \alpha_2) + (\beta_2 - \beta_3)(\alpha_2 - \alpha_3) + (\beta_3 - \beta_1)(\alpha_3 - \alpha_1) \tag{2.52a}$$

$$b_2 = (\beta_1 - \beta_2)(\mu_{p_1}^2 - \mu_{p_2}^2) + (\beta_2 - \beta_3)(\mu_{p_2}^2 - \mu_{p_3}^2) + (\beta_3 - \beta_1)(\mu_{p_3}^2 - \mu_{p_1}^2) \tag{2.52b}$$

Here β_i and α_i are optical and static polarizability components in the molecular frame for which the polarizability tensor is diagonal and μ_{p_i} are the components of the permanent dipole moment in the same frame. Equation (2.50) shows how the statistical average of the optical dipole moment along the applied quasistatic electric field changes from its isotropic value in (2.44). The physical significance of (2.52) is discussed in a simplified form in the following sections.

The average dipole moment $< \mu_{\perp_o} >$ when the optical electric field is perpendicular to the quasistatic field can also be found by approximately evaluating an integral similar

to (2.49) with $\hat{E}$ replaced by a unit vector perpendicular to the applied electric field. However due to its direct relevance to macroscopic theory we here note a theorem which relates $< \mu_{\perp_o} >$ and $< \mu_{||_o} >$ to the isotropic dipole moment average given in (2.44)

$$< \mu_{||_o} > +2 < \mu_{\perp_o} >= 3\overline{\beta} e_I \tag{2.53}$$

Equation (2.53) follows only from geometrical arguments [35]. Substituting (2.50) in (2.53) yields

$$< \mu_{\perp_o} >= \left[\overline{\beta} - \frac{k_m}{90} E_I^2\right] e_I \tag{2.54}$$

Permittivity Components For Kerr Media

The Clausius-Mossotti equation for optical fields in (2.48) follows from (2.44) with a derivation similar to that of quasistatic fields in (2.45)-(2.46). By similar arguments with $< \vec{\mu}_o >$ replaced by $< \mu_{||_o} >$ in (2.50) and $< \mu_{\perp_o} >$ in (2.54) we obtain

$$\frac{\epsilon_{||_o} - \epsilon_0}{\epsilon_{||_o} + 2\epsilon_0} = \frac{N}{3\epsilon_0}\left[\overline{\beta} + \frac{k_m}{45} E_I^2\right] = \frac{\epsilon - \epsilon_0}{\epsilon + 2\epsilon_0} + \frac{N}{3\epsilon_0}\frac{k_m}{45} E_I^2 \tag{2.55}$$

$$\frac{\epsilon_{\perp_o} - \epsilon_0}{\epsilon_{\perp_o} + 2\epsilon_0} = \frac{N}{3\epsilon_0}\left[\overline{\beta} - \frac{k_m}{90} E_I^2\right] = \frac{\epsilon - \epsilon_0}{\epsilon + 2\epsilon_0} - \frac{N}{3\epsilon_0}\frac{k_m}{90} E_I^2 \tag{2.56}$$

where we used (2.48). The differences between the permittivity components $\epsilon_{||_o}$ and $\epsilon_{\perp_o}$, and isotropic permittivity ϵ are small so that

$$\frac{\epsilon_{||_o} - \epsilon}{\epsilon_0} + O\left[\left|\frac{\epsilon - \epsilon_{||_o}}{\epsilon}\right|^2\right] = \frac{(\epsilon + 2\epsilon_0)^2}{3\epsilon_0^2}\frac{N}{3\epsilon_0}\frac{k_m}{45} E_I^2 \tag{2.57}$$

$$\frac{\epsilon_{\perp_o} - \epsilon}{\epsilon_0} + O\left[\left|\frac{\epsilon - \epsilon_{\perp_o}}{\epsilon}\right|^2\right] = -\frac{(\epsilon + 2\epsilon_0)^2}{3\epsilon_0^2}\frac{N}{3\epsilon_0}\frac{k_m}{90} E_I^2 \tag{2.58}$$

and we neglect the second order terms. Using (2.34), (2.57) and (2.58) yields

$$\Delta\epsilon \equiv \epsilon_{||_o} - \epsilon_{\perp_o} = \frac{(\epsilon + 2\epsilon_0)^2}{3\epsilon_0}\frac{N}{3\epsilon_0}\frac{k_m}{30}\frac{(\epsilon_s + 2\epsilon_0)^2}{9\epsilon_0^2} E^2 \tag{2.59}$$

Equation (2.59) is identical to the macroscopic conclusion of (2.30). Also note that (2.57) and (2.58) yield

$$\epsilon_{||_o} = \epsilon + \frac{2\Delta\epsilon}{3} \tag{2.60a}$$

$$\epsilon_{\perp_o} = \epsilon - \frac{\Delta\epsilon}{3} \tag{2.60b}$$

Equation (2.60) yields

$$\epsilon_{||_o} + 2\epsilon_{\perp_o} = 3\epsilon \tag{2.61}$$

which is a direct consequence of (2.53). Equation (2.61) is important for macroscopic theory as it shows the difference between the isotropic permittivity and the permittivity components after the application of the quasistatic electric field.

The Kerr Constant

The Kerr constant can be identified from (2.59) and (2.30) as

$$B = \frac{N(\epsilon + 2\epsilon_0)^2}{18n\lambda\epsilon_0^3}\frac{k_m}{30}\frac{(\epsilon_s + 2\epsilon_0)^2}{9\epsilon_0^2} \tag{2.62}$$

Equation (2.62) is equivalent to the formula given in [36] for dilute gases. Accurate formulas for liquid dielectrics require a more advanced treatment of internal electric field and intermolecular interactions but are otherwise identical to (2.62) [36].

Physical implications of (2.62) are best understood on a molecule which is symmetric with respect to the first molecular axis and for which optical and static polarizabilities are equal ($\alpha_2 = \alpha_3 = \beta_2 = \beta_3$ and $\alpha_1 = \beta_1$). Then (2.52) reduces to

$$b_1 = 2(\alpha_1 - \alpha_2)^2 \tag{2.63}$$

$$b_2 = (\alpha_1 - \alpha_2)[(\mu_{p_1}^2 - \mu_{p_2}^2) + (\mu_{p_1}^2 - \mu_{p_3}^2)] = 2(\alpha_1 - \alpha_2)\mu_p^2(1 - \frac{3}{2}\sin^2\chi) \tag{2.64}$$

where χ is the angle between the molecular symmetry axis and the permanent dipole. We define

$$\Delta\alpha = \alpha_1 - \alpha_2 \tag{2.65}$$

So that (2.62) reduces to

$$B = \frac{N(\epsilon + 2\epsilon_0)^2}{9n\epsilon_0^3} \frac{\Delta\alpha}{30kT} \left[\Delta\alpha + \frac{\mu^2}{kT}(1 - \frac{3}{2}\sin^2\chi)\right] \frac{(\epsilon_s + 2\epsilon_0)^2}{9\epsilon_0^2} \tag{2.66}$$

This equation is identical to those given in [2,3] when corrections due to the Lorentz field are omitted.

Equation (2.66) shows that materials with symmetric molecules ($\Delta\alpha = 0$) exhibit no Kerr effect. This is not strictly true as in a more advanced treatment of the Kerr effect hyperpolarizibilities (higher rank tensors that are used to model nonlinearities in (2.36) and (2.37) analogous to higher rank suspectibilities in (2.9)) also contribute but are negligible for our purposes. Typically $\Delta\alpha$ is small so that the effect is most important in polar liquids ($\mu^2 \gg kT\Delta\alpha$). For some molecules like alcohols χ is around $\pi/2$ and B may be negative. For most materials $\chi \approx 0$ so that the Kerr constant is positive.

The values of Kerr constants range from order of 10^{-15}m/V^2 for typically non-polar dielectrics to order of 10^{-12}m/V^2 for strongly birefringent polar materials relevant to this work. Even for nitrobenzene which has the largest known Kerr constant among liquid dielectrics ($\approx 3 \times 10^{-12}$m/V^2), Δn is around 0.002 even at near breakdown electric fields ($\approx$ 300kV/cm) thus

$$\Delta n \ll 1 \tag{2.67}$$

which experimentally verifies (2.31).

2.6 Light Propagation In Homogeneous Kerr Media

2.6.1 Light Propagation In Homogeneous Uniaxial Media

In Sections 2.5.2 and 2.5.3 we showed that the optical permittivity tensor is diagonal in the E-frame

$$[\bar{\bar{\epsilon}}]_{\mathbf{E}} = \begin{bmatrix} \epsilon_{\perp_o} & 0 & 0 \\ 0 & \epsilon_{\perp_o} & 0 \\ 0 & 0 & \epsilon_{||_o} \end{bmatrix} \tag{2.68}$$

Here we use $[\ ]_{\mathbf{E}}$ to denote the matrix form of a second rank tensor in the E-frame and $\epsilon_{\perp_o}$ and $\epsilon_{||_o}$ are related by

$$\epsilon_{||_o} - \epsilon_{\perp_o} = 2\epsilon_0 n\lambda B E^2 \tag{2.69}$$

$$\epsilon_{||_o} + 2\epsilon_{\perp_o} = 3\epsilon \tag{2.70}$$

where ϵ is the isotropic permittivity constant in the absence of the electric field. The coordinate system for which the permittivity tensor is diagonal is often known as the principal system.

The permittivity tensor in (2.68) shows that the first two coordinate axes are degenerate. Such media are said to be uniaxial and the axis which exhibits the anisotropy is called the optic axis. Thus the characteristics of light propagation in Kerr media are identical to electromagnetic wave propagation in uniaxial media with the optic axis in the applied electric field direction. Electromagnetic (plane) wave propagation in homogeneous uniaxial media is well understood [30, 31]. Here we present a derivation similar to that in Haus [30].

For uniaxial media the permittivity tensor is not a scalar and Maxwell's equations for monochromatic waves do not reduce to (2.13) but to

$$\vec{\nabla} \times \vec{\nabla} \times \vec{e}(\vec{r}) = \omega^2 \mu_0 \vec{d}(\vec{r}) \tag{2.71}$$

$$\vec{\nabla} \cdot \vec{d}(\vec{r}) = 0 \tag{2.72}$$

We begin with the assumed plane-wave solution

$$\vec{e}(\vec{r}) = \vec{e}\exp(-i\underline{\vec{k}} \cdot \vec{r}) = \vec{e}\exp(-i\underline{k}s) \tag{2.73}$$

where s is the coordinate along the light propagation direction as described in Section 2.4.1 and we use $\underline{k}$ as a generic wavenumber to be determined in terms of permittivity components and the frequency. We use the underline to distinguish $\underline{k}$ from the isotropic wavenumber in (2.17). Substituting (2.73) into the left hand side of (2.71) and evaluating the curls in the light frame yields

$$\vec{\nabla} \times \vec{\nabla} \times \vec{e}(\vec{r}) = \underline{k}^2(e_m\hat{m} + e_p\hat{p})\exp(-i\underline{k}s) = \underline{k}^2\vec{e}_T\exp(-i\underline{k}s) \tag{2.74}$$

where $\vec{e}_T$ is the transverse component of $\vec{e}$ with respect to the light propagation direction and can be identified in the middle equation of (2.74). Substituting (2.74) into

(2.71) results in

$$\underline{k}^2\vec{e}_T - \mu_0\omega^2\vec{d} = \underline{k}^2\vec{e}_T - \mu_0\omega^2\bar{\bar{\epsilon}}\cdot\vec{e} = 0 \tag{2.75}$$

Equation (2.75) shows that d_s, the component of the displacement vector along the light propagation direction is zero. This also follows by substituting (2.73) into Gauss's equation (2.72). Equation (2.75) is an eigenvalue problem for the wavenumber and it is most easily solved in the E_T-frame.

The permittivity tensor components in the E_T-frame follows from the components in the E-frame by a rotation transformation of (2.68) around $\hat{i}_{\perp_0^2}$ as shown in Figure 2.1

$$[\bar{\bar{\epsilon}}]_{\mathbf{E_T}} = \mathbf{T_2}(\psi)\,[\bar{\bar{\epsilon}}]_{\mathbf{E}}\,\mathbf{T_2^T}(\psi) \tag{2.76}$$

$$= \begin{bmatrix} \epsilon_{\|_o}\sin^2\psi + \epsilon_{\perp_o}\cos^2\psi & 0 & (\epsilon_{\|_o} - \epsilon_{\perp_o})\cos\psi\sin\psi \\ 0 & \epsilon_{\perp 0} & 0 \\ (\epsilon_{\|_o} - \epsilon_{\perp_o})\cos\psi\sin\psi & 0 & \epsilon_{\|_o}\cos^2\psi + \epsilon_{\perp_o}\sin^2\psi \end{bmatrix} \tag{2.77}$$

Here $\mathbf{T_2}$ is the rotation transformation matrix around the second coordinate direction

$$\mathbf{T_2}(\psi) = \begin{bmatrix} \cos\psi & 0 & -\sin\psi \\ 0 & 1 & 0 \\ \sin\psi & 0 & \cos\psi \end{bmatrix} \tag{2.78}$$

Since d_s is zero, e_s can be found in terms of $e_{\|}$ using (2.77) and the s component of (2.75)

$$e_s = -R_{s\|}e_{\|} \tag{2.79}$$

where

$$R_{s\|} = \frac{(\epsilon_{\|_o} - \epsilon_{\perp_o})\cos\psi\sin\psi}{\epsilon_{\|_o}\cos^2\psi + \epsilon_{\perp_o}\sin^2\psi} \tag{2.80}$$

The transverse equations in (2.75) can be written in matrix form for the components of the light electric field in the E_T frame $e_{\|}$ and $e_{\perp}$. Using (2.77) and (2.79) we obtain

$$\begin{bmatrix} \underline{k}^2 - \mu_0\omega^2\epsilon_{\|} & 0 \\ 0 & \underline{k}^2 - \mu_0\omega^2\epsilon_{\perp} \end{bmatrix} \begin{bmatrix} e_{\|} \\ e_{\perp} \end{bmatrix} = 0 \tag{2.81}$$

where

$$\epsilon_{\perp} = \epsilon_{\perp_o} \tag{2.82}$$

$$\begin{aligned} \epsilon_{||} &= \epsilon_{||_o} \sin^2\psi + \epsilon_{\perp_o} \cos^2\psi - \frac{(\epsilon_{||_o} - \epsilon_{\perp_o})^2 \cos^2\psi \sin^2\psi}{\epsilon_{||_o} \cos^2\psi + \epsilon_{\perp_o} \sin^2\psi} \\ &= \left[\frac{\cos^2\psi}{\epsilon_{\perp_o}} + \frac{\sin^2\psi}{\epsilon_{||_o}}\right]^{-1} \end{aligned} \tag{2.83}$$

Equation (2.81) identifies the characteristic values of $\underline{k}$ and the associated polarizations and thus describes the light propagation characteristic of waves in uniaxial media.

For nonzero electric field magnitude the wave number can have two values

$$k_{\perp} = \omega\sqrt{\mu_0\epsilon_{\perp}} \tag{2.84}$$

$$k_{\parallel} = \omega\sqrt{\mu_0\epsilon_{\parallel}} \tag{2.85}$$

The wave associated with $k_{\perp}$ is called the ordinary wave and polarized in the $\hat{i}_{\perp}$ direction

$$\frac{\vec{e}_{or}}{|\vec{e}_{or}|} = \hat{i}_{\perp} \tag{2.86}$$

and the wave associated with $k_{\parallel}$ is called the extraordinary wave and its polarization direction has both $\hat{s}$ and $\hat{i}_{\parallel}$ components whose interrelation is found using (2.79)

$$\frac{\vec{e}_{ex}}{|\vec{e}_{ex}|} = \frac{\hat{i}_{\parallel} + R_{s\parallel}\hat{s}}{\sqrt{1 + R_{s\parallel}^2}} \tag{2.87}$$

Equations (2.84) to (2.87) characterize wave propagation in uniaxial media in which polarized light separates into its ordinary and extraordinary components. Each component travels with different velocity causing a phase shift and change in the polarization of the light.

2.6.2 Kerr Media Specific Approximations

For Kerr media with the applied electric field direction and magnitude constant in the plane perpendicular to the light propagation direction, Section 2.6.1 completely

describes the birefringence. For this case $\psi = \pi/2$ and the light electric field has no component along the light propagation direction ($R_{s||} = 0$ in (2.80)) and $k_{||}$ in (2.85) reduces to $\omega\sqrt{\mu_0\epsilon_{||_0}}$ which results in the phase difference described in (1.12) using (2.31) and (2.69). When light propagates along the direction of the applied electric field ($\psi = 0, \pi$) $k_\perp = k_{||}$ and there is no birefringence. For other values of ψ, $k_{||}$ is a complicated function of ψ. This poses little difficulty for geometries with constant direction and magnitude applied electric field such as tilted parallel plate electrodes with the direction of light propagation at a non-perpendicular angle to the applied electric field. However to extend the analysis to inhomogeneous applied electric fields approximations based on (2.31) are necessary.

First notice from (2.80) that

$$\left|\frac{e_s}{e_{||}}\right| = \left|R_{s||}\right| \leq \left|\frac{\epsilon_{||_0} - \epsilon_{\perp_0}}{\epsilon_{||_0}\cos^2\psi + \epsilon_{\perp_0}\sin^2\psi}\right| \ll 1 \tag{2.88}$$

where we used (2.31). Thus to a very good approximation e_s is zero and the extraordinary wave is polarized along the transverse component of the electric field. Since with this approximation both e_s and d_s vanish, the electric field and the displacement field are two dimensional vectors in the plane perpendicular to the light propagation and the constitutive law reduces to a two dimensional matrix equation with a 2×2 dielectric matrix which is diagonal in the $\mathrm{E_T}$-frame

$$\begin{bmatrix} d_{||} \\ d_\perp \end{bmatrix} = \begin{bmatrix} \epsilon_{||} & 0 \\ 0 & \epsilon_\perp \end{bmatrix} \begin{bmatrix} e_{||} \\ e_\perp \end{bmatrix} \tag{2.89}$$

Furthermore $\epsilon_{||}$ can be written as

$$\epsilon_{||} = \left[\frac{\cos^2\psi}{\epsilon_{\perp_0}} + \frac{\sin^2\psi}{\epsilon_{||_0}}\right]^{-1} = \epsilon_{\perp_0} + \Delta\epsilon\sin^2\psi + O(\Delta\epsilon^2) \tag{2.90}$$

where $\Delta\epsilon$ is defined in (2.30). Neglecting the second order term due to (2.31) and using (2.82), (2.90) reduces to

$$\epsilon_{||} - \epsilon_\perp \approx 2\epsilon_0 n\lambda B E_T^2 \tag{2.91}$$

where $E_T = E\sin\psi$ is the magnitude of the transverse electric field. Equation (2.91) and the corresponding equation in terms of the refractive index components is generally

the accepted form of the Kerr effect in the dielectric literature. It directly follows from (2.31) that

$$\frac{\epsilon_{\parallel}-\epsilon_{\perp}}{\epsilon_0}, \frac{\epsilon_{\parallel}-\epsilon}{\epsilon_0}, \frac{\epsilon-\epsilon_{\perp}}{\epsilon_0} \ll 1 \tag{2.92}$$

2.7 Inhomogeneous Kerr Media

2.7.1 Assumptions

When the direction and the magnitude of the electric field changes along the light path Kerr media are equivalent to inhomogeneous uniaxial media. A rigorous formulation of wave propagation in uniaxial inhomogeneous media is rather complicated and is not tractable without simplifying assumptions. For typical applied electric field distributions in high voltage environments spatial variations of the electric field are much longer than the light wavelength so that we can write

$$\left|\nabla E^2(\vec{r})\right| \lambda \ll E^2(\vec{r}) \tag{2.93}$$

Equation (2.93) can be used for various approximations.

First we assume that light propagates in a straight line. This assumption is not true for a general inhomogeneous media whether it is isotropic or anisotropic. For the isotropic case it can be shown that when spatial variations in the refractive index are small the light propagation curve is essentially a line. Using (2.93) we will use this result for Kerr media without any attempt of further mathematical justification. Our Kerr electro-optic measurements show that there is no detectable bending in the light propagation direction giving an experimental justification to this assumption.

The homogeneous light propagation theory described in section 2.6 assumed light is a plane wave where transverse variations in the light wave-front are neglected

$$\frac{\partial}{\partial m} = \frac{\partial}{\partial p} \approx 0 \tag{2.94}$$

as discussed in Section 2.3. For inhomogeneous media the problem is more complicated as there are also transverse variations in the medium. Fortunately when (2.94) is assumed to be true for the wave front, it can be shown that [37,38] for small variations similar to (2.93) the transverse variations in the medium are negligible leaving (2.94) also valid for inhomogeneous media.

2.7.2 Constitutive Relations

Due to (2.94), light propagation in inhomogeneous Kerr media can be described in terms of one dimensional variations along the light path. Thus the constitutive law in (2.89) becomes

$$\begin{bmatrix} d_{\parallel}(s) \\ d_{\perp}(s) \end{bmatrix} = \begin{bmatrix} \epsilon_{\parallel}(s) & 0 \\ 0 & \epsilon_{\perp}(s) \end{bmatrix} \begin{bmatrix} e_{\parallel}(s) \\ e_{\perp}(s) \end{bmatrix} \tag{2.95}$$

Equation (2.95) expresses the approximate constitutive law in the E_T-frame. Its equivalent in the light-frame is

$$\begin{bmatrix} d_m(s) \\ d_p(s) \end{bmatrix} = \begin{bmatrix} \epsilon_{mm}(s) & \epsilon_{mp}(s) \\ \epsilon_{mp}(s) & \epsilon_{pp}(s) \end{bmatrix} \begin{bmatrix} e_m(s) \\ e_p(s) \end{bmatrix} \tag{2.96}$$

The permittivity tensor and electric field components in the light-frame and the E_T-frame are related by the usual rotation transformations

$$\begin{bmatrix} e_m(s) \\ e_p(s) \end{bmatrix} = \begin{bmatrix} \cos\varphi(s) & -\sin\varphi(s) \\ \sin\varphi(s) & \cos\varphi(s) \end{bmatrix} \begin{bmatrix} e_{\parallel}(s) \\ e_{\perp}(s) \end{bmatrix} \tag{2.97}$$

and

$$\begin{bmatrix} \epsilon_{mm}(s) & \epsilon_{mp}(s) \\ \epsilon_{mp}(s) & \epsilon_{pp}(s) \end{bmatrix} = \begin{bmatrix} \cos\varphi(s) & -\sin\varphi(s) \\ \sin\varphi(s) & \cos\varphi(s) \end{bmatrix} \begin{bmatrix} \epsilon_{\parallel}(s) & 0 \\ 0 & \epsilon_{\perp}(s) \end{bmatrix} \begin{bmatrix} \cos\varphi(s) & \sin\varphi(s) \\ -\sin\varphi(s) & \cos\varphi(s) \end{bmatrix} \tag{2.98}$$

Here $\varphi(s)$ is the direction of tranverse electric field in the mp-plane as indicated in Figure 2.1. Equation (2.98) can be used to obtain

$$\epsilon_{mm}(s) = \epsilon_{\parallel}(s)\cos^2\varphi(s) + \epsilon_{\perp}(s)\sin^2\varphi(s) \tag{2.99a}$$

$$\epsilon_{pp}(s) = \epsilon_{\perp}(s)\cos^2\varphi(s) + \epsilon_{\parallel}(s)\sin^2\varphi(s) \tag{2.99b}$$

$$\epsilon_{mp}(s) = \left[\epsilon_{\parallel}(s) - \epsilon_{\perp}(s)\right]\cos\varphi(s)\sin\varphi(s) \tag{2.99c}$$

Both (2.91) and (2.92) generalize to their inhomogeneous forms

$$\epsilon_{\parallel}(s) - \epsilon_{\perp}(s) = 2\epsilon_0 n\lambda B E_T^2(s) \tag{2.100}$$

$$\frac{\epsilon_{\parallel}(s)-\epsilon_{\perp}(s)}{\epsilon_0},\ \frac{\epsilon_{\parallel}(s)-\epsilon}{\epsilon_0},\ \frac{\epsilon-\epsilon_{\perp}(s)}{\epsilon_0} \ll 1 \tag{2.101}$$

Substituting (2.100) in (2.99) gives the expressions for the Kerr effect in the light-frame

$$\epsilon_{mm}(s)-\epsilon_{pp}(s) = 2\epsilon_0 n\lambda B\left[E_m^2(s)-E_p^2(s)\right] \tag{2.102a}$$

$$\epsilon_{mp}(s) = 2\epsilon_0 n\lambda B E_m(s)E_p(s) \tag{2.102b}$$

where $E_m(s) = E_T(s)\cos\varphi(s)$ and $E_p(s) = E_T(s)\sin\varphi(s)$ are the respective components of the applied transverse electric field. We finally note that using (2.99) the weak anisotropy conditions of (2.101) can be expressed in the light-frame as

$$\frac{|\epsilon_{mm}(s)-\epsilon_{pp}(s)|}{\epsilon_0},\ \frac{|\epsilon_{pp}(s)-\epsilon|}{\epsilon_0},\ \frac{|\epsilon_{mp}(s)-\epsilon|}{\epsilon_0},\ \frac{|\epsilon_{mp}(s)|}{\epsilon_0} \ll 1 \tag{2.103}$$

2.7.3 Governing Light Propagation Equations

In Kerr media with an inhomogeneous applied electric field the anisotropy is weak. For this case it is possible to obtain a reduced set of Maxwell's equations which are simple and easy to analyze. The derivation here is similar to Aben's [39].

Second Order Form

We begin with (2.71) in the light-frame which reduces to

$$\frac{d^2e_m(s)}{ds^2} + \mu_0\omega^2\left[\epsilon_{mm}(s)e_m(s)+\epsilon_{mp}(s)e_p(s)\right] = 0 \tag{2.104a}$$

$$\frac{d^2e_p(s)}{ds^2} + \mu_0\omega^2\left[\epsilon_{pp}(s)e_p(s)+\epsilon_{mp}(s)e_m(s)\right] = 0 \tag{2.104b}$$

using (2.94) and the constitutive law in (2.96). In this work we also use the E_T-frame. Using (2.99) and (2.97) in (2.104) the E_T-frame light components obey

$$\frac{d^2e_{\parallel}(s)}{ds^2} + \left[\mu_0\omega^2\epsilon_{\parallel}(s) - \left(\frac{d\varphi(s)}{ds}\right)^2\right]e_{\parallel}(s) - 2\frac{d\varphi(s)}{ds}\frac{de_{\perp}(s)}{ds} - \frac{d^2\varphi(s)}{ds^2}e_{\perp}(s) = 0 \tag{2.105a}$$

$$\frac{d^2e_\perp(s)}{ds^2}+\left[\mu_0\omega^2\epsilon_\perp(s)-\left(\frac{d\varphi(s)}{ds}\right)^2\right]e_\perp(s)+2\frac{d\varphi(s)}{ds}\frac{de_\parallel(s)}{ds}+\frac{d^2\varphi(s)}{ds^2}e_\parallel(s)=0 \tag{2.105b}$$

Reduced First Order Form

Using (2.103) we can assume solutions of the form

$$e_j(s)=a_j(s)\exp(-iks) \qquad j=m,p \tag{2.106}$$

in (2.104). Here $k=\omega\sqrt{\epsilon\mu_0}$ is the isotropic wave number and $a_j(s)$ is a slowly varying amplitude function of s due to the weak birefringence where

$$\left|\frac{da_j(s)}{ds}\right|\ll|ka_j(s)| \qquad j=m,p \tag{2.107}$$

which modulates the isotropic solution. Substituting (2.106) in (2.104) and neglecting the second order terms by virtue of (2.107) yields approximate first order equations

$$\frac{da_m(s)}{ds}\approx -i\frac{k}{2\epsilon}\big[\epsilon_{mm}(s)-\epsilon\big]a_m(s)-i\frac{k}{2\epsilon}\epsilon_{mp}(s)a_p(s) \tag{2.108a}$$

$$\frac{da_p(s)}{ds}\approx -i\frac{k}{2\epsilon}\big[\epsilon_{pp}(s)-\epsilon\big]a_p(s)-i\frac{k}{2\epsilon}\epsilon_{mp}(s)a_m(s) \tag{2.108b}$$

Equation (2.108) is first order as opposed to second order in (2.104) because with k positive, assumptions (2.106) and (2.107) eliminate the waves traveling in the $-s$ direction. Here we neglect any reflections so that for waves traveling in the $+s$ direction k is positive. It is clear from (2.106) that the rotation transformations in (2.97) are also valid for $a_j(s)$. By using (2.99) and (2.97), ($e_j(s)$ are replaced $a_j(s)$) (2.108) can also be expressed in the $\mathrm{E_T}$-frame as

$$\frac{da_\parallel(s)}{ds} = -i\frac{k}{2\epsilon}\big[\epsilon_\parallel(s)-\epsilon\big]a_\parallel(s)+\frac{d\varphi(s)}{ds}a_\perp(s) \tag{2.109a}$$

$$\frac{da_\perp(s)}{ds} = -i\frac{k}{2\epsilon}\big[\epsilon_\perp(s)-\epsilon\big]a_\perp(s)-\frac{d\varphi(s)}{ds}a_\parallel(s) \tag{2.109b}$$

Equation (2.108) may be further simplified by the transformations

$$a_j(s)=b_j(s)\exp\big(-i\phi(s)\big) \qquad j=m,\,p \tag{2.110}$$

where

$$\phi(s) = \frac{k}{4\epsilon}\int_0^s \big[\epsilon_{mm}(s') + \epsilon_{pp}(s') - 2\epsilon\big]ds' = \frac{k}{4\epsilon}\int_0^s \big[\epsilon_{\parallel}(s') + \epsilon_{\perp}(s') - 2\epsilon\big]ds' \tag{2.111}$$

Substituting (2.110) and (2.111) into (2.108) yields

$$\frac{db_m(s)}{ds} = -i\frac{k}{4\epsilon}\big[\epsilon_{mm}(s) - \epsilon_{pp}(s)\big]b_m(s) - i\frac{k}{2\epsilon}\epsilon_{mp}(s)b_p(s) \tag{2.112a}$$

$$\frac{db_p(s)}{ds} = -i\frac{k}{4\epsilon}\big[\epsilon_{pp}(s) - \epsilon_{mm}(s)\big]b_p(s) - i\frac{k}{2\epsilon}\epsilon_{mp}(s)b_m(s) \tag{2.112b}$$

Note that (2.110) eliminates common phase terms in a_m and a_p to obtain a version of (2.108) in (2.112) independent of ϵ.

It follows from (2.97), (2.106) and (2.110) that (2.112) can be expressed in the $\mathrm{E_T}$-frame as

$$b_m(s) = b_{\parallel}(s)\cos\varphi(s) - b_{\perp}(s)\sin\varphi(s) \tag{2.113a}$$

$$b_p(s) = b_{\perp}(s)\cos\varphi(s) + b_{\parallel}(s)\sin\varphi(s) \tag{2.113b}$$

Substituting (2.99) and (2.113) in (2.112) yields

$$\frac{db_{\parallel}(s)}{ds} = -i\frac{k}{4\epsilon}\big[\epsilon_{\parallel}(s) - \epsilon_{\perp}(s)\big]b_{\parallel}(s) + \frac{d\varphi(s)}{ds}b_{\perp}(s) \tag{2.114a}$$

$$\frac{db_{\perp}(s)}{ds} = -i\frac{k}{4\epsilon}\big[\epsilon_{\perp}(s) - \epsilon_{\parallel}(s)\big]b_{\perp}(s) - \frac{d\varphi(s)}{ds}b_{\parallel}(s) \tag{2.114b}$$

Here again the common phase terms in $a_{\parallel}$ and $a_{\perp}$ are eliminated.

Finally, respectively substituting (2.102) in (2.112) and (2.100) in (2.114) results in

$$\frac{db_m(s)}{ds} = -i\pi B\big[E_m^2(s) - E_p^2(s)\big]b_m(s) - 2i\pi BE_m(s)E_p(s)b_p(s) \tag{2.115a}$$

$$\frac{db_p(s)}{ds} = -i\pi B\big[E_p^2(s) - E_m^2(s)\big]b_p(s) - 2i\pi BE_m(s)E_p(s)b_m(s) \tag{2.115b}$$

and

$$\frac{db_{\parallel}(s)}{ds} = -i\pi BE_T^2(s)b_{\parallel}(s) + \frac{d\varphi(s)}{ds}b_{\perp}(s) \tag{2.116a}$$

$$\frac{db_{\perp}(s)}{ds} = i\pi BE_T^2(s)b_{\perp}(s) - \frac{d\varphi(s)}{ds}b_{\parallel}(s) \tag{2.116b}$$

as the approximate governing equations of light propagation in Kerr media. Note that the coefficients in (2.115) and (2.116) involve only the components of the applied electric field rather than permittivity matrix elements. From (2.106), (2.110) and (2.111) $b_j(s)$ are related to the light electric field components $e_j(s)$ by a phase factor

$$b_j(s) = e_j(s) \exp\left(\frac{ik}{4\epsilon}\int_0^s [\epsilon_{mm}(s') + \epsilon_{pp}(s') + 2\epsilon]\, ds'\right) \quad j = m,\ p,\ \|,\ \perp \tag{2.117}$$

Matrix Form

In the remainder of this work we often use the matrix forms of (2.115) and (2.116) which are

$$\frac{d\mathbf{b}(s)}{ds} = \mathbf{A}(s)\mathbf{b}(s) \tag{2.118}$$

$$\frac{d\mathbf{b}'(s)}{ds} = \mathbf{A}'(s)\mathbf{b}'(s) \tag{2.119}$$

respectively, where

$$\mathbf{A}(s) = -i\pi B \begin{bmatrix} E_m^2(s) - E_p^2(s) & 2E_m(s)E_p(s) \\ 2E_m(s)E_p(s) & -\left[E_m^2(s) - E_p^2(s)\right] \end{bmatrix} \tag{2.120}$$

$$\mathbf{A}'(s) = \begin{bmatrix} -i\pi B E_T^2(s) & \frac{d\varphi(s)}{ds} \\ -\frac{d\varphi(s)}{ds} & i\pi B E_T^2(s) \end{bmatrix} \tag{2.121}$$

$$\mathbf{b}(s) = \begin{bmatrix} b_m(s) \\ b_p(s) \end{bmatrix} \tag{2.122}$$

$$\mathbf{b}'(s) = \begin{bmatrix} b_\|(s) \\ b_\perp(s) \end{bmatrix} \tag{2.123}$$

$\mathbf{A}(s)$ and $\mathbf{A}'(s)$ are called the system matrices of (2.118) and (2.119) respectively. We also note from (2.113) that

$$\mathbf{b}'(s) = \mathbf{S}\left[\varphi(s)\right]\mathbf{b}(s) \tag{2.124}$$

where $\mathbf{S}$ is the rotation matrix

$$\mathbf{S}(\theta) = \begin{bmatrix} \cos\theta & \sin\theta \\ -\sin\theta & \cos\theta \end{bmatrix} \tag{2.125}$$

Real Matrix Form

Occasionally it becomes convenient to separate the real and imaginary parts of (2.118) or (2.119). We let

$$\mathbf{b}(s) = \mathbf{u}(s) + i\mathbf{v}(s) \tag{2.126}$$

$$\mathbf{b}'(s) = \mathbf{u}'(s) + i\mathbf{v}'(s) \tag{2.127}$$

where $\mathbf{u}(s) = \begin{bmatrix} u_m(s) \\ u_p(s) \end{bmatrix}$, $\mathbf{v}(s) = \begin{bmatrix} v_m(s) \\ v_p(s) \end{bmatrix}$, $\mathbf{u}'(s) = \begin{bmatrix} u_{\parallel}(s) \\ u_{\perp}(s) \end{bmatrix}$, and $\mathbf{v}'(s) = \begin{bmatrix} v_{\parallel}(s) \\ v_{\perp}(s) \end{bmatrix}$. The real form of (2.118) can then be written in block matrix form as

$$\frac{d}{ds}\begin{bmatrix} \mathbf{u}(s) \\ \mathbf{v}(s) \end{bmatrix} = \begin{bmatrix} \mathbf{0} & \mathbf{W}(s) \\ -\mathbf{W}(s) & \mathbf{0} \end{bmatrix}\begin{bmatrix} \mathbf{u}(s) \\ \mathbf{v}(s) \end{bmatrix} \tag{2.128}$$

where

$$\mathbf{W}(s) = i\mathbf{A}(s) = \pi B\begin{bmatrix} E_m^2(s) - E_p^2(s) & 2E_m(s)E_p(s) \\ 2E_m(s)E_p(s) & -\left[E_m^2(s) - E_p^2(s)\right] \end{bmatrix} \tag{2.129}$$

Similarly (2.119) becomes

$$\frac{d}{ds}\begin{bmatrix} \mathbf{u}'(s) \\ \mathbf{v}'(s) \end{bmatrix} = \begin{bmatrix} \mathbf{Q}'(s) & \mathbf{W}'(s) \\ -\mathbf{W}'(s) & \mathbf{Q}'(s) \end{bmatrix}\begin{bmatrix} \mathbf{u}'(s) \\ \mathbf{v}'(s) \end{bmatrix} \tag{2.130}$$

where

$$\mathbf{W}'(s) = \begin{bmatrix} \pi B E_T^2(s) & 0 \\ 0 & -\pi B E_T^2(s) \end{bmatrix} \tag{2.131}$$

$$\mathbf{Q}'(s) = \begin{bmatrix} 0 & \frac{d\varphi(s)}{ds} \\ -\frac{d\varphi(s)}{ds} & 0 \end{bmatrix} \tag{2.132}$$

2.7.4 The Kerr Parameters

The governing equations in the light-frame (2.118) and in the E_T-frame (2.119) respectively depend on $E_m^2(s) - E_p^2(s)$, $2E_m(s)E_p(s)$ and $\pi B E_T^2(s)$, $\frac{d\varphi(s)}{ds}$. Here these functions of the applied electric field are referred to as the Kerr parameters.

The Kerr parameters depend on both the applied electric field distribution and the light propagation direction. Thus given a fixed spatial position, the Kerr parameters

take on different values for different light propagation directions for the same applied field distribution. This observation is be particularly important in Part II.

The E_{T}-frame Kerr parameters $\pi B E_T^2(s)$ and $\frac{d\varphi(s)}{ds}$ can expressed in terms of the light-frame components of the applied electric field as

$$E_T^2(s) = E_m^2(s) + E_p^2(s) \tag{2.133a}$$

$$\frac{d\varphi(s)}{ds} = \frac{1}{E_T^2(s)}\left[E_m(s)\frac{dE_p(s)}{ds} - E_p(s)\frac{dE_m(s)}{ds}\right] \tag{2.133b}$$

where (2.133b) follows from the s-derivative of the identity

$$\tan\varphi(s) = \frac{E_p(s)}{E_m(s)} \tag{2.134}$$

The Kerr Parameters In Axisymmetric Kerr Media When $\hat{\mathbf{m}} = \hat{\mathbf{z}}$

When the applied electric field distribution is axisymmetric and the light propagation direction is on a plane that is perpendicular to the axisymmetry axis z, we can define the light frame so that $\hat{m} = \hat{z}$. Then

$$r^2 = s^2 + p^2 \tag{2.135}$$

For light propagating along $\hat{s}$, p is constant and thus taking the derivative of (2.135) we obtain

$$\frac{d}{ds} = \frac{s}{r}\frac{d}{dr} \tag{2.136}$$

$$ds = \frac{r\,dr}{\sqrt{r^2 - p^2}} \tag{2.137}$$

The Kerr parameters in (2.133) can then be expressed as

$$E_T^2(s) = {E_z}^2(s) + \frac{p^2}{r^2}{E_r}^2(s) \tag{2.138a}$$

$$\frac{d\varphi(s)}{ds} = \frac{1}{E_T^2(r)}\frac{ps}{r^2}\left[E_z(r)\frac{dE_r(r)}{dr} - \frac{E_z(r)E_r(r)}{r} - E_r(r)\frac{dE_z(r)}{dr}\right] \tag{2.138b}$$

Chapter 3

The Matricant

3.1 Introduction

The solutions to (2.118) and (2.119) at any point along the light path can be expressed in terms of initial conditions and 2×2 complex matrices called matricants of the respective systems. This chapter presents the matricant theory. We show existence and uniqueness and develop the properties that are important in Kerr electro-optic measurements. We show that the matricants reduce to the well know matrix exponential for special cases of the system matrices $\mathbf{A}(s)$ and $\mathbf{A}'(s)$ and analytically evaluate those cases. We finally discuss numerical evaluation of the matricant for arbitrary electric field distributions.

3.2 Solutions To The Governing Equations

Equation (2.118) is a linear ordinary differential equation with space varying coefficients. A solution to (2.118) refers to the evaluation of $\mathbf{b}(s)$ given an initial point s_0 with initial condition $\mathbf{b}(s_0)$, and the transverse electric field distribution $\mathbf{E}_{\mathrm{T}}(s)$ between s_0 and s. This problem is well known and $\mathbf{b}(s)$ uniquely exists for given s_0 and $\mathbf{b}(s_0)$ provided that each entry of $\mathbf{A}(s)$ obeys the Lipschitz condition

$$|A_{ij}(s') - A_{ij}(s_0)| \leq L\,|s' - s_0| \tag{3.1}$$

for some constant L which is valid for all s' between s_0 and s [40]. The Lipschitz condition is intermediate between continuous and continuously differentiable [41] and holds for physical electric field distributions relevant to this work. Hence for any initial

condition $\mathbf{b}(s_0)$, $\mathbf{b}(s)$ uniquely exists.

3.3 The Definition Of The Matricant

Clearly for a fixed initial condition the solution $\mathbf{b}(s)$ can be expressed in the form

$$\mathbf{b}(s) = \mathbf{\Omega}(s, s_0)\mathbf{b}(s_0) \tag{3.2}$$

where $\mathbf{\Omega}(s, s_0)$ is a 2×2 complex matrix. The question of interest is the existence of a matrix $\mathbf{\Omega}(s, s_0)$ such that (3.2) is valid for any initial condition at s_0. The answer is affirmative as shown in the next section.

The 2×2 complex matrix $\mathbf{\Omega}(s, s_0)$ is known as the matricant of (2.118). Apparently the name 'matricant' is not universally used for $\mathbf{\Omega}(s, s_0)$. The matrix is known as the 'state transition matrix' in control theory and also called 'matrizant' by some authors [42]. The presentation in this chapter heavily borrows from the books by Gantmacher [43] and Pease [41] and we follow their naming conventions as well.

All the results in this chapter are presented in terms of the matricant of (2.118) $\mathbf{\Omega}(s, s_0)$. However all the results are also true for the matricant of (2.119) or for the matricants of any other similar systems. We denote the matricant of (2.119) by $\mathbf{\Omega}'(s, s_0)$

$$\mathbf{b}'(s) = \mathbf{\Omega}'(s, s_0)\mathbf{b}'(s_0) \tag{3.3}$$

Note from (2.124) that both matricants are related as

$$\mathbf{\Omega}(s, s_0) = \mathbf{S}\big[-\varphi(s)\big]\mathbf{\Omega}'(s, s_0)\mathbf{S}\big[\varphi(s_0)\big] \tag{3.4}$$

$$\mathbf{\Omega}'(s, s_0) = \mathbf{S}\big[\varphi(s)\big]\mathbf{\Omega}(s, s_0)\mathbf{S}\big[-\varphi(s_0)\big] \tag{3.5}$$

where we note that from the definition of $\mathbf{S}$ in (2.125) that

$$\mathbf{S}^{-1}[\theta] = \mathbf{S}[-\theta] \tag{3.6}$$

3.4 The Peano Expansion and Existence

Integrating (2.118) yields

$$\mathbf{b}(s) = \mathbf{b}(s_0) + \int_{s_0}^{s} \mathbf{A}(s')\mathbf{b}(s')ds' \tag{3.7}$$

Equation (3.7) can be self-substituted on the right hand side to get

$$\mathbf{b}(s) = \mathbf{b}(s_0) + \int_{s_0}^{s} \mathbf{A}(s') \left[\mathbf{b}(s_0) + \int_{s_0}^{s'} \mathbf{A}(s'')\mathbf{b}(s'')ds'' \right] ds' \tag{3.8}$$

Repeatedly substituting (3.7) into (3.8) and comparing with (3.2) suggests the so called Peano expansion of the matricant [41, 43]

$$\mathbf{\Omega}(s, s_0) = \mathbf{I} + \int_{s_0}^{s} \mathbf{A}(s')ds' + \int_{s_0}^{s} \mathbf{A}(s') \int_{s_0}^{s'} \mathbf{A}(s'')ds''ds' + \cdots \tag{3.9}$$

where $\mathbf{I}$ is the identity matrix. The infinite sum in (3.9) is convergent [41] and can be term by term differentiated to

$$\frac{d\mathbf{\Omega}(s, s_0)}{ds} = \mathbf{A}(s)\mathbf{\Omega}(s, s_0) \tag{3.10}$$

Multiplying (3.10) with arbitrary $\mathbf{b}(s_0)$ and comparing with (2.118) and (3.2) proves the existence of the matricant.

Equation (3.9) is in general impractical to be employed to evaluate the matricant [41]. However it is useful to demonstrate certain properties. Equation (3.10) relates the matricant directly to the system matrix through a differential equation.

3.5 General Matricant Properties

We introduced the matricant without using any specific property of the system matrices of (2.118) or (2.119) except the Lipschitz condition. Here we list general properties which follow directly from the existence.

Property 1 (Initial Condition). *At $s = s_0$ the matricant reduces to the identity matrix.*

$$\mathbf{\Omega}(s_0, s_0) = \mathbf{I} \tag{3.11}$$

Proof. (3.11) directly follows from (3.2). Alternatively when $s = s_0$ all the integrals on the right hand side of (3.9) vanish and (3.9) yields (3.11). □

Property 2 (The Jacobi Identity).

$$|\mathbf{\Omega}(s, s_0)| = \exp\Big(\int_{s_0}^{s} \big[A_{11}(s') + A_{22}(s')\big] ds'\Big) \tag{3.12}$$

Proof. The determinant of $\mathbf{\Omega}(s, s_0)$ is

$$|\mathbf{\Omega}(s, s_0)| = \Omega_{11}(s, s_0)\Omega_{22}(s, s_0) - \Omega_{12}(s, s_0)\Omega_{21}(s, s_0) \tag{3.13}$$

Taking the derivative of (3.13) with respect to s and substituting (3.10) for the derivatives of Ω_{ij}, straight forward algebra yields

$$\frac{d\,|\mathbf{\Omega}(s, s_0)|}{ds} = |\mathbf{\Omega}(s, s_0)|\,\big[A_{11}(s) + A_{22}(s)\big] \tag{3.14}$$

The solution to (3.14) is given by (3.12) since $|\mathbf{\Omega}(s_0, s_0)| = 1$ from (3.11). □

Property 3 (Nonsingularity). *The matricant is nonsingular.*

Proof. It directly follows from (3.12) that $|\mathbf{\Omega}(s, s_0)|$ may never be 0. □

Property 4. *For two different initial points s_0 and s_0'*

$$\mathbf{\Omega}(s, s_0) = \mathbf{\Omega}(s, s_0')\mathbf{C} \tag{3.15}$$

where $\mathbf{C}$ *is a constant matrix.*

Proof. Since the matricant is nonsingular we can write

$$\frac{d\mathbf{\Omega}(s, s_0)}{ds} = \frac{d\Big(\mathbf{\Omega}(s, s_0')\big[\mathbf{\Omega}(s, s_0')\big]^{-1}\mathbf{\Omega}(s, s_0)\Big)}{ds} \tag{3.16}$$

$$= \frac{d\mathbf{\Omega}(s, s_0')}{ds}\big[\mathbf{\Omega}(s, s_0')\big]^{-1}\mathbf{\Omega}(s, s_0) + \mathbf{\Omega}(s, s_0')\frac{d\Big(\big[\mathbf{\Omega}(s, s_0')\big]^{-1}\mathbf{\Omega}(s, s_0)\Big)}{ds} \tag{3.17}$$

$$= \mathbf{A}(s)\mathbf{\Omega}(s, s_0) + \mathbf{\Omega}(s, s_0')\frac{d\Big(\big[\mathbf{\Omega}(s, s_0')\big]^{-1}\mathbf{\Omega}(s, s_0)\Big)}{ds} \tag{3.18}$$

where we used (3.10) (with s_0 replaced with s_0') to obtain (3.18) from (3.17). Again using (3.10) notice that the first term on the right hand side of (3.18) equals the left

hand side. Thus

$$\frac{d\Big(\big[\mathbf{\Omega}(s,s_0')\big]^{-1}\mathbf{\Omega}(s,s_0)\Big)}{ds}=0 \tag{3.19}$$

which implies (3.15). □

Equation (3.15) states that the matricants of a system for different initial values may only differ by the product of a constant matrix.

Property 5 (Transitivity). *For any three points s, s_0 and s_0'*

$$\mathbf{\Omega}(s,s_0)=\mathbf{\Omega}(s,s_0')\mathbf{\Omega}(s_0',s_0) \tag{3.20}$$

Proof. Evaluating (3.15) at $s=s_0'$ and (3.11) yields

$$\mathbf{C}=\mathbf{\Omega}(s_0',s_0) \tag{3.21}$$

□

Property 6 (Inverse).

$$\mathbf{\Omega}(s_0,s_0')=\big[\mathbf{\Omega}(s_0',s_0)\big]^{-1} \tag{3.22}$$

Proof. Equation (3.22) follows from evaluating (3.20) at $s=s_0$, (3.11) and nonsingularity of the matricant. □

Property 7 (Uniqueness). *Matricant is unique.*

Proof. Assume that $\mathbf{\Gamma}(s,s_0)$ is a matricant of (2.118) different from $\mathbf{\Omega}(s,s_0)$. Then with $\mathbf{\Omega}(s,s_0')$ replaced by $\mathbf{\Gamma}(s,s_0)$ in equations (3.16) to (3.18), (3.19) remains valid to yield

$$\mathbf{\Omega}(s,s_0)=\mathbf{\Gamma}(s,s_0)\mathbf{C} \tag{3.23}$$

where $\mathbf{C}$ is another constant matrix different than (3.21). Evaluating (3.23) at $s=s_0$ together with (3.11) shows that

$$\mathbf{C}=\mathbf{I} \tag{3.24}$$

Thus the matricant is unique. □

Property 8 (Multiplicative Derivative).

$$\mathbf{A}(s) = \frac{d\mathbf{\Omega}(s, s_0)}{ds}\left[\mathbf{\Omega}(s, s_0)\right]^{-1} \tag{3.25}$$

Proof. Equation (3.25) directly follows from (3.10) by postmultiplying both sides with the inverse of the matricant. □

Equation (3.25) gives $\mathbf{A}(s)$ in terms of $\mathbf{\Omega}(s, s_0)$ and is useful to express the entries of the system matrix in terms of the matricant entries.

The following identity will be useful in the next chapter.

Property 9.

$$\frac{d\mathbf{\Omega}(s, -s)}{ds} = \mathbf{A}(s)\mathbf{\Omega}(s, -s) + \mathbf{\Omega}(s, -s)\mathbf{A}(-s) \tag{3.26}$$

Proof. It follows from (3.20) that $\mathbf{\Omega}(-s, s_0)\mathbf{\Omega}(s_0, -s) = \mathbf{I}$. Thus

$$\mathbf{0} = \frac{d\left[\mathbf{\Omega}(-s, s_0)\mathbf{\Omega}(s_0, -s)\right]}{ds} = \frac{d\mathbf{\Omega}(-s, s_0)}{ds}\mathbf{\Omega}(s_0, -s) + \mathbf{\Omega}(-s, s_0)\frac{d\mathbf{\Omega}(s_0, -s)}{ds} \tag{3.27}$$

$$= -\mathbf{A}(-s) + \mathbf{\Omega}(-s, s_0)\frac{d\mathbf{\Omega}(s_0, -s)}{ds} \tag{3.28}$$

where we used (3.10) and (3.20). Equations (3.22) and (3.28) yield

$$\frac{d\mathbf{\Omega}(s_0, -s)}{ds} = \mathbf{\Omega}(s_0, -s)\mathbf{A}(-s) \tag{3.29}$$

For any s_0, $\mathbf{\Omega}(s, s_0)\mathbf{\Omega}(s_0, -s) = \mathbf{\Omega}(-s, s)$ and

$$\frac{d\mathbf{\Omega}(s, -s)}{ds} = \frac{d\mathbf{\Omega}(s, s_0)}{ds}\mathbf{\Omega}(s_0, -s) + \mathbf{\Omega}(s, s_0)\frac{d\mathbf{\Omega}(s_0, -s)}{ds} \tag{3.30}$$

$$= \mathbf{A}(s)\mathbf{\Omega}(s, -s) + \mathbf{\Omega}(s, s_0)\frac{d\mathbf{\Omega}(s_0, -s)}{ds} \tag{3.31}$$

Equation (3.26) follows by substituting (3.29) in (3.31) and using (3.20). □

3.6 Kerr Media Specific Properties

There are two very important properties of the matricant which are specific to Kerr media.

Property 10 (Unitarity). *The matricant for Kerr media is unitary*

$$\left[\mathbf{\Omega}(s, s_0)\right]^\dagger \mathbf{\Omega}(s, s_0) = \mathbf{\Omega}(s, s_0)\left[\mathbf{\Omega}(s, s_0)\right]^\dagger = \mathbf{I} \tag{3.32}$$

Proof. Notice from (2.120) that

$$\mathbf{A}(s) = -\mathbf{A}^\dagger(s) \tag{3.33}$$

where † denotes complex conjugate transpose. It then follows from (2.118) and (2.120) that

$$\begin{aligned} \frac{d}{ds}\left[\mathbf{b}^\dagger(s)\mathbf{b}(s)\right] &= \frac{d\mathbf{b}^\dagger(s)}{ds}\mathbf{b}(s) + \mathbf{b}^\dagger(s)\frac{d\mathbf{b}(s)}{ds} \\ &= \mathbf{b}^\dagger(s)\left[\mathbf{A}^\dagger(s) + \mathbf{A}(s)\right]\mathbf{b}(s) \\ &= \mathbf{0} \end{aligned} \tag{3.34}$$

Since $\mathbf{b}^\dagger(s)\mathbf{b}(s)$ does not change with s it should be equal to its initial value at $s = s_0$. Thus

$$\mathbf{b}^\dagger(s_0)\mathbf{b}(s_0) = \mathbf{b}^\dagger(s)\mathbf{b}(s) = \mathbf{b}^\dagger(s_0)[\mathbf{\Omega}(s, s_0)]^\dagger \mathbf{\Omega}(s, s_0)\mathbf{b}(s_0) \tag{3.35}$$

Equation (3.32) follows since (3.35) is true for any choice $\mathbf{b}(s_0)$. □

Since the electric field vector is related to $\mathbf{b}(s)$ by a common phase factor in (2.117) $\left[\mathbf{b}(s)\right]^\dagger \mathbf{b}(s) = \left[\mathbf{e}(s)\right]^\dagger \mathbf{e}(s)$ and (3.34) states that the intensity does not change as light propagates through Kerr media. This is expected since we assumed that the Kerr media is lossless. Matrices for which (3.32) is true are called unitary [44].

Property 11 directly follows from the Jacobi identity of (3.14) and (2.120).

Property 11 (Unimodularity). *The matricant for Kerr media is unimodular*

$$|\mathbf{\Omega}(s, s_0)| = 1 \tag{3.36}$$

3.7 The Matricants Of Related Systems

This section develops the relationships between the matricants of systems with related system matrices. The system in Section 3.7.2 is used for media with symmetric field distributions in Section 3.8.2. The other two related systems are not used in this thesis

but are included here due to our expectation that in future work they can be used to model secondary effects in Kerr electro-optic measurements such as temperature gradients and electrohydrodynamic motion.

3.7.1 Perturbation To The System Matrix

Consider that $\mathbf{A}(s)$ is perturbed so that the system matrix becomes

$$\mathbf{A}_{\mathrm{p}}(s) = \mathbf{A}(s) + \mathbf{A}_{\epsilon}(s) \tag{3.37}$$

The differential equation for the new system is given as

$$\frac{d\mathbf{\Omega}_{\mathrm{p}}(s, s_0)}{ds} = \left[\mathbf{A}(s) + \mathbf{A}_{\epsilon}(s)\right]\mathbf{\Omega}_{\mathrm{p}}(s, s_0) \tag{3.38}$$

We let

$$\mathbf{\Omega}_{\mathrm{p}}(s, s_0) = \mathbf{\Omega}(s, s_0)\mathbf{\Omega}_{\epsilon}(s, s_0) \tag{3.39}$$

and then

$$\frac{d\mathbf{\Omega}_{\epsilon}(s, s_0)}{ds} = \frac{d\left[\mathbf{\Omega}(s_0, s)\mathbf{\Omega}_{\mathrm{p}}(s, s_0)\right]}{ds} \tag{3.40}$$

$$= \mathbf{\Omega}(s_0, s)\frac{d\mathbf{\Omega}_{\mathrm{p}}(s, s_0)}{ds} + \frac{d\mathbf{\Omega}(s_0, s)}{ds}\mathbf{\Omega}_{\mathrm{p}}(s, s_0) \tag{3.41}$$

$$= \mathbf{\Omega}(s_0, s)\left[\mathbf{A}(s) + \mathbf{A}_{\epsilon}(s)\right]\mathbf{\Omega}_{\mathrm{p}}(s, s_0) - \mathbf{\Omega}(s_0, s)\mathbf{A}(s)\mathbf{\Omega}_{\mathrm{p}}(s, s_0) \tag{3.42}$$

$$= \mathbf{\Omega}(s_0, s)\mathbf{A}_{\epsilon}(s)\mathbf{\Omega}_{\mathrm{p}}(s, s_0) \tag{3.43}$$

Thus

$$\frac{d\mathbf{\Omega}_{\epsilon}(s, s_0)}{ds} = \left\{\left[\mathbf{\Omega}(s, s_0)\right]^{-1}\mathbf{A}_{\epsilon}(s)\mathbf{\Omega}(s, s_0)\right\}\mathbf{\Omega}_{\epsilon}(s, s_0) \tag{3.44}$$

where the bracketed term represents another system matrix. Equation (3.44) can be used to find the effects of the perturbation matrix on the matricant.

3.7.2 Complex Conjugation $(*)$ Of The System Matrix

We now investigate the matricant of the system whose system matrix is given by $\left[\mathbf{A}(s)\right]^*$. This matrix results for light waves traveling in the $-s$ direction, changing $\mathbf{A}(s)$

and $\mathbf{A}'(s)$ in (2.120) and (2.121) to their complex conjugates (cc). Let the matricant of this system be $\mathbf{\Omega}_{\rm cc}(s, s_0)$. Then from (3.9)

$$\begin{aligned}\mathbf{\Omega}_{\rm cc}(s, s_0) &= \mathbf{I} + \int_{s_0}^{s} \big[\mathbf{A}(s')\big]^* ds' + \int_{s_0}^{s} \big[\mathbf{A}(s')\big]^* \int_{s_0}^{s'} \big[\mathbf{A}(s'')\big]^* ds'' ds' + \cdots \\ &= \left[\mathbf{I} + \int_{s_0}^{s} \mathbf{A}(s') ds' + \int_{s_0}^{s} \mathbf{A}(s') \int_{s_0}^{s'} \mathbf{A}(s'') ds'' ds' + \cdots\right]^* \\ &= \big[\mathbf{\Omega}(s, s_0)\big]^* \end{aligned} \tag{3.45}$$

Hence if the system matrix is replaced by its complex-conjugate the matricant of the new system is also replaced by its complex-conjugate.

This property can also be shown beginning with the differential equation of the new system

$$\frac{d\mathbf{b}_{cc}(s)}{ds} = \big[\mathbf{A}(s)\big]^* \mathbf{b}_{cc}(s) \tag{3.46}$$

Taking the complex conjugate of (3.46) yields

$$\frac{d\mathbf{b}^*_{cc}(s)}{ds} = \mathbf{A}(s)\mathbf{b}^*_{cc}(s) \tag{3.47}$$

from which it follows that

$$\mathbf{b}^*_{cc}(s) = \mathbf{\Omega}(s, s_0)\mathbf{b}^*_{cc}(s_0) \tag{3.48}$$

or

$$\mathbf{b}_{cc}(s) = \big[\mathbf{\Omega}(s, s_0)\big]^* \mathbf{b}_{cc}(s_0) \tag{3.49}$$

which shows that

$$\mathbf{\Omega}_{\rm cc}(s, s_0) = \big[\mathbf{\Omega}(s, s_0)\big]^* \tag{3.50}$$

3.7.3 Addition Of A Source Term

We now consider the solutions to the system with a source term

$$\frac{d\mathbf{b}(s)}{ds} = \mathbf{A}(s)\mathbf{b}(s) + \mathbf{d}(s) \tag{3.51}$$

Assume a solution of the form

$$\mathbf{b}(s) = \mathbf{\Omega}(s, s_0)\mathbf{x}(s) \tag{3.52}$$

where $\mathbf{\Omega}(s, s_0)$ remains the homogeneous solution to (3.52) with $\mathbf{d}(s) = 0$. Substituting (3.52) in (3.51) together with (3.10) yields

$$\mathbf{\Omega}(s, s_0)\frac{d\mathbf{x}(s)}{ds} = \mathbf{d}(s) \tag{3.53}$$

from which it follows that

$$\mathbf{x}(s) = \mathbf{x}(s_0) + \int_{s_0}^{s} \left[\mathbf{\Omega}(s', s_0)\right]^{-1}\mathbf{d}(s')ds' \tag{3.54}$$

Substituting (3.54) into (3.52) gives the solution to (3.51)

$$\mathbf{b}(s) = \mathbf{\Omega}(s, s_0)\mathbf{x}(s_0) + \mathbf{\Omega}(s, s_0)\int_{s_0}^{s} \left[\mathbf{\Omega}(s', s_0)\right]^{-1}\mathbf{d}(s')ds' \tag{3.55a}$$

$$= \mathbf{\Omega}(s, s_0)\mathbf{b}(s_0) + \int_{s_0}^{s} \mathbf{\Omega}(s, s')\mathbf{d}(s')ds' \tag{3.55b}$$

where we used (3.11) and (3.20). Note that the first term on the right is the homogeneous solution and the second term is the particular solution. $\mathbf{\Omega}(s, s')$ which is used to find the effects of the source term is sometimes called the Cauchy matrix [41].

3.8 Matricant For Special Case Systems

3.8.1 Matricant As A Matrix Exponential

For the special case when $\mathbf{A}(s)$ is constant

$$\mathbf{A}(s) = \mathbf{A} \tag{3.56}$$

(3.9) reduces to

$$\begin{aligned}\mathbf{\Omega}(s_0, s) &= \mathbf{I} + \mathbf{A}\int_{s_0}^{s} ds' + \mathbf{A}^2\int_{s_0}^{s}\int_{s_0}^{s'} ds''ds' + \cdots \\ &= \exp\left[(s - s_0)\mathbf{A}\right]\end{aligned} \tag{3.57}$$

where

$$\exp\big[(s-s_0)\mathbf{A}\big] = \mathbf{I} + (s-s_0)\mathbf{A} + (s-s_0)^2\frac{\mathbf{A}^2}{2!} + (s-s_0)^3\frac{\mathbf{A}^3}{3!} + \cdots \tag{3.58}$$

is the well known matrix exponential.

For constant $\mathbf{A}(s)$ the matrix exponential can also be directly shown to be the solution to (3.10) by taking the derivative of both sides of (3.58)

$$\frac{d\exp\big[(s-s_0)\mathbf{A}\big]}{ds} = \mathbf{A} + (s-s_0)\mathbf{A}^2 + (s-s_0)^2\frac{\mathbf{A}^3}{2!} + \cdots \tag{3.59a}$$

$$= \mathbf{A}\exp\big[(s-s_0)\mathbf{A}\big] \tag{3.59b}$$

In analogy to the scalar case it is natural to expect that for a general $\mathbf{A}(s)$ the matricant is given as

$$\mathbf{\Omega}(s_0, s) = \exp\big[\mathbf{V}(s, s_0)\big] \tag{3.60}$$

where

$$\mathbf{V}(s, s_0) = \int_{s_0}^{s} \mathbf{A}(s')ds' \tag{3.61}$$

However taking the derivative of $\exp[\mathbf{V}(s, s_0)]$ shows

$$\begin{aligned}\frac{d\exp\big[\mathbf{V}(s, s_0)\big]}{ds} &= \mathbf{A}(s) + \frac{1}{2!}\left[\mathbf{V}(s, s_0)\mathbf{A}(s) + \mathbf{A}(s)\mathbf{V}(s, s_0)\right] \\ &\quad + \frac{1}{3!}\left[\mathbf{V}^2(s, s_0)\mathbf{A}(s) + \mathbf{V}(s, s_0)\mathbf{A}(s)\mathbf{V}(s, s_0) + \mathbf{A}(s)\mathbf{V}^2(s, s_0)\right]\cdots\end{aligned} \tag{3.62}$$

and it is recognized from (3.62) that the exponential of $\mathbf{V}(s, s_0)$ satisfies (3.10) only if it commutes with $\mathbf{A}(s)$

$$\mathbf{V}(s, s_0)\mathbf{A}(s) = \mathbf{A}(s)\mathbf{V}(s, s_0) \tag{3.63}$$

and (3.63) is not true for a general system matrix.

Equation (3.63) does suggest special cases for which (3.60) is a solution. One such case for example is when $\mathbf{A}(s)$ or $\mathbf{A}'(s)$ is diagonal. Some other cases are considered in Section 3.10. The most general case for (3.60) to be a solution to (3.10) may be found

in [41]. If some details, mainly due to repeated eigenvalues, are set aside, it is required for $\int_{s_0}^{s} \mathbf{A}(s')ds'$ and $\mathbf{A}(s)$ to have the same set of s independent eigenvectors.

3.8.2 Matricant Of Symmetric Kerr Media

We call a Kerr medium symmetric if the transverse component of the applied electric field distribution has a plane of symmetry that is perpendicular to the propagation direction of light. Without loss of generality let this plane be $s = 0$. Then by (3.20) with $s_0' = 0$ and $s_0 = -s$

$$\mathbf{\Omega}(s, -s) = \mathbf{\Omega}(s, 0)\mathbf{\Omega}(0, -s) \tag{3.64}$$

Since the medium is symmetric, the matricant $\mathbf{\Omega}(0, -s)$ for light that travels from $-s$ to 0 in the $+s$ direction is equivalent to the matricant $\mathbf{\Omega}(0, s)$ for light that travels from s to 0 in the $-s$ direction.

For light propagation in the $-s$ direction the derivation of (2.118) can be repeated beginning with a $\exp(iks)$ dependence in (2.106). The result is (2.112) and (2.114) with k replaced by $-k$. Then $\mathbf{A}(s)$ in (2.118) and (2.120) is replaced by $\left[\mathbf{A}(s)\right]^*$

$$\frac{d\underline{\mathbf{b}}(s)}{ds} = \left[\mathbf{A}(s)\right]^* \underline{\mathbf{b}}(s) \tag{3.65}$$

where

$$\underline{\mathbf{b}}(s) = \mathbf{b}(s) \exp\left(-\frac{ik}{2\epsilon} \int_0^s \left[\epsilon_{mm}(s') + \epsilon_{pp}(s') + 2\epsilon\right] ds'\right) \tag{3.66}$$

However since Kerr electro-optic measurements are intensity based, the phases of the components of $\mathbf{b}(s)$ are irrelevant and a distinction between $\mathbf{b}$ and $\underline{\mathbf{b}}$ is not necessary.

Consistent with Section 3.7.2 we denote the matricant for light propagation in the $-s$ direction by $\mathbf{\Omega}_{cc}(s, s_0)$. It follows from (3.22), (3.32) and (3.45) that for two points s_1 and s_2 in Kerr media

$$\mathbf{\Omega}_{cc}(s_1, s_2) = \left[\mathbf{\Omega}(s_2, s_1)\right]^{\mathrm{T}} \tag{3.67}$$

Using (3.67) for symmetric media we obtain for $s_1 = 0$ and $s_2 = s$

$$\mathbf{\Omega}(0, -s) = \mathbf{\Omega}_{cc}(0, s) = \left[\mathbf{\Omega}(s, 0)\right]^{\mathrm{T}} \tag{3.68}$$

Substituting (3.68) in (3.64) yields

$$\boldsymbol{\Omega}(s,-s) = \boldsymbol{\Omega}(s,0)\big[\boldsymbol{\Omega}(s,0)\big]^{\mathrm{T}} \tag{3.69}$$

It follows that for symmetric media, the matricant between two points that are symmetric with respect to the plane of symmetry is symmetric. Important examples of symmetric media are media with axisymmetric electric field distributions and media with constant magnitude and direction electric field distributions (which are also axisymmetric).

3.9 A General Form For The Matricant

The relationships between the entries of a 2×2 unitary matrix can be obtained from (3.32) as

$$|\Omega_{11}(s,s_0)|^2 + |\Omega_{12}(s,s_0)|^2 = 1 \tag{3.70a}$$

$$|\Omega_{21}(s,s_0)|^2 + |\Omega_{22}(s,s_0)|^2 = 1 \tag{3.70b}$$

$$|\Omega_{11}(s,s_0)|^2 + |\Omega_{21}(s,s_0)|^2 = 1 \tag{3.70c}$$

and

$$\Omega_{11}(s,s_0)\Omega_{21}^*(s,s_0) + \Omega_{12}^*(s,s_0)\Omega_{22}(s,s_0) = 0 \tag{3.71}$$

Any other relationship can be expressed in terms of (3.70) and (3.71). From (3.70) it is clear that the magnitudes of the entries can be identified by a single parameter less than one. Equation (3.71) supplies a relationship between the arguments of $\Omega_{ij}(s,s_0)$, thus at most three parameters are needed to express the arguments of $\Omega_{ij}(s,s_0)$. A general form with four parameters that satisfies (3.70) and (3.71) can be deduced by inspection as

$$\boldsymbol{\Omega}(s,s_0) = \exp\big[i\eta(s,s_0)\big] \begin{bmatrix} \exp\big[i\xi(s,s_0)\big]\cos\theta(s,s_0) & \exp\big[i\zeta(s,s_0)\big]\sin\theta(s,s_0) \\ -\exp\big[-i\zeta(s,s_0)\big]\sin\theta(s,s_0) & \exp\big[-i\xi(s,s_0)\big]\cos\theta(s,s_0) \end{bmatrix} \tag{3.72}$$

By direct substitution it is easily shown that (3.72) satisfies (3.32). Here $\theta(s, s_0)$ is the parameter that identifies the magnitudes of the entries hence

$$0 \leq \theta(s, s_0) \leq \frac{\pi}{2} \tag{3.73}$$

It follows from the Jacobi identity (3.36) that the determinant of $\mathbf{\Omega}(s, s_0)$ must be unity and $\eta(s, s_0) = 0$ in (3.72). Thus $\mathbf{\Omega}(s, s_0)$ reduces to

$$\mathbf{\Omega}(s, s_0) = \begin{bmatrix} \exp\big[i\xi(s, s_0)\big] \cos\theta(s, s_0) & \exp\big[i\zeta(s, s_0)\big] \sin\theta(s, s_0) \\ -\exp\big[-i\zeta(s, s_0)\big] \sin\theta(z, z_0) & \exp\big[-i\xi(s, s_0)\big] \cos\theta(s, s_0) \end{bmatrix} \tag{3.74}$$

Equation (3.74) states that the matricant for Kerr media can be expressed in terms of three parameters (ξ, θ, ζ).

The reason that $\eta(s, s_0) = 0$ is because of the exact form of the transformation in (2.117) relating $b_j(s)$ and $e_j(s)$. If the Kerr electro-optic measurement theory is developed using the electric field $\mathbf{e}$ instead of $\mathbf{b}$ then for the matricant relating input and output electric fields using (2.117) we obtain

$$\eta(s, s_0) = -\frac{ik}{4\epsilon} \int_{s_0}^{s} [\epsilon_{mm}(s') + \epsilon_{pp}(s') + 2\epsilon]\, ds' \tag{3.75}$$

Beginning with (2.70) it is possible to relate η directly to the applied electric field and the isotropic permittivity. Thus if measured, η can be useful. However η is not available from intensity based Kerr electro-optic measurements and some other measurement methodology must be developed.

3.10 Analytical Evaluation

Despite the simple forms of (2.118) and (2.119), general analytical evaluation of their matricants is difficult. In this section we consider some simple electric field distributions for which analytical evaluations are possible. Section 3.10.1 finds the matricant when the direction of the (transverse) electric field is constant along the light path which most past Kerr effect analysis and measurements have been limited to. The other special cases are particularly useful for testing numerical algorithms to be used for the usual electric field distributions that do not allow closed form solutions and thus require numerical evaluation of (2.118) and (2.119). All these cases are in fact matrix exponentials and can be found as such although we find them by straight-forward

integration.

3.10.1 Constant $\mathbf{E}_{\mathrm{T}}(s)$ Direction

Such electric field distributions are typically the cases for parallel plane, coaxial cylinder and parallel cylinder electrodes; on the ground plane of an electrode system such as point/plane electrodes; or certain planes of symmetric electrode systems such as the center plane of sphere/sphere electrodes or along the axis of point/plane electrodes.

If the direction φ of the (transverse) electric field is constant along the light path then $\frac{d\varphi}{ds} = 0$ and (2.119), (2.121) and (2.123) yield

$$\begin{bmatrix} \frac{db_{\parallel}(s)}{ds} \\ \frac{db_{\perp}(s)}{ds} \end{bmatrix} = \begin{bmatrix} -i\pi BE_T^2(s) & 0 \\ 0 & i\pi BE_T^2(s) \end{bmatrix} \begin{bmatrix} b_{\parallel}(s) \\ b_{\perp}(s) \end{bmatrix} \tag{3.76}$$

which can be easily be integrated to give

$$\mathbf{b}'(s) = \mathbf{G}\big[\gamma(s, s_0)\big]\mathbf{b}'(s_0) \tag{3.77}$$

where

$$\mathbf{G}(\theta) = \begin{bmatrix} e^{-i\theta} & 0 \\ 0 & e^{i\theta} \end{bmatrix} \tag{3.78}$$

and

$$\gamma(s, s_0) = \int_{s_0}^{s} \pi BE_T^2(s')ds' \tag{3.79}$$

with $\gamma(s, s_0)$ being half the phase shift between the electric field components $e_{\parallel}(s)$ and $e_{\perp}(s)$ polarized parallel and perpendicular to $\mathbf{E}_{\mathrm{T}}$. The matrices $\mathbf{\Omega}'(s, s_0)$ and $\mathbf{\Omega}(s, s_0)$ follow as

$$\mathbf{\Omega}'(s, s_0) = \mathbf{G}\big[\gamma(s, s_0)\big] \tag{3.80}$$

$$\mathbf{\Omega}(s, s_0) = \mathbf{S}(-\varphi)\mathbf{G}\big[\gamma(s, s_0)\big]\mathbf{S}(\varphi) \tag{3.81}$$

3.10.2 Constant $\mathbf{E}_{\mathrm{T}}(s)$ Direction and Magnitude

When the magnitude of the electric field is also constant along the light path (3.79) reduces to

$$\gamma(s, s_0) = (s - s_0)\pi B E_T^2 \tag{3.82}$$

This case is frequently used in the coming chapters since the most straight forward discretizations of nonuniform electric field distributions are made of regions with electric fields that are constant in magnitude and direction. We use $\mathbf{\Omega_c}$ to denote the matricant for such a region. Thus (3.81) and (3.82) yield

$$\mathbf{\Omega_c} = \mathbf{S}(-\varphi)\mathbf{G}(\pi B E_T^2 l)\mathbf{S}(\varphi) \tag{3.83}$$

where $l = s_{\text{out}} - s_{\text{in}}$ and s_{in} and s_{out} are the s-coordinates of the entrance and the emergence points of the light ray to and from the field stressed regions.

With l giving the electrode length, (3.83) is also the matricant solution of one dimensional electrode geometries like parallel plate electrodes. The solution for two dimensional geometries like two long concentric or parallel cylinders are also given by (3.83) provided that the light propagation direction is in the direction along the long symmetry axis. Thus for one or two dimensional geometries we have

$$E_T = \sqrt{\frac{\gamma}{\pi l B}} \tag{3.84}$$

that allows determination of E_T from γ. As discussed in chapter 1 this is the basis of the earlier Kerr electro-optic measurements.

Also notice that

$$\mathbf{\Omega_c^T} = \mathbf{S^T}(\varphi)\mathbf{G^T}(\pi B E_T^2 l)\mathbf{S^T}(-\varphi) = \mathbf{S}(-\varphi)\mathbf{G}(\pi B E_T^2 l)\mathbf{S}(\varphi) \tag{3.85}$$

$$= \mathbf{\Omega_c} \tag{3.86}$$

Thus $\mathbf{\Omega_c}$ is symmetric. Equations (3.32) and (3.86) also yield the inverse of $\mathbf{\Omega_c}$ as

$$[\mathbf{\Omega_c}]^{-1} = \mathbf{S}(-\varphi)\mathbf{G}(-\pi B E_T^2 l)\mathbf{S}(\varphi) \tag{3.87}$$

3.10.3 Constant $\frac{d\varphi(s)}{ds}/E_T^2(s)$

We first write (2.119) in the form

$$\frac{d\mathbf{b}'(s)}{ds} = \pi B E_T^2(s)\mathbf{N}'\,\mathbf{b}'(s) \tag{3.88}$$

where $\mathbf{N}'$ is the constant matrix

$$\mathbf{N}' = \begin{bmatrix} -i & R' \\ -R' & i \end{bmatrix} \tag{3.89}$$

$$R' = \frac{\frac{d\varphi(s)}{ds}}{\pi B E_T^2(s)} \tag{3.90}$$

Equation (3.88) can be solved by diagonalizing $\mathbf{N}'$ (see for example [44] for diagonalization, eigenvectors, and eigenvalues). The eigenvalues are $\pm iS'$ where

$$S' = \sqrt{1 + R'^2} \tag{3.91}$$

and the eigenvector matrix $\mathbf{V}_{\mathbf{N}'}$ is found as

$$\mathbf{V}_{\mathbf{N}'} = \begin{bmatrix} \frac{R'}{\sqrt{2S'(S'+1)}} & \frac{R'}{\sqrt{2S'(S'-1)}} \\ \frac{i(1+S')}{\sqrt{2S'(S'+1)}} & \frac{i(1-S')}{\sqrt{2S'(S'-1)}} \end{bmatrix} \tag{3.92}$$

We define

$$\mathbf{c}'(s) = \mathbf{V}_{\mathbf{N}'}^{\dagger}\mathbf{b}'(s) \tag{3.93}$$

where $\mathbf{V}_{\mathbf{N}'}^{\dagger} = \left[\mathbf{V}_{\mathbf{N}'}^{\mathrm{T}}\right]^*$.

Substituting (3.93) into (3.88) we get the differential equation for $\mathbf{c}'(s)$

$$\frac{d\mathbf{c}'(s)}{ds} = \pi B E_T^2(s)\mathbf{N}'_{\mathbf{d}}\mathbf{c}'(s) \tag{3.94}$$

where $\mathbf{N}'_{\mathbf{d}} = \mathbf{V}_{\mathbf{N}'}^{\dagger}\mathbf{N}'\mathbf{V}_{\mathbf{N}'} = \left[\begin{smallmatrix} iS' & 0 \\ 0 & -iS' \end{smallmatrix}\right]$ is the diagonalized matrix. Equation (3.94) is easily solved to yield

$$\mathbf{c}'(s) = \mathbf{G}\left[-\eta'(s, s_0)\right]\mathbf{c}'(s_0) \tag{3.95}$$

where $\mathbf{G}(\theta)$ is defined in (3.78) and

$$\eta'(s, s_0) = S' \int_{s_0}^{s} \pi B E_T^2(s') ds' \tag{3.96}$$

Using (3.3), (3.93) and (3.95) $\mathbf{\Omega}'(s, s_0) = \mathbf{V}_{\mathbf{N}'} \mathbf{G}\big[-\eta'(s, s_0)\big] \mathbf{V}_{\mathbf{N}'}^{\dagger}$ and can be obtained by direct multiplication as

$$\mathbf{\Omega}'(s, s_0) = \begin{bmatrix} \cos\eta'(s, s_0) - i\frac{1}{S'} \sin\eta'(s, s_0) & \frac{R'}{S'} \sin\eta'(s, s_0) \\ -\frac{R'}{S'} \sin\eta'(s, s_0) & \cos\eta'(s, s_0) + i\frac{1}{S'} \sin\eta'(s, s_0) \end{bmatrix} \tag{3.97}$$

If both $E_T^2(s)$ and $\frac{d\varphi(s)}{ds}$ are constants then $\eta(s, s_0)$ reduces to

$$\eta'(s, s_0) = (s - s_0) \sqrt{(\pi B E_T^2)^2 + \left(\frac{d\varphi}{ds}\right)^2} \tag{3.98}$$

Note that if $\frac{d\varphi}{ds} = 0$, then (3.98) reduces to (3.82).

3.10.4 Constant $\left[E_m(s) E_p(s) / \left[E_m^2(s) - E_p^2(s)\right]\right)$

We first write (2.118) in the form

$$\frac{d\mathbf{b}(s)}{ds} = -\pi B \big[E_m^2(s) - E_p^2(s)\big] \mathbf{N}\, \mathbf{b}(s) \tag{3.99}$$

where $\mathbf{N}$ is the constant matrix

$$\mathbf{N} = \begin{bmatrix} 1 & R \\ R & -1 \end{bmatrix} \tag{3.100}$$

$$R = \frac{2E_m(s) E_p(s)}{E_m^2(s) - E_p^2(s)} \tag{3.101}$$

Equation (3.99) can be solved similar to (3.88). The eigenvalues of $\mathbf{N}$ are $\pm S$ where

$$S = \sqrt{1 + R^2} \tag{3.102}$$

and the eigenvector matrix $\mathbf{V}_{\mathbf{N}}$ is

$$\mathbf{V}_{\mathbf{N}} = \frac{1}{\sqrt{2S}} \begin{bmatrix} \sqrt{S+1} & -\sqrt{S-1} \\ \sqrt{S-1} & \sqrt{S+1} \end{bmatrix} \tag{3.103}$$

We define

$$\mathbf{c}(s) = \mathbf{V}_\mathbf{N}^\dagger \mathbf{b}(s) \tag{3.104}$$

and substitute (3.93) in (3.99) to get the differential equation for $\mathbf{c}(s)$

$$\frac{d\mathbf{c}(s)}{ds} = -i\pi B\big[E_m^2(s) - E_p^2(s)\big]\mathbf{N_d}\mathbf{c}(s) \tag{3.105}$$

Here $\mathbf{N_d} = \mathbf{V}_\mathbf{N}^\dagger \mathbf{N} \mathbf{V_N} = \left[\begin{smallmatrix} S & 0 \\ 0 & -S \end{smallmatrix}\right]$. Equation (3.105) is easily solved to yield

$$\mathbf{c}(s) = \mathbf{G}\big[\eta(s, s_0)\big]\mathbf{c}(s_0) \tag{3.106}$$

where $\mathbf{G}(\theta)$ is defined in (3.78) and

$$\eta(s, s_0) = S \int_{s_0}^{s} \pi B\big[E_m^2(s) - E_p^2(s)\big] ds' \tag{3.107}$$

Using (3.3), (3.93) and (3.106), $\mathbf{\Omega}(s, s_0) = \mathbf{V_N}\mathbf{G}\big[\eta(s, s_0)\big]\mathbf{V}_\mathbf{N}^\dagger$ and is found by direct multiplication as

$$\mathbf{\Omega}(s, s_0) = \begin{bmatrix} \cos\eta(s, s_0) - i\frac{1}{S}\sin\eta(s, s_0) & -i\frac{R}{S}\sin\eta(s, s_0) \\ -i\frac{R}{S}\sin\eta(s, s_0) & \cos\eta(s, s_0) + i\frac{1}{S}\sin\eta(s, s_0) \end{bmatrix} \tag{3.108}$$

3.10.5 Concentric Spherical Electrodes

The electric field distribution of concentric spherical electrodes in space provides an excellent debugging tool during the software development for the forward theory of Kerr electro-optic measurements. For any line in space the matricant is available analytically. This geometry may also be practical as conducting film coated transparent glass can be used as spherical electrodes making Kerr electro-optic measurements possible.

The potential and electric field distribution of concentric spherical electrodes are spherically symmetric. We assume the inner electrode of radius R is at potential V and the outer electrode of radius R_{out} is grounded. Then the potential is found by matching the boundary conditions for the spherically symmetric $1/r$ Laplacian solution

$$\phi(r) = V\left(1 - \frac{R}{R_{\text{out}}}\right)^{-1}\left(\frac{R}{r} - \frac{R}{R_{\text{out}}}\right) = \tilde{V}\left(\frac{R}{r} - \frac{R}{R_{\text{out}}}\right) \tag{3.109}$$

where $\tilde{V} = V\left(1 - \frac{R}{R_{\text{out}}}\right)^{-1}$ is defined to make the coming Kerr electro-optic measurement expressions less cumbersome. Here the origin of the fixed xyz-frame is chosen to coincide with the centers of the spheres.

Notice that due to the spherical symmetry, light rays at the same distance to the inner spherical electrode (or origin) yield the same Kerr electro-optic measurement. As an illustration, in Figure 3.1 (left) we show three light rays at the same distance to the inner electrode which would result in the same Kerr electro-optic measurement.

To derive the analytical expressions for the Kerr electro-optic measurements we choose the light frame so that $\hat{m}$ points from the light ray's closest point to the inner spherical electrode to the origin as illustrated in Figure 3.1 (right). We let d be the distance of the light ray to the origin ($d = 2R$ for the illustration in Figure 3.1-right). When the *mps* coordinate system is fixed to a light ray it is an ordinary cartesian frame. In particular we have

$$r = \sqrt{m^2 + p^2 + s^2} \tag{3.110}$$

and the applied electric field components in space are found by taking the negative gradient of (3.109) after substituting (3.110)

$$\vec{E}(m,p,s) = -\vec{\nabla}\phi(r) = -\left[\frac{\partial\phi(r)}{\partial m}\hat{m} + \frac{\partial\phi(r)}{\partial p}\hat{p} + \frac{\partial\phi(r)}{\partial s}\hat{s}\right] \tag{3.111}$$

$$= \frac{\tilde{V}R}{(m^2 + p^2 + s^2)^{3/2}}\left[m\hat{m} + p\hat{p} + s\hat{s}\right] \tag{3.112}$$

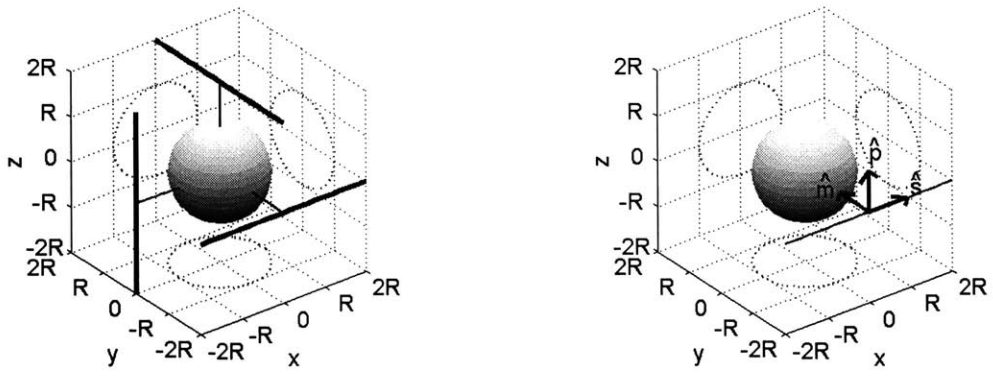

Figure 3.1: (left) Three light rays that would result in the same Kerr electro-optic measurement. (right) The light frame chosen for the particular line.

Along the light ray $m = d$ and $p = 0$, thus (3.112) reduces to

$$\vec{E}(m,p,s)\Big|_{m=d,p=0} = \frac{\tilde{V}Rd}{(d^2+s^2)^{3/2}}\hat{m} + \frac{\tilde{V}Rs}{(d^2+s^2)^{3/2}}\hat{s} \tag{3.113}$$

Since E_s is along the light path it does not effect the Kerr electro-optic measurements. Thus $\varphi(s)$ is constant and equal to 0 and the matricant between two points s_0 and s_1 follows from (3.80) as

$$\mathbf{\Omega}(s_1,s_0) = \mathbf{G}\big[\gamma(s_1,s_0)\big] \tag{3.114}$$

where

$$\gamma(s_1,s_0) = \pi B\int_{s_0}^{s_1} E_m^2(s)\,ds = \pi B\tilde{V}^2R^2d^2\int_{s_0}^{s_1}\frac{ds}{(d^2+s^2)^3} \tag{3.115}$$

$$= \pi B\tilde{V}^2R^2\left[\frac{1}{4}\frac{s}{(d^2+s^2)^2} + \frac{3}{8d^2}\frac{s}{d^2+s^2} + \frac{3}{8d^3}\arctan\frac{s}{d}\right]\Bigg|_{s=s_0}^{s=s_1} \tag{3.116}$$

Since $\varphi(s) = 0$ throughout the ray, it follows from (3.81) that the matricants in the light frame and E_T-frame are identical.

$$\mathbf{\Omega}'(s,s_0) = \mathbf{\Omega}(s,s_0) \tag{3.117}$$

If s_0 and s_1 are chosen to be the points where the light ray enters and leaves the inter-electrode region, simulating the case when the spherical electrodes are transparent, we have

$$s_0 = -\sqrt{R_{\text{out}}^2 - d^2} \tag{3.118}$$

$$s_1 = \sqrt{R_{\text{out}}^2 - d^2} \tag{3.119}$$

and (3.116) reduces to

$$\gamma = \pi B\tilde{V}^2R^2\left[\frac{1}{2}\frac{\sqrt{R_{\text{out}}^2-d^2}}{R_{\text{out}}^4} + \frac{3}{4d^2}\frac{\sqrt{R_{\text{out}}^2-d^2}}{R_{\text{out}}^2} + \frac{3}{4d^3}\arctan\frac{\sqrt{R_{\text{out}}^2-d^2}}{d}\right] \tag{3.120}$$

when $R_{\text{out}} > d > R$ and

$$\gamma = \pi B\tilde{V}^2R^2\left[\frac{1}{2}\frac{\sqrt{R_{\text{out}}^2-d^2}}{R_{\text{out}}^4} + \frac{3}{4d^2}\frac{\sqrt{R_{\text{out}}^2-d^2}}{R_{\text{out}}^2} + \frac{3}{4d^3}\arctan\frac{\sqrt{R_{\text{out}}^2-d^2}}{d}\right.$$

$$- \frac{\sqrt{R^2-d^2}}{R^4} - \frac{3}{4d^2}\frac{\sqrt{R^2-d^2}}{R^2} - \frac{3}{4d^3}\arctan\frac{\sqrt{R^2-d^2}}{d}\Bigg] \quad (3.121)$$

when $R > d$. For $d > R_{\text{out}}$ the retardation γ is zero as the electric field in this region is zero.

Also note that for an isolated sphere such that $R_{\text{out}} \to \infty$, $\tilde{V} = V$ and (3.120) reduces to

$$\gamma = \frac{3\pi^2 B V^2 R^2}{8d^3} \quad (3.122)$$

3.11 Numerical Evaluation Of The Matricant

Equations (2.118) and (2.119) are ordinary differential equations and for a given $\mathbf{E}_{\text{T}}(s)$ distribution, many well established methods exist for their numerical solution. We use the well known fourth order Runge-Kutta method with a straightforward adaptive stepsize control. The method is well documented in the literature and will not be repeated here [45, 46]. Here we mention a few issues.

3.11.1 Evaluation of the Matricant Elements

To find the elements of $\mathbf{\Omega}(s, s_0)$ from a numerical integration of (2.118) notice from (3.2) that

$$\mathbf{b}(s_0) = \mathbf{e}_1 = \begin{bmatrix} 1 \\ 0 \end{bmatrix} \Longrightarrow \mathbf{\Omega}_{:1}(s, s_0) = \mathbf{b}(s) \quad (3.123)$$

where $\mathbf{e}_1 = \left[\begin{smallmatrix} 1 \\ 0 \end{smallmatrix}\right]$ and $\mathbf{\Omega}_{:1}$ denotes the first column of $\mathbf{\Omega}$. Thus integrating (2.128) with the initial conditions $\mathbf{u}(s_0) = \mathbf{e}_1$ and $\mathbf{v}(s_0) = 0$ gives the first column of the matricant. Since the second column is completely determined by the first column (see (3.74)), the matricant is totally determined. Similarly by using the identity

$$\mathbf{b}'(s) = \mathbf{e}_1 \Longrightarrow \mathbf{\Omega}_{:1}{}'(s, s_0) = \mathbf{b}'(s) \quad (3.124)$$

together with (2.127) and (2.130), $\mathbf{\Omega}'(s, s_0)$ can be determined.

3.11.2 Modified Real Form Of The Governing Equations

A direct application of the initial conditions described in (3.123) and (3.124) to (2.128) and (2.130) can be numerically problematic since at start the change in the first rows of $\mathbf{u}(s)$ and $\mathbf{u}'(s)$ can be very small compared to 1. To avoid this difficulty and introduce the adaptive criterion in Section 3.11.3 we define

$$\mathbf{u_d}(s) = \mathbf{u}(s) - \mathbf{e_1} \tag{3.125}$$

$$\mathbf{u_d}'(s) = \mathbf{u}'(s) - \mathbf{e_1} \tag{3.126}$$

where $\mathbf{u_d}(s) = \begin{bmatrix} u_d(s) \\ u_p(s) \end{bmatrix}$ with $u_d(s) = u_m(s) - 1$ and $\mathbf{u_d}'(s) = \begin{bmatrix} u_d'(s) \\ u_\perp(s) \end{bmatrix}$ with $u_d'(s) = u_\parallel(s) - 1$ and $\mathbf{e_1}$ is defined in (3.123). Substituting (3.125) into (2.128) yields

$$\frac{d}{ds}\begin{bmatrix} \mathbf{u_d}(s) \\ \mathbf{v}(s) \end{bmatrix} = \pi B \begin{bmatrix} \mathbf{0} & \mathbf{W}(s) \\ -\mathbf{W}(s) & \mathbf{0} \end{bmatrix} \begin{bmatrix} \mathbf{u_d}(s) \\ \mathbf{v}(s) \end{bmatrix} - \begin{bmatrix} \mathbf{0} \\ \mathbf{W}_{:1}(s) \end{bmatrix} \tag{3.127}$$

The extra source term introduced in (3.127) causes no difficulty for numerical integration while avoiding the numerical problem. With vanishing initial conditions $\mathbf{u_d}(s_0) = \mathbf{v}(s_0) = \mathbf{0}$, numerical integration of (3.127) yields the first column of $\mathbf{\Omega}$

$$\mathbf{\Omega}_{:1}(s, s_0) = \mathbf{e_1} + \mathbf{u_d}(s) + i\mathbf{v}(s) \tag{3.128}$$

Similarly substituting (3.126) into (2.130) yields

$$\frac{d}{ds}\begin{bmatrix} \mathbf{u_d}'(s) \\ \mathbf{v}'(s) \end{bmatrix} = \begin{bmatrix} \mathbf{Q}'(s) & \mathbf{W}'(s) \\ -\mathbf{W}'(s) & \mathbf{Q}'(s) \end{bmatrix} \begin{bmatrix} \mathbf{u_d}'(s) \\ \mathbf{v}'(s) \end{bmatrix} + \begin{bmatrix} \mathbf{Q}'_{:1}(s) \\ -\mathbf{W}'_{:1}(s) \end{bmatrix} \tag{3.129}$$

and numerical integration of (3.129) yields the first colum of $\mathbf{\Omega}'$

$$\mathbf{\Omega}'_{:1}(s, s_0) = \mathbf{e_1} + \mathbf{u_d}'(s) + i\mathbf{v}'(s) \tag{3.130}$$

3.11.3 Adaptive Stepsize Criterion

Since the intensity of the light does not change while propagating through Kerr media, using (3.123) and (3.124) we obtain

$$|\mathbf{u}(s)|^2 + |\mathbf{v}(s)|^2 = (u_d(s) + 1)^2 + u_p^2(s) + v_m^2(s) + v_p^2(s) = 1 \tag{3.131}$$

which implies that

$$u_d^2(s) + u_p^2(s) + v_m^2(s) + v_p^2(s) = -2u_d \tag{3.132}$$

Hence any numerical error in u_p, v_m or v_p also effects u_d. Motivated by this observation, as the adaptive error criterion we use the error in u_d.

In our numerical computations we typically begin with a very small step size h with respect to the geometry dimensions and at each step we calculate the solution at $2h$ with both two steps of h and one step of $2h$. Then we consider the inequality

$$e(u_d) = \left| \frac{u_{d_{2h}} - u_{d_h}}{u_{d_h}} \right| < 0.001 \tag{3.133}$$

where $u_{d_{2h}}$ and u_{d_h} are the results for the step size of $2h$ and h respectively. If (3.133) is true then we double the step size as the accuracy is unnecessarily high. If $e(u_d)$ is between 0.005 and 0.001 no action is taken. Otherwise the step is halved. An identical adaptive scheme is used for (2.130) with u_d' replacing u_d in (3.133). The numbers 0.005 and 0.001 can be decreased for higher accuracy.

Chapter 4

The Characteristic Parameters

4.1 Introduction

Chapter 3 established that the matricant for Kerr media can be described in terms of three parameters. It is plausible to continue the development with the parameters used in (3.74). However for reasons that will become clear in Chapter 5 it is much more convenient to use the so called characteristic parameters. This chapter introduces the characteristic parameters and continues the development of the forward Kerr electro-optic measurement theory in terms of these parameters.

4.2 A New General Form For The Matricant

4.2.1 Existence

Equation (3.74) is a general form of a unitary matrix with unit determinant and follows directly from (3.70) and (3.71). A less obvious general form is a combination of two rotators and a retarder

$$\mathbf{\Omega}(s, s_0) = \mathbf{S}\big[-\alpha_f(s, s_0)\big]\mathbf{G}\big[\gamma(s, s_0)\big]\mathbf{S}\big[\alpha_0(s, s_0)\big] \tag{4.1}$$

Here $\mathbf{S}$ and $\mathbf{G}$ are the rotator and retarder matrices that are respectively given in (2.125) and (3.78). The explicit form of (4.1) can be found by direct multiplication of matrices on the right hand side

$$\mathbf{\Omega}(s,s_0) = \cos\gamma(s,s_0)\begin{bmatrix}\cos\alpha_-(s,s_0) & \sin\alpha_-(s,s_0)\\ -\sin\alpha_-(s,s_0) & \cos\alpha_-(s,s_0)\end{bmatrix} + i\sin\gamma(s,s_0)\begin{bmatrix}-\cos\alpha_+(s,s_0) & -\sin\alpha_+(s,s_0)\\ -\sin\alpha_+(s,s_0) & \cos\alpha_+(s,s_0)\end{bmatrix} \tag{4.2}$$

where

$$\alpha_+(s,s_0) = \alpha_0(s,s_0) + \alpha_f(s,s_0) \tag{4.3}$$

$$\alpha_-(s,s_0) = \alpha_0(s,s_0) - \alpha_f(s,s_0) \tag{4.4}$$

To prove the assertion that it is possible to express $\mathbf{\Omega}(s,s_0)$ as in (4.1), we compare (3.74) and (4.2) to obtain

$$\tan\alpha_-(s,s_0) = \tan\theta(s,s_0)\frac{\cos\zeta(s,s_0)}{\cos\xi(s,s_0)} \tag{4.5a}$$

$$\tan\alpha_+(s,s_0) = \tan\theta(s,s_0)\frac{\sin\zeta(s,s_0)}{\sin\xi(s,s_0)} \tag{4.5b}$$

$$\tan\gamma(s,s_0) = \tan\xi(s,s_0)\frac{\cos\alpha_+(s,s_0)}{\cos\alpha_-(s,s_0)} \tag{4.5c}$$

With the possible exception of indeterminate forms such as $\cos\xi(s,s_0) = \cos\zeta(s,s_0) = 0$, for any $\theta(s,s_0)$, $\xi(s,s_0)$ and $\zeta(s,s_0)$, equation (4.5) yields a solution for $\alpha_-(s,s_0)$, $\alpha_+(s,s_0)$ and $\gamma(s,s_0)$. For each indeterminate form in (4.5), it can be individually checked that solutions for $\alpha_-(s,s_0)$, $\alpha_+(s,s_0)$ and $\gamma(s,s_0)$ exist (also see section 4.2.2). From $\alpha_-(s,s_0)$ and $\alpha_+(s,s_0)$ we can determine $\alpha_0(s,s_0)$ and $\alpha_f(s,s_0)$

$$\alpha_0(s,s_0) = \frac{\alpha_+(s,s_0) + \alpha_-(s,s_0)}{2} \tag{4.6}$$

$$\alpha_f(s,s_0) = \frac{\alpha_+(s,s_0) - \alpha_-(s,s_0)}{2} \tag{4.7}$$

Thus (4.5) proves that the matricant can be expressed as in (4.1).

4.2.2 Relations To The Rectangular Form

Typically the numerical integrations (see Section 3.11) to find the matricant yields a rectangular form which we express as

$$\mathbf{\Omega}(s, s_0) = \begin{bmatrix} \mathrm{p}(s, s_0) - i\mathrm{q}(s, s_0) & \mathrm{r}(s, s_0) - i\mathrm{t}(s, s_0) \\ -\mathrm{r}(s, s_0) - i\mathrm{t}(s, s_0) & \mathrm{p}(s, s_0) + i\mathrm{q}(s, s_0) \end{bmatrix} \tag{4.8}$$

where we explicitly separate the real and imaginary parts of each matrix element in (3.74)

$$\mathrm{p}(s, s_0) = \cos\xi(s, s_0)\cos\theta(s, s_0) \qquad \mathrm{q}(s, s_0) = -\sin\xi(s, s_0)\cos\theta(s, s_0) \tag{4.9a}$$

$$\mathrm{r}(s, s_0) = \cos\zeta(s, s_0)\sin\theta(s, s_0) \qquad \mathrm{t}(s, s_0) = -\sin\zeta(s, s_0)\sin\theta(s, s_0) \tag{4.9b}$$

Here $\mathrm{p}(s, s_0)$, $\mathrm{q}(s, s_0)$, $\mathrm{r}(s, s_0)$ and $\mathrm{t}(s, s_0)$ are real and because the determinant of $\mathbf{\Omega}(s, s_0)$ is one

$$\mathrm{p}^2(s, s_0) + \mathrm{q}^2(s, s_0) + \mathrm{r}^2(s, s_0) + \mathrm{t}^2(s, s_0) = 1 \tag{4.10}$$

Equations (4.8) and (4.10) directly follow from (3.74). A comparison between (4.2) and (4.8) yields

$$\alpha_-(s, s_0) = \begin{cases} \arctan_2\left[\mathrm{r}(s, s_0), \mathrm{p}(s, s_0)\right] & \mathrm{p}(s, s_0) \neq 0 \\ \frac{\pi}{2}\mathrm{sgn}\left[\mathrm{r}(s, s_0)\right] & \mathrm{p}(s, s_0) = 0 \end{cases} \tag{4.11a}$$

$$\alpha_+(s, s_0) = \begin{cases} \arctan_2\left[\mathrm{t}(s, s_0), \mathrm{q}(s, s_0)\right] & \mathrm{q}(s, s_0) \neq 0 \\ \frac{\pi}{2}\mathrm{sgn}\left[\mathrm{t}(s, s_0)\right] & \mathrm{q}(s, s_0) = 0 \end{cases} \tag{4.11b}$$

$$\gamma(s, s_0) = \arctan\sqrt{\frac{\mathrm{t}^2(s, s_0) + \mathrm{q}^2(s, s_0)}{\mathrm{r}^2(s, s_0) + \mathrm{p}^2(s, s_0)}} \tag{4.11c}$$

where we adopt the C/C++ math library convention that $\arctan_2(y, x)$ returns the arctangent of y/x in the right quadrant between $-\pi$ to π (signs of y and x respectively match to those of $\sin\left[\arctan_2(y, x)\right]$ and $\cos\left[\arctan_2(y, x)\right]$) and $\arctan(x)$ returns the arctangent of x between $-\pi/2$ to $\pi/2$. sgn denotes the sign function defined as $+1$ for positive argument and -1 for a negative argument.

Equation (4.11) addresses every possible indeterminate form except $\mathrm{p}(s, s_0) = \mathrm{r}(s, s_0) = 0$ and $\mathrm{q}(s, s_0) = \mathrm{t}(s, s_0) = 0$. These cases respectively imply $\gamma(s, s_0) = \pi/2$

and $\gamma(s, s_0) = 0$ and any respective value of $\alpha_-(s, s_0)$ and $\alpha_+(s, s_0)$ will work. This discussion and (4.11) also address all possible indeterminate forms in (4.5).

4.2.3 E_T-Frame

Since the properties of $\mathbf{\Omega}(s, s_0)$ that lead to (4.1) are also true for $\mathbf{\Omega}'(s, s_0)$, it can also be expressed in a similar form. We introduce two additional parameters $\beta_0(s, s_0)$ and $\beta_f(s, s_0)$ and express $\mathbf{\Omega}'(s, s_0)$ as

$$\mathbf{\Omega}'(s, s_0) = \mathbf{S}\big[-\beta_f(s, s_0)\big]\mathbf{G}\big[\gamma(s, s_0)\big]\mathbf{S}\big[\beta_0(s, s_0)\big] \tag{4.12}$$

The equality of $\gamma(s, s_0)$ in (4.1) and in (4.12) follows from (3.4). From (3.4), (4.1) and (4.12) we conclude that

$$\alpha_0(s, s_0) = \beta_0(s, s_0) + \varphi(s_0) \tag{4.13}$$

$$\alpha_f(s, s_0) = \beta_f(s, s_0) + \varphi(s) \tag{4.14}$$

The explicit form of $\mathbf{\Omega}'(s, s_0)$ is identical to the form in (4.2)

$$\begin{aligned}\mathbf{\Omega}'(s, s_0) = \cos\gamma(s, s_0) &\begin{bmatrix} \cos\beta_-(s, s_0) & \sin\beta_-(s, s_0) \\ -\sin\beta_-(s, s_0) & \cos\beta_-(s, s_0) \end{bmatrix} \\ &+ i\sin\gamma(s, s_0)\begin{bmatrix} -\cos\beta_+(s, s_0) & -\sin\beta_+(s, s_0) \\ -\sin\beta_+(s, s_0) & \cos\beta_+(s, s_0) \end{bmatrix}\end{aligned} \tag{4.15}$$

where

$$\beta_-(s, s_0) = \beta_0(s, s_0) - \beta_f(s, s_0) \tag{4.16}$$

$$\beta_+(s, s_0) = \beta_0(s, s_0) + \beta_f(s, s_0) \tag{4.17}$$

4.2.4 Symmetric Kerr Media

The transpose of the matricant $\mathbf{\Omega}(s, s_0)$ in (4.1) is found by the transpose rule of matrix products where each matrix is transposed and the product order is reversed

$$\begin{aligned}\mathbf{\Omega}^{\mathrm{T}}(s, s_0) &= \mathbf{S}^{\mathrm{T}}\big[\alpha_0(s, s_0)\big]\mathbf{G}^{\mathrm{T}}\big[\gamma(s, s_0)\big]\mathbf{S}^{\mathrm{T}}\big[-\alpha_f(s, s_0)\big] \\ &= \mathbf{S}\big[-\alpha_0(s, s_0)\big]\mathbf{G}\big[\gamma(s, s_0)\big]\mathbf{S}\big[\alpha_f(s, s_0)\big]\end{aligned} \tag{4.18}$$

Here $\mathbf{G} = \mathbf{G}^{\mathrm{T}}$ since it is diagonal and $\mathbf{S}^{\mathrm{T}}(\theta) = \mathbf{S}(-\theta)$ which is clear from the definition of the rotation matrix $\mathbf{S}$ in (2.125).

As discussed in Section 3.8.2 the matricant between the symmetry points of symmetric Kerr media is symmetric. Then for $s_0 = -s$ the matricant in (4.1) and its transpose in (4.18) are equal implying that for symmetric media $\alpha_0(s,-s)$ and $\alpha_f(s,-s)$ ($s=0$ is the symmetry plane) are equal and reduce to a single parameter which we denote by $\alpha_s(s)$

$$\alpha_s(s) = \alpha_0(s,-s) = \alpha_f(s,-s) \tag{4.19}$$

Thus, for symmetric media (4.3) and (4.4) reduce

$$\alpha_+(s,-s) = 2\alpha_s(s) \tag{4.20}$$

$$\alpha_-(s,-s) = 0 \tag{4.21}$$

To stress that the symmetry is valid only when $s_0 = -s$ we also define

$$\gamma_s(s) = \gamma(s,-s) \tag{4.22}$$

Thus the matricant for symmetric Kerr media is described by two parameters $\gamma_s(s)$ and $\alpha_s(s)$.

Using (4.20), (4.21) and (4.22) equations (4.2) and (4.11) respectively reduce to

$$\mathbf{\Omega}(s,-s) = \begin{bmatrix} \cos\gamma_s(s) - i\sin\gamma_s(s)\cos 2\alpha_s(s) & -i\sin\gamma_s(s)\sin 2\alpha_s(s) \\ -i\sin\gamma_s(s)\sin 2\alpha_s(s) & \cos\gamma_s(s) + i\sin\gamma_s(s)\cos 2\alpha_s(s) \end{bmatrix} \tag{4.23}$$

and

$$\alpha_s(s) = \begin{cases} \frac{1}{2}\arctan_2\left[\mathrm{t}(s,-s), \mathrm{q}(s,-s)\right] & \mathrm{q}(s,-s) \neq 0 \\ \frac{\pi}{4}\mathrm{sgn}\left[\mathrm{t}(s,-s)\right] & \mathrm{q}(s,-s) = 0 \end{cases} \tag{4.24a}$$

$$\gamma_s(s) = \arctan\sqrt{\frac{\mathrm{t}^2(s,-s) + \mathrm{q}^2(s,-s)}{\mathrm{p}^2(s,-s)}} \tag{4.24b}$$

Notice that $\mathrm{r}(s,-s) = 0$.

Since for symmetric media $\varphi(s) = \varphi(-s)$, it follows from (4.13) and (4.14) that

$\mathbf{\Omega}'(s,-s)$ in (4.12) is also symmetric for symmetric media. We introduce the parameter $\beta_s(s)$

$$\beta_s(s) = \beta_0(s,-s) = \beta_f(s,-s) \tag{4.25}$$

where

$$\alpha_s(s) = \beta_s(s) + \varphi(s) \tag{4.26}$$

4.2.5 Kerr Media With Constant Direction E-Field

If the direction of the (transverse) applied electric field $\varphi(s)$ is constant a comparison between (3.81) and (4.1) shows that

$$\alpha_0(s,s_0) = \alpha_f(s,s_0) = \varphi \tag{4.27}$$

4.3 Definition Of The Characteristic Parameters

4.3.1 General Kerr Medium

The coordinates s and s_0 are any two points inside the Kerr media. To find the total action of the Kerr media we let $s_0 = s_{\text{in}}$ and $s = s_{\text{out}}$ where s_{in} and s_{out} are the entrance and emergence points of the light beam in and out of the Kerr media. In the following when the parameters α_0, α_f and γ are used without argument, the arguments s and s_0 are respectively understood to be s_{in} and s_{out}.

$$\alpha_0 = \alpha_0(s_{\text{out}}, s_{\text{in}}) \tag{4.28a}$$

$$\alpha_f = \alpha_f(s_{\text{out}}, s_{\text{in}}) \tag{4.28b}$$

$$\gamma = \gamma(s_{\text{out}}, s_{\text{in}}) \tag{4.28c}$$

The parameters α_0, α_f and γ are well known in photoelasticity and are called the characteristic parameters [39]. The parameters α_0 and α_f are called the primary and secondary characteristic angles respectively, while γ is called the characteristic phase retardation. Since the first and last matrices in (4.1) are rotators, α_0 and α_f are the angles between the m-axis of the light frame and the so called characteristic directions.

Consider incident normalized light vector $\mathbf{b}(s_{\text{in}}) = b_0 \left[\begin{smallmatrix}\cos\alpha_0\\ \sin\alpha_0\end{smallmatrix}\right]$ linearly polarized along

the first characteristic direction. Then the output light vector is found by multiplication with the matricant in (4.1)

$$\mathbf{b}(s_{\text{out}}) = \mathbf{\Omega}(s_{\text{out}}, s_{\text{in}})\mathbf{b}(s_{\text{in}}) = \exp(i\gamma)b_0 \begin{bmatrix} \cos\alpha_f \\ \sin\alpha_f \end{bmatrix} \tag{4.29}$$

where we used $\mathbf{S}(\alpha_0)\left[\begin{smallmatrix}\cos\alpha_0\\ \sin\alpha_0\end{smallmatrix}\right] = \left[\begin{smallmatrix}1\\0\end{smallmatrix}\right]$. Equation (4.29) shows that incident light linearly polarized parallel to the primary characteristic direction α_0 leaves the Kerr medium linearly polarized parallel to the secondary characteristic direction α_f. It can also be similarly shown that incident light linearly polarized perpendicular to the primary characteristic direction α_0 leaves the Kerr medium linearly polarized perpendicular to the secondary characteristic direction α_f.

The characteristic parameters are important because they are measurable by various polariscope systems. Once they are measured they can be used to recover the electric field distribution.

4.3.2 Symmetric Kerr Medium

For a symmetric Kerr medium with $s_{\text{out}} = -s_{\text{in}}$ the characteristic parameters are

$$\alpha_s = \alpha_s(s_{\text{out}}) = \alpha_s(-s_{\text{in}}) \tag{4.30a}$$

$$\gamma_s = \gamma_s(s_{\text{out}}) = \gamma_s(-s_{\text{in}}) \tag{4.30b}$$

4.3.3 Kerr Media With Constant Direction E-Field

If the applied electric field direction is constant it follows from (3.81) that

$$\alpha_f = \alpha_0 = \varphi \tag{4.31}$$

$$\gamma = \gamma(s_{\text{in}}, s_{\text{out}}) \tag{4.32}$$

This case will be particularly important in Part II where we often discretize the applied electric distribution in a step-wise constant manner. We define

$$\gamma_c = \gamma(s_{\text{in}}, s_{\text{out}}) = \pi B E_{\text{T}}^2 l \tag{4.33}$$

as the characteristic retardation of a Kerr medium with constant direction electric field with path length of length $l = |s_{\text{out}} - s_{\text{in}}|$. We will denote the characteristic

angles directly with φ.

4.4 Governing Differential Equations

The characteristic parameters completely describe the action of a Kerr medium on light propagation. However previous sections offer little insight into the actual relations between the applied non-uniform electric field and the characteristic parameters. The following sections establish these relations by deriving the differential equations for $\gamma(s, s_0)$, $\alpha_0(s, s_0)$ and $\alpha_f(s, s_0)$ in terms of the applied electric field.

4.4.1 General Form

To relate the characteristic parameters directly to the applied electric field we use (3.10) in the E_T-frame

$$\frac{d\mathbf{\Omega}'(s, s_0)}{ds} = \mathbf{A}'(s)\mathbf{\Omega}'(s, s_0) \tag{4.34}$$

The explicit form of $\mathbf{\Omega}'(s, s_0)$ and $\mathbf{A}'(s)$ are respectively given in (4.15) and (2.121). The first row of (4.34) yields

$$\frac{d\Omega'_{11}(s, s_0)}{ds} = A'_{11}(s)\Omega'_{11}(s, s_0) + A'_{12}(s)\Omega'_{21}(s, s_0) \tag{4.35}$$

$$\frac{d\Omega'_{12}(s, s_0)}{ds} = A'_{11}(s)\Omega'_{12}(s, s_0) + A'_{12}(s)\Omega'_{22}(s, s_0) \tag{4.36}$$

It is clear from (4.15) that the second row in (4.34) gives the complex conjugates for Ω'_{11} and Ω'_{12} and thus does not provide any independent information from (4.35) and (4.36).

The left hand sides of (4.35) and (4.36) follows from the derivative of (4.15)

$$\frac{d\Omega'_{11}}{ds} = -\sin\gamma\cos\beta_-\frac{d\gamma}{ds} - \cos\gamma\sin\beta_-\frac{d\beta_-}{ds} - i\cos\gamma\cos\beta_+\frac{d\gamma}{ds} + i\sin\gamma\sin\beta_+\frac{d\beta_+}{ds} \tag{4.37}$$

$$\frac{d\Omega'_{12}}{ds} = -\sin\gamma\sin\beta_-\frac{d\gamma}{ds} + \cos\gamma\cos\beta_-\frac{d\beta_-}{ds} - i\cos\gamma\sin\beta_+\frac{d\gamma}{ds} - i\sin\gamma\cos\beta_+\frac{d\beta_+}{ds} \tag{4.38}$$

where we did not show the functional dependences on s and s_0. The right hand sides

of (4.35) and (4.36) directly follow by substituting the respective elements in (4.15) and (2.121)

$$A'_{11}\Omega'_{11} + A'_{12}\Omega'_{21} = -i\pi BE_T^2 \{\cos\gamma\cos\beta_- - i\sin\gamma\cos\beta_+\} + \frac{d\varphi}{ds}\{-\cos\gamma\sin\beta_- - i\sin\gamma\sin\beta_+\} \tag{4.39}$$

$$A'_{11}\Omega'_{12} + A'_{12}\Omega_{22} = -i\pi BE_T^2 \{\cos\gamma\sin\beta_- - i\sin\gamma\sin\beta_+\} + \frac{d\varphi}{ds}\{\cos\gamma\cos\beta_- + i\sin\gamma\cos\beta_+\} \tag{4.40}$$

Substituting (4.37) to (4.40) in (4.35) and (4.36) and expressing the result in matrix form we obtain

$$\begin{bmatrix} -\sin\gamma\cos\beta_- & -\cos\gamma\sin\beta_- & 0 \\ -\cos\gamma\cos\beta_+ & 0 & \sin\gamma\sin\beta_+ \\ -\sin\gamma\sin\beta_- & \cos\gamma\cos\beta_- & 0 \\ -\cos\gamma\sin\beta_+ & 0 & -\sin\gamma\cos\beta_+ \end{bmatrix} \begin{bmatrix} \frac{d\gamma}{ds} \\ \frac{d\beta_-}{ds} \\ \frac{d\beta_+}{ds} \end{bmatrix} = \begin{bmatrix} -\sin\gamma\cos\beta_+ & -\cos\gamma\sin\beta_- \\ -\cos\gamma\cos\beta_- & -\sin\gamma\sin\beta_+ \\ -\sin\gamma\sin\beta_+ & \cos\gamma\cos\beta_- \\ -\cos\gamma\sin\beta_- & \sin\gamma\cos\beta_+ \end{bmatrix} \begin{bmatrix} \pi BE_T^2 \\ \frac{d\varphi}{ds} \end{bmatrix} \tag{4.41}$$

In order to simplify (4.41) so that simple differential equations result for γ, β_- and β_+ we premultiply both sides of (4.41) with the matrix

$$\begin{bmatrix} \cos\beta_- & \cos\beta_+ & \sin\beta_- & \sin\beta_+ \\ \sin\beta_- & 0 & -\cos\beta_- & 0 \\ 0 & \sin\beta_+ & 0 & -\cos\beta_+ \end{bmatrix}$$

which results in

$$\frac{d\gamma(s,s_0)}{ds} = \pi BE_T^2(s)\cos\big[\beta_+(s-s_0) - \beta_-(s,s_0)\big] \tag{4.42a}$$

$$\cos\gamma(s,s_0)\frac{d\beta_-(s,s_0)}{ds} = \pi BE_T^2(s)\sin\gamma(s,s_0)\sin\big[\beta_-(s,s_0) - \beta_+(s,s_0)\big] + \cos\gamma(s,s_0)\frac{d\varphi(s)}{ds} \tag{4.42b}$$

$$\sin\gamma(s,s_0)\frac{d\beta_+(s,s_0)}{ds} = \pi B E_T^2(s)\cos\gamma(s,s_0)\sin\big[\beta_-(s,s_0)-\beta_+(s,s_0)\big] - \sin\gamma(s,s_0)\frac{d\varphi(s)}{ds} \tag{4.42c}$$

Equation (4.42) can be rearranged using (4.16), (4.17), (4.13) and (4.14) to get

$$\frac{d\gamma(s,s_0)}{ds} = \pi B E_T^2(s)\cos\big[2\varphi(s)-2\alpha_f(s,s_0)\big] \tag{4.43a}$$

$$\frac{d\alpha_0(s,s_0)}{ds} = \pi B E_T^2(s)\csc 2\gamma(s,s_0)\sin\big[2\varphi(s)-2\alpha_f(s,s_0)\big] \tag{4.43b}$$

$$\frac{d\alpha_f(s,s_0)}{ds} = \cos 2\gamma(s,s_0)\frac{d\alpha_0(s,s_0)}{ds} \tag{4.43c}$$

Equation (4.43) can be integrated from s_{in} to s_{out} to yield the characteristic parameters directly. The initial conditions can be found by considering an infinitesimal layer for which the electric field direction and magnitude may be assumed constant

$$\gamma(s_0,s_0) = 0 \tag{4.44a}$$

$$\alpha_f(s_0,s_0) = \varphi(s_0) \tag{4.44b}$$

$$\alpha_0(s_0,s_0) = \varphi(s_0) \tag{4.44c}$$

Note that at $s = s_0$ (4.43b) has an indefinite form but can be evaluated using the L'Hopital rule, so that (4.43a) and (4.43c) give

$$\left.\frac{d\alpha_0(s,s_0)}{ds}\right|_{s=s_0} = \frac{1}{2}\left.\frac{d\varphi(s)}{ds}\right|_{s=s_0} \tag{4.45}$$

We now write (4.43a) and (4.43b) in matrix form as

$$\begin{bmatrix} \dfrac{d\gamma(s,s_0)}{ds} \\ \sin 2\gamma(s,s_0)\dfrac{d\alpha_0(s,s_0)}{ds} \end{bmatrix} = \begin{bmatrix} \cos 2\alpha_f(s,s_0) & \sin 2\alpha_f(s,s_0) \\ -\sin 2\alpha_f(s,s_0) & \cos 2\alpha_f(s,s_0) \end{bmatrix} \begin{bmatrix} \pi B E_T^2(s)\cos 2\varphi(s) \\ \pi B E_T^2(s)\sin 2\varphi(s) \end{bmatrix} \tag{4.46}$$

which may be easily inverted to yield

$$\pi B E_T^2(s)\cos 2\varphi(s) = \cos 2\alpha_f(s,s_0)\frac{d\gamma(s,s_0)}{ds} - \sin 2\gamma(s,s_0)\sin 2\alpha_f(s,s_0)\frac{d\alpha_0(s,s_0)}{ds} \tag{4.47}$$

$$\pi B E_T^2(s) \sin 2\varphi(s) = \sin 2\alpha_f(s, s_0) \frac{d\gamma(s, s_0)}{ds} + \sin 2\gamma(s, s_0) \cos 2\alpha_f(s, s_0) \frac{d\alpha_0(s, s_0)}{ds} \tag{4.48}$$

Unfortunately, it appears from (4.47) and (4.48) that it is not possible to express the characteristic parameters directly in terms of the applied electric field for the general case.

4.4.2 Symmetric Kerr Media

We now derive the differential equations for the characteristic parameters in symmetric media. The starting equation is (3.26) in the E_T-frame

$$\frac{d\mathbf{\Omega}'(s, -s)}{ds} = \mathbf{A}'(s)\mathbf{\Omega}'(s, -s) + \mathbf{\Omega}'(s, -s)\mathbf{A}'(-s) \tag{4.49}$$

The explicit form of $\mathbf{\Omega}'(s, -s)$ is identical in form to (4.23) with β_s replacing α_s

$$\mathbf{\Omega}'(s, -s) = \begin{bmatrix} \cos\gamma_s(s) - i\sin\gamma_s(s)\cos 2\beta_s(s) & -i\sin\gamma_s(s)\sin 2\beta_s(s) \\ -i\sin\gamma_s(s)\sin 2\beta_s(s) & \cos\gamma_s(s) + i\sin\gamma_s(s)\cos 2\beta_s(s) \end{bmatrix} \tag{4.50}$$

and $\mathbf{A}'(s)$ is given in (2.121). Only two entries in (4.49) are independent. Using elemental relations in (4.23) and (2.121) the first row of (4.49) yields

$$\frac{d\Omega'_{11}(s, -s)}{ds} = 2A'_{11}(s)\Omega'_{11}(s, -s) + A'_{12}(s)\Omega'_{12}(s, -s) \tag{4.51a}$$

$$\frac{d\Omega'_{12}(s, -s)}{ds} = A'_{12}(s)\left[\Omega'_{22}(s, -s) - \Omega'_{11}(s, -s)\right] \tag{4.51b}$$

Substituting the appropriate elements of (2.121) and (4.50) in (4.51) results in

$$-\sin\gamma_s(s)\frac{d\gamma_s(s)}{ds} = -2\sin\gamma_s(s)\cos 2\beta_s(s)\pi B E_T^2(s) \tag{4.52}$$

$$\begin{aligned} -\cos\gamma_s(s)\cos 2\beta_s \frac{d\gamma_s(s)}{ds} + 2\sin\gamma_s(s)\sin 2\beta_s \frac{d\beta_s(s)}{ds} \\ = -2\cos\gamma_s(s)\pi B E_T^2(s) - 2\sin\gamma_s(s)\sin 2\beta_s(s)\frac{d\varphi(s)}{ds} \end{aligned} \tag{4.53}$$

$$-\cos\gamma_s(s)\sin 2\beta_s(s)\frac{d\gamma_s(s)}{ds} - 2\sin\gamma_s(s)\cos 2\beta_s(s)\frac{d\beta_s(s)}{ds} = 2\sin\gamma_s(s)\cos 2\beta_s(s)\frac{d\varphi(s)}{ds} \tag{4.54}$$

It is possible to obtain (4.52) from (4.53) and (4.54). Equations (4.53) and (4.54) can be rearranged using (4.26) to get

$$\frac{d\gamma_s(s)}{ds} = 2\pi B E_T^2(s)\cos\big[2\varphi(s) - 2\alpha_s(s)\big] \tag{4.55a}$$

$$\frac{d\alpha_s(s)}{ds} = \pi B E_T^2(s)\cot\gamma_s(s)\sin\big[2\varphi(s) - 2\alpha_s(s)\big] \tag{4.55b}$$

as the governing differential equations in symmetric Kerr media. Similar to general Kerr media the initial conditions are

$$\gamma_s(0) = 0 \tag{4.56}$$

$$\alpha_s(0) = \varphi(0) \tag{4.57}$$

and at $s = 0$ (4.55b) must be evaluated using the L'Hopital rule

$$\left.\frac{d\alpha_s(s)}{ds}\right|_{s=0} = \frac{1}{2}\left.\frac{d\varphi(s)}{ds}\right|_{s=0} \tag{4.58}$$

Equation (4.55) can be written in matrix form as

$$\begin{bmatrix} \dfrac{d\gamma(s)}{ds} \\ 2\tan\gamma(s)\dfrac{d\alpha_s(s)}{ds} \end{bmatrix} = \begin{bmatrix} \cos 2\alpha_s(s) & \sin 2\alpha_s(s) \\ -\sin 2\alpha_s(s) & \cos 2\alpha_s(s) \end{bmatrix} \begin{bmatrix} 2\pi B E_T^2(s)\cos 2\varphi(s) \\ 2\pi B E_T^2(s)\sin 2\varphi(s) \end{bmatrix} \tag{4.59}$$

Inverting (4.59) yields

$$2\pi B E_T^2(s)\cos 2\varphi(s) = \cos 2\alpha_s(s)\frac{d\gamma_s(s)}{ds} - 2\tan\gamma_s(s)\sin 2\alpha_s(s)\frac{d\alpha_s(s)}{ds} \tag{4.60a}$$

$$2\pi B E_T^2(s)\sin 2\varphi(s) = \sin 2\alpha_s(s)\frac{d\gamma_s(s)}{ds} + 2\tan\gamma_s(s)\cos 2\alpha_s(s)\frac{d\alpha_s(s)}{ds} \tag{4.60b}$$

Again it appears from (4.60) that it is not possible to express the characteristic parameters directly in terms of the applied electric field.

4.4.3 Reduced Form For Weak Kerr Media

We define a Kerr medium to be weak when either the Kerr constant, the applied electric field, or the path length is small enough such that

$$\pi B \int_{s_{\text{in}}}^{s_{\text{out}}} E_T^2(s) ds \ll 1 \tag{4.61}$$

It then follows from (4.43a) and (4.44a) that $\gamma(s, s_0)$ stays small and

$$\sin \gamma(s, s_0) \approx \gamma(s, s_0) \tag{4.62a}$$

$$\cos \gamma(s, s_0) \approx 1 \tag{4.62b}$$

Using (4.62) we conclude from (4.43c) and (4.44) that $\alpha_0(s, s_0)$ and $\alpha_f(s, s_0)$ degenerate into a single parameter which we denote by $\alpha(s, s_0)$

$$\alpha(s, s_0) \equiv \alpha_0(s, s_0) \approx \alpha_f(s, s_0) \tag{4.63}$$

Thus weak Kerr media are described by only two parameters even if the medium is not symmetric. Furthermore substituting (4.62) and (4.63) in (4.47) and (4.48) yields

$$\begin{aligned} \pi B E_T^2(s) \cos 2\varphi(s) &\approx \cos 2\alpha(s, s_0) \frac{d\gamma(s, s_0)}{ds} - 2\gamma(s, s_0) \sin 2\alpha(s, s_0) \frac{d\alpha(s, s_0)}{ds} \\ &\approx \frac{d\big[\gamma(s, s_0) \cos 2\alpha(s, s_0)\big]}{ds} \end{aligned} \tag{4.64}$$

$$\begin{aligned} \pi B E_T^2(s) \sin 2\varphi(s) &\approx \sin 2\alpha(s, s_0) \frac{d\gamma(s, s_0)}{ds} + 2\gamma(s, s_0) \cos 2\alpha_f(s, s_0) \frac{d\alpha(s, s_0)}{ds} \\ &\approx \frac{d\big[\gamma(s, s_0) \sin 2\alpha(s, s_0)\big]}{ds} \end{aligned} \tag{4.65}$$

Integrating (4.64) and (4.65) from $s_0 = s_{\text{in}}$ to $s = s_{\text{out}}$ yields

$$\pi B \int_{s_{\text{in}}}^{s_{\text{out}}} E_T^2(s) \cos 2\varphi(s)\, ds \approx \gamma \cos 2\alpha \tag{4.66a}$$

$$\pi B \int_{s_{\text{in}}}^{s_{\text{out}}} E_T^2(s) \sin 2\varphi(s)\, ds \approx \gamma \sin 2\alpha \tag{4.66b}$$

It is clear from Figure 2.1 that

$$E_T^2(s) \cos 2\varphi(s) = E_T^2(s) \cos^2 \varphi(s) - E_T^2(s) \sin^2 \varphi(s) = E_m^2(s) - E_p^2(s) \tag{4.67a}$$

$$E_T^2(s)\sin 2\varphi(s) = 2E_T(s)\sin\varphi(s)E_T(s)\cos\varphi(s) = 2E_m(s)E_p(s) \tag{4.67b}$$

Substituting (4.67) in (4.66) results in

$$\pi B\int_{s_{\text{in}}}^{s_{\text{out}}}\left[E_m^2(s) - E_p^2(s)\right]ds \approx \gamma\cos 2\alpha \tag{4.68a}$$

$$\pi B\int_{s_{\text{in}}}^{s_{\text{out}}} 2E_m(s)E_p(s)\,ds \approx \gamma\sin 2\alpha \tag{4.68b}$$

Equation (4.68) directly relates the characteristic parameters to the applied electric field distribution.

4.4.4 Reduced Form For Weak Axisymmetric Kerr Media When $\hat{\mathbf{m}} = \hat{\mathbf{z}}$

For axisymmetric Kerr media, when the direction of light propagation along the s-axis is perpendicular to the axisymmetric axis z, we can choose the axes so that $\hat{m} = \hat{z}$. Then (4.68) can be written only in terms of the radial and axial components of the applied electric field. First note that

$$ds = \frac{r\,dr}{\sqrt{r^2 - p^2}} \tag{4.69}$$

$$E_p = \frac{p}{r}E_r \tag{4.70}$$

For axisymmetric applied electric fields, $E_p(s)$ and $E_z(s)$ are even functions of s so that

$$\gamma\cos 2\alpha = 2\pi B\int_p^\infty \left[E_z^2(r) - \frac{p^2}{r^2}E_r^2(r)\right]\frac{r\,dr}{\sqrt{r^2 - p^2}} \tag{4.71a}$$

$$\gamma\sin 2\alpha = 2\pi B\int_p^\infty \frac{2p}{r}E_z(r)E_r(r)\frac{r\,dr}{\sqrt{r^2 - p^2}} \tag{4.71b}$$

Equation (4.71) has the added advantage over (4.68) that the components of the electric field inside the integrals does not depend on the light propagation direction. Equation (4.71) is closely related to the Abel transform of scalar funtions. This relation is further investigated in Section 9.2.

4.4.5 Layered Media Approach

Equation (4.66) may alternatively be derived by considering a layered medium. First note that if the transverse electric field direction and magnitude are constant within a layer between s_{in} and s_{out} then the matricant will be denoted by $\mathbf{\Omega}_{\text{c}}(s_{\text{in}}, s_{\text{out}})$ and given from (4.23) with $\gamma_c = \gamma_s(s_{\text{out}}) = \pi B E_T^2 l$ and $\alpha_s(s_{\text{out}}) = \varphi$ as

$$\mathbf{\Omega}_{\text{c}}(s_{\text{out}}, s_{\text{in}}) = \begin{bmatrix} \cos\gamma_c - i\sin\gamma_c\cos 2\varphi & -i\sin\gamma_c\sin 2\varphi \\ -i\sin\gamma_c\sin 2\varphi & \cos\gamma_c + i\sin\gamma_c\cos 2\varphi \end{bmatrix} \tag{4.72}$$

where E_T is the magnitude of the transverse electric field, $l = |s_{\text{out}} - s_{\text{in}}|$ is the length of the path, and φ is the direction of the transverse field as shown in Figure 2.1.

Now assume that there are n layers between s_{in} and s_{out}, the m'th layer is between s_{m-1} and s_m, and φ_m and $(E_T^2)_m$ are the values of the direction and the magnitude of the transverse electric field in the m'th layer respectively (Fig. 4.1). We define

$$\delta_m = \pi B \left(E_T^2\right)_m l_m \tag{4.73}$$

where l_m is the length of the m'th layer. Assuming n is sufficiently large so that l_i is sufficiently small we have

$$\delta_m \ll 1 \tag{4.74}$$

Then for the i'th layer from (4.72) we have

$$\mathbf{\Omega}_{\text{c}}(s_m, s_{m-1}) \approx \begin{bmatrix} 1 - \delta_m\cos 2\varphi_m & -i\delta_m\sin 2\varphi_m \\ -i\delta_m\sin 2\varphi_m & 1 + i\delta_m\cos 2\varphi_m \end{bmatrix} \tag{4.75}$$

For two consecutive layers using (4.75) we obtain to first order in δ_m

$$\mathbf{\Omega}_{\text{c}}(s_{m+1}, s_m)\mathbf{\Omega}_{\text{c}}(z_m, z_{m-1}) \approx \begin{bmatrix} 1 - i\delta_{m+1}\cos 2\varphi_{m+1} & -i\delta_{m+1}\sin 2\varphi_{m+1} \\ -i\delta_{m+1}\sin 2\varphi_{m+1} & 1 + i\delta_{m+1}\cos 2\varphi_{m+1} \end{bmatrix} \times \begin{bmatrix} 1 - i\delta_m\cos 2\varphi_m & -i\delta_m\sin 2\varphi_m \\ -i\delta_m\sin 2\varphi_m & 1 + i\delta_m\cos 2\varphi_m \end{bmatrix}$$

$$= \begin{bmatrix} 1 - i\delta_{m+1}\cos 2\varphi_{m+1} - i\delta_m\cos 2\varphi_m & -i\delta_{m+1}\sin 2\varphi_{m+1} - i\delta_m\sin 2\varphi_m \\ -i\delta_{m+1}\sin 2\varphi_{m+1} - i\delta_m\sin 2\varphi_m & 1 + i\delta_{m+1}\cos 2\varphi_{m+1} + i\delta_m\cos 2\varphi_m \end{bmatrix} \tag{4.76}$$

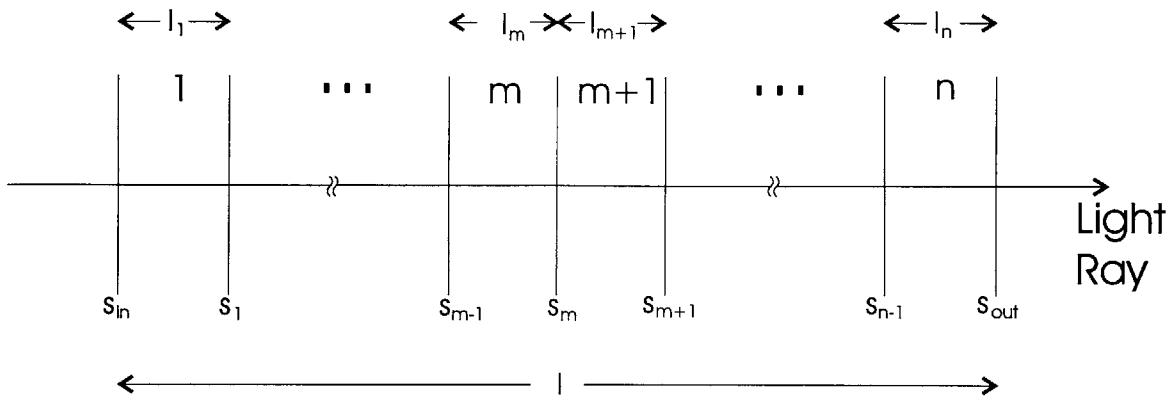

Figure 4.1: The layered medium used for the derivation of integral relations between the electric field and the characteristic parameters.

where we neglected the terms of second order in δ's. Repeating the above procedure for all n layers we obtain

$$\prod_{m=n}^{1} \Omega_c(s_m, s_{m-1}) = \begin{bmatrix} 1 - i\sum_{m=1}^{n} \delta_m \cos 2\varphi_m & -i\sum_{m=1}^{n} \delta_m \sin 2\varphi_m \\ -i\sum_{m=1}^{n} \delta_m \sin 2\varphi_m & 1 + i\sum_{m=1}^{n} \delta_m \cos 2\varphi_m \end{bmatrix} \tag{4.77}$$

$$= \begin{bmatrix} 1 - i\pi B\sum_{m=1}^{n} (E_T^2)_m l_m \cos 2\varphi_m & -i\pi B\sum_{m=1}^{n} (E_T^2)_m l_m \sin 2\varphi_m \\ -i\pi B\sum_{m=1}^{n} (E_T^2)_m l_m \sin 2\varphi_m & 1 + i\pi B\sum_{m=1}^{n} (E_T^2)_m l_m \cos 2\varphi_m \end{bmatrix} \tag{4.78}$$

Inherent to this procedure is the assumption that

$$\pi B \sum_{m=1}^{n} (E_T^2)_m l_m \ll 1 \tag{4.79}$$

within each layer.

In the limit that the thickness of each layer approaches 0 ($l_m \to 0$) and number of layers approaches infinity ($n \to \infty$) (4.78) reduces to

$$\Omega(s_{\text{out}}, s_{\text{in}}) = \begin{bmatrix} 1 - i\int_{s=s_{in}}^{s_{out}} \pi B E_T^2(s) \cos 2\varphi(s) ds & -i\int_{s=s_{in}}^{s_{out}} \pi B E_T^2(s) \sin 2\varphi(s) ds \\ -i\int_{s=s_{in}}^{s_{out}} \pi B E_T^2(s) \sin 2\varphi(s) ds & 1 + i\int_{s=z_{in}}^{s_{out}} \pi B E_T^2(s) \cos 2\varphi(s) ds \end{bmatrix} \tag{4.80}$$

Comparing equations (4.80) and (4.2) ($\gamma \ll 1$) yields (4.63), (4.66a) and (4.66b). Also the limiting case of (4.79) is identical to (4.61).

Chapter 5

Measurement Of The Characteristic Parameters

5.1 Introduction

In this chapter we introduce various optical polariscope systems which can be used to determine characteristic parameters. We discuss only the so called direct methods as they do not involve measuring the azimuth and/or the ellipticity of the light ellipse [47]. These optical polariscope systems employ polarizers, quarter wave plates and half wave plates placed before and/or after the Kerr medium. Jones calculus can be employed to find input-output intensity relations [48]. These relations are in terms of the characteristic parameters and the orientation of the optical elements. Measurements of the output intensity together with the orientations enable the determination of the characteristic parameters.

When γ is not small direct measurements are adequate to determine the characteristic parameters. If γ is small however measurements are difficult and it is necessary to use the AC modulation method which is studied in section 5.5.

5.2 The Jones Calculus

5.2.1 Description

The Jones calculus can be conveniently used for the propagation of polarized light through polarizers and birefringent elements. In Jones calculus, optical elements are

represented by two by two complex 'Jones' matrices. The light, which is assumed to be propagating along the $+s$-direction, has its electric field in the plane transverse to $\hat{s}$ and is represented by a two dimensional complex vector whose entries are the m and p components. The propagation of light through an optical system is then equivalent to multiplication of the light electric field vector with a series of Jones matrices.

Table 5.1 gives the explicit forms of three basic Jones matrices which are used to express all the other Jones matrices used in this work. A polarizer linearly polarizes the light along its transmission axis which is assumed to be in the m-direction in Table 5.1. A retarder introduces a phase difference between light components polarized along its fast and slow axes. In Table 5.1 the slow axis of the retarder is assumed to be in the m-direction. A rotator is not really a physical element but is used to represent arbitrarily oriented polarizers and retarders. Since Kerr media is essentially equivalent to two rotators and a retarder, it fits nicely to the Jones formalism.

We are interested only in the final intensity of light and the common phase factors that the light vector components may have (for example the phase factor introduced by propagation) is irrelevant. For that matter a distinction between the electric field of the light vector $\mathbf{e}$ and the normalized electric field vector of Kerr media $\mathbf{b}$ of (2.117) is not necessary. This also implies that the matrices in Table 5.1 are not unique and any Jones matrix obtained by multiplying these matrices with a constant phase factor $\exp i\theta$ is equally valid.

Polarizer (in m)	Retarder (in m)	Rotator
$\mathbf{U}_\mathrm{p} = \begin{bmatrix} 1 & 0 \\ 0 & 0 \end{bmatrix}$	$\mathbf{G}(\theta) = \begin{bmatrix} \exp -i\theta & 0 \\ 0 & \exp i\theta \end{bmatrix}$	$\mathbf{S}(\theta) = \begin{bmatrix} \cos\theta & \sin\theta \\ -\sin\theta & \cos\theta \end{bmatrix}$

Table 5.1: Basic Jones matrices. The Jones matrices of all the optical elements used in this work can be expressed in terms of these three. In this table the transmission axis of the polarizer and the slow axis of the retarder are assumed to be in the m-direction. Jones matrices of arbitrarily oriented polarizers and retarders can be obtained using these and rotators (see Table 5.2). The arguments of the rotator and the retarder are respectively the counterclockwise angle from m to the rotator's first axis and half the phase shift (retardation) that the retarder introduces between polarized light electric field components.

5.2.2 Jones Matrices Of Optical Elements And Kerr Medium

All the polariscope systems used in this work employ two basic optical elements, namely perfect polarizers and retardation plates. A retardation plate is respectively named a quarter wave plate and half wave plate when it introduces $\frac{\pi}{2}$ and π phase differences between light components polarized along its fast and slow axes.

In Table 5.2 we give the Jones matrices of the basic optical elements and Kerr medium. Polarizer and retardation plates are the generalizations of the ones in Table 5.1 with arbitrarily oriented transmission and slow axes. Quarter and half wave plates are special case retardation plates with respective retardations of $\pi/2$ and π. The Jones matrix for Kerr media is the matricant between s_{in} and s_{out}, where s_{in} and s_{out} are the entrance and the emergence points of light in and out of the Kerr media. In this chapter we use $\mathbf{U}_{\mathrm{m}}$ to denote the Jones matrix of Kerr media, instead of $\mathbf{\Omega}(s_{in}, s_{out})$ of Chapter 4, to stress the functional dependence of $\mathbf{U}_{\mathrm{m}}$ on the three characteristic parameters: the primary characteristic angle, α_0, the secondary characteristic angle, α_f, and the characteristic phase retardation, γ. The first form of the Jones matrix for Kerr medium is a restatement of (4.1). The second form also directly follows from (4.1) and demonstrates that Kerr media is optically equivalent to a retardation plate followed by a rotator with the angle $\alpha_0 - \alpha_f$.

Optical Element	Jones Matrix
Polarizer	$\mathbf{U}_{\mathrm{p}}(\theta) = \mathbf{S}(-\theta)\mathbf{U}_{\mathrm{p}}\mathbf{S}(\theta)$
Retardation Plate	$\mathbf{U}_{\mathrm{r}}(\zeta, \theta) = \mathbf{S}(-\theta)\mathbf{G}(\frac{\zeta}{2})\mathbf{S}(\theta)$
Quarter Wave Plate	$\mathbf{U}_{\mathrm{q}}(\theta) = \mathbf{U}_{\mathrm{r}}(\frac{\pi}{2}, \theta) = \mathbf{S}(-\theta)\mathbf{G}(\frac{\pi}{4})\mathbf{S}(\theta)$
Half Wave Plate	$\mathbf{U}_{\mathrm{h}}(\theta) = \mathbf{U}_{\mathrm{r}}(\pi, \theta) = \mathbf{S}(-\theta)\mathbf{G}(\frac{\pi}{2})\mathbf{S}(\theta)$
Kerr Medium	$\mathbf{U}_{\mathrm{m}}(\alpha_0, \alpha_f, \gamma) = \mathbf{S}(-\alpha_f)\mathbf{G}(\gamma)\mathbf{S}(\alpha_0) = \mathbf{S}(\alpha_0 - \alpha_f)\mathbf{U}_{\mathrm{r}}(2\gamma, \alpha_0)$

Table 5.2: Jones matrices of the optical elements used in this work. The arguments of the retardation plate are respectively the phase difference that the retardation plate introduces between it fast and slow axes and the counterclockwise angle from m to its slow axes. The arguments of the polarizer, the wave plates and the Kerr medium are respectively the counterclockwise angle from m to the transmission axis, the counterclockwise angle from m to the slow axis, and the characteristic parameters.

5.3 Polariscope Systems

A polariscope system consists of optical elements placed before and/or after the Kerr medium. In Figure 5.1 we show typical polariscope systems that can be used to measure the characteristic parameters. The names "linear polariscope" and "circular polariscope" are frequently used in the literature while the other names are here defined in this work for easy reference as there are no apparent names given in the literature.

For all the polariscope systems the first element is a polarizer with transmission axis at angle θ_p. If the optical electric field at the output of the laser just before the first polarizer is $\mathbf{e}_\mathrm{l}$, then the electric field on the other side of the polarizer $\mathbf{e}_\mathrm{p}$ is then

$$\mathbf{e}_\mathrm{p} = \mathbf{U}_\mathrm{p}(\theta_p)\mathbf{e}_\mathrm{l} = e_0 \begin{bmatrix} \cos\theta_p \\ \sin\theta_p \end{bmatrix} \tag{5.1}$$

where e_0 is the light electric field magnitude just after the polarizer. The light intensity I_0 just after the polarizer is then proportional to the square of the light electric field magnitude

$$I_0 \propto |\mathbf{e}_\mathrm{p}|^2 = |e_0|^2 \tag{5.2}$$

The relationship between the output light intensity of the laser and I_0 depends if the laser light is polarized, partially polarized or unpolarized and if any other optical elements such as filtering polarizers exist inbetween the laser and the first polarizer of the polariscope system.

The light intensity I_f at the output of the optical system after the last polarizer which is called the analyzer, is then

$$\frac{I_f}{I_0} = \frac{|\mathbf{e}_\mathrm{f}|^2}{|e_0|^2} = \frac{\mathbf{e}_\mathrm{f}{}^\dagger \mathbf{e}_\mathrm{f}}{|e_0|^2} \tag{5.3}$$

where $\mathbf{e}_\mathrm{f}$ is the final light electric field polarization given by

$$\mathbf{e}_\mathrm{f} = \mathbf{U}_\mathrm{sys}\mathbf{e}_\mathrm{l} \tag{5.4}$$

Here $\mathbf{U}_\mathrm{sys}$ is the Jones matrix of the overall polariscope system which can be expressed in terms of the individual optical elements by matrix multiplications. For example for

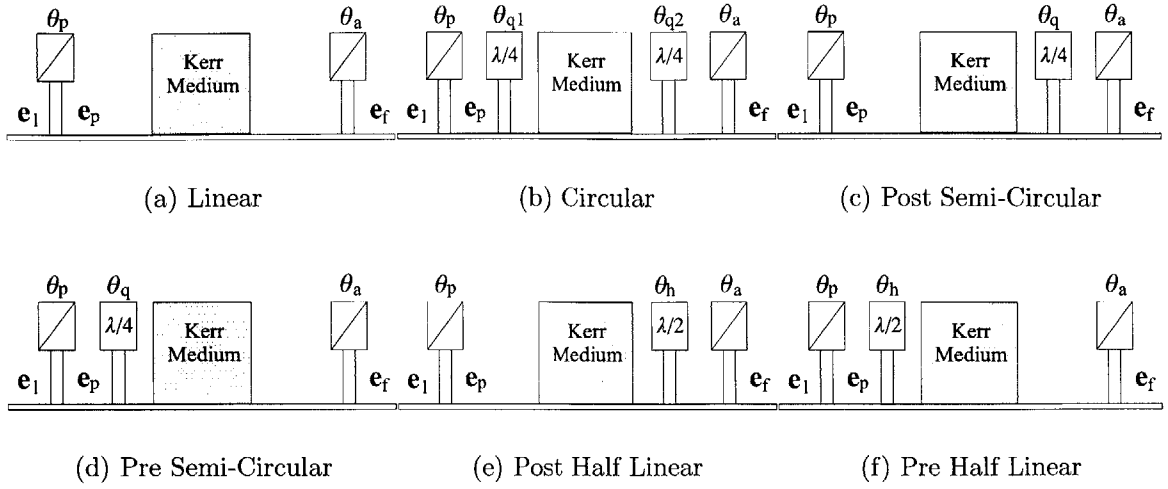

Figure 5.1: Polariscope systems used in the determination of the characteristic parameters

the circular polariscope

$$\mathbf{U}_{\text{sys}} = \mathbf{U}_{\text{p}}(\theta_a)\mathbf{U}_{\text{q}}(\theta_{q_2})\mathbf{U}_{\text{m}}(\alpha_0, \alpha_f, \gamma)\mathbf{U}_{\text{q}}(\theta_{q_1})\mathbf{U}_{\text{p}}(\theta_p) \tag{5.5}$$

where θ_p, θ_a, θ_{q_1} and θ_{q_2} are respectively the angular positions of the polarizer, analyzer and first and second quarter wave plates. $\mathbf{U}_{\text{sys}}$ for the other systems are similar to (5.5) with appropriate optical element matrices removed.

Once $\mathbf{U}_{\text{sys}}$ is specified I_f/I_0 is found from

$$\frac{I_f}{I_0} = \frac{|\mathbf{e}_{\text{f}}|^2}{|e_0|^2} = \frac{\mathbf{e}_{\text{l}}{}^{\dagger}\mathbf{U}_{\text{sys}}^{\dagger}\mathbf{U}_{\text{sys}}\mathbf{e}_{\text{l}}}{|e_0|^2} \tag{5.6}$$

Equation (5.6) is evaluated first by substituting (5.1) and then performing a series of matrix vector multiplications. The result is in terms of the positions of the optical elements. Table 5.3 summarizes these relations for the polariscopes in Figure 5.1. We respectively use θ_p, θ_a, θ_h, and θ_q to denote the counter-clockwise angular positions from a zero angle reference of the polarizer transmission axis, analyzer transmission axis, half wave plate slow axis and quarter wave plate slow axis.

5.4 Measurement Techniques

5.4.1 Linear Polariscope

Crossed And Aligned Linear Polarizers

The complex expressions in Table 5.3 can be simplified by imposing relations between the positions of the optical elements. For the linear polariscopes two frequently used cases are aligned polarizers (AP), $\theta_a = \theta_p$, and crossed polarizers (CP), $\theta_a = \theta_p + \frac{\pi}{2}$. For aligned and crossed polarizers, the linear polariscope intensity relations respectively reduce to

$$\frac{I_f}{I_0} = \cos^2\gamma\cos^2(\alpha_0 - \alpha_f) + \sin^2\gamma\cos^2(\alpha_0 + \alpha_f - 2\theta_p) \quad \text{(AP)} \tag{5.7}$$

$$\frac{I_f}{I_0} = \cos^2\gamma\sin^2(\alpha_0 - \alpha_f) + \sin^2\gamma\sin^2(\alpha_0 + \alpha_f - 2\theta_p) \quad \text{(CP)} \tag{5.8}$$

Measurement Of α_f and α_0

A linear polariscope may be used to find the bisector of the angle between the primary and secondary characteristic directions [39], which can then be used to find the characteristic parameters. Let the polarizer and the analyzer be crossed. Then it is clear from (5.8) that the minimum intensity occurs when

$$\theta_p = \frac{\alpha_0 + \alpha_f}{2} + \frac{k\pi}{2} \quad \text{(CP)} \tag{5.9}$$

where k is a positive or negative integer. Hence the orientation of the polarizer determines the bisector of the angle between primary and secondary characteristic directions when the measured intensity is minimum. Once the bisector is determined then the analyzer and polarizer may be rotated in the opposite directions to each other by the same amount θ'_p so that $\theta_a - \theta_p = \frac{\pi}{2} - 2\theta'_p$ and $\theta_a + \theta_p = \alpha_0 + \alpha_f$. It follows from the linear polariscope intensity relation in Table 5.3 that

$$\frac{I_f}{I_0} = \cos^2\gamma\sin^2(\alpha_0 - \alpha_f - 2\theta'_p) \tag{5.10}$$

as the second term on the right is zero. Hence when the light becomes completely extinguished, the orientation of the analyzer and/or the polarizer determine $\alpha_- =$

Linear	$I_f/I_0 = \cos^2\gamma\cos^2(\alpha_0 - \alpha_f + \theta_a - \theta_p) + \sin^2\gamma\cos^2(\alpha_0 + \alpha_f - \theta_p - \theta_a)$
Post Semi Circular	$I_f/I_0 = (1/2) + (1/2)\sin 2\gamma\sin(2\theta_a - 2\theta_q)\sin(2\alpha_0 - 2\theta_p)$ $+(1/2)\cos(2\theta_a - 2\theta_q)\Big\{\cos^2\gamma\cos(2\theta_p - 2\alpha_0 - 2\theta_q + 2\alpha_f)$ $+\sin^2\gamma\cos(2\theta_p - 2\alpha_0 + 2\theta_q - 2\alpha_f)\Big\}$
Pre Semi Circular	$I_f/I_0 = (1/2) + (1/2)\sin 2\gamma\sin(2\theta_p - 2\theta_q)\sin(2\alpha_f - 2\theta_a)$ $+(1/2)\cos(2\theta_p - 2\theta_q)\Big\{\cos^2\gamma\cos(2\alpha_0 - 2\theta_q + 2\theta_a - 2\alpha_f)$ $+\sin^2\gamma\cos(2\alpha_0 - 2\theta_q - 2\theta_a + 2\alpha_f)\Big\}$
Pre Half Linear	$I_f/I_0 = \cos^2\gamma\cos^2(\alpha_0 - \alpha_f + \theta_p + \theta_a - 2\theta_h)$ $+\sin^2\gamma\cos^2(\alpha_0 + \alpha_f + \theta_p - \theta_a - 2\theta_h)$
Post Half Linear	$I_f/I_0 = \cos^2\gamma\cos^2(\alpha_f - \alpha_0 + \theta_p + \theta_a - 2\theta_h)$ $+\sin^2\gamma\cos^2(\alpha_0 + \alpha_f - \theta_p + \theta_a - 2\theta_h)$
Circular	$I_f/I_0 = (1/2) - (1/2)\cos 2\gamma\sin(2\theta_p - 2\theta_{q1})\sin(2\theta_a - 2\theta_{q2})$ $+(1/2)\sin 2\gamma\sin(2\theta_p - 2\theta_{q1})\cos(2\theta_a - 2\theta_{q2})\sin(2\alpha_f - 2\theta_{q2})$ $+(1/2)\sin 2\gamma\cos(2\theta_p - 2\theta_{q1})\sin(2\theta_a - 2\theta_{q2})\sin(2\alpha_0 - 2\theta_{q1})$ $+(1/2)\cos(2\theta_p - 2\theta_{q1})\cos(2\theta_a - 2\theta_{q2})$ $\times\cos(2\alpha_0 - 2\theta_{q1})\cos(2\alpha_f - 2\theta_{q2})$ $+(1/2)\cos 2\gamma\cos(2\theta_p - 2\theta_{q1})\cos(2\theta_a - 2\theta_{q2})$ $\times\sin(2\alpha_0 - 2\theta_{q1})\sin(2\alpha_f - 2\theta_{q2})$

Table 5.3: Input/output intensity relations for the polariscopes in Figure 5.1.

$\alpha_0 - \alpha_f$

$$\theta_p' = \frac{\alpha_0 - \alpha_f}{2} + \frac{k\pi}{2} \tag{5.11}$$

From $\alpha_- = \alpha_0 - \alpha_f$ in (5.11) and $\alpha_+ = \alpha_0 + \alpha_f$ in (5.9), α_0 and α_f follow.

Rotating the analyzer and polarizer with equal speed in the opposite direction may be experimentally difficult. This procedure may be avoided by introducing a half-wave plate between the first polarizer and the medium [39]. When the half wave plates' slow axis is set to coincide with the bisector of the characteristic directions $\theta_h = (\alpha_0 + \alpha_f)/2$ and polarizer and analyzer are crossed $\theta_a = \theta_p + \pi/2$, the intensity relation for the prehalf linear polariscope in Table 5.3 reduces to

$$\frac{I_f}{I_0} = \cos^2\gamma\sin^2(2\alpha_f - 2\theta_p) \tag{5.12}$$

Clearly $I_f = 0$ when

$$\theta_p = \alpha_f + \frac{k\pi}{2} \tag{5.13}$$

Hence when the intensity goes to zero, the polarizer coincides with the secondary characteristic direction. With α_f found, knowing $\alpha_0 - \alpha_f$ determines α_0.

Symmetric Kerr Media

If the media is symmetric, ($\alpha_s = \alpha_0 = \alpha_f$), (5.7) and (5.8) respectively reduce to particularly simple forms

$$\frac{I_f}{I_0} = 1 - \sin^2\gamma \sin^2(2\alpha_s - 2\theta_p) \qquad \text{(AP)} \tag{5.14}$$

$$\frac{I_f}{I_0} = \sin^2\gamma \sin^2(2\alpha_s - 2\theta_p) \qquad \text{(CP)} \tag{5.15}$$

from which α_s may be determined directly. In particular, α_s is determined by the polarizer angle if the polarizers are crossed and the intensity is minimum, or when the polarizers are aligned and intensity is a maximum

$$\theta_p = \alpha_s + \frac{k\pi}{2} \tag{5.16}$$

where k is any integer.

Kerr Media With Constant Direction Electric Field

For constant direction electric field ($\alpha_s = \varphi$) along the light path, similar to the symmetric media case, (5.7) and (5.8) respectively reduce to

$$\frac{I_f}{I_0} = 1 - \sin^2\gamma \sin^2(2\varphi - 2\theta_p) \qquad \text{(AP)} \tag{5.17}$$

$$\frac{I_f}{I_0} = \sin^2\gamma \sin^2(2\varphi - 2\theta_p) \qquad \text{(CP)} \tag{5.18}$$

Equations (5.17) and (5.18) agree with the usual Kerr light intensity relations [3].

For constant direction electric field distributions linear polariscope systems are simplest to build and avoid the use of quarter or half wave plates which are typically less ideal than polarizers. There are field direction dependent light extrema known as isoclinic lines when $\varphi = \theta_p + k\pi/2$, and field magnitude dependent extrema when $\gamma = \frac{n\pi}{2}$

$(n = 1, 2, 3, \cdots)$ which can be used to find γ and φ from optical fringe patterns of light maxima and minima.

5.4.2 Semicircular Polariscopes

Measurement Of α_f-Presemicircular Polariscope

When the polarizer angle is set to make an angle of $\frac{\pi}{4}$ with the slow axis of the quarter wave plate, $\theta_q = \theta_p - \frac{\pi}{4}$, the presemicircular polariscope intensity relation in Table 5.3 reduces to

$$\frac{I_f}{I_0} = \frac{1}{2} + \frac{\sin 2\gamma \sin(2\alpha_f - 2\theta_a)}{2} \tag{5.19}$$

For $\sin 2\gamma > 0$ light intensity maxima occur when

$$\theta_a = \alpha_f - \frac{\pi}{4} + k\pi \tag{5.20}$$

and minima occur when

$$\theta_a = \alpha_f + \frac{\pi}{4} + k\pi \tag{5.21}$$

Equations (5.20) and (5.21) can be used to find α_f.

Measurement Of α_0-Postsemicircular Polariscope

When the analyzer angle is set to make an angle of $\frac{\pi}{4}$ with the slow axis of the quarter wave plate, $\theta_q = \theta_a - \frac{\pi}{4}$, the postsemicircular polariscope intensity relation in Table 5.3 reduces to

$$\frac{I_f}{I_0} = \frac{1}{2} + \frac{\sin 2\gamma \sin(2\alpha_0 - 2\theta_p)}{2} \tag{5.22}$$

For $\sin 2\gamma > 0$ light intensity maxima occur when

$$\theta_p = \alpha_0 - \frac{\pi}{4} + k\pi \tag{5.23}$$

and minima occur when

$$\theta_p = \alpha_0 + \frac{\pi}{4} + k\pi \tag{5.24}$$

Equations (5.23) and (5.24) can be used to find α_0.

Both this system and the previous one have the added advantage that for small γ the intensity relation depends only linearly on γ, while that of (5.7) and (5.8) depend on γ^2.

Measurement Of γ

The presemicircular polariscope is also used to measure γ. The method is known as the Reversed Tamry method [49]. In this method the analyzer is set to $\frac{\pi}{4}$ radians to α_f found in (5.20) and the quarter wave plate is set to $\frac{\pi}{4}$ radians to α_0. The intensity relation then reduces to

$$\frac{I_f}{I_0} = \cos^2(\gamma + \theta_p - \alpha_0 + \frac{\pi}{4}) \tag{5.25}$$

Then when the intensity is maximum the polarizer angle yields γ

$$\theta_p = \alpha_0 - \frac{\pi}{4} - \gamma + k\pi \tag{5.26}$$

5.4.3 Circular Polariscope

The complex circular polariscope intensity relation in Table 5.3 is greatly simplified when the polarizer and analyzer angles are set to make an angle of $\frac{\pi}{4}$ with the slow axis of the quarter wave plates before and after the medium respectively. The result is

$$\frac{I_f}{I_0} = \sin^2\gamma \tag{5.27}$$

The polarizer and analyzer angles can be arbitrary, but for best operation to minimize non-ideal effects of the quarter wave plates, the polarizer and analyzer angles should be either aligned or crossed.

With a similar arrangement with the analyzer angle set to make an angle of $-\frac{\pi}{4}$ with the slow axis of the quarter wave plate after the medium the light intensity becomes

$$\frac{I_f}{I_0} = \cos^2\gamma \tag{5.28}$$

With these two complementary configurations the circular polariscope is very useful to find the characteristic phase retardation if absolute intensity measurements or optical fringe patterns are available.

Assuming the secondary characteristic direction α_f is known, the circular polariscope can also be used to measure γ with the orientation of the analyzer. In this arrangement, known as the Tardy method [49], the angle between the polarizer and the first quarter wave plate is set to $\frac{\pi}{4}$ and the angle between the second quarter wave plate and the secondary characteristic direction is set to $-\frac{\pi}{4}$. The intensity relation follows from Table 5.3

$$\frac{I_f}{I_0} = \frac{1}{2} - \frac{1}{2}\cos(2\gamma - 2\theta_a + 2\alpha_f) \tag{5.29}$$

When the intensity is an extremum, the analyzer angle measures γ

$$\theta_a = \gamma + \alpha_f + \frac{k\pi}{2}$$

5.5 AC Modulation Method

For most materials of interest the Kerr constant and consequently the characteristic phase retardation γ are very small. Directly measuring such a small phase retardation with desired accuracy is difficult. The AC modulation method can be used to increase the sensitivity of Kerr effect measurements [8, 9, 20–22].

In this method an ac voltage with known radian frequency is superposed on a dc voltage. Then the (transverse) electric field in the Kerr media has a dc and an ac component (Figure 5.2). If there is no space charge the ac and dc components are in the same direction. In the presence of space charge, however, the direction of the dc component may be different than the ac component which is not affected by the space charge if the frequency is high enough [6]. Since B is small, primary and secondary characteristic directions are the same ($\alpha = \alpha_f = \alpha_0$) and the characteristic parameters are related to the applied electric field by (4.66). To measure ac and dc components of the electric field, the semicircular polariscope system described in Section 5.4.2 is used. The output-input intensity ratio is given by (5.19) and for small γ ($\gamma \ll \frac{\pi}{2}$) approximately reduces to

$$\frac{I_f}{I_0} \approx \frac{1 + 2\gamma\sin(2\alpha - 2\theta_a)}{2} \tag{5.30}$$

To find the measured intensity in terms of the ac and dc components of the electric

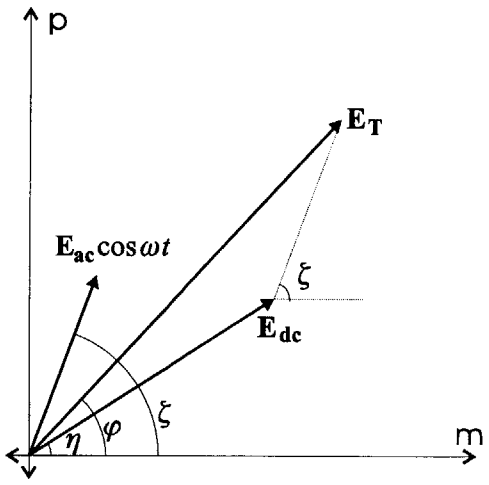

Figure 5.2: When an ac voltage is superposed on a dc voltage, the electric field in Kerr media has dc and ac components. If there is no space charge both components have the same direction ($\eta = \zeta$). If there is space charge the direction generally differs ($\eta \neq \zeta$). Often, the frequency of the ac field is chosen high enough so that the ac component of the electric field is not affected by the space charge.

field, we first note from Figure 5.2 that

$$E_T(s)\cos\varphi(s) = E_{T_{dc}}(s)\cos\eta(s) + E_{T_{ac}}(s)\cos\omega t\cos\zeta(s) \tag{5.31}$$

$$E_T(s)\sin\varphi(s) = E_{T_{dc}}(s)\sin\eta(s) + E_{T_{ac}}(s)\cos\omega t\sin\zeta(s) \tag{5.32}$$

E_T, $E_{T_{dc}}$, and $E_{T_{ac}}$ are amplitudes and without loss of generality are taken to be positive. Substituting (5.31) and (5.32) into (4.66) and substituting the results into (5.30) results in dc, fundamental frequency and double frequency harmonic light intensity components

$$I_f = I_{dc} + I_\omega\cos\omega t + I_{2\omega}\cos 2\omega t \tag{5.33}$$

where

$$\frac{I_{dc}}{I_0} = (1/2) + \pi B\int_{s_{in}}^{s_{out}}\left[E_{T_{dc}}^2(s)\sin\big[2\eta(s) - 2\theta_a\big] + \frac{E_{T_{ac}}^2(s)}{2}\sin\big[2\zeta(s) - 2\theta_a\big]\right]ds \tag{5.34}$$

$$\frac{I_\omega}{I_0} = 2\pi B\int_{s_{in}}^{s_{out}} E_{T_{dc}}(s)E_{T_{ac}}(s)\sin\big[\eta(s) + \zeta(s) - 2\theta_a\big]\,ds \tag{5.35}$$

$$\frac{I_{2\omega}}{I_0} = \pi B\int_{s_{in}}^{s_{out}}\frac{E_{T_{ac}}^2(s)}{2}\sin\big[2\zeta(s) - 2\theta_a\big]\,ds \tag{5.36}$$

Note that I_ω and $I_{2\omega}$ in (5.33) are the peak amplitudes of the fundamental frequency and double frequency harmonics respectively.

Since B is very small, it follows from (5.34) that

$$I_{dc} \approx \frac{I_0}{2} \tag{5.37}$$

so that (5.36) and (5.36) approximately reduce to

$$I_\omega / I_{dc} \approx 4\pi B \int_{s_{in}}^{s_{out}} E_{T_{dc}}(s) E_{T_{ac}}(s) \sin\big[\eta(s) + \zeta(s) - 2\theta_a\big]\, ds \tag{5.38}$$

$$I_{2\omega} / I_{dc} \approx \pi B \int_{s_{in}}^{s_{out}} E_{T_{ac}}^2(s) \sin\big[2\zeta(s) - 2\theta_a\big]\, ds \tag{5.39}$$

Both I_ω / I_{dc} and $I_{2\omega} / I_{dc}$ may be accurately measured by a lock-in amplifier tuned respectively to frequencies ω and 2ω. $I_{2\omega} / I_{dc}$ may be used to find the characteristic parameters, γ_{ac} and α_{ac}, that correspond to the space-charge free electric field distribution whose transverse component's magnitude and direction are given by $E_{T_{ac}}$ and ζ respectively. Expanding (5.39) and using (4.66a) and (4.66b), we obtain

$$I_{2\omega} / I_{dc} = \gamma_{ac} \sin(2\alpha_{ac} - 2\theta_a) \tag{5.40}$$

$$\gamma_{ac} \cos 2\alpha_{ac} = \pi B \int_{s_{in}}^{s_{out}} E_{T_{ac}}^2(s) \cos 2\zeta(s)\, ds \tag{5.41}$$

$$\gamma_{ac} \sin 2\alpha_{ac} = \pi B \int_{s_{in}}^{s_{out}} E_{T_{ac}}^2(s) \sin 2\zeta(s)\, ds \tag{5.42}$$

Using (5.40), light intensity measurements determine γ_{ac} and α_{ac}. If the period $T = \frac{2\pi}{\omega}$ is much shorter than the transport time for ions to migrate significant distances over the course of a sinusoidal angle, the ac charge density is essentially zero and $E_{T_{ac}}(s)$ and $\zeta(s)$ can be described by solutions to Laplace's equation.

On the other hand I_ω / I_{dc} may be used to find the characteristic parameters, γ_{hy} and α_{hy}, of a *hybrid* electric field distribution whose transverse component's magnitude and direction are given as

$$E_{hy}(s) = 2\sqrt{E_{T_{dc}}(s) E_{T_{ac}}(s)} \tag{5.43}$$

$$\varphi_{hy}(s) = \frac{\eta(s) + \zeta(s)}{2} \tag{5.44}$$

respectively. Now expanding (5.38) and again using (4.66a) and (4.66b), we obtain

$$I_\omega / I_{dc} = \gamma_{hy} \sin\bigl(2\alpha_{hy}(s) - 2\theta_a\bigr) \tag{5.45}$$

$$\gamma_{hy} \cos 2\alpha_{hy} = \pi B \int_{s_{in}}^{s_{out}} E_{hy}^2(s) \cos 2\varphi_{hy}(s)\, ds \tag{5.46}$$

$$\gamma_{hy} \sin 2\alpha_{hy} = \pi B \int_{s_{in}}^{s_{out}} E_{hy}^2(s) \sin 2\varphi_{hy}(s)\, ds \tag{5.47}$$

Using (5.45), light intensity measurements determine γ_{hy} and α_{hy}.

Using trigonometric identities, (5.41), (5.42), (5.46) and (5.47) can also be expressed in terms of the light frame components of the applied ac and dc electric fields

$$\gamma_{ac} \cos 2\alpha_{ac} = \pi B \int_{s_{in}}^{s_{out}} \left[E_{m_{ac}}^2(s) - E_{p_{ac}}^2(s)\right] ds \tag{5.48a}$$

$$\gamma_{ac} \sin 2\alpha_{ac} = \pi B \int_{s_{in}}^{s_{out}} 2E_{m_{ac}}(s) E_{p_{ac}}(s)\, ds \tag{5.48b}$$

and

$$\gamma_{hy} \cos 2\alpha_{hy} = 4\pi B \int_{s_{in}}^{s_{out}} E_{m_{ac}}(s) E_{m_{dc}}(s) ds - 4\pi B \int_{s_{in}}^{s_{out}} E_{p_{ac}}(s) E_{p_{dc}}(s) ds \tag{5.49a}$$

$$\gamma_{hy} \sin 2\alpha_{hy} = 4\pi B \int_{s_{in}}^{s_{out}} E_{p_{ac}}(s) E_{m_{dc}}(s) ds + 4\pi B \int_{s_{in}}^{s_{out}} E_{m_{ac}}(s) E_{p_{dc}}(s) ds \tag{5.49b}$$

Of particular interest is the case when the applied electric field is axisymmetric and the light propagation direction is perpendicular the axisymmetry axis z. Then $\hat{m}$ can be chosen to equal to $\hat{z}$ and (5.48) and (5.49) can be expressed as

$$\gamma_{ac} \cos 2\alpha_{ac} = 2\pi B \int_{p}^{r_{\text{out}}} \left[E_{z_{ac}}^2(r) - \frac{p^2}{r^2} E_{r_{ac}}^2(r)\right] \frac{r\, dr}{\sqrt{r^2 - p^2}} \tag{5.50a}$$

$$\gamma_{ac} \sin 2\alpha_{ac} = 2\pi B \int_{0}^{r_{\text{out}}} \frac{2p}{r} E_{z_{ac}}(r) E_{r_{ac}}(r) \frac{r\, dr}{\sqrt{r^2 - p^2}} \tag{5.50b}$$

and

$$\begin{aligned} \gamma_{hy} \cos 2\alpha_{hy} = {} & 8\pi B \int_{p}^{r_{out}} E_{z_{ac}}(r) E_{z_{dc}}(r) \frac{r\, dr}{\sqrt{r^2 - p^2}} \\ & - 8\pi B \int_{p}^{r_{out}} \frac{p^2}{r^2} E_{r_{ac}}(r) E_{r_{dc}}(r) \frac{r\, dr}{\sqrt{r^2 - p^2}} \end{aligned} \tag{5.51a}$$

$$\gamma_{hy} \sin 2\alpha_{hy} = 8\pi B \int_p^{r_{out}} \frac{p}{r} E_{r_{ac}}(r) E_{z_{dc}}(r) \frac{r\,dr}{\sqrt{r^2 - p^2}} + 8\pi B \int_p^{r_{out}} \frac{p}{r} E_{z_{ac}}(r) E_{r_{dc}}(r) \frac{r\,dr}{\sqrt{r^2 - p^2}} \tag{5.51b}$$

5.6 Effects Of Gaussian Beam For Point Measurement Scheme

The ongoing experimental Kerr electro-optic work at MIT is focused on the point/plane electrode geometry in transformer oil. This section estimates the effects of finite beam size and gaussian beam expansion on an infinite extent point/plane electrode geometry whose geometric parameters are chosen similar to those used in our experiments. In the absence of space charge the electric field distribution from point/plane electrodes of infinite extent can be found analytically (Appendix A) which then can be used to find the characteristic parameters by numerical integration of (2.118) or (2.119) as discussed in Section 3.11.

Gaussian beam propagation in isotropic media is well understood [30]. According to theory the light electric field has a gaussian amplitude distribution in the plane perpendicular to the propagation direction

$$|e_T| \propto \exp\left(-\frac{m^2 + p^2}{w^2}\right) \tag{5.52}$$

where e_T is the transverse component of the light electric field, m and p are the tranverse coordinates of the light frame whose third coordinate s is aligned with the light propagation direction as described in Section 2.4.1, and w is the radius of the beam which expands according to

$$w^2(s) = w_0^2 \left(1 + \frac{4s^2}{k^2 w_0^4}\right) \tag{5.53}$$

as it propagates. Here w_0 is the initial beam size of the gaussian beam at $s = 0$ and k is the wave number. Here we do not go into details on gaussian beam propagation whose fundamentals can only be thoroughly understood by studying the phase factors that are absent in the amplitude distribution of (5.52) [30]. Equations (5.52) and (5.53) are adequate for our purpose of modelling the effects of finite beam size and slight diffraction on Kerr electro-optic measurements.

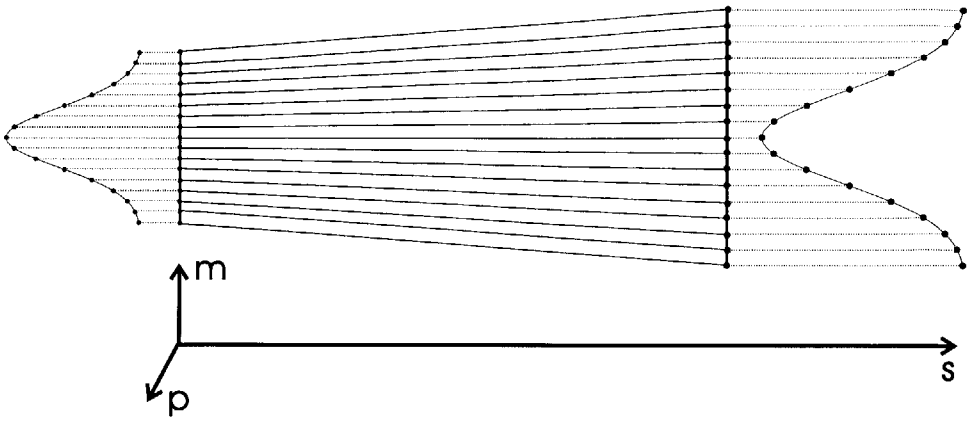

Figure 5.3: The light propagation theory developed in Chapter 2 neglects the variation of the applied electric field within the finite beam. Here we discretize the gaussian light beam into infinitesimal light beams each of which propagates as described in Chapter 2. A gaussian weighted average of the intensity measurements from each infinitesimal light beam is then used to model the effects of the finite beam size on the Kerr electro-optic measurements. The slight diffraction effects are also modelled by assuming that the propagation directions of each infinitesimal light beam is slightly different from $\hat{s}$ forming an expanded beam at the output.

In our typical Kerr experimental set up light propagates around 50 cm in air before entering the test cell that houses the high voltage stressed dielectric liquid. Thus (5.53) shows that a 632 nm wavelength laser beam of initial radius 0.5 mm expands approximately to 0.55 mm before entering the Kerr medium. Within the Kerr medium the light propagates typically around 25 cm so that the final beam size at the exit of the Kerr medium is expected to be at most 0.60 mm. Here we assume that the Kerr medium has a refractive index of unity. For larger refractive indices the wavenumber k is larger so that the diffractive effects as described in (5.53) are further weakened.

To estimate the effects of the gaussian beam on Kerr electrooptic measurements we discretize input and output gaussian beams as shown in Figure 5.3. Each point in the input beam is associated with a point on the output beam. Between associated points it is assumed the theory in Chapter 2 is valid and the matricant is calculated. A gaussian weighted average of these matricants are taken to find the estimate of the effective characteristic parameters.

The geometry chosen is a point/plane electrode configuration with tip/plane distance of 5 mm and point radius of curvature of 0.5 mm with an applied voltage of 15 kV in transformer oil. The results are shown in Figure 5.4.

In the top figures we show the characteristic retardation γ and characteristic angle

α on light path lines that are parallel to the axisymmetry axis z at a radial distance p. Here the solid lines show the results without gaussian averaging and dots illustrate the effects of gaussian averaging. The finite size of the beam has essentially no significant effect on the measurements unless part of the beam is blocked by the point electrode. Qualitatively the electric field magnitude and direction variation over the light beam is small enough so that they can be linearized. Then over the beam area the effects of symmetrical points on the gaussian beam cancel each other leaving the average to be very close to results at the center of the beam. When there is blocking however, this symmetry is destroyed resulting in a change in the characteristic parameters.

The middle and bottom figures show the characteristic parameters on lines perpendicular to the axisymmetry axis z. The middle figures are for positions when the needle electrode does not block the beam. Again the averaged and direct results are very close except for the characteristic angle at $z = 0$ where part of the beam is blocked by the ground plane. For the bottom figures the effects of blocking by the point electrode is again observed.

5.7 Measurements From Optical Fringe Patterns

5.7.1 Two Dimensional Electric Fields

Much of the earlier work on the Kerr electro-optic effect use optical fringe patterns for measurements of two dimensional electric fields [3, 12–15, 23]. The advantages of this method have already been discussed in Chapter 1. This section presents calculated optical patterns for the two dimensional analog (an infinite blade/plane) of the point/plane electrode geometry illustrated in Figure C.1 and reviews a few details of the measurements. For the simulations the length of the two dimensional blade of radius of curvature 0.5 mm is taken to be 5 mm, the applied voltage is 40 kV across a 2.5 mm gap and the medium is nitrobenzene ($B \approx 3 \times 10^{-12}$ m/V^2). In Section 5.7.2 the calculated optical patterns for this two dimensional blade/plane electrode geometry are contrasted to calculated optical patterns for the analog axisymmetric geometry with point/plane electrodes.

To obtain Kerr electro-optic fringe patterns, typically linear and circular polariscopes are employed. For linear polariscopes (LP) the polarizer and analyzer are either set to be aligned or crossed so that the input/output intensity relationships simplify to those given in (5.17) and (5.18). Similarly for circular polariscopes (CP) the

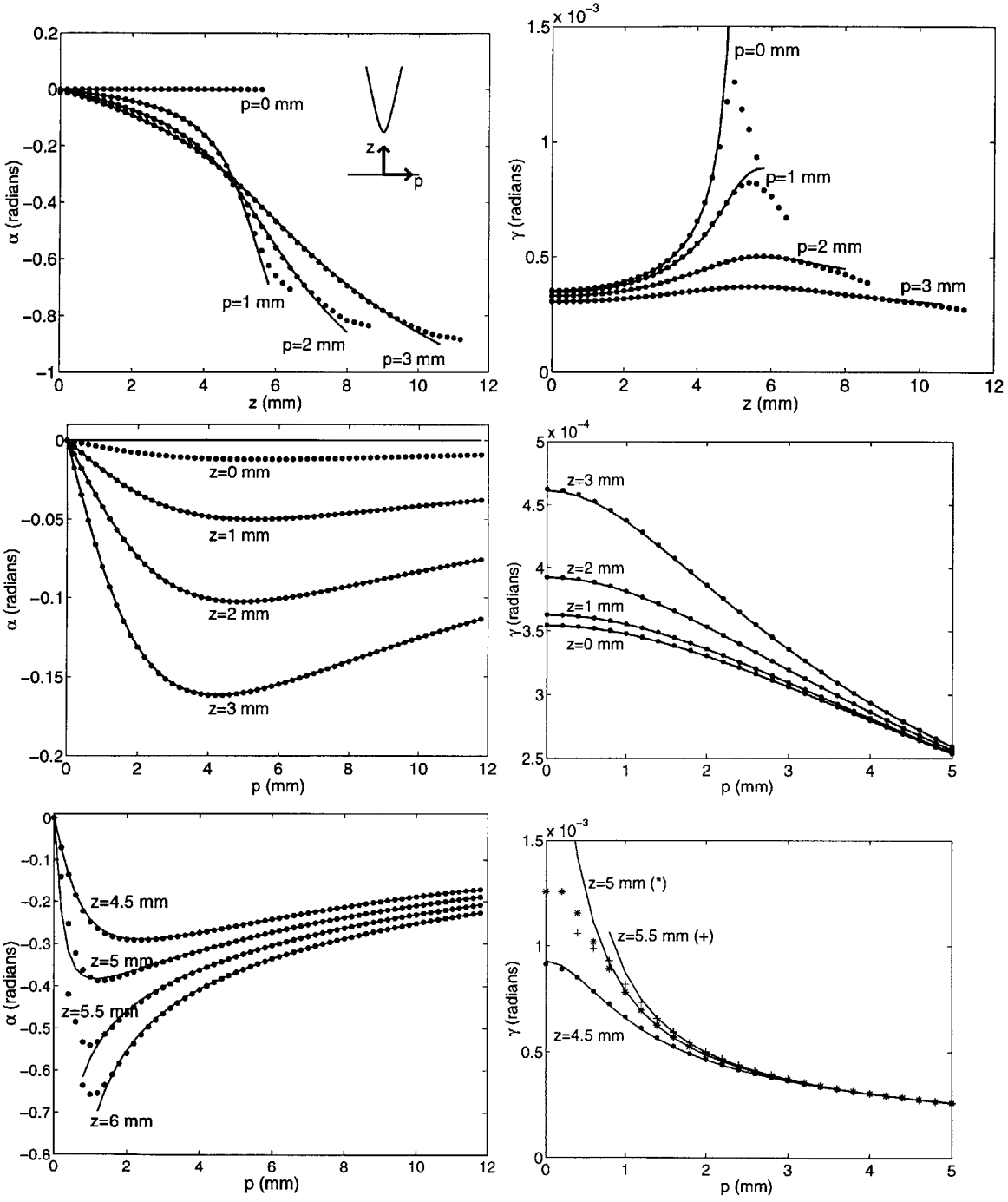

Figure 5.4: A comparison between ideal space charge free Kerr electro-optic data (solid lines) and calculated data (symbols including dots) obtained by averaging over a gaussian beam of 0.55 mm radius for infinite extent point/plane electrodes with 5 mm gap and 0.5 mm point radius of curvature in transformer oil ($B \approx 3 \times 10^{-15}$ m/V^2) stressed by 15 kV.

angle between the polarizer and the input quarter wave plate and the angle between the analyzer and the output quarter wave plate are set to be $\pm\pi/4$ resulting in the simple relations of (5.27) and (5.28). Note that the two polarizer angles can be arbitrarily set in relation to each other. In this section we focus on the linear polariscope with crossed polarizers and circular polariscope with aligned polarizers when the quarter wave plate slow axes are also aligned and are at angle $\pi/4$ with respect to the polarizers transmission axes. For these cases the input/output intensity relations are respectively given in (5.18) and (5.27) and repeated here for easy reference

$$\frac{I_f}{I_0} = \sin^2\gamma_c \sin^2(2\varphi - 2\theta_p) \quad \text{(LP)} \tag{5.54}$$

$$\frac{I_f}{I_0} = \sin^2\gamma_c \qquad \text{(CP)} \tag{5.55}$$

Here φ is the direction of the two dimensional electric field and θ_p is the position of the polarizer transmission axis both with respect to some fixed direction. The parameter $\gamma_c = \pi B E^2 l$ is half of the optical phase shift in (1.12). Here we assume that the light propagation direction is along the infinite axis of the two dimensional geometry.

In Figure 5.5 we present the calculated optical patterns for the circular polariscope and two optical patterns for the crossed linear polariscope with polarizer angles at $\pi/4$ and $\pi/2$ with respect to the vertical axis of the blade electrode. The right most plots expand the region near the blade tip where there are many fringes because of the high electric field near the tip.

For the circular polariscope the fringe patterns are governed by (5.55) and are independent of the direction of the electric field φ. The condition for light minima follows from (5.55) as

$$\gamma_c = \pi B E^2 l = n\pi \qquad n = 0, 1, 2, \cdots \tag{5.56}$$

These field magnitude dependent lines are called isochromatic lines [3]. For each minimum, n can be found by counting the number of previous minima between the positions where the electric field goes to zero which, for this geometry, are at the lower right and lower left corners.

For the linear polariscope, in addition to the same isochromatic lines as for the circular polariscope there exist superposed field direction dependent minima known as isoclinic lines whenever the applied electric field direction φ is either parallel or perpendicular to the light polarization θ_p. The condition for these minima follows

from (5.54) as

$$\varphi - \theta_p = \frac{n\pi}{2} \qquad n = \cdots, -2, -1, 0, 1, 2, \cdots \tag{5.57}$$

Note that in Figure 5.5, all three cases have the same isochromatic lines as given by (5.56). While the circular polariscope has no isoclinic lines, the isoclinic lines in Figure 5.5 (a) and (b) differ because of the different light polarization directions θ_p.

5.7.2 Axisymmetric Electric Fields

For axisymmetric electric field distributions, when the light propagation direction is perpendicular to the axisymmetry axis the input/output intensity relations in (5.54) and (5.55) are respectively replaced by

$$\frac{I_f}{I_0} = \sin^2\gamma_s \sin^2(2\alpha_s - 2\theta_p) \tag{5.58}$$

$$\frac{I_f}{I_0} = \sin^2\gamma_s \tag{5.59}$$

where α_s and γ_s are the characteristic parameters for a symmetric medium which are described in Section 4.2.4. Equations (5.58) and (5.59) show that the same experimental setups used for measurements of the magnitude and the direction of two dimensional electric fields can in principle be used for measurements of α_s and γ_s. Furthermore, it is natural to expect the existence of analogs of isoclinic and isochromatic lines of Section 5.7.1.

In Figure 5.6 we show the calculated optical fringe patterns for the point/plane electrode geometry of Figure C.1 which has a point plane gap of 2.5 mm. Similar to Figure 5.5 there are light maxima and minima dependent only on γ_s for the circular polariscope. For the linear polariscope α_s dependent minima are introduced. There are however visible differences. One immediate observation is that at light minima of the circular polariscope the light intensity does not become completely extinct. Furthermore, for the linear polariscope when $\theta_p = \pi/4$ the intensity pattern near the tip is essentially unmodified and there are no real analogs of isoclinic lines except the ones that extend from the lower right and left corners towards the needle. Even these lines do not extend right to the needle.

To understand these differences for linear and circular polariscopes, in Figure 5.7 and Figure 5.8 we plot α_s and γ_s along $z = 2.1$ mm, $z = 2.2$ mm, $z = 2.3$ mm, $z = 2.4$

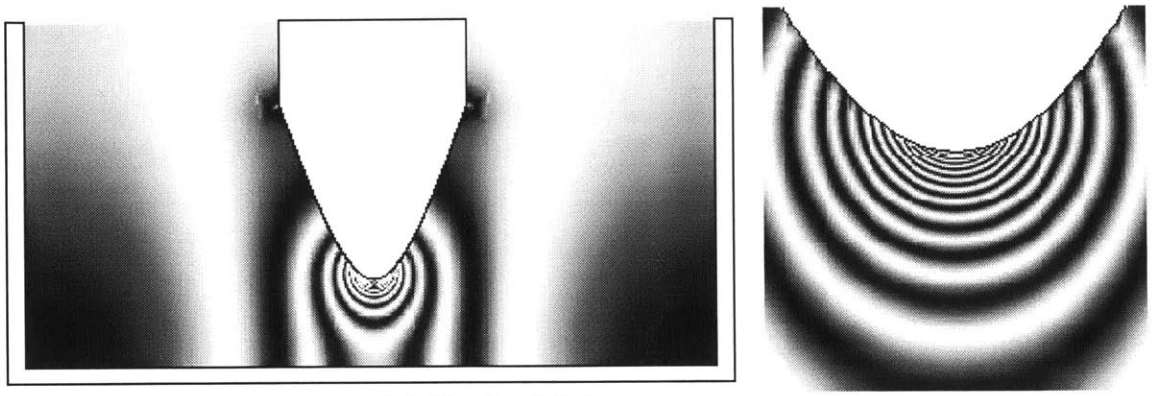

(a) Circular Polariscope

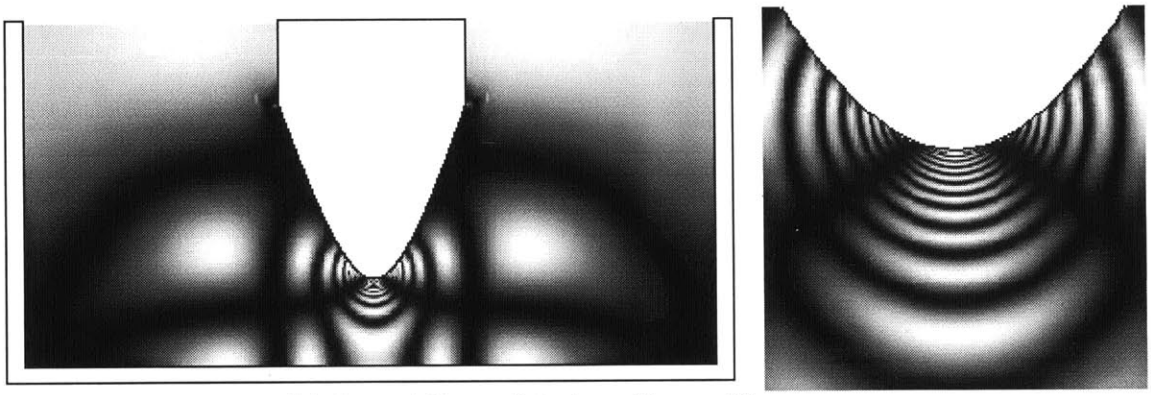

(b) Crossed Linear Polarizers ($\theta_p = \pi/4$)

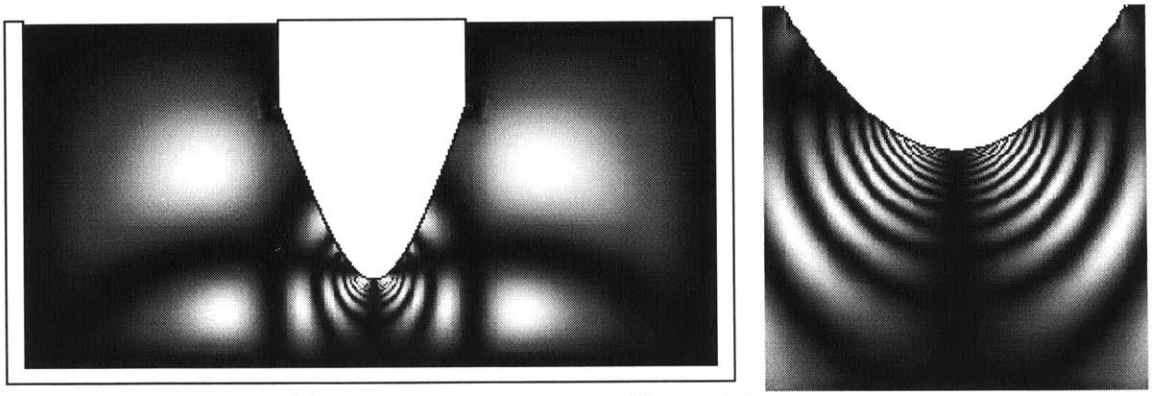

(c) Crossed Linear Polarizers ($\theta_p = \pi/2$)

Figure 5.5: Calculated circular and linear polariscope light intensity patterns for a two dimensional electric field distribution from a blade/plane electrode geometry with gap of 2.5 mm, blade radius of curvature of 0.5 mm, and depth of 5 mm in nitrobenzene ($B \approx 3 \times 10^{-12}$ m/V^2) stressed by 40 kV.

mm, and $z = 2.5$ mm. The dotted lines on the γ_s plots correspond to $\gamma_s = \pi$ and $\gamma_s = \pi/2$ and the dotted lines on the α_s plots correspond to $\alpha_s = n\pi/4$ where n is an integer.

Figure 5.7 and Figure 5.8 show that there are striking differences between α_s and γ_s and their two dimensional counterparts φ and γ_c. The characteristic angle γ_s never reaches $n\pi$ with the possible exception of the axisymmetry axis $p = 0$. Therefore, the isochromatic light minima lines in Figure 5.6 can never have zero intensity except at $p = 0$. Characteristic angle α_s is not totally independent of γ_s but is affected by the minima and maxima of γ_s. In fact near the maxima and minima of γ_s, α_s sharply increases with increasing p and the slope of this sharp change decreases at points further away from the needle. For example, in the $z = 2.1$ mm plot the slope at around $p = 0.5$ mm is so large that the curve is essentially vertical within the scale chosen, while at $p = 2.2$ mm the slope is less.

To explain these phenomena we go back to the governing differential equations for α_s and γ_s derived in Section 4.4.2 and repeated here for convenience

$$\frac{d\gamma_s(s)}{ds} = 2\pi B E_T^2(s) \cos\big[2\varphi(s) - 2\alpha_s(s)\big] \tag{5.60}$$

$$\frac{d\alpha_s(s)}{ds} = \pi B E_T^2(s) \cot\gamma_s(s) \sin\big[2\varphi(s) - 2\alpha_s(s)\big] \tag{5.61}$$

Recall that $\alpha_s = \alpha_s(s_{\text{out}})$ and $\gamma_s = \gamma_s(s_{\text{out}})$ where s_{out} is the exit point of the light from the medium. Although Figure 5.7 shows the p dependence of γ_s and α_s, (5.60) and (5.61) can still be used to qualitatively interpret the results by assuming that the electric field distribution along the light path are approximately equal for close p and the variations of α_s and γ_s with respect to p are due to the change in the path length within the medium (change of s_{out}). In fact any change in the electric field can also be lumped into a change in s_{out} for qualitative interpretation.

Near $p = 10$ mm $s_{\text{out}} \approx 0$, and γ_s is around 0 and $\alpha_s = \varphi = \pi/2$ where the angles are measured with respect to the symmetry axis z. The singularity in (5.61) can be avoided using the L'Hopital rule yielding

$$\left.\frac{d\alpha_s(s)}{ds}\right|_{s=0} = \frac{1}{2}\left.\frac{d\varphi(s)}{ds}\right|_{s=0} \tag{5.62}$$

Thus as the electric field increases with decreasing p towards the point electrode, γ_s and α_s also increase in accordance with (5.60), (5.61) and (5.62). There are no notable

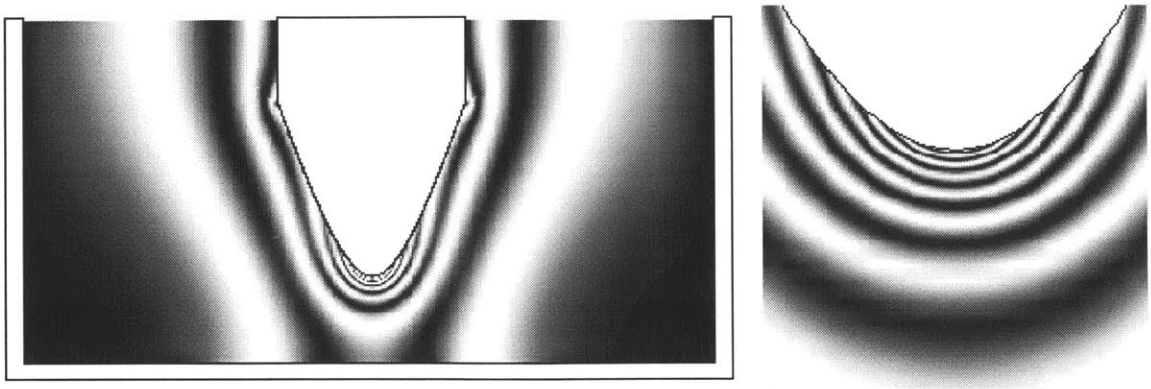

(a) Circular Polariscope

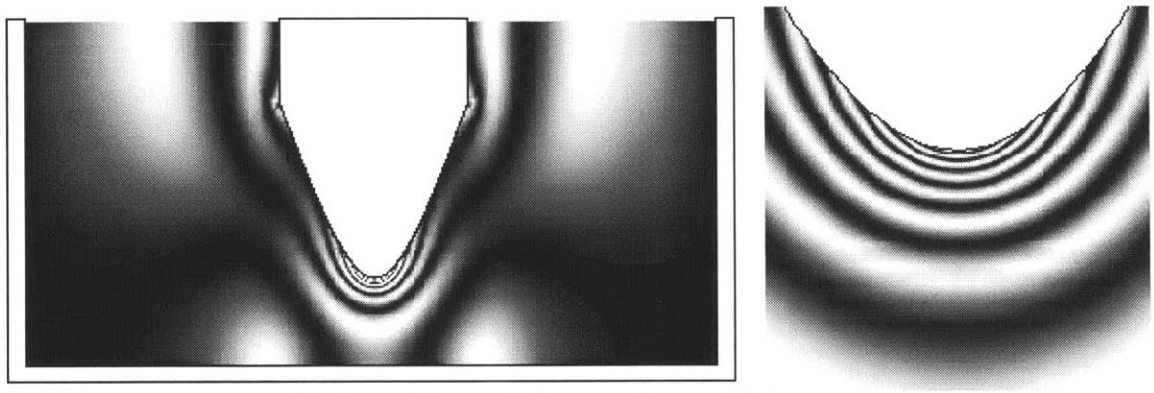

(b) Crossed Linear Polarizers ($\theta_p = \pi/4$)

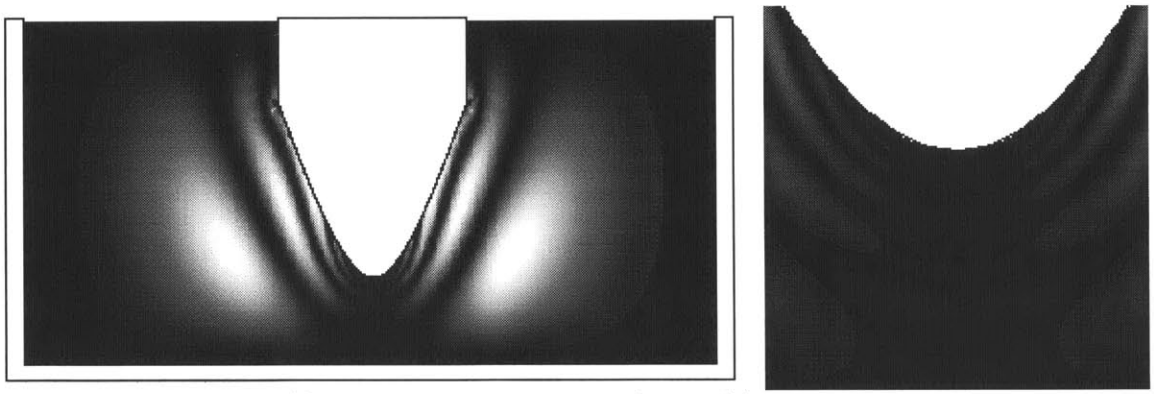

(c) Crossed Linear Polarizers ($\theta_p = \pi/2$)

Figure 5.6: Calculated circular and linear polariscope light intensity patterns for the axisymmetric finite point/plane electrode geometry of Figure C.1. The medium is nitrobenzene, the applied volage is 40 kV, tip-plane distance is 2.5 mm, and point plane electrode radius of curvature is 0.5 mm.

characteristics until γ_s crosses $\frac{\pi}{2}$. At this juncture, which is around $p = 3.8$ mm, α_s reaches a maximum as predicted by the sign change of $\cot\gamma_s$ in (5.61). The picture gets complicated when γ_s nears π. Then $\cot\gamma_s$ nears infinity and the rate of change in α_s increases as predicted by (5.61). The value of α_s falls sharply to change the sign of $\cos\big[2\varphi(s) - 2\alpha_s(s)\big]$ in (5.60). When this happens, γ_s reaches a maximum and begins to decrease. This also decreases the rate of change in α_s until γ_s nears 0. The cycle of occurrence of minima and maxima of γ_s and sharp decrease in α_s repeats until $p = 0$.

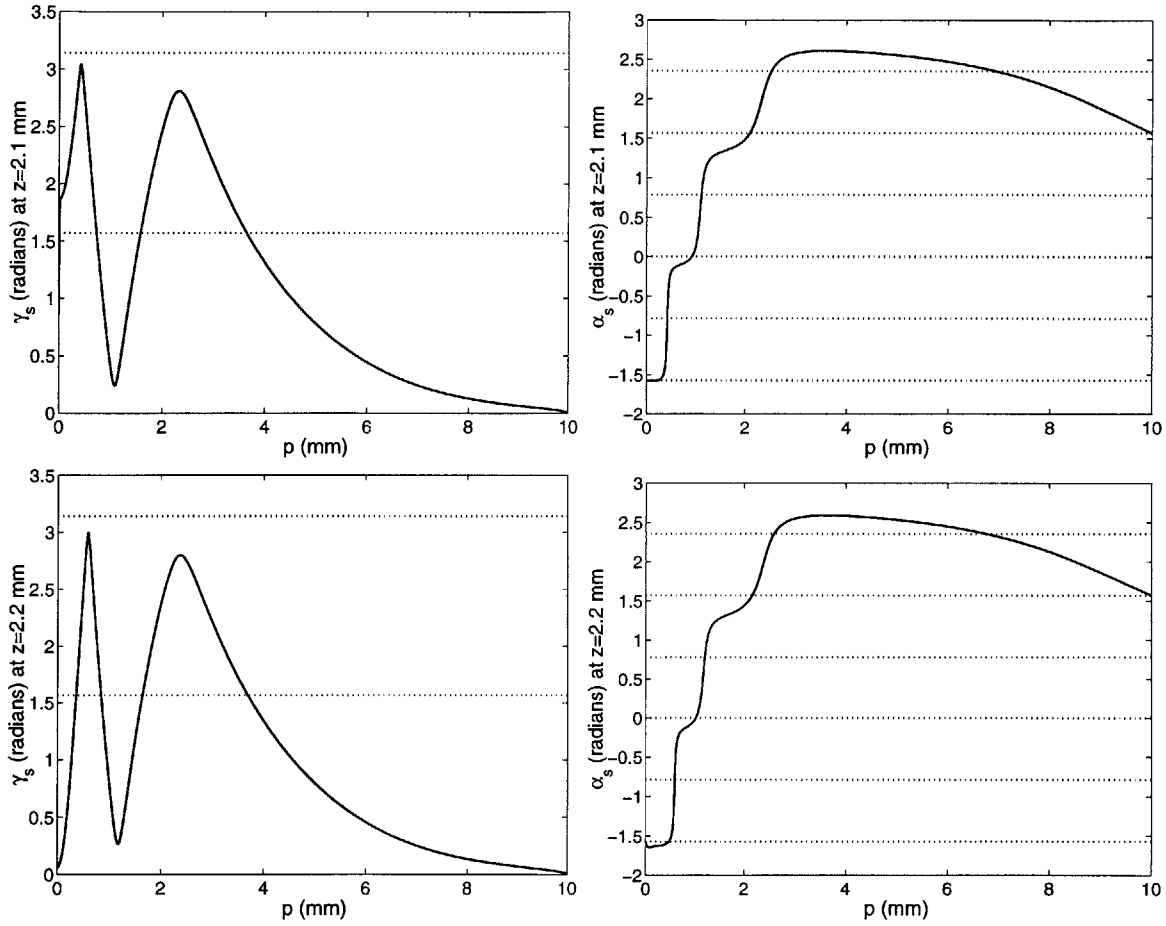

Figure 5.7: The characteristic parameters α_s and γ_s along $z = 2.1$ mm and $z = 2.2$ mm.

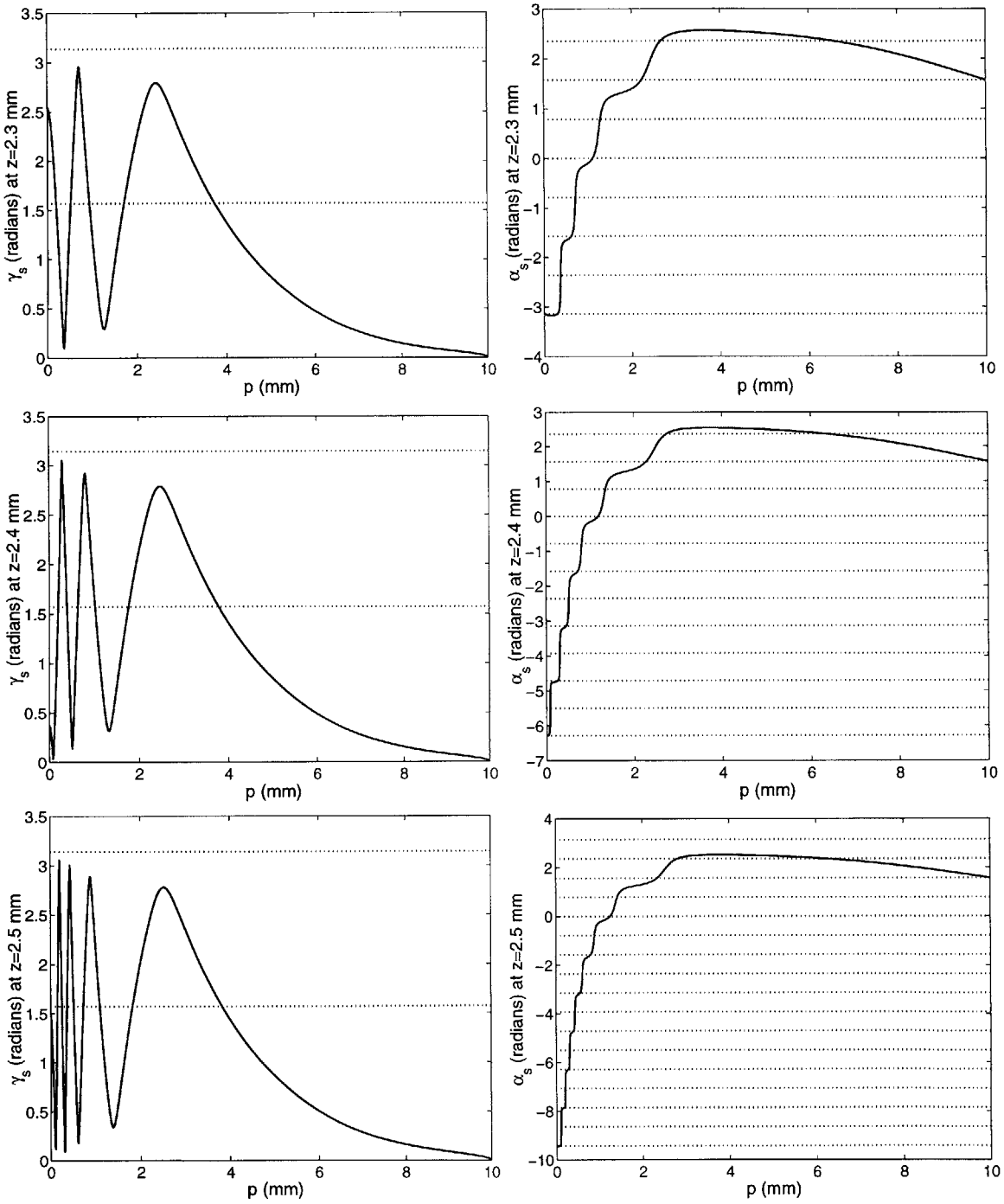

Figure 5.8: The characteristic parameters α_s and γ_s along $z = 2.3$ mm, $z = 2.4$ mm, and $z = 2.5$ mm.

Part II

The Inverse Problem

Chapter 6

The Onion Peeling Method

6.1 Introduction

The most straight-forward discretization of axisymmetric geometries is to use planar layers perpendicular to the axisymmetry axis and further discretizing the planes with annular rings as shown in Figure 6.1 for a point/plane electrode geometry. An approximate electric field distribution with unknown parameters can then be constructed in terms of this discretization. The inverse problem of reconstructing the applied electric field from Kerr electro-optic measurements then reduces to determination of these unknown parameters.

Postulating an electric field distribution with stepwise constant radial and axial components in each ring is the most obvious choice for approximation. This introduces two unknowns for each ring. Assuming the electric field vanishes outside the discretization region, if we assign a Kerr electro-optic measurement for each ring from which we can determine two characteristic parameters, we can obtain a mathematically square system where the number of independent equations equal the number of unknowns. The original onion peeling algorithm proposed by Aben [50] solves this square sytem to obtain the unknown electric field components. The algorithm is so called because it recovers the electric field layer by layer from outside to inside. This chapter describes and improves the method, and applies it to a point/plane electrode geometry.

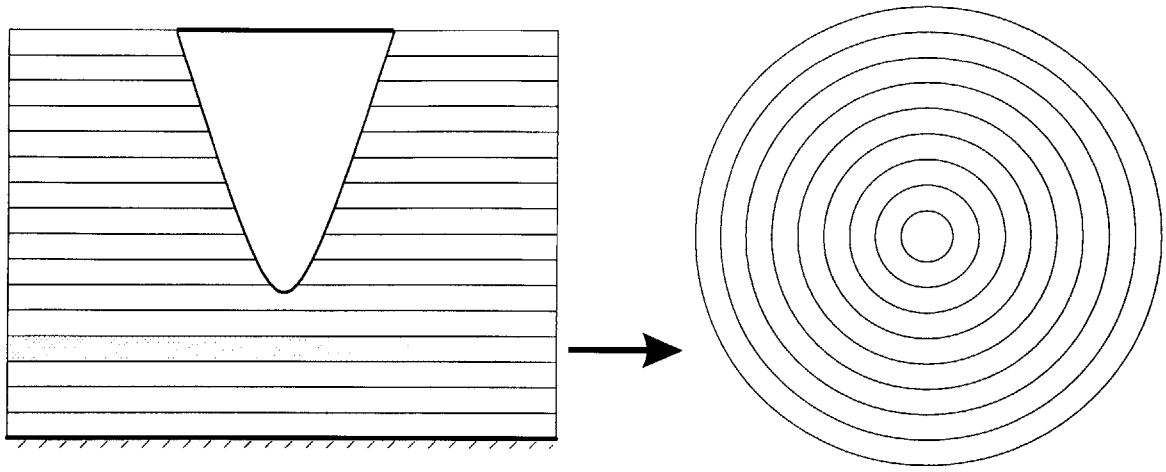

Figure 6.1: Discretization of space with planar layers and annular rings for axisymmetric geometries shown on a point/plane electrode geometry.

6.2 Spatial Discretization

6.2.1 A Two Layer Artificial Kerr Medium

For the sake of simplicity we describe the onion peeling algorithm on the two layer artificial Kerr medium shown in Figure 6.2. Generalization to arbitrary axisymmetric geometries is straight-forward and presented in section 6.2.2. Our concise matrix approach is a simpler description of the algorithm than Aben's [50].

In Figure 6.2, outside the two rings the electric field vanishes. Within each ring the electric field magnitude E and the angle between the z-axis and the electric field ψ are assumed to be constant. Magnitude E and angle ψ completely specify the axisymmetric electric field components E_z and E_r

$$E_z = E\cos\psi \tag{6.1}$$

$$E_r = E\sin\psi \tag{6.2}$$

The transverse component of the electric field is in the zp-plane so only E_z and E_p effect Kerr electro-optic measurements. The z-component E_z is expressed in terms of E and ψ in (6.1). The angle θ in Figure 6.2 is defined so that E_p can be expressed in terms of E and ψ as

$$E_p = E_r\cos\theta = E\sin\psi\cos\theta \tag{6.3}$$

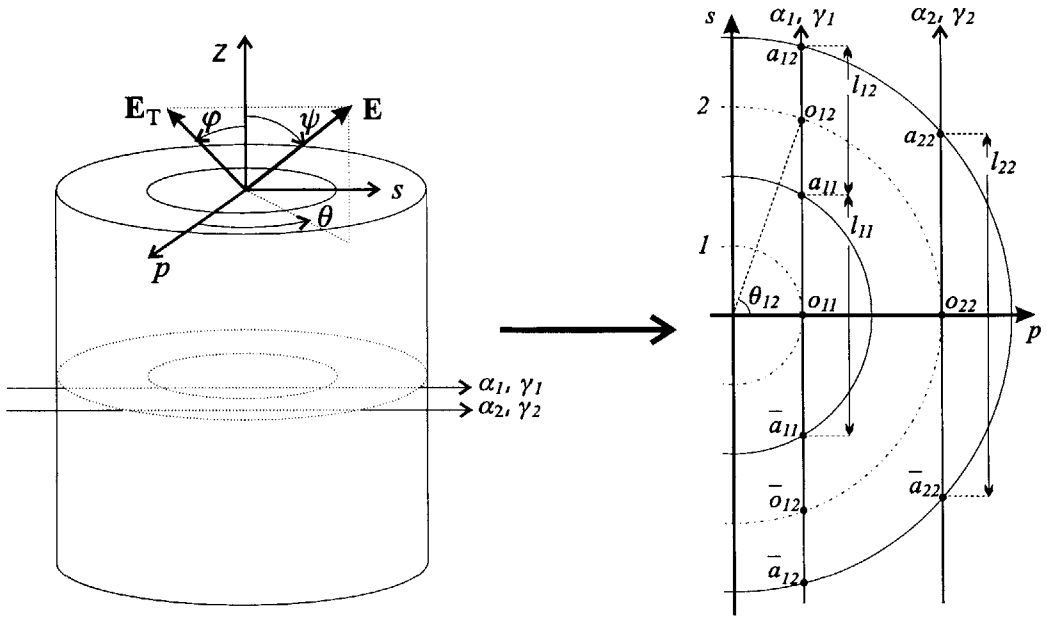

Figure 6.2: The discretized two ring artificial cylindrical geometry used for illustration of the onion peeling method. In both rings the magnitude of the electric field E_1 and E_2 and angles ψ_1 and ψ_2 are taken to be constant. In the outer region the electric field vanishes.

It follows from (6.1) and (6.3) that

$$\tan\varphi = \frac{E_p}{E_z} = \tan\psi\cos\theta \tag{6.4}$$

where φ is the direction of the transverse electric field in the zp-plane as shown in Figure 6.2.

The magnitude and angle of the electric field in ring 1 and ring 2 are denoted by E_1, ψ_1, E_2 and ψ_2 respectively with 1 and 2 referring to the inner and outer layers respectively. These unknowns are to be found from the experimental data of α_1, γ_1, α_2 and γ_2, the characteristic parameters obtained from the two light rays shown in Figure 6.2. The light rays are s directed and parallel to the zs-plane with light ray 2 passing through the midpoint of the outer layer (o_{22}) and light ray 1 passing through both layers and the midpoint of the inner layer (o_{11}).

The method recovers the electric field magnitude and angle from the characteristic parameters by comparing the experimental matricants to the approximate matricants that are obtained in terms of the constant electric field magnitude and angle within

each of the ring layers. For the two light rays in Figure 6.2 the experimental matricants are

$$\mathbf{\Omega}_{e_1} = \mathbf{S}(-\alpha_1)\mathbf{G}(\gamma_1)\mathbf{S}(\alpha_1) \tag{6.5}$$

$$\mathbf{\Omega}_{e_2} = \mathbf{S}(-\alpha_2)\mathbf{G}(\gamma_2)\mathbf{S}(\alpha_2) \tag{6.6}$$

respectively.

The magnitude and the angle of the approximate transverse electric field distributions along the second ray are respectively denoted by $E_{T_2}(s)$ and $\varphi_2(s)$ to differentiate it from those along the first ray $E_{T_1}(s)$ and $\varphi_1(s)$. To determine the approximate matricant for the second ray first notice that although E_2 and ψ_2 are assumed to be constant along the path within ring 2, $E_{T_2}(s)$ and $\varphi_2(s)$ are still functions of s. To avoid steps that would require numerical integration in the algorithm we further approximate the electric field distribution so that $E_{T_2}(s)$ and $\varphi_2(s)$ are constant on the path within a ring and approximately equal to their values at the middle point (o_{22}). Then between points a_{22} and $\overline{a}_{22}$ shown in Figure 6.2

$$E_{T_2}(s)|_{-s_{22}\le s\le s_{22}} \approx E_{T_2}(o_{22}) \equiv E_{T_{22}} \tag{6.7}$$

$$\varphi_2(s)|_{-s_{22}\le s\le s_{22}} \approx \varphi_2(o_{22}) \equiv \varphi_{22} \tag{6.8}$$

where s_{22} is the s-coordinate of the point a_{22} and we use the double subscripts in $E_{T_{22}}$ and φ_{22} to indicate the ray and the ring numbers respectively.

Now that $E_{T_2}(s)$ and $\varphi_2(s)$ are approximated to be constants the approximate matricant for the second ray follows from (3.83)

$$\mathbf{\Omega}_{a_2} \equiv \mathbf{\Omega}_{\mathbf{c}_{22}} = \mathbf{S}(-\varphi_{22})\mathbf{G}(\gamma_{c_{22}})\mathbf{S}(\varphi_{22}) \tag{6.9}$$

where $\mathbf{\Omega}_{\mathbf{c}_{22}}$ is the matricant between the points a_{22} and $\overline{a}_{22}$ defined in Fig. 6.2 to be the exit and entrance points of the light into the non-zero field region with light path length $l_{22} = 2s_{22}$ and $\gamma_{c_{22}} = \pi B E_{T_{22}}^2 l_{22}$ is the corresponding characteristic phase retardation. The zero-field region does not effect the approximate matricant.

On the point o_{22} the axisymmetry of the field requires that E_s is zero hence

$$E_{T_{22}} = E_2 \tag{6.10}$$

$$\varphi_{22} = \psi_2 \tag{6.11}$$

consequently (6.9) reduces to

$$\mathbf{\Omega}_{a_2} = \mathbf{S}(-\psi_2)\mathbf{G}(\pi B E_2^2 l_{22})\mathbf{S}(\psi_2) \tag{6.12}$$

Comparing $\mathbf{\Omega}_{a_2}$ to $\mathbf{\Omega}_{e_2}$ in (6.6) yields E_2 and ψ_2 in terms of α_2 and γ_2

$$E_2 = \sqrt{\frac{\gamma_2}{\pi B l_{22}}} \tag{6.13}$$

$$\psi_2 = \alpha_2 \tag{6.14}$$

With E_2 and ψ_2 recovered the next step is to recover E_1 and ψ_1 using E_2, ψ_2, α_1 and γ_1. Notice that there are three regions through which the first ray passes. To obtain the approximate matricant for the first ray, $E_{T_1}(s)$ and $\varphi_1(s)$ are approximated by their values at the respective middle points of the paths inside the regions ($\overline{o}_{12}$, o_{11} and o_{12}). Then between the points a_{11} and $\overline{a}_{11}$

$$E_{T_1}(s)|_{-s_{11}\le s\le s_{11}} \approx E_{T_1}(o_{11}) \equiv E_{T_{11}} \tag{6.15}$$

$$\varphi_1(s)|_{-s_{11}\le s\le s_{11}} \approx \varphi_1(o_{11}) \equiv \varphi_{11} \tag{6.16}$$

where s_{11} is the s-coordinate of the point a_{11}. Again, the condition of axisymmetry has E_s zero on o_{11} hence

$$E_{T_{11}} = E_1 \tag{6.17}$$

$$\varphi_{11} = \psi_1 \tag{6.18}$$

Thus

$$\mathbf{\Omega}_{\mathbf{c}_{11}} = \mathbf{S}(-\varphi_{11})\mathbf{G}(\gamma_{c_{11}})\mathbf{S}(\varphi_{11}) = \mathbf{S}(-\varphi_{11})\mathbf{G}(\pi B E_{T_1}^2 l_{11})\mathbf{S}(\varphi_{11}) \tag{6.19}$$

$$= \mathbf{S}(-\psi_1)\mathbf{G}(\pi B E_1^2 l_{11})\mathbf{S}(\psi_1) \tag{6.20}$$

Again with the midpoint approximation, between the points a_{11} and a_{12}

$$E_{T_1}(s)|_{s_{11}<s\le s_{12}} \approx E_{T_1}(o_{12}) \equiv E_{T_{12}} \tag{6.21}$$

$$\varphi_1(s)|_{s_{11}<s\le s_{12}} \approx \varphi_1(o_{12}) \equiv \varphi_{12} \tag{6.22}$$

where s_{11} and s_{12} are respectively the s-coordinates of the points a_{11} and a_{12}. With

θ_{12} defined in Figure 6.2, $E_{T_{12}}$ and φ_{12} can be found in terms of E_2 and ψ_2 using (6.1) and (6.3)

$$E_{T_{12}}^2 \equiv E_{T_1}^2(o_{12}) = E_z^2(o_{12}) + E_p^2(o_{12}) \tag{6.23}$$

$$= E_2^2\big(\cos^2\psi_2 + \sin^2\psi_2\cos^2\theta_{12}\big) \tag{6.24}$$

$$\tan\varphi_{12} = \frac{E_p(o_{12})}{E_z(o_{12})} = \frac{E_2\sin\psi_2\cos\theta_{12}}{E_2\cos\psi_2} \tag{6.25}$$

$$= \tan\psi_2\cos\theta_{12} \tag{6.26}$$

Note that (6.26) is just a restatement of (6.4) for a particular θ. The matricant between a_{11} and a_{12} can be written in terms of $E_{T_{12}}$ and θ_{12}

$$\mathbf{\Omega}_{\mathbf{c}_{12}} = \mathbf{S}(-\varphi_{12})\mathbf{G}(\gamma_{c_{12}})\mathbf{S}(\varphi_{12}) = \mathbf{S}(-\varphi_{12})\mathbf{G}(\pi B E_{T_{12}}^2 l_{12})\mathbf{S}(\varphi_{12}) \tag{6.27}$$

The approximate matricant $\mathbf{\Omega}_{\mathbf{c}_{1\overline{2}}}$ between $\overline{a}_{11}$ and $\overline{a}_{12}$ can be written in terms of $\mathbf{\Omega}_{\mathbf{c}_{12}}$ using the properties of symmetric media in (3.67)

$$\mathbf{\Omega}_{\mathbf{c}_{1\overline{2}}} = \mathbf{\Omega}_{\mathbf{c}_{12}}^{\mathrm{T}} = \mathbf{\Omega}_{\mathbf{c}_{12}} \tag{6.28}$$

where the second equality follows from (3.86) which states that $\mathbf{\Omega}_{\mathbf{c}_{12}}$ is symmetric. Using (6.28) the approximate matricant for the first ray follows as

$$\mathbf{\Omega}_{a_1} = \mathbf{\Omega}_{\mathbf{c}_{12}}\mathbf{\Omega}_{\mathbf{c}_{11}}\mathbf{\Omega}_{\mathbf{c}_{1\overline{2}}} = \mathbf{\Omega}_{\mathbf{c}_{12}}\mathbf{\Omega}_{\mathbf{c}_{11}}\mathbf{\Omega}_{\mathbf{c}_{12}} \tag{6.29}$$

or explicitly in terms of rotator and retarder matrices

$$\mathbf{\Omega}_{a_1} = \mathbf{S}(-\varphi_{12})\mathbf{G}(\gamma_{c_{12}})\mathbf{S}(\varphi_{12})\mathbf{S}(-\psi_1)\mathbf{G}(\pi B E_1^2 l_{11})\mathbf{S}(\psi_1)\mathbf{S}(-\varphi_{12})\mathbf{G}(\gamma_{c_{12}})\mathbf{S}(\varphi_{12}) \tag{6.30}$$

Comparing $\mathbf{\Omega}_{a_1}$ and $\mathbf{\Omega}_{e_1}$ in (6.5) results in

$$\mathbf{S}(-\psi_1)\mathbf{G}(\pi B E_1^2 l_{11})\mathbf{S}(\psi_1) = \mathbf{S}(-\varphi_{12})\mathbf{G}(-\gamma_{c_{12}})\mathbf{S}(\varphi_{12})\mathbf{S}(-\alpha_1)\mathbf{G}(\gamma_1)\mathbf{S}(\alpha_1)$$
$$\mathbf{S}(-\varphi_{12})\mathbf{G}(-\gamma_{c_{12}})\mathbf{S}(\varphi_{12}) \tag{6.31}$$

where we used (3.87). We define $\mathbf{A}_{\mathbf{rhs}}$ to be the result of the matrix multiplication on

the right hand side of (6.31). Then

$$\mathbf{A_{rhs}} = \begin{bmatrix} \mathrm{p_{rhs}} - i\mathrm{q_{rhs}} & -i\mathrm{t_{rhs}} \\ -i\mathrm{t_{rhs}} & \mathrm{p_{rhs}} + i\mathrm{q_{rhs}} \end{bmatrix} \tag{6.32}$$

where $\mathrm{p_{rhs}}$, $\mathrm{q_{rhs}}$, and $\mathrm{t_{rhs}}$ are found by explicit multiplications

$$\mathrm{p_{rhs}} = \cos\gamma_1 \cos 2\gamma_{c12} - \sin\gamma_1 \sin\gamma_{c12} \cos 2(\alpha_1 - \varphi_{12}) \tag{6.33a}$$

$$\begin{aligned} \mathrm{q_{rhs}} = &\Big[\cos\gamma_1 \sin 2\gamma_{c12} + \sin\gamma_1 \cos 2\gamma_{c12} \cos 2(\alpha_1 - \varphi_{12})\Big] \cos 2\varphi_{12} \\ &- \sin\gamma_1 \sin 2(\alpha_1 - \varphi_{12}) \sin 2\varphi_{12} \end{aligned} \tag{6.33b}$$

$$\begin{aligned} \mathrm{t_{rhs}} = &\Big[\cos\gamma_1 \sin 2\gamma_{c12} + \sin\gamma_1 \cos 2\gamma_{c12} \cos 2(\alpha_1 - \varphi_{12})\Big] \sin 2\varphi_{12} \\ &+ \sin\gamma_1 \sin 2(\alpha_1 - \varphi_{12}) \cos 2\varphi_{12} \end{aligned} \tag{6.33c}$$

The left hand side of (6.31) which we denote by $\mathbf{A_{lhs}}$ can also be found by explicit multiplications

$$\mathbf{A_{lhs}} = \begin{bmatrix} \cos\gamma_{c11} - i\sin\gamma_{c11}\cos 2\psi & -i\sin\gamma_{c11}\sin 2\psi \\ -i\sin\gamma_{c11}\sin 2\psi & \cos\gamma_{c11} - i\sin\gamma_{c11}\cos 2\psi \end{bmatrix} \tag{6.34}$$

where $\gamma_{c11} = \pi B E_1^2 l_{11}$. Comparing (6.34) to (6.32) yields E_1 and ψ_1

$$E_1 = \sqrt{\frac{\arccos \mathrm{p_{rhs}}}{\pi B l_{11}}} \tag{6.35}$$

$$\psi_1 = \arctan(\mathrm{t_{rhs}}/\mathrm{q_{rhs}}) \tag{6.36}$$

This concludes the recovery of E_1, E_2, ψ_1, ψ_2 from α_1, γ_1, α_2 and γ_2.

6.2.2 For Arbitrary Axisymmetric Kerr Media

The method is easily generalized to arbitrary axisymmetric electric field distributions. The distribution is first discretized into slices parallel to the *ps*-plane at constant values of z and each slice is radially discretized into the n rings shown in Figure 6.3. There are $2n$ unknowns (E_i, ψ_i, $i = 1, 2, \cdots n$) and $2n$ measured values (α_i, γ_i, $i = 1, 2, \cdots n$) for each slice. Like the two layer example geometry the method begins with the outermost layer. In the i'th step E and ψ of all the ($i + 1$ to n) outer layers are known and E_i

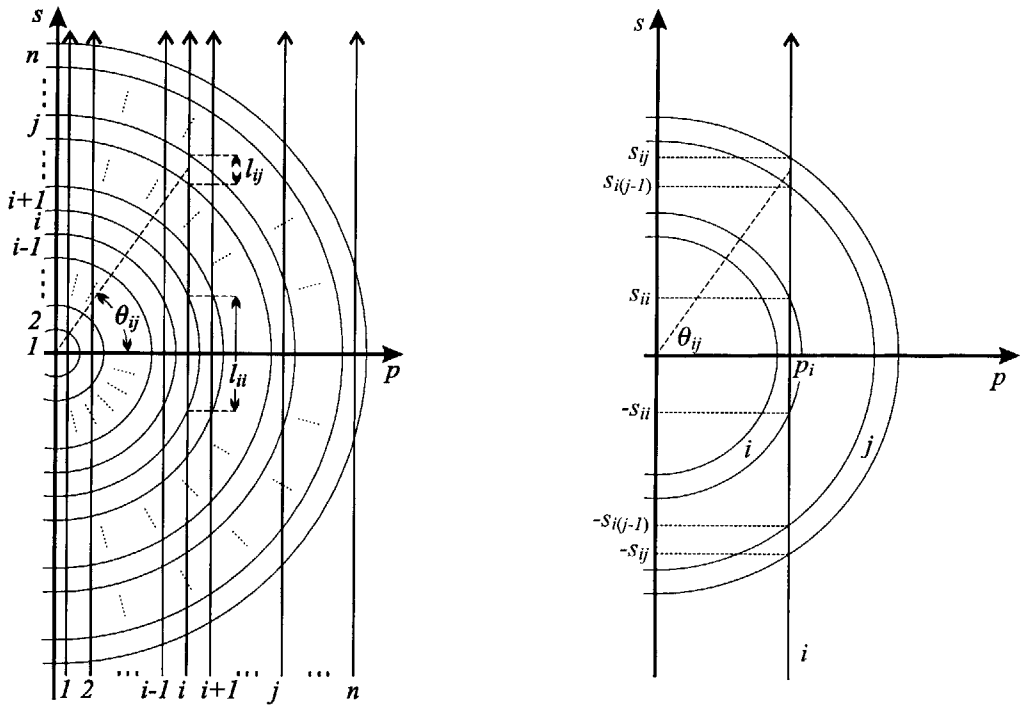

(a) n-Layer Discretization

(b) ps Coordinates of Important Points

Figure 6.3: The discretization of a general axisymmetric electric field distribution for the onion peeling method.

and ψ_i are found from

$$\mathbf{S}(-\psi_i)\mathbf{G}(\pi B E_i^2 l_{ii})\mathbf{S}(\psi_i) = \left[\prod_{j=i+1}^{n} \mathbf{\Omega}_{\mathbf{c}_{ij}}^{-1}\right] \times \mathbf{\Omega}_{\mathbf{e}_i} \times \left[\prod_{j=n}^{i+1} \mathbf{\Omega}_{\mathbf{c}_{ij}}^{-1}\right] \tag{6.37}$$

$$= \left[\prod_{j=i+1}^{n} \mathbf{\Omega}_{\mathbf{c}_{ij}}^{*}\right] \times \mathbf{\Omega}_{\mathbf{e}_i} \times \left[\prod_{j=n}^{i+1} \mathbf{\Omega}_{\mathbf{c}_{ij}}^{*}\right] \tag{6.38}$$

where $\prod$ denotes product and $\mathbf{\Omega}_{\mathbf{c}}$ is symmetric and unitary. Equation (6.38) explicitly is

$$\begin{aligned}
&\mathbf{S}(-\psi_i)\mathbf{G}(\pi B E_i^2 l_{ii})\mathbf{S}(\psi_i) = \\
&\quad \mathbf{S}(-\varphi_{i(i+1)})\mathbf{G}(-\gamma_{c_{i(i+1)}})\mathbf{S}(\varphi_{i(i+1)})\mathbf{S}(-\varphi_{i(i+2)})\mathbf{G}(-\gamma_{c_{i(i+2)}})\mathbf{S}(\varphi_{i(i+2)})\cdots \\
&\quad \mathbf{S}(-\varphi_{in})\mathbf{G}(-\gamma_{c_{in}})\mathbf{S}(\varphi_{in})\mathbf{S}(-\alpha_i)\mathbf{G}(\gamma_i)\mathbf{S}(\alpha_i)\mathbf{S}(-\varphi_{in})\mathbf{G}(-\gamma_{c_{in}})\mathbf{S}(\varphi_{in})
\end{aligned}$$

$$\mathbf{S}(-\varphi_{i(n-1)})\mathbf{G}(-\gamma_{c_{i(n-1)}})\mathbf{S}(\varphi_{i(n-1)})\cdots\mathbf{S}(-\varphi_{i(i+1)})\mathbf{G}(-\gamma_{c_{i(i+1)}})\mathbf{S}(\varphi_{i(i+1)}) \quad (6.39)$$

Here $\mathbf{\Omega}_{\mathbf{c}_{ij}}^{-1}$ follows from (3.87) as

$$\mathbf{\Omega}_{\mathbf{c}_{ij}}^{-1} = \mathbf{\Omega}_{\mathbf{c}_{ij}}^{*} = \mathbf{S}\big(-\varphi_{ij}\big)\mathbf{G}\big(-\pi B E_{T_{ij}}^{2} l_{ij}\big)\mathbf{S}\big(\varphi_{ij}\big) \quad (6.40)$$

where

$$E_{T_{ij}}^{2} = E_{j}^{2}(\cos^{2}\psi_{j} + \sin^{2}\psi_{j}\cos^{2}\theta_{ij}) \quad (6.41)$$

$$\varphi_{ij} = \arctan(\tan\psi_{j}\cos\theta_{ij}) \quad (6.42)$$

and θ_{ij} and l_{ij} are shown in Figure 6.3 and can be expressed in terms of the coordinates as

$$l_{ij} = \begin{cases} s_{ij} - s_{i(j-1)} & i < j \\ 2s_{ii} & i = j \end{cases} \quad (6.43)$$

$$\cos\theta_{ij} = \frac{p_{i}}{\sqrt{p_{i}^{2} + \left[0.5(s_{ij} + s_{i(j-1)})\right]^{2}}} \quad (6.44)$$

We can express p_i and s_{ij} in terms of the discretization layer thickness Δr

$$p_{i} = (i - 0.5)\Delta r \quad (6.45)$$

$$s_{ij} = \left(\sqrt{j^{2} - (i - 0.5)^{2}}\right)\Delta r \quad (6.46)$$

Notice that the layer thickness Δr is equal to the distance between consecutive measurements $\Delta p = p_{i+1} - p_i$.

We note that the onion peeling method can recover the direction of the electric field up to a multiple of π. Thus the sign of the components of the electric field can not be determined from the algorithm alone. This is the direct result of the quadratic dependence of the Kerr effect on the applied electric field magnitude. This however is not a serious problem since the sign of the electric field components is often determined by the physics of the problem.

6.3 Application Of The Algorithm

In this section we apply the onion peeling algorithm to synthetic data for the finite point/plane electrode geometry described in Appendix C when the medium is nitrobenzene. The space charge distribution chosen is described in Figure C.4 with $\tilde{\rho}_0 = 0.12$ C/m^3. Measurement sampling rate Δp and discretization layer thickness Δr are chosen to be 0.0001 mm.

Figure 6.4 shows the data at three values of $z = 1$ mm, $z = 2$ mm and $z = 2.5$ mm. Plots show the general characteristics of γ_s and α_s discussed in Section 5.7.2. In particular α_s decreases rapidly near the maxima and minima of γ_s.

Figure 6.5 compares the reconstructed electric field distributions at $z = 1$ mm, $z = 2$ mm and $z = 2.5$ mm using the onion peeling method from data shown in Figure 6.4 to theoretical finite element method calculated field distributions. We only show the region between $r = 0$ mm and $r = 4$ mm. In the region between $r = 4$ mm and $r = 10$ mm the algorithm reconstructs the electric field almost perfectly for all three z values. Between $r = 0$ mm and $r = 4$ mm at $z = 1$ mm there is practically no difference between the numerical electric field and reconstructed electric field. At $z = 2$ mm there are slight differences although the overall match is good while at $z = 2.5$ the reconstructed electric field, especially the r component, is in serious disagreement with the numerical electric field. A close look at Figure 6.4 and Figure 6.5 reveals that the point that the disagreements begin corresponds to the steep decrease in α_s at around $p = 1$ mm.

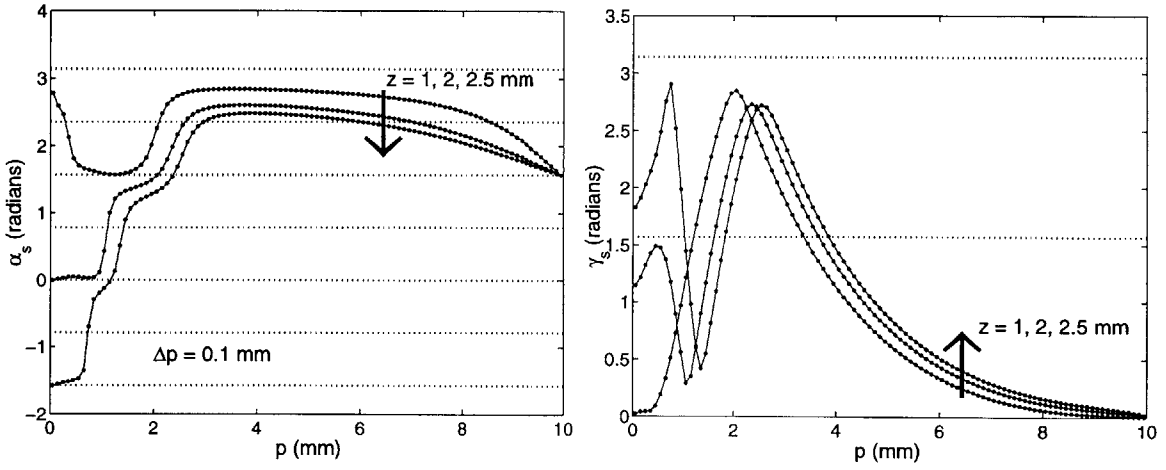

Figure 6.4: Calculated characteristic parameter data for the system described in Appendix C.

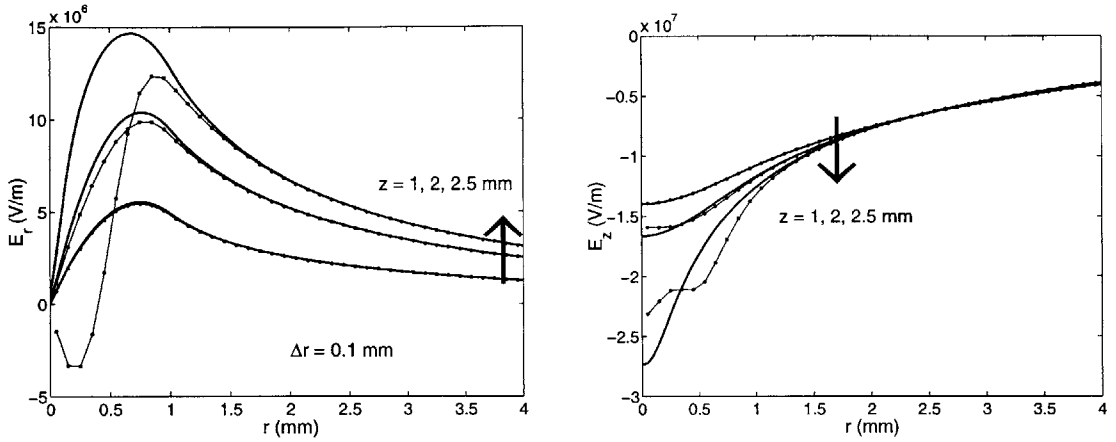

Figure 6.5: Reconstructed electric field components from the characteristic parameter data in Figure 6.4 (dotted lines) compared to theoretical space charge free electric fields calculated from the finite element method (solid lines).

In Figure 6.6 we show reconstructions at $z = 2.5$ mm for different sampling rates. When the sampling rate is increased the reconstructed electric field progressively approaches the theoretical electric field. We conclude that for highly birefringent media the onion peeling method performs well when the data sampling rate is high enough to characterize the steep decreases in α_s that occur around the maxima and minima of γ_s. When the electric field magnitude distribution is small enough or the medium is weakly birefringent so that the steep decreases in α_s do not exist, the onion peeling method almost perfectly recovers the electric field for perfect artificial data.

Note that a 1 μm sampling rate is not realistic since it is too close to the wavelength of typical laser light used in Kerr electro-optic measurements ($\lambda \approx 600$ nm). However also notice that the point $r = 0$ and $z = 2.5$ mm is the point where the electric field changes most rapidly and has the highest magnitude. For planes below or above this extreme case the onion peeling method will work with much higher sampling rates as exemplified for the $z = 2$ and $z = 1$ mm planes in Figure 6.5.

6.4 Reformulation For Weak Kerr Media

6.4.1 Description

The onion peeling method can be reformulated for weak Kerr media for which (4.68) is valid. In this formulation the assumption that for a particular ray the transverse

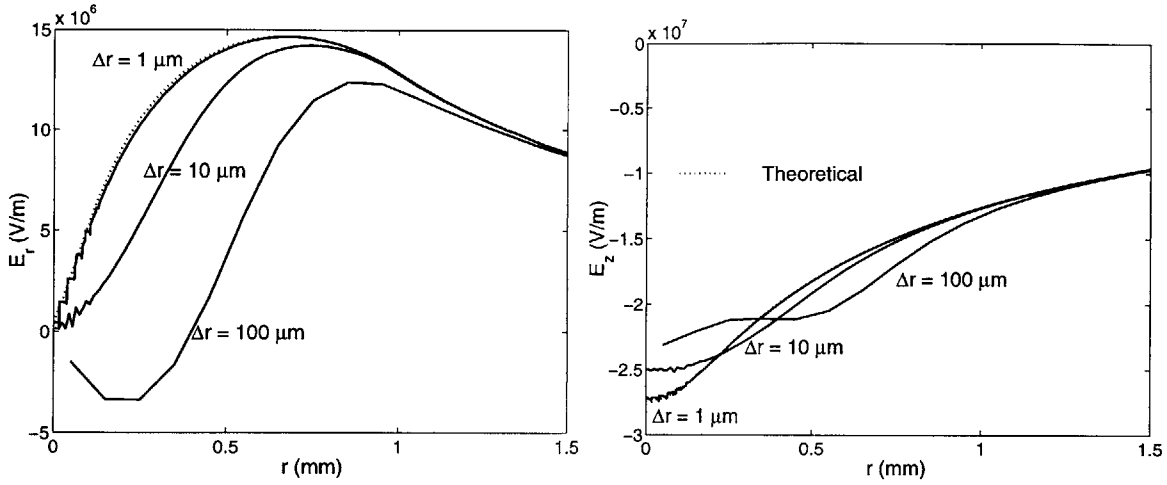

Figure 6.6: Reconstructed electric field components for different spatial sampling rates at $z = 2.5$ mm. For a 1 μm sampling rate the onion peeling algorithm almost perfectly recovers the theoretical electric field.

component of the electric field is constant within each layer is unnecessary. Also the matrix multiplications are avoided.

We begin by expressing (4.68) in index form for each measurement in Figure 6.3.

$$\gamma_i \cos 2\alpha_i = \pi B \int_{\mathcal{L}_i} \left[E_z^2(s) - E_p^2(s) \right] ds \tag{6.47a}$$

$$\gamma_i \sin 2\alpha_i = \pi B \int_{\mathcal{L}_i} 2E_z(s)E_p(s)\, ds \tag{6.47b}$$

where $\mathcal{L}_i$ denotes the path of the ith light ray. We define s_{ij} to be the s coordinate of the point where the ith ray emerges from the jth layer in the positive s-axis as shown in Figure 6.3. The exact right hand side of (6.47) is then approximated in terms of the discretization as

$$\begin{aligned} \gamma_i \cos 2\alpha_i \approx \pi B \sum_{j=N}^{i+1} \int_{-s_{ij}}^{-s_{i(j-1)}} \left[E_{z_j}^2 - E_{r_j}^2 \cos^2\theta(s) \right] ds \\ + \pi B \int_{-s_{ii}}^{s_{ii}} \left[E_{z_i}^2 - E_{r_i}^2 \cos^2\theta(s) \right] ds \\ + \pi B \sum_{j=i+1}^{N} \int_{s_{i(j-1)}}^{s_{ij}} \left[E_{z_j}^2 - E_{r_j}^2 \cos^2\theta(s) \right] ds \end{aligned} \tag{6.48a}$$

$$\gamma_i \sin 2\alpha_i \approx \pi B \sum_{j=N}^{i+1} \int_{-s_{ij}}^{-s_{i(j-1)}} 2E_{z_j} E_{r_j} \cos\theta(s)\, ds + \pi B \int_{-s_{ii}}^{s_{ii}} 2E_{z_i} E_{r_i} \cos\theta(s)\, ds + \pi B \sum_{j=i+1}^{N} \int_{s_{i(j-1)}}^{s_{ij}} 2E_{z_j} E_{r_j} \cos\theta(s)\, ds \tag{6.48b}$$

In (6.48) E_{z_i} and E_{r_i} are constants and the integrals involving $\cos\theta(s) = p/\sqrt{p^2+s^2}$ (see Figure 6.2) can be evaluated analytically

$$\int \cos^2\theta(s)\, ds = \int \frac{p^2\, ds}{p^2+s^2} = p \arctan\frac{s}{p} \tag{6.49a}$$

$$\int \cos\theta(s)\, ds = \int \frac{p\, ds}{\sqrt{p^2+s^2}} = p \ln\left[\sqrt{p^2+s^2}+s\right] \tag{6.49b}$$

We define

$$\mathcal{U}_{ij} \equiv \begin{cases} p_i \left[\arctan\dfrac{s_{ij}}{p_i} - \arctan\dfrac{s_{i(j-1)}}{p_i}\right] & i<j \\ 2p_i \arctan\dfrac{s_{ii}}{p_i} & i=j \end{cases} \tag{6.50a}$$

$$\mathcal{V}_{ij} \equiv \begin{cases} 2p_i \ln\dfrac{\sqrt{p_i^2+s_{ij}^2}+s_{ij}}{\sqrt{p_i^2+s_{i(j-1)}^2}+s_{i(j-1)}} & i<j \\ 2p_i \ln\dfrac{\sqrt{p_i^2+s_{ii}^2}+s_{ii}}{\sqrt{p_i^2+s_{ii}^2}-s_{ii}} & i=j \end{cases} \tag{6.50b}$$

$$\mathcal{W}_{ij} \equiv \begin{cases} 2p_i \ln\dfrac{\sqrt{p_i^2+s_{i(j-1)}^2}-s_{i(j-1)}}{\sqrt{p_i^2+s_{ij}^2}-s_{ij}} & i<j \end{cases} \tag{6.50c}$$

Using (6.50) and (6.43), (6.48) is compactly written as

$$\gamma_i \cos 2\alpha_i \approx \pi B \left\{ l_{ii} E_{z_i}^2 - \mathcal{U}_{ii} E_{r_i}^2 + 2 \sum_{j=i+1}^{N} \left[l_{ij} E_{z_j}^2 - \mathcal{U}_{ij} E_{r_j}^2 \right] \right\} \tag{6.51a}$$

$$\gamma_i \sin 2\alpha_i \approx \pi B \left\{ \mathcal{V}_{ii} E_{z_i} E_{r_i} + \sum_{j=i+1}^{N} \left[\mathcal{V}_{ij} + \mathcal{W}_{ij}\right] E_{z_j} E_{r_j} \right\} \tag{6.51b}$$

Equation (6.51) can now be used to reformulate the onion peeling method for weak

Kerr media. As in the previous section the method begins with the outermost ring and reconstructs each of the inner rings recursively. At the ith step all the discrete electric field values outside the ith ring are known and (6.51) yields

$$l_{ii}E_{z_i}^2 - \mathcal{U}_{ii}E_{r_i}^2 = \mathcal{A}_i \tag{6.52a}$$

$$\mathcal{V}_{ii}E_{z_i}E_{r_i} = \mathcal{B}_i \tag{6.52b}$$

where

$$\mathcal{A}_i = \frac{\gamma_i \cos 2\alpha_i}{\pi B} - 2\sum_{j=i+1}^{N}\left[l_{ij}E_{z_j}^2 - \mathcal{U}_{ij}E_{r_j}^2\right] \tag{6.53}$$

$$\mathcal{B}_i = \frac{\gamma_i \sin 2\alpha_i}{\pi B} - \sum_{j=i+1}^{N}\left[\mathcal{V}_{ij} + \mathcal{W}_{ij}\right]E_{z_j}E_{r_j} \tag{6.54}$$

Assuming E_{z_i} is non-zero, (6.52) can be solved to yield

$$l_{ii}\mathcal{V}_{ii}^2E_{z_i}^4 - \mathcal{A}_i\mathcal{V}_{ii}^2E_{z_i}^2 - \mathcal{U}_{ii}\mathcal{B}_i^2 = 0 \tag{6.55}$$

The positive solution of the quadratic algebraic equation in (6.55) yields $E_{z_i}^2$. Thus

$$E_{z_i} = \pm\left(\frac{\mathcal{A}_i\mathcal{V}_{ii}^2 + \sqrt{\mathcal{A}_i^2\mathcal{V}_{ii}^4 + 4l_{ii}\mathcal{V}_{ii}^2\mathcal{U}_{ii}\mathcal{B}_i^2}}{2l_{ii}\mathcal{V}_{ii}^2}\right)^{\frac{1}{2}} \tag{6.56}$$

The sign uncertainity in (6.56)is resolved by physical considerations. Once E_{z_i} is found E_{r_i} can be found from (6.52).

6.4.2 Application Of The Algorithm

Other numerical experiments similar to those in Section 6.3 using the finite point/plane geometry of Appendix C with the weakly birefringent transformer oil as the dielectric show that the algorithm described almost perfectly recovers the electric field from perfect data without significant differences between the theory and reconstructions from perfect data due to finite spatial sampling rate. Figure 6.10 in Section 6.6 shows some representative reconstructions from perfect data in Figure 6.9. The impact of noise is also illustrated in these figures and discussed in Section 6.6.

6.5 Missing Outer Ring Data

The case study geometry of the previous two sections, which was the finite point/plane electrode geometry of Appendix C, differs from typical Kerr electro-optic experimental set-ups by being confined to a region 10 mm in radius. We use this geometry to keep the numerical analysis simple. In current experiments this radius is typically an order of magnitude higher. However, as discussed in Appendix C the 10 mm radial extent case study geometry adequately represents the electric field distributions of large radial extent point/plane geometries as the 10 mm radial extent is large enough so that the right-hand ground wall does not appreciably effect the electric field near the needle and the space charge near the needle does not appreciably effect the electric field near the wall. For the experimental setup used at MIT at the time of this work, the test chamber illustrated in Figure 1.1 acted as the surrounding electrode with 25 cm radius. If the full data set in the whole 25 cm region was available, the characteristics of the onion peeling method reconstructed electric fields would remain the same with the case studies of the previous two sections. However measurements could only be taken in the region up to $r = 12$ mm due to the small window size which is the most interesting region near the point electrode tip. For such data sets, performance of the direct application of the onion peeling method is degraded due to the assumption that outside the solution region the electric field vanishes.

To illustrate these effects we use an infinite extent point/plane electrode geometry (see Appendix A) with tip plane distance of 5 mm, needle radius of curvature of 0.55 mm and an applied voltage of 20 kV. General characteristics of the measurements at constant values of z are illustrated in Figure 6.7 for different values of z. It is clear from the plots that the electric field magnitude is not negligible outside the data range of 12 mm as γ_s and α_s have significant values near $p = 12$ mm.

To show the effects of the assumption that the electric field vanishes outside the reconstruction region of the onion peeling method we use the measurements at $z = 3$ mm with a sampling rate of $\Delta p = 0.5$ mm. The direct application of the weak medium onion peeling algorithm results in plus markers in Figure 6.8 which also provides the plots for the analytical solution of the electric field components. The other two markers are the results of improved algorithms discussed in Section 6.5.1 and Section 6.5.2.

The results show that the impact of the assumption that the electric field vanishes outside $r = 12$ mm is important. Although the difference between the analytical and reconstructed electric field components progressively come closer towards $r = 0$ mm

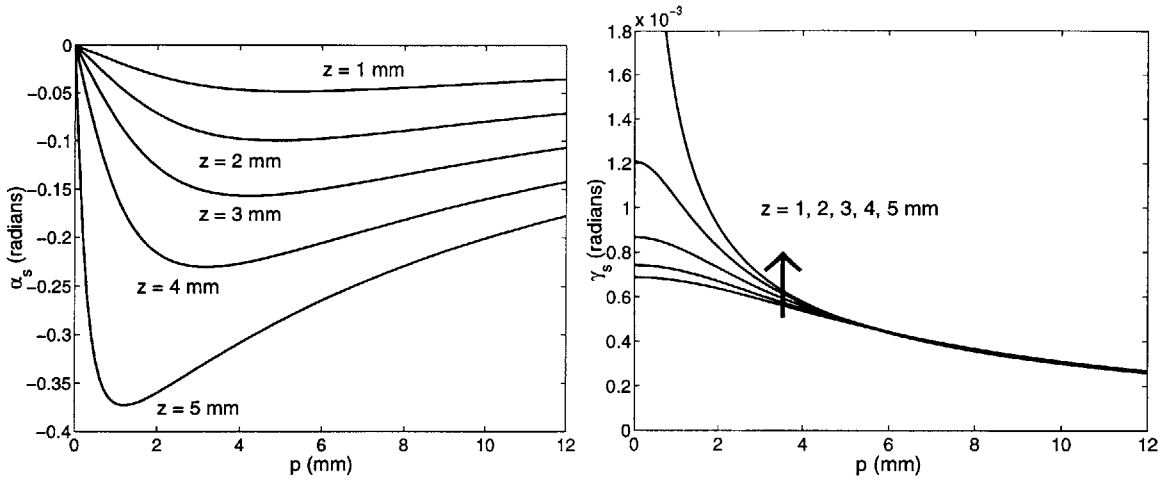

Figure 6.7: Artificial Kerr electro-optic measurements for infinite point/plane electrodes with tip-plane distance of 5 mm and point radius of curvature of 0.55 mm. The medium is transformer oil with applied voltage of 20 kV.

there still remains a noticable difference between z components. The figure also shows that the reconstructed electric field is not reliable for $r \gtrapprox 6$ mm.

One immediate solution to the problem is to use space charge free solutions that are available analytically and numerically. For point/plane geometries the space charge is typically confined around the needle tip axis. As illustrated in Appendix C the solutions converge to those of the space charge free case for large r. If the region for which no measurement is available is distant enough one can use the space charge free solutions to obtain artificial measurements. The onion peeling method can then be directly applied to the full data set which now consists of actual data in the measurement zone and artificial data outside the measurement zone.

Use of space charge free solutions requires software for numerically finding the electric field distribution for the geometry and using it for numerical integrations necessary to find matricants. Automation of such a procedure is difficult with commercial software and for that reason we developed our custom software for this work. Still, methods that decrease the impact of the end effects without using space charge free solutions might be helpful if the modelling of the geometry under investigation proves difficult or if the space charge effects outside the measurement zone are not negligible. In the next two sections we propose two ways to decrease these end ring effects.

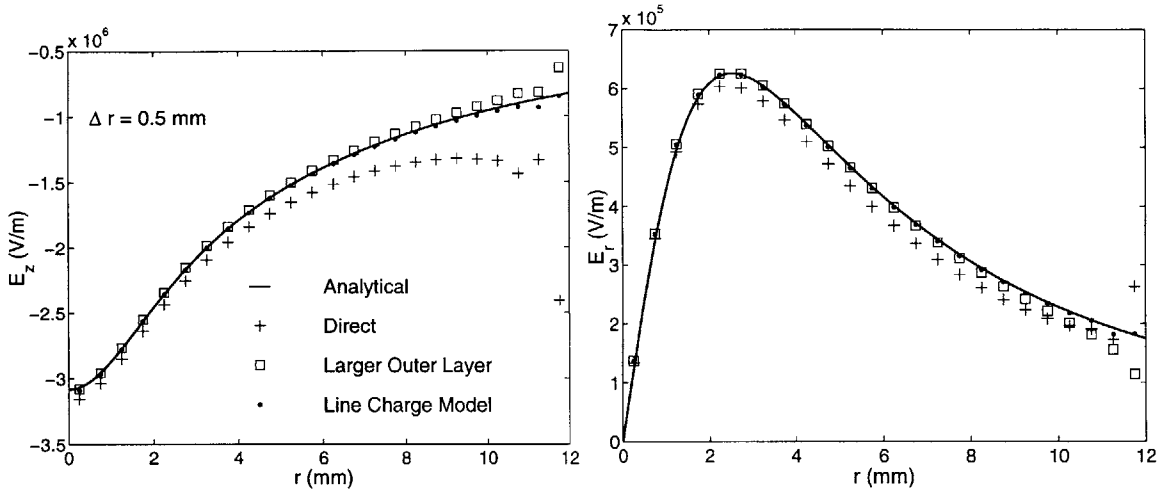

Figure 6.8: Onion peeling method for various reconstruction methods of electric field components from $z = 3$ mm data in Figure 6.7. The analytical electric field components are also shown for comparison purposes.

6.5.1 Larger Outer Ring

It is clear from direct application of the onion peeling method in Figure 6.8 that the electric field magnitude on the outer ring is much larger than the analytical. This is the direct result of the assumption that the electric field vanishes outside. In effect with this assumption the electric field distribution of the outside region is modelled by a single thin ring.

To improve the modelling of the outside region one immediate method is to use an outer layer with thickness larger than the discretization thickness. With such a layer the onion peeling algorithm remains the same except (6.46) is replaced by

$$s_{ij} = \begin{cases} \left(\sqrt{j^2 - (i-0.5)^2}\right) \Delta r & j \neq n \\ \left(\sqrt{\xi^2 - (i-0.5)^2}\right) \Delta r & j = n \end{cases} \tag{6.57}$$

where ξ is the normalized radius of the outer ring which is much larger than the discretization elements n.

It is clear that a larger outer ring decreases the magnitude of the reconstructed electric field at the outmost layer. The thickness of the layer however is still arbitrary and to be determined by some criterion. In this work we increase the thickness until the electric field magnitude monotonically decreases for the last three layers. The results of the algorithm with these modifications are shown in Figure 6.8 with square markers.

The improvements in the reconstruction results are remarkable.

6.5.2 Far Field Approximations

In the previous section we used a larger outer ring with constant electric field components. In this section we propose an infinite outermost ring with a simple postulated electric field distribution for large r. The geometry dictates the kind of postulates to be made. In Appendix D we provide a few simple charge singularities which can be used to model the large r electric field distributions.

For the infinite point/plane electrode case study of this section, we use the electric field distribution of a semi-infinite line charge above a ground plane which is described in Section D.3. In the large r limit of the distributions of (D.6), there are two parameters to be matched; the line charge density and z position. We find these parameters by comparing the characteristic parameters of the outer measurement to those resulting from (D.12). Thus the last ring determines the unknown parameters in the postulated electric field and for the inner rings the postulated electric field distribution serves to find the effects of the outer region in which previously the electric field distribution is assumed to vanish.

The results of the algorithm with these modifications are shown in Figure 6.8 with dot markers. Again there are significant improvements over the direct application of the onion peeling algorithm.

6.6 Impact Of Error

In this section we evaluate the performance of the onion peeling algorithm for imperfect measurements in transformer oil. The case geometry is identical to that of Section 6.3 except the medium is transformer oil instead of nitrobenzene. We use measurements at $z = 2$.

The errors introduced to γ_s and α_s are respectively denoted by $\Delta\gamma_s$ and $\Delta\alpha_s$ and are given by the following formulas

$$\Delta\gamma_s = 0.1 \times [\text{random}() - 0.5] \times \gamma_s \tag{6.58a}$$

$$\Delta\alpha_s = 0.1 \times [\text{random}() - 0.5] \times \alpha_s \tag{6.58b}$$

where random() denotes a random function generator which generates random numbers

between 0 and 1. In this work we use standard C/C++ routine rand() which, for a given seed, generates deterministic number sequences which emulate random numbers.

Figure 6.9 (left) shows the characteristic parameters α_s and γ_s with and without the error described in (6.58). Figure 6.10 shows the reconstructed electric field components both from perfect data and from error introduced data. The electric field components reconstructed from perfect data match almost perfectly with the numerical electric field components available from the finite element method. The match in the presence of noise however is not very good. The results show that the five percent error introduced according to (6.58) results in errors as large as twenty percent near $r = 0$.

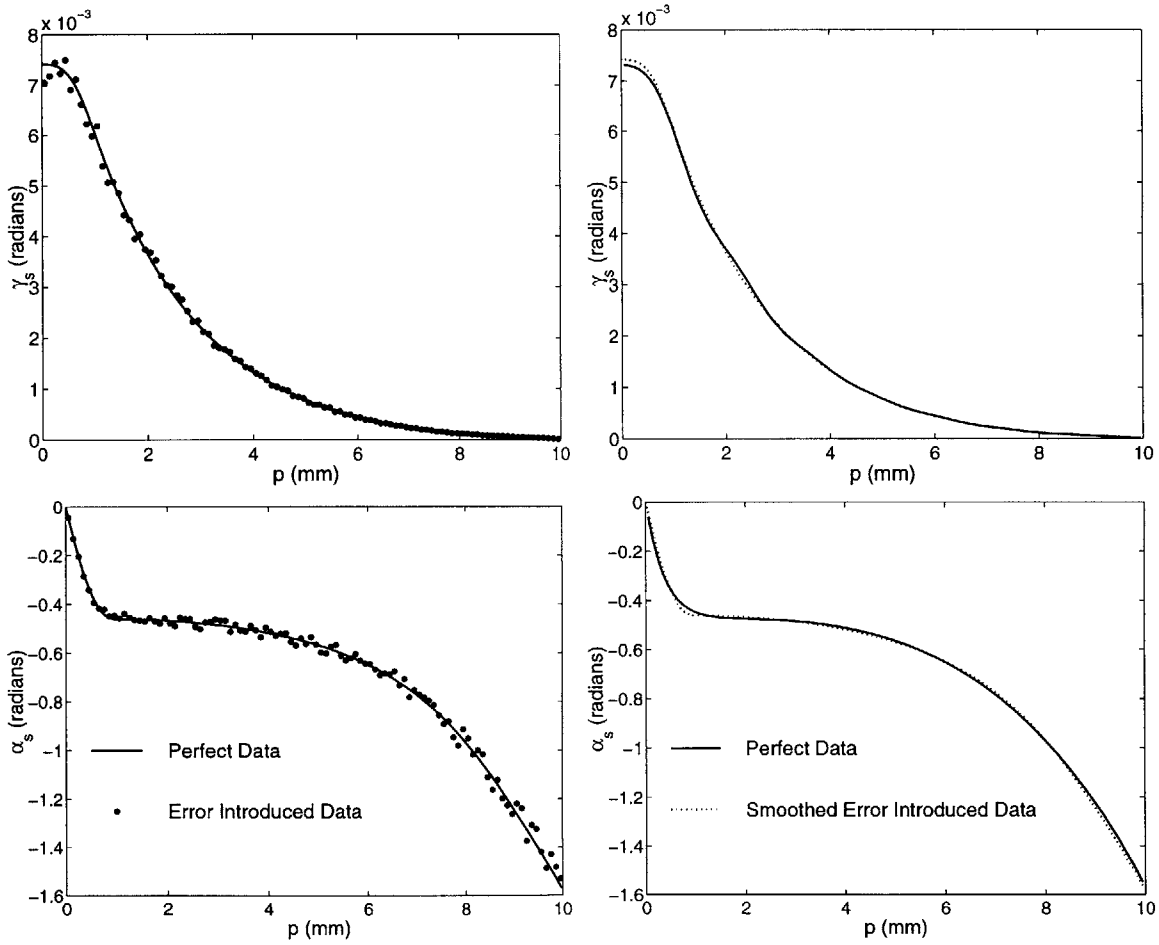

Figure 6.9: Kerr electro-optic synthetic data for the finite point/plane electrode geometry of Appendix C in transformer oil for perfect and error introduced data (left) and smoothed error introduced data (right). For γ_s data smoothing is done by using a perfect discrete low pass filter and for α_s data smoothing is done by using interpolating functions (exponential and fourth order polynomial).

To decrease the impact of the error we smooth the data as shown in Figure 6.9 (right). Smoothing can be done by various techniques. In Figure 6.9 we smooth γ_s data by using a perfect discrete low pass filter and we smooth α_s data by using interpolating functions. The functions employed are an exponential for the first nine data points and fourth order polynomials for the rest. The results of reconstruction using the smoothed data are shown in Figure 6.10 (right). The results are remarkably better and illustrate that the onion peeling methods can be reliably used to reconstruct the electric field in the presence of noise if sophisticated smoothing techniques are used.

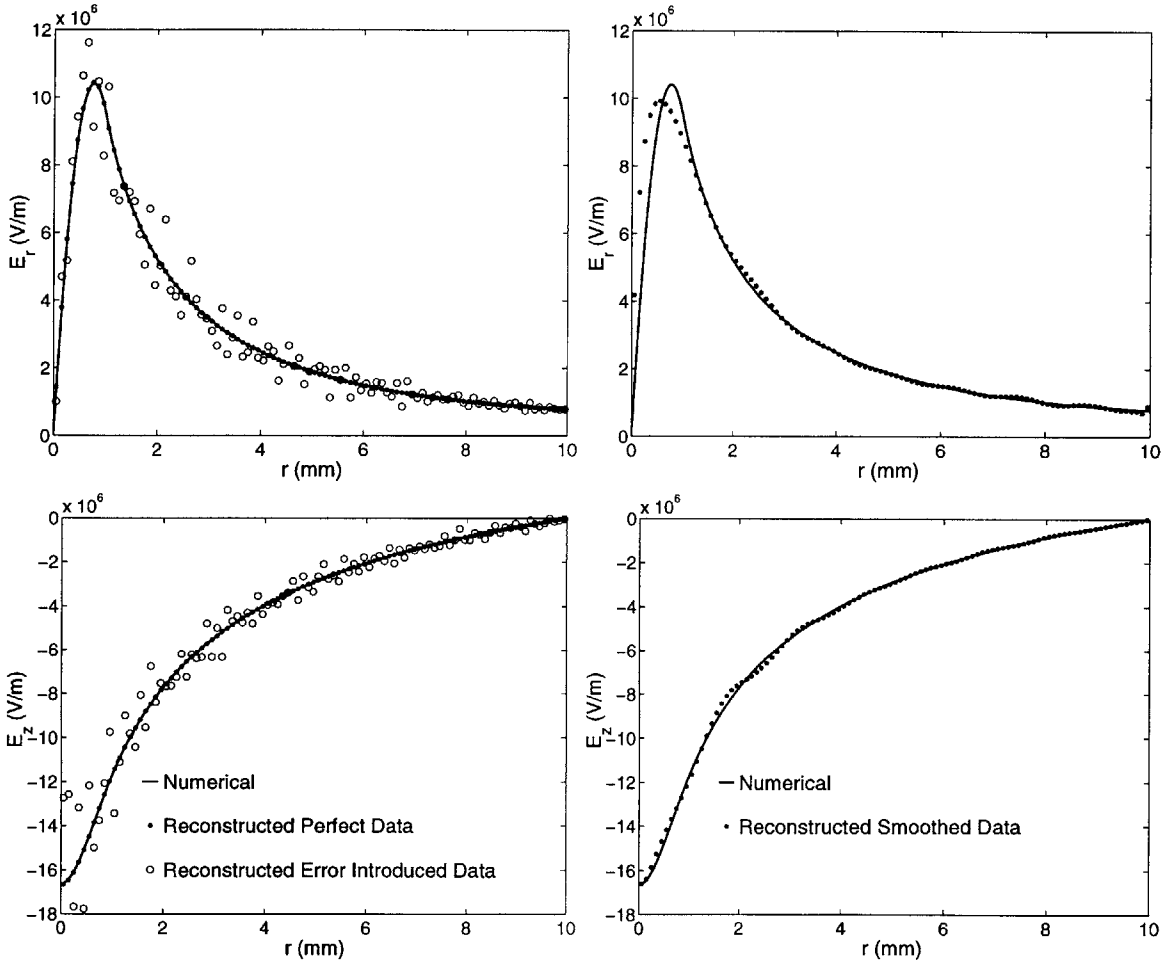

Figure 6.10: The effects of noise on the onion peeling method reconstructed electric field for reconstructed error introduced data (left) and reconstructed smoothed data (right).

Chapter 7

Algebraic Reconstruction Techniques For Kerr Electro-Optic Measurements

7.1 Introduction

Algebraic reconstruction techniques (ART hereafter) [51] have been used for scalar tomography for over two decades. The basic idea of ART is to discretize the plane, guess an initial solution for the quantity to be reconstructed in term of the discretization, and iteratively improve the solution by minimizing the difference between the predicted measurements based on the current solution and the actual measurements.

For most applications that utilize scalar tomography the performance of ART algorithms is typically worse than those that depend on transform methods (see Chapter 9). Yet, there is still continued interest in ART because of the poor performance of the transform methods for highly under-determined systems while ART is applicable to essentially any problem with ease of incorporation of a priori information. In this chapter we review the literature that apply ART to Kerr electro-optic measurements.

7.2 ART for Constant Direction Kerr Media

ART algorithms were applied to Kerr electro-optic measurements first by Hertz [52] and later by Ihori et al. [53] for cases when the applied electric field direction was constant along the light path. They respectively used a nonuniform prism/plane elec-

trodes and sphere/plane electrodes and reconstructed the electric field magnitude on the ground plane. For these cases the electric field is completely specified by its magnitude. The inverse problem is then equivalent to that of scalar tomography where a function is reconstructed from its line integrals which are available experimentally. For Kerr electro-optic measurements the square of the magnitude of the applied electric field $E^2(x, y)$ and the characteristic phase retardation γ respectively constitute the function and the line integrals. Assuming a set of measurements on the plane for which k serves as the index variable we have

$$\gamma_k = \pi B \int_{\mathcal{L}_k} E^2\big[x(s), y(s)\big]\, ds \tag{7.1}$$

where $\mathcal{L}_k$ identifies the path of the kth ray from which the measurement is taken. Here we assume that the electric field is perpendicular to the propagation direction of the light ray.

In this section we present well known ART algorithms of scalar tomography that can reconstruct $E^2(x, y)$ from γ_k. To simplify the expressions we define

$$f(x, y) \equiv \pi B E^2(x, y) \tag{7.2}$$

so that (7.1) reduces to

$$\gamma_k = \int_{\mathcal{L}_k} f\big[x(s), y(s)\big]\, ds \tag{7.3}$$

7.2.1 General Setup

The first step for ART is to postulate an approximate electric field distribution by a linear combination of predetermined basis functions $b_n(x, y)$

$$f(x, y) \approx \sum_{n=1}^{N} f_n b_n(x, y) \tag{7.4}$$

Here f_n are the unknown constants to be determined during the reconstruction and N is the number of basis functions.

The basis functions are typically specified in terms of a discretization of the plane. The most common discretization uses uniform squares as shown in Figure 7.1. The most common basis functions based on this discretization are known as the pixel functions

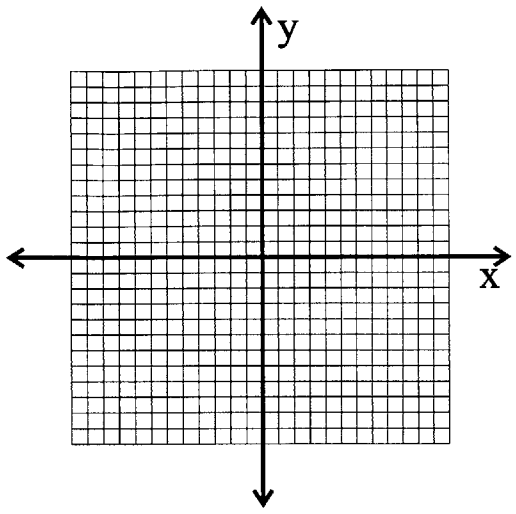

Figure 7.1: Discretization of plane with uniform squares which is the most common discretization for ART algorithms.

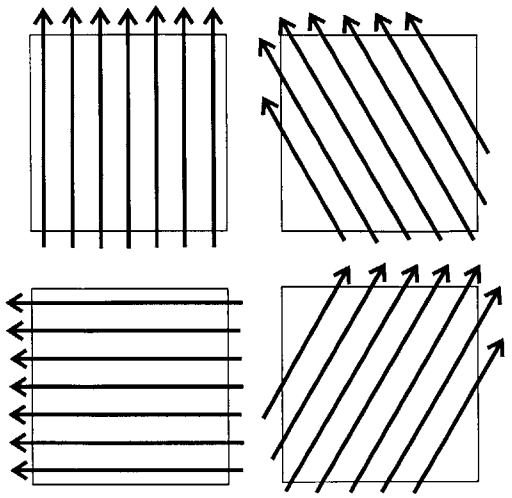

Figure 7.2: An example measurement set for ART algorithms. Typically actual reconstructions use more views.

and are defined as

$$b_n(x,y) = \begin{cases} 1 & (x,y) \in \mathcal{C}_n \\ 0 & (x,y) \notin \mathcal{C}_n \end{cases} \tag{7.5}$$

where $\mathcal{C}_n$ denotes the nth individual square discretization element. The electric field is assumed to vanish outside the discretized region.

In Figure 7.2 we show a typical set of rays from which the measurements are taken. Sets of rays in the same direction are called views. Figure 7.2 shows four views each consisting of seven lines. In a real application more views are often used.

ART algorithms are iterative methods. The solution process begins with an initial guess and updates the solution until some type of convergence (or divergence) criterion is satisfied. Each iteration itself consists of iterative steps over measurements. To identify these updates we let f_n be a function of two indices $f_n(i,k)$ where i denotes the iteration and k serves as an index over the measurements.

In the absence of any a priori information the initial guess that the iterations begin with is typically a constant function whose value is an average based on the measurements. For Kerr electro-optic measurements the most straight forward average

value is

$$f_n(1,1) = \frac{1}{K} \sum_{k'=1}^{K} \frac{\gamma_k}{l_k} \tag{7.6}$$

Here K is the number of measurements and l_k is the length of the path of the kth ray inside the non-zero field region.

At each sequential step over the measurements, the measurement is predicted by the underlying forward theory based on the current solution $f_n(i,k)$. We denote this prediction by γ_a. It follows from (7.3) and (7.4) that

$$\gamma_a(i,k) = \sum_{n=1}^{N} f_n(i,k) d_n(k) \tag{7.7}$$

where

$$d_n(k) = \int_{\mathcal{L}_k} b_n\big[x(s), y(s)\big]\, ds \tag{7.8}$$

If $b_n(x,y)$ are the pixel functions, (7.5) and (7.8) yield

$$d_n(k) = \begin{cases} l_{nk} & \mathcal{C}_n \cap \mathcal{L}_k \neq \emptyset \\ 0 & \mathcal{C}_n \cap \mathcal{L}_k = \emptyset \end{cases} \tag{7.9}$$

where l_{nk} is the path length of the kth ray inside the $\mathcal{C}_n$. Most $d_n(k)$ are zero since each ray intersects only a few $\mathcal{C}_n$. For ones that intersect, l_{nk} can be found from geometry.

Each step over the measurements updates the values of $f_n(i,k)$ by minimizing the difference between the predicted measurements $\gamma_a(i,k)$ and the actual measurements γ_k. The two original algorithms, which are respectively known as the additive and multiplicative ART (AART and MART here after), differ in this minimization process.

7.2.2 AART - Additive ART

In AART the difference between the predicted measurement and the actual measurement is added to $f_n(i,k)$ by a weight factor

$$f_n(i,k+1) = f_n(i,k) + \frac{d_n(k)}{\left[\sum_{n=1}^{N} d_n(k)\right]^2}\Big[\gamma_k - \gamma_a(i,k)\Big] \tag{7.10}$$

Notice that if $\mathcal{C}_n \cap \mathcal{L}_k = \emptyset$ then $d_n(k) = 0$ and thus if $\mathcal{C}_n$ does not intersect with the path of the kth ray then f_n is not updated in the kth step. Notice from (7.7) that prediction based on $f_n(i,k+1)$ is equal to γ_k minimizing the difference between the prediction and measurements.

Once k ranges over every measurement the resulting $f_n(i,K+1)$ constitutes the initial solution of the next iteration

$$f_n(i+1,1) = f_n(i,K+1) \tag{7.11}$$

Iterations continue until a convergence criterion is satisfied.

7.2.3 MART - Multiplicative ART

In MART each update step in (7.10) is replaced by

$$f_n(i,k+1) = \begin{cases} f_n(i,k)\big[\gamma_k/\gamma_a(i,k)\big] & \mathcal{C}_n \cap \mathcal{L}_k \neq \emptyset \\ 0 & \mathcal{C}_n \cap \mathcal{L}_k = \emptyset \end{cases} \tag{7.12}$$

where each $f_n(i,k)$ that effects the kth measurement is scaled.

7.2.4 Applications

In Figure 7.3 we show the AART and MART reconstructed electric field magnitude on the ground plane of sphere/plane electrodes described in Appendix B from computational Kerr electro-optic measurements after 10 iterations. The geometry parameters are similar to those used by Ihori et al. [53].

The discrete appearance of the reconstructed electric field magnitude is typical of ART algorithms and in principle can be avoided by smoothing the reconstructed electric field. Here we did not employ any convergence criterion. If computational time is not

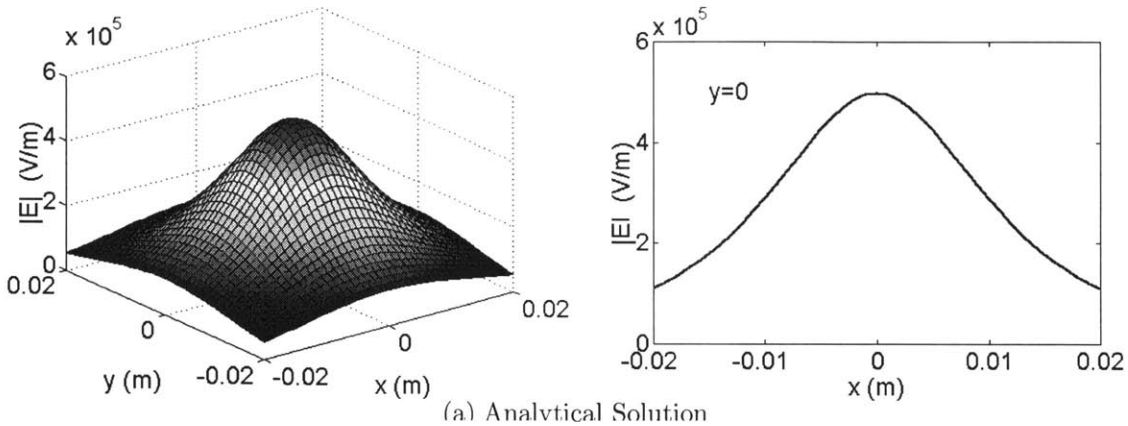

(a) Analytical Solution

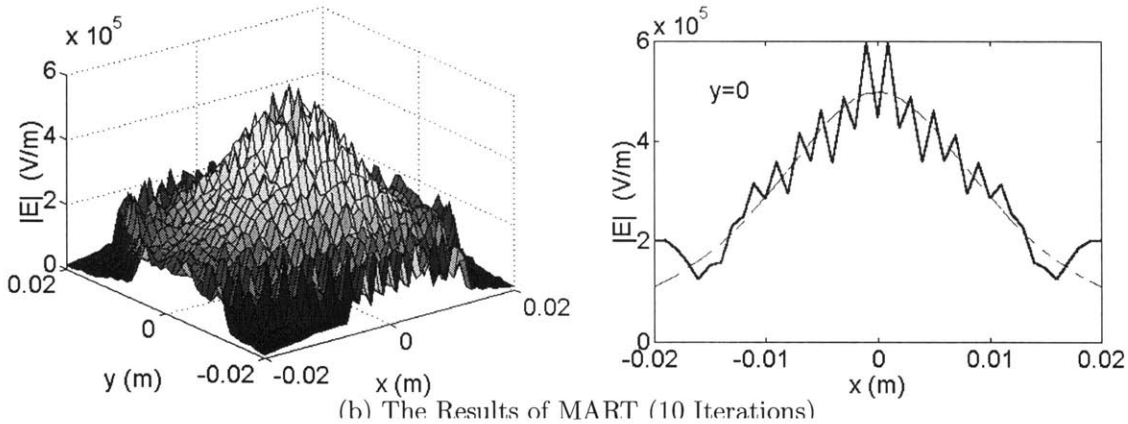

(b) The Results of MART (10 Iterations)

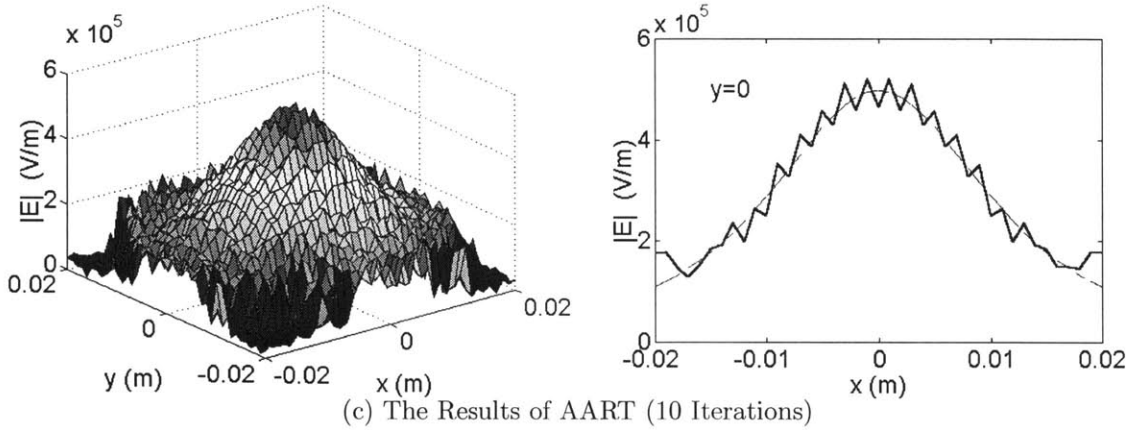

(c) The Results of AART (10 Iterations)

Figure 7.3: ART reconstruction from synthetic data of the electric field magnitude distribution in nitrobenzene on the ground plane of a sphere/plane electrode geometry with sphere to plane distance $D = 16.5$ mm, sphere radius $R = 10$ mm and $V = 4$ kV. The synthetic data are from six views like those in Figure 7.2 but 30° apart, each consisting of 41 lines.

at a premium a large number of iterations can be performed and the iteration that minimizes the forward prediction and the actual measurements can be chosen. Note that a larger number of iterations does not necessarily mean better solutions as the reconstructed electric fields tend to diverge if too many iterations are used.

7.3 ART for General Kerr Media

A series of papers by Arii et al. extended the Kerr electro-optic measurement technique to arbitrary nonuniform electric field distributions using ART [54–56]. Their final algorithm was used for reconstruction of the electric field distribution between sphere/plane and sphere/sphere electrodes on planes other than where the electric field direction is constant [57]. Their research has been continuing parallel to this work.

In the algorithm, similar to the scalar ART, the electric field is approximated by a linear combination of pixel functions $b_n(x, y)$

$$\mathbf{E}(x, y) \approx \sum_{n=1}^{N} \mathbf{E}_n b_n(x, y) \tag{7.13}$$

The predicted measurements based on this approximation can be computed by forward Kerr electro-optic theory. Ihori et al. use a layered approach which adds up to the discretization of (4.68) and is limited to weak Kerr media. Substituting (7.13) in (4.68) yield

$$\gamma_a(i,k)\cos 2\alpha_a(i,k) = \pi B \sum_{n=1}^{N} \Big[E^2_{m_n}(i,k) - E^2_{p_n}(i,k)\Big] d_n(k) \tag{7.14}$$

$$\gamma_a(i,k)\sin 2\alpha_a(i,k) = \pi B \sum_{n=1}^{N} \Big[2E_{m_n}(i,k)E_{p_n}(i,k)\Big] d_n(k) \tag{7.15}$$

These predicted measurements are to be compared to the actual measurements.

Ihori at al. propose that the magnitude of the electric field is to be updated similar to the MART step in (7.12) using the ratio of γ_k to $\gamma_a(i,k)$

$$\mathbf{E}_n(n, k+1/2) = \begin{cases} \sqrt{\dfrac{\gamma_k}{\gamma_a(i,k)}}\mathbf{E}_n(i,k) & \mathcal{C}_n \cap \mathcal{L}_k \neq \emptyset \\ \mathbf{E}_n(i,k) & \mathcal{C}_n \cap \mathcal{L}_k = \emptyset \end{cases} \tag{7.16a}$$

where we use 1/2 to indicate that this is an intermediate step. Once the magnitude is updated using (7.16a) the angle of the transverse electric field components are updated using

$$E_{m_n}(i,k+1) = \begin{cases} \cos\eta\sqrt{E^2_{m_n}(i,k+1/2) + E^2_{p_n}(i,k+1/2)} & \mathcal{C}_n \cap \mathcal{L}_k \neq \emptyset \\ E_{m_n}(i,k+1/2) & \mathcal{C}_n \cap \mathcal{L}_k = \emptyset \end{cases} \tag{7.16b}$$

$$E_{p_n}(i,k+1) = \begin{cases} \sin\eta\sqrt{E^2_{m_n}(i,k+1/2) + E^2_{p_n}(i,k+1/2)} & \mathcal{C}_n \cap \mathcal{L}_k \neq \emptyset \\ E_{p_n}(i,k+1/2) & \mathcal{C}_n \cap \mathcal{L}_k = \emptyset \end{cases} \tag{7.16c}$$

where

$$\eta = \arctan\frac{E_{p_n}(i,k+1/2)}{E_{m_n}(i,k+1/2)} + \Big[\alpha_k - \alpha_a(i,k)\Big] \tag{7.17}$$

An implementation of the method for the mid plane of sphere/plane electrodes of Appendix B for which the electric field direction is not constant is shown in Figure 7.4. This reconstruction used Ihori et al.'s geometric parameters and computational measurements.

For axisymmetric Kerr media ART has no apparent advantage over the onion peeling method. For arbitrary weak Kerr media we believe that the finite element based algorithm we developed in Chapter 8 is superior and more applicable. The only area that ART seem to be useful is arbitrary three dimensional Kerr media which are highly birefringent. Then the algorithm described in this chapter is not directly applicable because there are three characteristic parameters. The modification of (7.16) is necessary and this is not trivial and involves guesswork as much as anything else. Thus we do not further investigate improvements on ART algorithms.

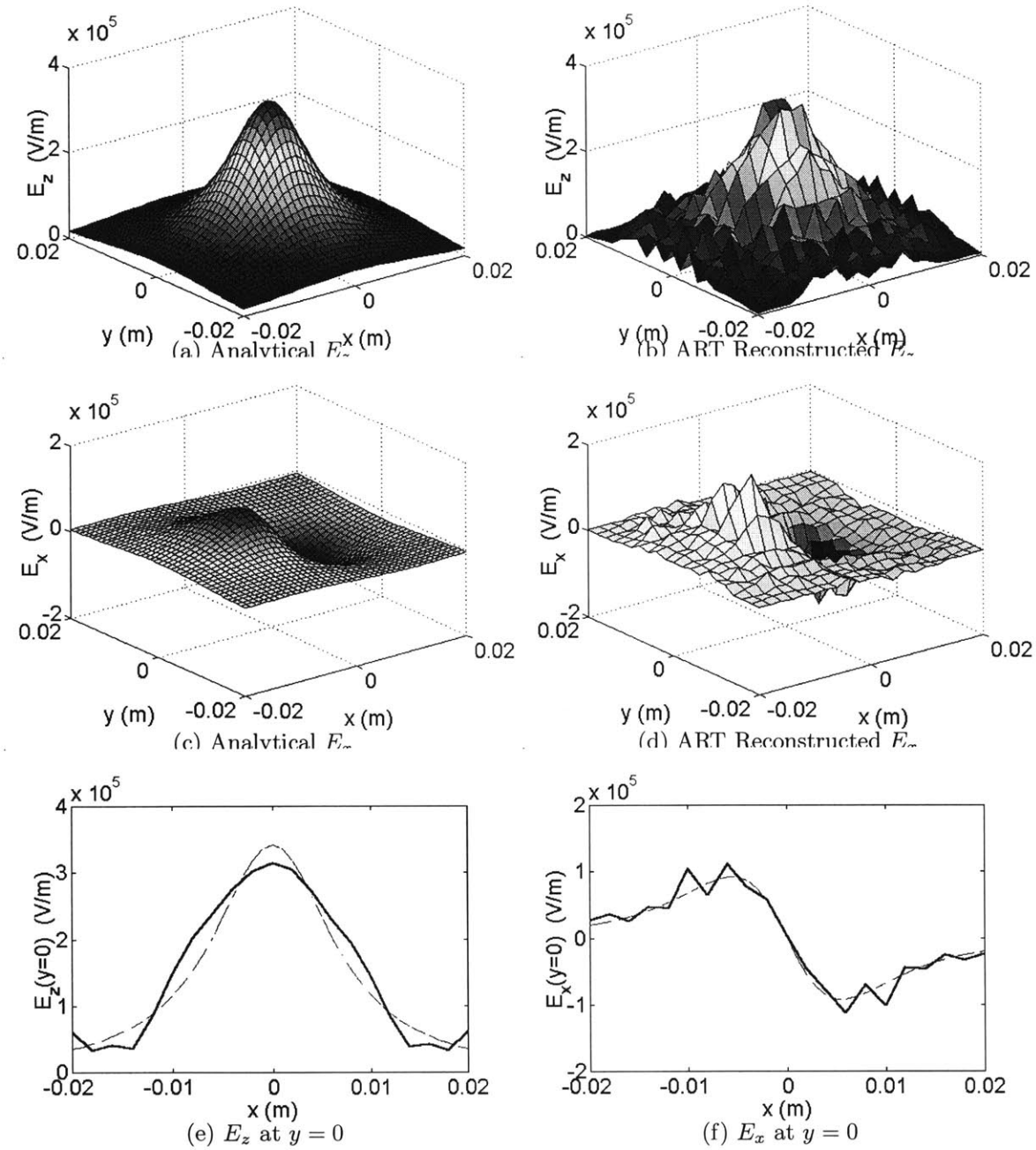

Figure 7.4: ART reconstruction from synthetic data of the electric field components in nitrobenzene in the mid-plane of a sphere/plane electrode geometry with sphere to plane distance $D = 13.5$ mm, sphere radius $R = 3.5$ mm and $V = 10$ kV. The synthetic data are from six views 30° apart each consisting of 21 lines.

Chapter 8

Finite Element Based Kerr Electro-Optic Reconstruction Algorithm (FEBKER)

8.1 Introduction

In this chapter we introduce a new algorithm which is built on the finite element method for Poisson's equation and named the finite element based Kerr electro-optic reconstruction algorithm (FEBKER hereafter). The algorithm uses the basics of the finite element method (FEM) to relate the potential and space charge density distributions of an electrode system in a matrix equation. A second matrix equation is obtained by expressing the Kerr electro-optic measurements in terms of the potential distribution. The resulting two matrix equations are then solved as a least squares problem to yield the space charge distribution.

FEBKER is applicable to weak Kerr media when the ac modulation method is used to increase the sensitivity of Kerr electro-optic measurements. The algorithm can be used for arbitrary three dimensional electrode systems. However in this work we limit the implementation and application of the algorithm to axisymmetric problems and in particular to the point/plane electrode geometry. This limitation is primarily due to implementation complexity in discretization of three-dimensional geometries. FEBKER can use single parameter Kerr electro-optic measurements and thus makes it easier to investigate transient charge injection and transport phenomena by avoiding time consuming rotation of optical elements during experiments.

8.2 Discretization and Interpolating Polynomials

8.2.1 Triangular Discretization

Unlike the onion peeling method of Chapter 6 for which one dimensional radial discretizations are used, FEBKER requires two dimensional discretizations of the rz-plane for axisymmetric geometries. Two dimensional discretizations often use triangles and/or quadrilaterals as the discretizing elements. In this work we only use triangles. In Figure 8.1 we show a simple point/plane like geometry and a triangular discretization which we use for descriptive purposes in this chapter.

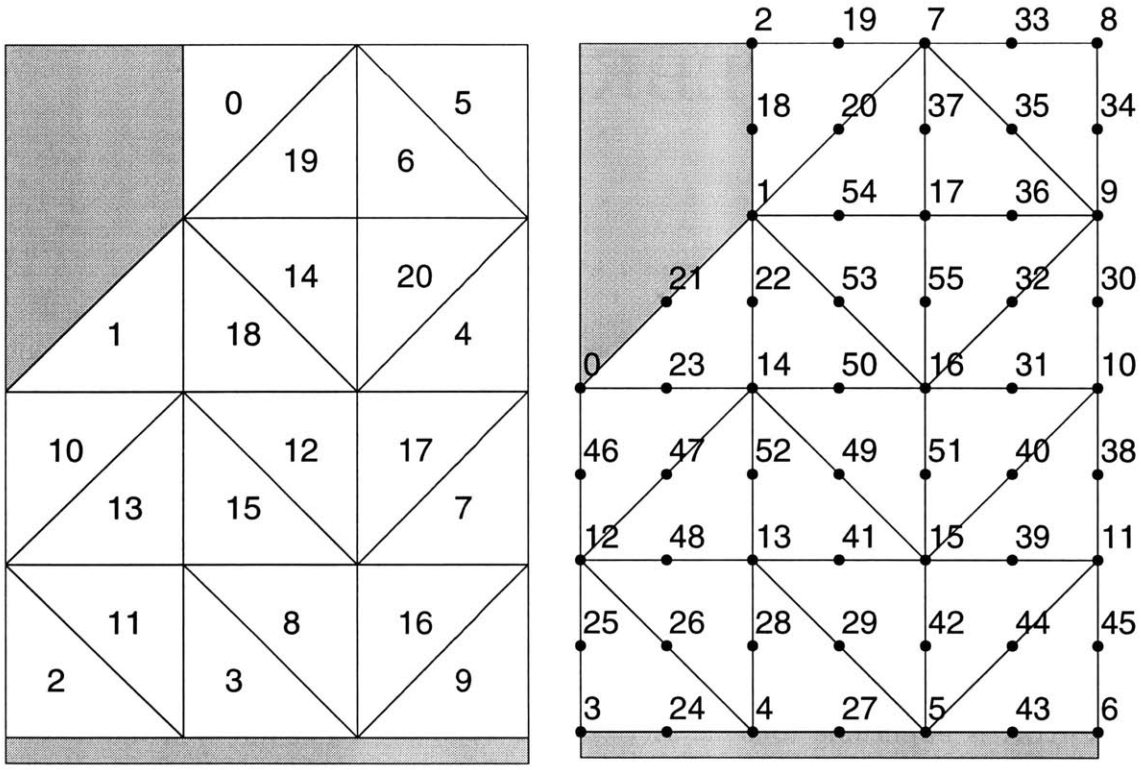

(a) Triangle Numbering

(b) Point Numbering

Figure 8.1: The discretized axisymmetric point/plane like geometry (axisymmetry axis is the left hand edge) which is used for illustrative purposes in this chapter. The discretizing elements are triangles numbered from 0 to 20 in no particular order, typical for automatically generated meshes. For each triangle there correspond six nodes. Within each triangle the electric potential is approximated by its point values on the nodes and known interpolating functions. The overall potential distribution can then be described by a finite number of parameters: the point values on the nodes.

The purpose of the discretization is to approximate the local continuous field quantities electric potential, electric field and space charge density by a finite number of parameters. The simplest approach to approximate any particular quantity is to assume that it is step-wise constant within each triangle. In this work this approach is used for space charge density. As will be described in Section 8.3, to find numerical solutions to Poisson's equation, the finite element method postulates and minimizes an integrated error criterion. The criterion used in this work depends on the gradient of the potential which excludes step-wise constant potentials as a basis within triangles. Instead, first and second order polynomials are commonly used; second order polynomials are often preferred to make the electric field continuous from triangle to triangle. In this work we employ second order polynomials to discretize the electric potential distribution. The electric field components are then found by taking the gradient of the potential resulting in first order polynomials.

8.2.2 Triangular Coordinates

Interpolating polynomials within a triangle are best expressed with the so called triangular coordinates, which are first order polynomials that are associated with the vertices of the individual triangles. In fact, there are three triangular coordinates, one for each vertex. They take the value one on the vertex they are associated with and 0 on the other vertices. We denote the triangular coordinates by $\tilde{\zeta}_i$, where $i = 1, 2, 3$. By definition [58]

$$\tilde{\zeta}_i(r, z) = \tilde{A}_i r + \tilde{B}_i z + \tilde{C}_i \tag{8.1}$$

and

$$\tilde{\zeta}_i(\tilde{r}_{v_j}, \tilde{z}_{v_j}) = \begin{cases} 1 & i = j \\ 0 & i \neq j \end{cases} \tag{8.2}$$

Here $(\tilde{r}_{v_j}, \tilde{z}_{v_j})$ is the coordinate of the jth vertex of the triangle. In this chapter we use tildes to differentiate triangle specific local description of quantities from global descriptions. For example the coordinates of the upper-right point in Figure 8.1 might be denoted by (r_8, z_8) in the global description and by $(\tilde{r}_i, \tilde{z}_i)$ where $1 \leq i \leq 3$ in the description local to the fifth triangle.

Equations (8.1) and (8.2) yield three matrix equations

$$\begin{bmatrix} \tilde{r}_{v_i} & \tilde{z}_{v_i} & 1 \\ \tilde{r}_{v_j} & \tilde{z}_{v_j} & 1 \\ \tilde{r}_{v_k} & \tilde{z}_{v_k} & 1 \end{bmatrix} \begin{bmatrix} \tilde{A}_i \\ \tilde{B}_i \\ \tilde{C}_i \end{bmatrix} = \begin{bmatrix} 1 \\ 0 \\ 0 \end{bmatrix} \tag{8.3}$$

where (i, j, k) are the even permutations of $(1, 2, 3)$. The solution to (8.3) gives

$$\tilde{A}_i = \frac{\tilde{z}_{v_j} - \tilde{z}_{v_k}}{\Delta} \tag{8.4a}$$

$$\tilde{B}_i = \frac{\tilde{r}_{v_k} - \tilde{r}_{v_j}}{\Delta} \tag{8.4b}$$

$$\tilde{C}_i = \frac{\tilde{r}_{v_j}\tilde{z}_{v_k} - \tilde{r}_{v_k}\tilde{z}_{v_j}}{\Delta} \tag{8.4c}$$

where Δ is the determinant of the matrix in (8.3)

$$\Delta = \begin{vmatrix} \tilde{r}_{v_i} & \tilde{z}_{v_i} & 1 \\ \tilde{r}_{v_j} & \tilde{z}_{v_j} & 1 \\ \tilde{r}_{v_k} & \tilde{z}_{v_k} & 1 \end{vmatrix} \tag{8.5}$$

Since triangular coordinates are linear functions that take values 1 and 0 on the vertices we have

$$0 \leq \tilde{\zeta}_i \leq 1 \quad i = 1, 2, 3 \tag{8.6}$$

and by substituting (8.4) into (8.1) it can be directly shown that

$$\tilde{\zeta}_1(r, z) + \tilde{\zeta}_2(r, z) + \tilde{\zeta}_3(r, z) = 1 \tag{8.7}$$

for any point (r, z) inside the triangle.

8.2.3 First Order Interpolating Polynomials

The triangular coordinates can be directly used as the interpolating polynomials for values on the vertices of the triangles. Consider an electric potential distribution that has values $\tilde{\phi}_{v_1}$, $\tilde{\phi}_{v_2}$ and $\tilde{\phi}_{v_3}$ on the vertices. Then the first order polynomial over the triangle which interpolates these values can be expressed in terms of the triangular

coordinates using (8.2)

$$\tilde{\phi}(r,z) = \tilde{\phi}_{v_1}\tilde{\zeta}_1(r,z) + \tilde{\phi}_{v_2}\tilde{\zeta}_2(r,z) + \tilde{\phi}_{v_3}\tilde{\zeta}_3(r,z) \tag{8.8}$$

We define the column vectors $\tilde{\boldsymbol{\zeta}}(r,z)$ and $\tilde{\boldsymbol{\phi}}_{\mathbf{v}}$

$$\tilde{\boldsymbol{\zeta}}(r,z) = \begin{bmatrix}\tilde{\zeta}_1(r,z) & \tilde{\zeta}_2(r,z) & \tilde{\zeta}_3(r,z)\end{bmatrix}^{\mathrm{T}} \tag{8.9}$$

$$\tilde{\boldsymbol{\phi}}_{\mathbf{v}} = \begin{bmatrix}\tilde{\phi}_{v_1} & \tilde{\phi}_{v_2} & \tilde{\phi}_{v_3}\end{bmatrix}^{\mathrm{T}} \tag{8.10}$$

so that (8.8) can be written in the convenient matrix form as

$$\tilde{\phi}(r,z) = \tilde{\boldsymbol{\zeta}}^{\mathrm{T}}(r,z)\,\tilde{\boldsymbol{\phi}}_{\mathbf{v}} \tag{8.11}$$

8.2.4 Second Order Interpolating Polynomials

A second order polynomial has 6 coefficients for r, r^2, z, z^2, rz and 1. Thus it can be used to interpolate six nodal values in a triangle. Beside the vertices three additional nodes are often chosen to be the middle points of the edges as illustrated in Figure 8.1. Once the nodes are specified as such the second order polynomial in terms of the values on the nodes can be written in terms of the triangular coordinates as

$$\begin{aligned}\tilde{\phi}(r,z) = {} & \tilde{\phi}_{v_1}\tilde{\zeta}_1(r,z)\big[2\tilde{\zeta}_1(r,z)-1\big] + 4\tilde{\phi}_{m_3}\tilde{\zeta}_1(r,z)\tilde{\zeta}_2(r,z) \\ & \tilde{\phi}_{v_2}\tilde{\zeta}_2(r,z)\big[2\tilde{\zeta}_2(r,z)-1\big] + 4\tilde{\phi}_{m_1}\tilde{\zeta}_2(r,z)\tilde{\zeta}_3(r,z) \\ & \tilde{\phi}_{v_3}\tilde{\zeta}_3(r,z)\big[2\tilde{\zeta}_3(r,z)-1\big] + 4\tilde{\phi}_{m_2}\tilde{\zeta}_3(r,z)\tilde{\zeta}_1(r,z)\end{aligned} \tag{8.12}$$

Here $\tilde{\phi}_{v_1}$, $\tilde{\phi}_{v_2}$ and $\tilde{\phi}_{v_3}$ are the values on the vertices and $\tilde{\phi}_{m_1}$, $\tilde{\phi}_{m_2}$ and $\tilde{\phi}_{m_3}$ are respectively the values at the mid points of the edges opposite to the 1st, 2nd, and 3rd vertex. Using (8.2) it can be directly checked that $\tilde{\phi}(\tilde{r}_{v_i},\tilde{z}_{v_i}) = \tilde{\phi}_{v_i}$. At each of the middle point of the edges, the triangular coordinate associated with the node opposite to the edge is zero and the other two triangular coordinates take the value 0.5. Using these values it can be directly checked that $\tilde{\phi}(\tilde{r}_{m_i},\tilde{z}_{m_i}) = \tilde{\phi}_{m_i}$. Thus (8.12) defines the second order polynomial that interpolates $\tilde{\phi}_{v_1}$, $\tilde{\phi}_{v_2}$, $\tilde{\phi}_{v_3}$, $\tilde{\phi}_{m_1}$, $\tilde{\phi}_{m_2}$ and $\tilde{\phi}_{m_3}$.

We define column vectors $\tilde{\boldsymbol{\eta}}(r,z)$ and $\tilde{\boldsymbol{\phi}}$

$$\tilde{\boldsymbol{\eta}}(r,z) = \begin{bmatrix}\tilde{\zeta}_1(r,z)\big[2\tilde{\zeta}_1(r,z)-1\big] & 4\tilde{\zeta}_1(r,z)\tilde{\zeta}_2(r,z) & \tilde{\zeta}_2(r,z)\big[2\tilde{\zeta}_2(r,z)-1\big]\end{bmatrix}$$

$$4\tilde{\zeta}_2(r,z)\tilde{\zeta}_3(r,z) \quad \tilde{\zeta}_3(r,z)\big[2\tilde{\zeta}_3(r,z)-1\big] \quad 4\tilde{\zeta}_3(r,z)\tilde{\zeta}_1(r,z)\Big]^{\mathrm{T}} \tag{8.13}$$

and

$$\tilde{\boldsymbol{\phi}} = \begin{bmatrix} \tilde{\phi}_{v_1} & \tilde{\phi}_{m_3} & \tilde{\phi}_{v_2} & \tilde{\phi}_{m_1} & \tilde{\phi}_{v_3} & \tilde{\phi}_{m_2} \end{bmatrix}^{\mathrm{T}} \tag{8.14}$$

so that (8.12) can be expressed in matrix form as

$$\tilde{\phi}(r,z) = \tilde{\boldsymbol{\eta}}^{\mathrm{T}}(r,z)\tilde{\boldsymbol{\phi}} \tag{8.15}$$

In this work, within each triangle the potential takes the form (8.15). The matrix form in (8.15) is particularly useful as it separates the spatial dependence from the nodal values that are being interpolated. Once the potential is expressed in (8.15) the electric field is found by taking the gradient. Using the chain rule we have

$$\frac{\partial\tilde{\boldsymbol{\eta}}(r,z)}{\partial r} = \sum_{i=1}^{3}\frac{\partial\tilde{\zeta}_i}{\partial r}\frac{\partial\tilde{\boldsymbol{\eta}}}{\partial\tilde{\zeta}_i} = \sum_{i=1}^{3}\tilde{A}_i\frac{\partial\tilde{\boldsymbol{\eta}}}{\partial\tilde{\zeta}_i} \tag{8.16a}$$

$$\frac{\partial\tilde{\boldsymbol{\eta}}(r,z)}{\partial z} = \sum_{i=1}^{3}\frac{\partial\tilde{\zeta}_i}{\partial z}\frac{\partial\tilde{\boldsymbol{\eta}}}{\partial\tilde{\zeta}_i} = \sum_{i=1}^{3}\tilde{B}_i\frac{\partial\tilde{\boldsymbol{\eta}}}{\partial\tilde{\zeta}_i} \tag{8.16b}$$

where we used (8.1) to evaluate the r and z derivatives of $\tilde{\zeta}_i$. The derivatives of $\tilde{\boldsymbol{\eta}}$ with respect to $\tilde{\zeta}_i$ directly follows from (8.13) and can be expressed in terms of $\tilde{\boldsymbol{\zeta}}$ in (8.9) with the help of (8.7)

$$\frac{\partial\tilde{\boldsymbol{\eta}}^{\mathrm{T}}}{\partial\zeta_1} = \tilde{\boldsymbol{\zeta}}^{\mathrm{T}}\mathbf{G_1} = \begin{bmatrix}\zeta_1(r,z) & \zeta_2(r,z) & \zeta_3(r,z)\end{bmatrix}\begin{bmatrix} 3 & 0 & 0 & 0 & 0 & 0 \\ -1 & 4 & 0 & 0 & 0 & 0 \\ -1 & 0 & 0 & 0 & 0 & 4 \end{bmatrix} \tag{8.17a}$$

$$\frac{\partial\tilde{\boldsymbol{\eta}}^{\mathrm{T}}}{\partial\zeta_2} = \tilde{\boldsymbol{\zeta}}^{\mathrm{T}}\mathbf{G_2} = \begin{bmatrix}\zeta_1(r,z) & \zeta_2(r,z) & \zeta_3(r,z)\end{bmatrix}\begin{bmatrix} 0 & 4 & -1 & 0 & 0 & 0 \\ 0 & 0 & 3 & 0 & 0 & 0 \\ 0 & 0 & -1 & 4 & 0 & 0 \end{bmatrix} \tag{8.17b}$$

$$\frac{\partial\tilde{\boldsymbol{\eta}}^{\mathrm{T}}}{\partial\zeta_3} = \tilde{\boldsymbol{\zeta}}^{\mathrm{T}}\mathbf{G_3} = \begin{bmatrix}\zeta_1(r,z) & \zeta_2(r,z) & \zeta_3(r,z)\end{bmatrix}\begin{bmatrix} 0 & 0 & 0 & 0 & -1 & 4 \\ 0 & 0 & 0 & 4 & -1 & 0 \\ 0 & 0 & 0 & 0 & 3 & 0 \end{bmatrix} \tag{8.17c}$$

$\mathbf{G_i}$ are independent of the parameters of the mesh triangles and are known as the

universal matrices [58]. Substituting (8.17) in (8.16) we obtain

$$\frac{\partial \tilde{\boldsymbol{\eta}}^{\mathrm{T}}(r,z)}{\partial r} = \tilde{\boldsymbol{\zeta}}^{\mathrm{T}}(r,z)\tilde{\mathbf{D}}_{\mathbf{r}} \tag{8.18a}$$

$$\frac{\partial \boldsymbol{\eta}^{\mathrm{T}}(r,z)}{\partial z} = \tilde{\boldsymbol{\zeta}}^{\mathrm{T}}(r,z)\tilde{\mathbf{D}}_{\mathbf{z}} \tag{8.18b}$$

where

$$\tilde{\mathbf{D}}_{\mathbf{r}} = \sum_{i=1}^{3} \tilde{A}_i \mathbf{G}_{\mathbf{i}} \tag{8.19a}$$

$$\tilde{\mathbf{D}}_{\mathbf{z}} = \sum_{i=1}^{3} \tilde{B}_i \mathbf{G}_{\mathbf{i}} \tag{8.19b}$$

The electric field components follow from (8.15) and (8.18)

$$-\tilde{E}_r(r,z) = \frac{\partial \tilde{\phi}(r,z)}{\partial r} = \tilde{\boldsymbol{\zeta}}^{\mathrm{T}}(r,z)\tilde{\mathbf{D}}_{\mathbf{r}}\tilde{\boldsymbol{\phi}} \tag{8.20a}$$

$$-\tilde{E}_z(r,z) = \frac{\partial \tilde{\phi}(r,z)}{\partial z} = \tilde{\boldsymbol{\zeta}}^{\mathrm{T}}(r,z)\tilde{\mathbf{D}}_{\mathbf{z}}\tilde{\boldsymbol{\phi}} \tag{8.20b}$$

In the following sections we also need the squares of electric field components which directly follow from (8.20)

$$\left[\tilde{E}_r(r,z)\right]^2 = \left[\frac{\partial \tilde{\phi}(r,z)}{\partial r}\right]^2 = \tilde{\boldsymbol{\phi}}^{\mathrm{T}}\tilde{\mathbf{D}}_{\mathbf{r}}^{\mathrm{T}}\tilde{\boldsymbol{\zeta}}(r,z)\tilde{\boldsymbol{\zeta}}^{\mathrm{T}}(r,z)\tilde{\mathbf{D}}_{\mathbf{r}}\tilde{\boldsymbol{\phi}} \tag{8.21a}$$

$$\left[\tilde{E}_z(r,z)\right]^2 = \left[\frac{\partial \tilde{\phi}(r,z)}{\partial z}\right]^2 = \tilde{\boldsymbol{\phi}}^{\mathrm{T}}\tilde{\mathbf{D}}_{\mathbf{z}}^{\mathrm{T}}\tilde{\boldsymbol{\zeta}}(r,z)\tilde{\boldsymbol{\zeta}}^{\mathrm{T}}(r,z)\tilde{\mathbf{D}}_{\mathbf{z}}\tilde{\boldsymbol{\phi}} \tag{8.21b}$$

The forms in (8.21) are chosen to isolate the spatial dependencies as a matrix in the middle, $\tilde{\boldsymbol{\zeta}}(r,z)\tilde{\boldsymbol{\zeta}}^{\mathrm{T}}(r,z)$.

8.3 The Finite Element Method

8.3.1 Basics

The finite element method (FEM) is one of the most widely used numerical methods for solution of the Poisson equation. There are many excellent books on the subject.

In particular [58] is a very easy to read book and was frequently consulted for this work. For a more detailed treatment we refer the reader to the book by Hughes [59]. Here we give a brief discussion.

The two basic steps of the FEM are the postulation of a trial electric potential solution in terms of undetermined parameters and determination of these parameters by some error criterion. Typically the solution region is discretized into smaller elements, such as triangles in Figure 8.1, and within each element the trial potential solutions are specified locally using interpolating functions. In this work these local trial solutions are second order polynomials as discussed in Section 8.2.4. The undetermined parameters are values of these polynomials on the vertices and the edge midpoints of the triangles. Note that on the element edges the second order trial solutions of neighboring triangles conform, enforcing continuity on both the trial solution and the gradient of the trial solution throughout the geometry.

Once the trial potential functions are postulated, the unknown parameters are to be found such that the resulting solution is as close to the actual solution of Poisson's equation as possible. Various error functionals are in use to measure the closeness of a numerical solution. In this work we use the simple energy functional for a Poissonian system which is given as

$$\mathcal{L}[\phi] = \iiint_V \left[\frac{1}{2}\epsilon\left|\nabla\phi(\vec{r})\right|^2 - \rho(\vec{r})\phi(\vec{r})\right] dV \tag{8.22}$$

The minimum energy principle states that the solution of the Poisson's equation minimizes the energy functional (8.22). Thus if the unknown parameters for an approximate solution is chosen such that they minimize (8.22) then the resulting solution is as close to the actual solution as possible in the total energy sense. Of course if the actual solution is not a second order polynomial the numerical solution will be only as good as second order polynomials can represent. Fortunately, the Taylor series expansions of arbitrary functions demonstrate that if the discretization is fine enough a second order polynomial can adequately approximate any function.

Now that the trial local functions and the error criterion have been specified, it remains is to express the energy functional in terms of the local trial functions and to minimize the resulting expression with respect to the unknown parameters, i.e. the nodal values of the potential. We begin by expressing the energy functional in terms of the local interpolating polynomials.

8.3.2 The Energy Functional

The formulation here is limited to axisymmetric problems and thus we begin by reducing the volume integral in (8.22) to an area integral over the rz-plane. Using cylindrical coordinates

$$\mathcal{L}[\phi] = \int_0^{2\pi} \iint_A \left[\frac{1}{2}\epsilon\left|\nabla\phi(\vec{r})\right|^2 - \rho(\vec{r})\phi(\vec{r})\right] r\, dr\, dz\, d\theta \tag{8.23}$$

$$= \iint_A 2\pi r\left[\frac{1}{2}\epsilon\left|\nabla\phi(r,z)\right|^2 - \rho(r,z)\phi(r,z)\right] dr\, dz \tag{8.24}$$

$$= \iint_A 2\pi r\left\{\frac{1}{2}\epsilon\left[\frac{\partial\phi(r,z)}{\partial r}\right]^2 + \frac{1}{2}\epsilon\left[\frac{\partial\phi(r,z)}{\partial z}\right]^2 - \rho(r,z)\phi(r,z)\right\} dr\, dz \tag{8.25}$$

where A is the area of the two dimensional projection of the solution region in the rz-plane.

Since the solution region is discretized into triangles and $\phi(r,z)$ and $\rho(r,z)$ are locally approximated within each triangle, (8.25) reduces to a sum over the triangles

$$\mathcal{L}[\phi] = \sum_{e=1}^{n} \iint_{\tilde{A}_e} 2\pi r\left\{\frac{1}{2}\epsilon\left[\frac{\partial\tilde{\phi}_e(r,z)}{\partial r}\right]^2 + \frac{1}{2}\epsilon\left[\frac{\partial\tilde{\phi}_e(r,z)}{\partial z}\right]^2 - \tilde{\rho}_e(r,z)\tilde{\phi}_e(r,z)\right\} dr\, dz \tag{8.26}$$

Here e ranges over all the triangles of the discretization and $\tilde{A}_e$ is the area of the eth triangle. Within each triangle the space charge density is assumed to be constant. Thus using (8.15) for the potential

$$\tilde{\rho}_e(r,z)\tilde{\phi}_e(r,z) = \tilde{\rho}_e\tilde{\boldsymbol{\eta}}_e^{\mathrm{T}}(r,z)\tilde{\boldsymbol{\phi}}_e \tag{8.27}$$

The squares of r and z derivatives of $\tilde{\phi}_e(r,z)$ are given in (8.21) and within each triangle r can be exactly expressed in terms of the triangle coordinates since it is a first order polynomial

$$r = \tilde{\boldsymbol{\zeta}}_e^{\mathrm{T}}(r,z)\,\tilde{\mathbf{r}}_{\mathbf{v}_e} \tag{8.28}$$

where $\tilde{\mathbf{r}}_{\mathbf{v}_e}$ is the column vector of the r coordinates of the vertices of the triangular elements.

We define

$$\tilde{\mathbf{M}}_e = \iint\limits_{\tilde{A}_e} \left(\tilde{\boldsymbol{\zeta}}_e^{\mathrm{T}}(r,z)\,\tilde{\mathbf{r}}_{\mathbf{v}_e}\right) \tilde{\boldsymbol{\zeta}}_e(r,z)\tilde{\boldsymbol{\zeta}}_e^{\mathrm{T}}(r,z)\,dr\,dz \tag{8.29}$$

$$\tilde{\mathbf{N}}_e = \iint\limits_{\tilde{A}_e} \left(\tilde{\boldsymbol{\zeta}}_e^{\mathrm{T}}(r,z)\,\tilde{\mathbf{r}}_{\mathbf{v}_e}\right) \tilde{\boldsymbol{\eta}}_e^{\mathrm{T}}(r,z)\,dr\,dz \tag{8.30}$$

so that the energy functional in (8.26) can now be compactly written using (8.21), (8.27), (8.29), and (8.30)

$$\mathcal{L}[\phi] = \sum_{e=1}^{n} \frac{1}{2}\tilde{\boldsymbol{\phi}}_e^{\mathrm{T}}\tilde{\mathbf{P}}_e\tilde{\boldsymbol{\phi}}_e - \tilde{\rho}_e\tilde{\mathbf{T}}_e\tilde{\boldsymbol{\phi}}_e \tag{8.31}$$

where

$$\tilde{\mathbf{P}}_e = 2\pi\epsilon\left(\tilde{\mathbf{D}}_{\mathbf{z}_e}^{\mathrm{T}}\tilde{\mathbf{M}}_e\tilde{\mathbf{D}}_{\mathbf{z}_e} + \tilde{\mathbf{D}}_{\mathbf{r}_e}^{\mathrm{T}}\tilde{\mathbf{M}}_e\tilde{\mathbf{D}}_{\mathbf{r}_e}\right) \tag{8.32}$$

$$\tilde{\mathbf{T}}_e = 2\pi\tilde{\mathbf{N}}_e \tag{8.33}$$

Considering (8.29), we have

$$\tilde{\mathbf{M}}_e = \iint\limits_{\tilde{A}_e} \left(\tilde{\boldsymbol{\zeta}}_e^{\mathrm{T}}(r,z)\,\tilde{\mathbf{r}}_{\mathbf{v}_e}\right) \tilde{\boldsymbol{\zeta}}_e(r,z)\tilde{\boldsymbol{\zeta}}_e^{\mathrm{T}}(r,z)\,dr\,dz \tag{8.34}$$

$$= \sum_{i=1}^{3} \tilde{r}_{v_i}^{(e)} \iint\limits_{\tilde{A}_e} \tilde{\zeta}_{i_e}(r,z)\,\tilde{\boldsymbol{\zeta}}_e(r,z)\tilde{\boldsymbol{\zeta}}_e^{\mathrm{T}}(r,z)\,dr\,dz \tag{8.35}$$

$$= \tilde{A}_e\left(\tilde{r}_{v_1}^{(e)}\mathbf{M}_1 + \tilde{r}_{v_2}^{(e)}\mathbf{M}_2 + \tilde{r}_{v_3}^{(e)}\mathbf{M}_3\right) \tag{8.36}$$

where we used superscript (e) notation to avoid triple subscripts. Here $\tilde{r}_{v_i}^{(e)}$ denote the r-coordinate of the ith vertex in eth element. Using (8.9) we identify

$$\tilde{A}_e\mathbf{M}_1 = \begin{bmatrix} \iint\limits_{\tilde{A}_e} \tilde{\zeta}_{1_e}^3\,dr\,dz & \iint\limits_{\tilde{A}_e} \tilde{\zeta}_{1_e}^2\tilde{\zeta}_{2_e}\,dr\,dz & \iint\limits_{\tilde{A}_e} \tilde{\zeta}_{1_e}^2\tilde{\zeta}_{3_e}\,dr\,dz \\ \iint\limits_{\tilde{A}_e} \tilde{\zeta}_{1_e}^2\tilde{\zeta}_{2_e}\,dr\,dz & \iint\limits_{\tilde{A}_e} \tilde{\zeta}_{1_e}\tilde{\zeta}_{2_e}^2\,dr\,dz & \iint\limits_{\tilde{A}_e} \tilde{\zeta}_{1_e}\tilde{\zeta}_{2_e}\tilde{\zeta}_{3_e}\,dr\,dz \\ \iint\limits_{\tilde{A}_e} \tilde{\zeta}_{1_e}^2\tilde{\zeta}_{3_e}\,dr\,dz & \iint\limits_{\tilde{A}_e} \tilde{\zeta}_{1_e}\tilde{\zeta}_{2_e}\tilde{\zeta}_{3_e}\,dr\,dz & \iint\limits_{\tilde{A}_e} \tilde{\zeta}_{1_e}\tilde{\zeta}_{3_e}^2\,dr\,dz \end{bmatrix} \tag{8.37}$$

and $\mathbf{M}_2$ and $\mathbf{M}_3$ are similarly identified. These integrals can be explicitly evaluated [58]

yielding

$$\iint_{\tilde{A}_e} \tilde{\zeta}_{1_e}^{n_1} \tilde{\zeta}_{2_e}^{n_2} \tilde{\zeta}_{3_e}^{n_3} dr\, dz = \frac{2\, n_1!\, n_2!\, n_3!\, \tilde{A}_e}{(n_1 + n_2 + n_3 + 2)!} \tag{8.38}$$

where n_i are nonnegative integers and $\tilde{A}_e$ is the triangle area. Using (8.38) we obtain

$$\mathbf{M}_1 = \frac{1}{60}\begin{bmatrix} 6 & 2 & 2 \\ 2 & 2 & 1 \\ 2 & 1 & 2 \end{bmatrix} \quad \mathbf{M}_2 = \frac{1}{60}\begin{bmatrix} 2 & 2 & 1 \\ 2 & 6 & 2 \\ 1 & 2 & 2 \end{bmatrix} \quad \mathbf{M}_3 = \frac{1}{60}\begin{bmatrix} 2 & 1 & 2 \\ 1 & 2 & 2 \\ 2 & 2 & 6 \end{bmatrix} \tag{8.39}$$

where $\mathbf{M}_1$, $\mathbf{M}_2$ and $\mathbf{M}_3$ are universal matrices independent of the triangular elements. Notice that $\mathbf{M}_i$ and correspondingly $\tilde{\mathbf{M}}_e$ and $\tilde{\mathbf{P}}_e$ are symmetric.

$\tilde{\mathbf{N}}_e$ can be determined similarly as

$$\tilde{\mathbf{N}}_e = \iint_{\tilde{A}_e} \left(\tilde{\boldsymbol{\zeta}}_e^{\mathrm{T}}(r,z)\, \tilde{\mathbf{r}}_{\mathbf{v}_e}\right) \tilde{\boldsymbol{\eta}}_e^{\mathrm{T}}(r,z)\, dr\, dz \tag{8.40}$$

$$= \sum_{i=1}^{3} \tilde{r}_{v_i}^{(e)} \iint_{\tilde{A}_e} \tilde{\zeta}_{i_e}(r,z)\, \tilde{\boldsymbol{\eta}}_e^{\mathrm{T}}(r,z)\, dr\, dz \tag{8.41}$$

$$= \tilde{A}_e \left(\tilde{r}_{v_1}^{(e)} \mathbf{N}_1 + \tilde{r}_{v_2}^{(e)} \mathbf{N}_2 + \tilde{r}_{v_3}^{(e)} \mathbf{N}_3\right) \tag{8.42}$$

where (8.13) is used to get

$$\tilde{A}_e \mathbf{N}_1 = \iint_{\tilde{A}_e} \Big[\tilde{\zeta}_{1_e}^2(2\tilde{\zeta}_{1_e} - 1) \quad 4\tilde{\zeta}_{1_e}^2 \tilde{\zeta}_{2_e} \quad \tilde{\zeta}_{1_e}\tilde{\zeta}_{2_e}(2\tilde{\zeta}_{2_e} - 1)$$

$$4\tilde{\zeta}_{1_e}\tilde{\zeta}_{2_e}\tilde{\zeta}_{2_e} \quad \tilde{\zeta}_{1_e}\tilde{\zeta}_{3_e}(2\tilde{\zeta}_{3_e} - 1) \quad 4\tilde{\zeta}_{1_e}^2 \tilde{\zeta}_{3_e}\Big]\, dr\, dz \tag{8.43}$$

and $\mathbf{N}_2$ and $\mathbf{N}_3$ follow. Then, from (8.38)

$$\iint_{\tilde{A}_e} \zeta_{k_e}(r,z)\tilde{\zeta}_{i_e}(r,z)\big[2\tilde{\zeta}_{i_e}(r,z) - 1\big]\, dr\, dz = \begin{cases} \frac{\tilde{A}_e}{30} & k = i \\ -\frac{\tilde{A}_e}{60} & k \neq i \end{cases} \tag{8.44}$$

$$\iint_{\tilde{A}_e} 4\tilde{\zeta}_{k_e}(r,z)\tilde{\zeta}_{i_e}(r,z)\tilde{\zeta}_{j_e}(r,z) = \begin{cases} \frac{\tilde{A}_e}{15} & k \neq i \neq j \\ \frac{\tilde{A}_e}{12} & \text{otherwise} \end{cases} \tag{8.45}$$

so that explicit forms of $\mathbf{N}_1$, $\mathbf{N}_2$ and $\mathbf{N}_3$ are

$$\mathbf{N}_1 = \frac{1}{60}\begin{bmatrix} 2 & 5 & -1 & 4 & -1 & 5 \end{bmatrix} \tag{8.46a}$$

$$\mathbf{N}_2 = \frac{1}{60}\begin{bmatrix} -1 & 5 & 2 & 5 & -1 & 4 \end{bmatrix} \tag{8.46b}$$

$$\mathbf{N}_3 = \frac{1}{60}\begin{bmatrix} -1 & 4 & -1 & 5 & 2 & 5 \end{bmatrix} \tag{8.46c}$$

8.3.3 Global Equations

Equation (8.31) is expressed in terms of local matrices, potential, and space charge density. This local representation is essential for evaluation of integrals which resulted in universal matrices in (8.39) and (8.46). However the energy minimization principle applies to the whole sum and the minimization has to be done globally.

To proceed we express the potential distribution by a column vector $\mathbf{\Phi}$ whose rows contain the nodal values. For each triangle element e and for each entry of $\tilde{\mathbf{\Phi}}_e$ there corresponds an entry in $\mathbf{\Phi}$. Similarly the local space charge density values are grouped into a column vector $\boldsymbol{\rho}$. Each entry of $\boldsymbol{\rho}$ is an elemental (piecewise-constant) charge density ρ_e. The summation form of the energy functional in (8.31) can then be expressed globally as a matrix equation

$$\mathcal{L}[\phi] = \frac{1}{2}\mathbf{\Phi}^{\mathrm{T}}\mathbf{P}\mathbf{\Phi} - \mathbf{\Phi}^{\mathrm{T}}\mathbf{T}\boldsymbol{\rho} \tag{8.47}$$

where matrices $\mathbf{P}$ and $\mathbf{T}$ are assembled from the local matrices $\tilde{\mathbf{P}}_e$ and $\tilde{\mathbf{T}}_e$ in accordance with the sum in (8.31). It follows from the symmetry of $\tilde{\mathbf{P}}_e$ that $\mathbf{P}$ is symmetric.

On the electrodes the potential is known and equal to the applied voltages. Boundaries on which the potential is known are called the Dirichlet boundaries and the corresponding boundary condition is called a Dirichlet boundary condition. Dirichlet boundary conditions can directly be imposed on $\mathbf{\Phi}$ by requiring the values on the nodes that reside on the electrodes to be that of the applied voltages. To this end we partition $\mathbf{\Phi}$ into two parts

$$\mathbf{\Phi} = \begin{bmatrix} \mathbf{\Phi}_{\mathbf{u}} \\ \mathbf{\Phi}_{\mathbf{d}} \end{bmatrix} \tag{8.48}$$

Here $\mathbf{\Phi}_{\mathbf{u}}$ and $\mathbf{\Phi}_{\mathbf{d}}$ are themselves column vectors $\mathbf{\Phi}_{\mathbf{d}}$ (d stands for Dirichlet) that constrains the values that correspond to the nodes on the electrodes and $\mathbf{\Phi}_{\mathbf{u}}$ contains the

others (u stands for unknown). Thus the finite element problem of solving Poisson's equation reduces to finding $\mathbf{\Phi_u}$.

Substituting (8.48) in (8.47) yields

$$\mathcal{L}[\phi] = \frac{1}{2}\mathbf{\Phi}_\mathrm{u}^\mathrm{T}\mathbf{P}_{\mathbf{uu}}\mathbf{\Phi}_u + \frac{1}{2}\mathbf{\Phi}_\mathrm{u}^\mathrm{T}\mathbf{P}_{\mathbf{ud}}\mathbf{\Phi}_\mathrm{d} + \frac{1}{2}\mathbf{\Phi}_\mathrm{d}^\mathrm{T}\mathbf{P}_{\mathbf{du}}\mathbf{\Phi}_\mathrm{u} + \frac{1}{2}\mathbf{\Phi}_\mathrm{d}^\mathrm{T}\mathbf{P}_{\mathbf{dd}}\mathbf{\Phi}_\mathrm{d} - \mathbf{\Phi}_\mathrm{u}^\mathrm{T}\mathbf{T}_\mathrm{u}\boldsymbol{\rho} - \mathbf{\Phi}_\mathrm{d}^\mathrm{T}\mathbf{T}_\mathrm{d}\boldsymbol{\rho} \tag{8.49}$$

$$= \frac{1}{2}\mathbf{\Phi}_\mathrm{u}^\mathrm{T}\mathbf{P}_{\mathbf{uu}}\mathbf{\Phi}_\mathrm{u} + \mathbf{\Phi}_\mathrm{u}^\mathrm{T}\mathbf{P}_{\mathbf{ud}}\mathbf{\Phi}_\mathrm{d} + \frac{1}{2}\mathbf{\Phi}_\mathrm{d}^\mathrm{T}\mathbf{P}_{\mathbf{dd}}\mathbf{\Phi}_\mathrm{d} - \mathbf{\Phi}_\mathrm{u}^\mathrm{T}\mathbf{T}_\mathrm{u}\boldsymbol{\rho} - \mathbf{\Phi}_\mathrm{d}^\mathrm{T}\mathbf{T}_\mathrm{d}\boldsymbol{\rho} \tag{8.50}$$

where we also partitioned $\mathbf{P}$ and $\mathbf{T}$ in terms of the elements corresponding to $\mathbf{\Phi_u}$ and $\mathbf{\Phi_d}$ and used the fact that $\mathbf{P}_{\mathbf{ud}} = \mathbf{P}_{\mathbf{du}}^\mathrm{T}$ which follows from the symmetry of $\mathbf{P}$.

Now we are ready to minimize the energy with respect to the elements of $\mathbf{\Phi_u}$. Taking the derivative of (8.50) with respect to the ith entry of $\mathbf{\Phi_u}$ and equating the result to zero yields

$$\frac{\partial\mathcal{L}[\phi]}{\partial\Phi_{u_i}} = \frac{1}{2}\left[\mathbf{P}_{\mathbf{uu}}\mathbf{\Phi}_u\right]_i + \frac{1}{2}\left[\mathbf{\Phi}_\mathrm{u}^\mathrm{T}\mathbf{P}_{\mathbf{uu}}\right]_i + \left[\mathbf{P}_{\mathbf{ud}}\mathbf{\Phi}_\mathrm{d}\right]_i - \left[\mathbf{T}_\mathrm{u}\boldsymbol{\rho}\right]_i \tag{8.51}$$

$$= \left[\mathbf{P}_{\mathbf{uu}}\mathbf{\Phi}_u\right]_i + \left[\mathbf{P}_{\mathbf{ud}}\mathbf{\Phi}_\mathrm{d}\right]_i - \left[\mathbf{T}_\mathrm{u}\boldsymbol{\rho}\right]_i = 0 \tag{8.52}$$

Here $[\ ]_i$ denotes the ith element of the column or row vector inside and we used the fact that $\mathbf{P}_{\mathbf{uu}}$ is symmetric. When i ranges over all the elements of $\mathbf{\Phi}_u$ (8.52) results in a square matrix equation

$$\mathbf{P}_{\mathbf{uu}}\mathbf{\Phi}_\mathrm{u} = \mathbf{T}_\mathrm{u}\boldsymbol{\rho} - \mathbf{P}_{\mathbf{ud}}\mathbf{\Phi}_\mathrm{d} \tag{8.53}$$

Equation (8.53) is the final equation of the finite element method. In the usual finite element problem $\boldsymbol{\rho}$ is known and (8.53) yields $\mathbf{\Phi_u}$. $\mathbf{P}_{\mathbf{uu}}$ is a sparse, symmetric and positive-definite matrix and solution of the matrix equation for $\mathbf{\Phi_u}$ poses no difficulty. However, in our work $\boldsymbol{\rho}$ is also an unknown which is desired to be determined from Kerr electro-optic measurements.

8.4 Kerr Electro-Optic Measurement Expressions

In the AC modulation method used for sensitive Kerr electro-optic measurements the potential is composed of DC and AC parts

$$\mathbf{\Phi} = \mathbf{\Phi_{dc}} + \mathbf{\Phi_{ac}} \cos \omega t \tag{8.54}$$

The ac potential is not affected by the space charge and thus the unknown entries directly follow from (8.53) with $\boldsymbol{\rho} = \mathbf{0}$

$$\mathbf{\Phi_{u_{ac}}} = -\mathbf{P_{uu}^{-1}} \mathbf{P_{ud_{ac}}} \mathbf{\Phi_{d_{ac}}} \tag{8.55}$$

Equation (8.53) however cannot be used for the dc potential since $\boldsymbol{\rho}$ is not known and in fact is the quantity to be determined in Kerr electro-optic measurements. To incorporate Kerr electro-optic data to (8.53) it is necessary to express the Kerr electro-optic measurements in terms of the dc potential distribution.

Consider a set of Kerr electro-optic measurements indexed by i. The measured characteristic parameters are related to the electric field from (5.48) and (5.49) as

$$\gamma_{ac}^{(i)} \cos 2\alpha_{ac}^{(i)} = \pi B \int_{s_{\text{in}}^{(i)}}^{s_{\text{out}}^{(i)}} \left[E_{m_{ac}}^2(s) - E_{p_{ac}}^2(s) \right] \, ds \tag{8.56a}$$

$$\gamma_{ac}^{(i)} \sin 2\alpha_{ac}^{(i)} = \pi B \int_{s_{\text{in}}^{(i)}}^{s_{\text{out}}^{(i)}} 2 E_{m_{ac}}(s) E_{p_{ac}}(s) \, ds \tag{8.56b}$$

and

$$\gamma_{hy}^{(i)} \cos 2\alpha_{hy}^{(i)} = 4\pi B \int_{s_{\text{in}}^{(i)}}^{s_{\text{out}}^{(i)}} E_{m_{ac}}(s) E_{m_{dc}}(s) \, ds - 4\pi B \int_{s_{\text{in}}^{(i)}}^{s_{\text{out}}^{(i)}} E_{p_{ac}}(s) E_{p_{dc}}(s) \, ds \tag{8.57a}$$

$$\gamma_{hy}^{(i)} \sin 2\alpha_{hy}^{(i)} = 4\pi B \int_{s_{\text{in}}^{(i)}}^{s_{\text{out}}^{(i)}} E_{p_{ac}}(s) E_{m_{dc}}(s) \, ds + 4\pi B \int_{s_{\text{in}}^{(i)}}^{s_{\text{out}}^{(i)}} E_{m_{ac}}(s) E_{p_{dc}}(s) \, ds \tag{8.57b}$$

Here we limit the formulation to the case when all measurements are taken from light rays that are perpendicular to the axisymmetry axis z. Then $\hat{m}$ can be chosen to be equal to $\hat{z}$ so that (5.50) and (5.51) are valid

$$k_{c_{ac}}^{(i)} \equiv \frac{\gamma_{ac}^{(i)} \cos 2\alpha_{ac}^{(i)}}{\pi B} = 2 \int_{p_i}^{r_{\text{out}}^{(i)}} \left[E_{z_{ac}}^2(r, z_i) - \frac{p_i^2}{r^2} E_{r_{ac}}^2(r, z_i) \right] \frac{r \, dr}{\sqrt{r^2 - p_i^2}} \tag{8.58a}$$

$$k_{s_{ac}}^{(i)} \equiv \frac{\gamma_{ac}^{(i)} \sin 2\alpha_{ac}^{(i)}}{\pi B} = 4 \int_{p_i}^{r_{\text{out}}^{(i)}} E_{z_{ac}}(r, z_i) \frac{p_i}{r} E_{r_{ac}}(r, z_i) \frac{r\, dr}{\sqrt{r^2 - p_i^2}} \tag{8.58b}$$

and

$$k_{c_{hy}}^{(i)} \equiv \frac{\gamma_{hy}^{(i)} \cos 2\alpha_{hy}^{(i)}}{4\pi B} = 2 \int_{p_i}^{r_{\text{out}}^{(i)}} \left[E_{z_{ac}}(r, z_i) E_{z_{dc}}(r, z_i) - \frac{p_i^2}{r^2} E_{r_{ac}}(r, z_i) E_{r_{dc}}(r, z_i) \right] \frac{r\, dr}{\sqrt{r^2 - p_i^2}} \tag{8.58c}$$

$$k_{s_{hy}}^{(i)} \equiv \frac{\gamma_{hy}^{(i)} \sin 2\alpha_{hy}^{(i)}}{4\pi B} = 2 \int_{p_i}^{r_{\text{out}}^{(i)}} \frac{p_i}{r} \left[E_{r_{ac}}(r, z_i) E_{z_{dc}}(r, z_i) + E_{z_{ac}}(r, z_i) E_{r_{dc}}(r, z_i) \right] \frac{r\, dr}{\sqrt{r^2 - p_i^2}} \tag{8.58d}$$

where (p_i, z_i) is the position of the ith measurement as described in Figure 8.2 and $k_{c_{ac}}$, $k_{s_{ac}}$, $k_{c_{hy}}$, and $k_{s_{hy}}$ are defined to simplify coming expressions with the subscripts c and s to respectively represent cosine and sine terms. Equation (8.58) is a set of line integrals on the rz-plane over line segments with constant z coordinates. The triangular mesh partitions the line segments so that they are composed of smaller line segments each belonging to a single triangle element.

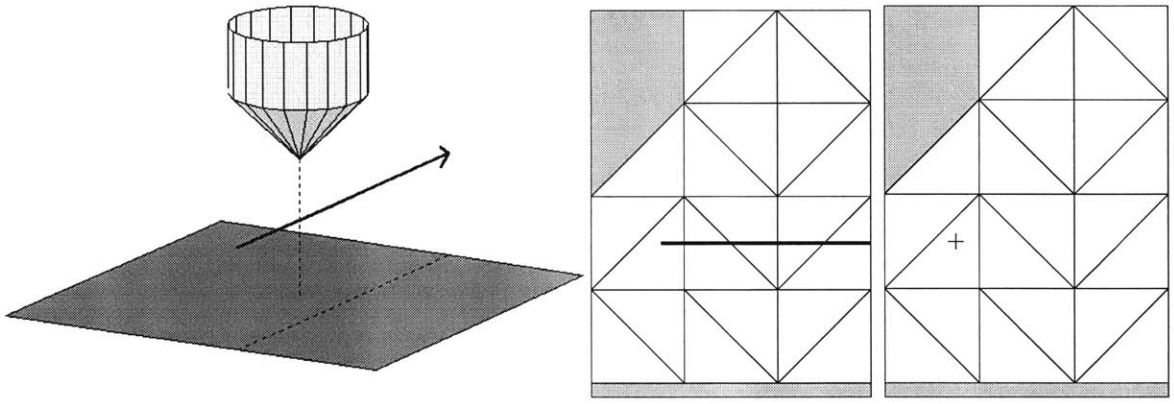

Figure 8.2: A Kerr electro-optic measurement path (left) is projected onto the rz-plane (middle) and partitioned into smaller paths each of which belongs to a single element. The line integrals that define the characteristic parameters can then be expressed as a sum over the elemental paths and evaluated in terms of the nodal values of the potential. In this work all measurements are taken from light rays that are perpendicular to the axisymmetry axis z so that the first point of the projected path completely describes the measurement. In this chapter this point is referred to as the position of the measurement. The right-hand figure illustrates the measurement position for the projected path in the middle figure.

Each integral in (8.58) can be expressed as the sum of integrals on elemental line segments

$$k_{c_{ac}}^{(i)} = 2\sum_e \left[\tilde{a}_{zz_e}(p_i, z_i) - \tilde{a}_{rr_e}(p_i, z_i)\right] \tag{8.59a}$$

$$k_{s_{ac}}^{(i)} = 4\sum_e \tilde{a}_{rz_e}(p_i, z_i) \tag{8.59b}$$

$$k_{c_{hy}}^{(i)} = 2\sum_e \left[\tilde{h}_{zz_e}(p_i, z_i) - \tilde{h}_{rr_e}(p_i, z_i)\right] \tag{8.59c}$$

$$k_{s_{hy}}^{(i)} = 2\sum_e \left[\tilde{h}_{rz_e}(p_i, z_i) + \tilde{h}_{zr_e}(p_i, z_i)\right] \tag{8.59d}$$

where

$$\tilde{a}_{zz_e}(p_i, z_i) = \int_{\tilde{r}_{0_e}}^{\tilde{r}_{1_e}} \frac{\tilde{E}_{z_{ac}}^2(r, z_i) r\, dr}{\sqrt{r^2 - p_i^2}} \tag{8.60a}$$

$$\tilde{a}_{rr_e}(p_i, z_i) = \int_{\tilde{r}_{0_e}}^{\tilde{r}_{1_e}} \frac{p_i^2 \tilde{E}_{r_{ac}}^2(r, z_i)\, dr}{r\sqrt{r^2 - p_i^2}} \tag{8.60b}$$

$$\tilde{a}_{rz_e}(p_i, z_i) = \int_{\tilde{r}_{0_e}}^{\tilde{r}_{1_e}} \frac{p_i \tilde{E}_{z_{ac}}(r, z_i) \tilde{E}_{r_{ac}}(r, z_i)\, dr}{\sqrt{r^2 - p_i^2}} \tag{8.60c}$$

$$\tilde{h}_{zz_e}(p_i, z_i) = \int_{\tilde{r}_{0_e}}^{\tilde{r}_{1_e}} \frac{\tilde{E}_{z_{ac}}(r, z_i) \tilde{E}_{z_{dc}}(r, z_i) r\, dr}{\sqrt{r^2 - p_i^2}} \tag{8.60d}$$

$$\tilde{h}_{rr_e}(p_i, z_i) = \int_{\tilde{r}_{0_e}}^{\tilde{r}_{1_e}} \frac{p_i^2 \tilde{E}_{r_{ac}}(r, z_i) \tilde{E}_{r_{dc}}(r, z_i)\, dr}{r\sqrt{r^2 - p_i^2}} \tag{8.60e}$$

$$\tilde{h}_{zr_e}(p_i, z_i) = \int_{\tilde{r}_{0_e}}^{\tilde{r}_{1_e}} \frac{p_i \tilde{E}_{r_{ac}}(r, z_i) \tilde{E}_{z_{dc}}(r, z_i)\, dr}{\sqrt{r^2 - p_i^2}} \tag{8.60f}$$

$$\tilde{h}_{rz_e}(p_i, z_i) = \int_{\tilde{r}_{0_e}}^{\tilde{r}_{1_e}} \frac{p_i \tilde{E}_{z_{ac}}(r, z_i) \tilde{E}_{r_{dc}}(r, z_i)\, dr}{\sqrt{r^2 - p_i^2}} \tag{8.60g}$$

and $\tilde{r}_{0_e}$ and $\tilde{r}_{1_e}$ denotes the points that the light ray enters and exits the eth triangular discretization element.

Each integral in (8.60) is within a triangular element on which the electric field components are polynomials in terms of the nodal values of the potential. Using the polynomial expressions in (8.20) and (8.21), we write (8.60) as

$$\tilde{a}_{zz_e}(p_i, z_i) = \tilde{\boldsymbol{\phi}}_{\mathbf{ac}_e}^{\mathrm{T}} \tilde{\mathbf{D}}_{\mathbf{z}_e}^{\mathrm{T}} \tilde{\mathbf{m}}_{\mathbf{zz}_e}(p_i, z_i) \tilde{\mathbf{D}}_{\mathbf{z}_e} \tilde{\boldsymbol{\phi}}_{\mathbf{ac}_e} \tag{8.61a}$$

$$\tilde{a}_{rr_e}(p_i, z_i) = \tilde{\boldsymbol{\phi}}_{\mathbf{ac}_e}^{\mathrm{T}} \tilde{\mathbf{D}}_{\mathbf{r}_e}^{\mathrm{T}} \tilde{\mathbf{m}}_{\mathbf{rr}_e}(p_i, z_i) \tilde{\mathbf{D}}_{\mathbf{r}_e} \tilde{\boldsymbol{\phi}}_{\mathbf{ac}_e} \tag{8.61b}$$

$$\tilde{a}_{rz_e}(p_i, z_i) = \tilde{\boldsymbol{\phi}}_{\mathbf{ac}_e}^{\mathrm{T}} \tilde{\mathbf{D}}_{\mathbf{r}_e}^{\mathrm{T}} \tilde{\mathbf{m}}_{\mathbf{rz}_e}(p_i, z_i) \tilde{\mathbf{D}}_{\mathbf{z}_e} \tilde{\boldsymbol{\phi}}_{\mathbf{ac}_e} \tag{8.61c}$$

$$\tilde{h}_{zz_e}(p_i, z_i) = \tilde{\boldsymbol{\phi}}_{\mathbf{ac}_e}^{\mathrm{T}} \tilde{\mathbf{D}}_{\mathbf{z}_e}^{\mathrm{T}} \tilde{\mathbf{m}}_{\mathbf{zz}_e}(p_i, z_i) \tilde{\mathbf{D}}_{\mathbf{z}_e} \tilde{\boldsymbol{\phi}}_{\mathbf{dc}_e} \tag{8.61d}$$

$$\tilde{h}_{rr_e}(p_i, z_i) = \tilde{\boldsymbol{\phi}}_{\mathbf{ac}_e}^{\mathrm{T}} \tilde{\mathbf{D}}_{\mathbf{r}_e}^{\mathrm{T}} \tilde{\mathbf{m}}_{\mathbf{rr}_e}(p_i, z_i) \tilde{\mathbf{D}}_{\mathbf{r}_e} \tilde{\boldsymbol{\phi}}_{\mathbf{dc}_e} \tag{8.61e}$$

$$\tilde{h}_{zr_e}(p_i, z_i) = \tilde{\boldsymbol{\phi}}_{\mathbf{ac}_e}^{\mathrm{T}} \tilde{\mathbf{D}}_{\mathbf{r}_e}^{\mathrm{T}} \tilde{\mathbf{m}}_{\mathbf{rz}_e}(p_i, z_i) \tilde{\mathbf{D}}_{\mathbf{z}_e} \tilde{\boldsymbol{\phi}}_{\mathbf{dc}_e} \tag{8.61f}$$

$$\tilde{h}_{rz_e}(p_i, z_i) = \tilde{\boldsymbol{\phi}}_{\mathbf{ac}_e}^{\mathrm{T}} \tilde{\mathbf{D}}_{\mathbf{z}_e}^{\mathrm{T}} \tilde{\mathbf{m}}_{\mathbf{rz}_e}(p_i, z_i) \tilde{\mathbf{D}}_{\mathbf{r}_e} \tilde{\boldsymbol{\phi}}_{\mathbf{dc}_e} \tag{8.61g}$$

where

$$\tilde{\mathbf{m}}_{\mathbf{zz}_e}(p_i, z_i) = \int_{\tilde{r}_{0_e}}^{\tilde{r}_{1_e}} \tilde{\boldsymbol{\zeta}}_e(r, z_i) \tilde{\boldsymbol{\zeta}}_e^{\mathrm{T}}(r, z_i) \frac{r\, dr}{\sqrt{r^2 - p_i^2}} \tag{8.62a}$$

$$\tilde{\mathbf{m}}_{\mathbf{rr}_e}(p_i, z_i) = \int_{\tilde{r}_{0_e}}^{\tilde{r}_{1_e}} \tilde{\boldsymbol{\zeta}}_e(r, z_i) \tilde{\boldsymbol{\zeta}}_e^{\mathrm{T}}(r, z_i) \frac{p_i^2\, dr}{r\sqrt{r^2 - p_i^2}} \tag{8.62b}$$

$$\tilde{\mathbf{m}}_{\mathbf{rz}_e}(p_i, z_i) = \int_{\tilde{r}_{0_e}}^{\tilde{r}_{1_e}} \tilde{\boldsymbol{\zeta}}_e(r, z_i) \tilde{\boldsymbol{\zeta}}_e^{\mathrm{T}}(r, z_i) \frac{p_i\, dr}{\sqrt{r^2 - p_i^2}} \tag{8.62c}$$

Here (8.61) expresses each integral in (8.60) in terms of the nodal values of the potential on the triangle.

To evaluate (8.62) analytically we note that each line integral is on a constant z line segment and for constant z_i, $\tilde{\zeta}_j$ in (8.1) is a first order polynomial in r

$$\tilde{\zeta}_j = \tilde{A}_j r + [\tilde{B}_j z_i + C_j] \tag{8.63}$$

Thus the elements of $\tilde{\boldsymbol{\zeta}}_e(r, z_i)\tilde{\boldsymbol{\zeta}}_e^{\mathrm{T}}(r, z_i)$ in (8.62) are second order polynomials in r. To simplify the evaluated forms of (8.62) we define three matrices $\boldsymbol{\chi}_{\mathbf{0}_e}$, $\boldsymbol{\chi}_{\mathbf{1}_e}$ and $\boldsymbol{\chi}_{\mathbf{2}_e}$ by

$$\tilde{\boldsymbol{\zeta}}_e(r, z_i)\tilde{\boldsymbol{\zeta}}_e^{\mathrm{T}}(r, z_i) = \boldsymbol{\chi}_{0_e}(z_i) + \boldsymbol{\chi}_{\mathbf{1}_e}(z_i) r + \boldsymbol{\chi}_{\mathbf{2}_e} r^2 \tag{8.64}$$

whose elements follow from (8.63) as

$$\left[\boldsymbol{\chi}_{\mathbf{0}_e}(z_i)\right]_{nj} = [C_n + B_n z_i][C_j + B_j z_i] \tag{8.65}$$

$$\left[\boldsymbol{\chi}_{\mathbf{0}_e}(z_i)\right]_{nj} = A_n[C_j + B_j z_i] + A_j[C_n + B_n z_i] \tag{8.66}$$

$$\left[\boldsymbol{\chi}_{0_e}\right]_{nj} = A_n A_j \tag{8.67}$$

Substituting (8.64) in (8.62) identifies the integrals to be evaluated as

$$\mathcal{I}_3(\tilde{r}_{1_e},\tilde{r}_{0_e}) = \int_{\tilde{r}_{0_e}}^{\tilde{r}_{1_e}} \frac{r^3\,dr}{\sqrt{r^2-p_i^2}} = \left[\frac{1}{3}\sqrt{(r^2-p_i^2)^3}+p_i^2\sqrt{r^2-p_i^2}\right]_{\tilde{r}_{0_e}}^{\tilde{r}_{1_e}} \tag{8.68a}$$

$$\mathcal{I}_2(\tilde{r}_{1_e},\tilde{r}_{0_e}) = \int_{\tilde{r}_{0_e}}^{\tilde{r}_{1_e}} \frac{r^2\,dr}{\sqrt{r^2-p_i^2}} = \left[\frac{r}{2}\sqrt{r^2-p_i^2}+\frac{p_i^2}{2}\ln\left[r+\sqrt{r^2-p_i^2}\right]\right]_{\tilde{r}_{0_e}}^{\tilde{r}_{1_e}} \tag{8.68b}$$

$$\mathcal{I}_1(\tilde{r}_{1_e},\tilde{r}_{0_e}) = \int_{\tilde{r}_{0_e}}^{\tilde{r}_{1_e}} \frac{r\,dr}{\sqrt{r^2-p_i^2}} = \left[\sqrt{r^2-p_i^2}\right]_{\tilde{r}_{0_e}}^{\tilde{r}_{1_e}} \tag{8.68c}$$

$$\mathcal{I}_0(\tilde{r}_{1_e},\tilde{r}_{0_e}) = \int_{\tilde{r}_{0_e}}^{\tilde{r}_{1_e}} \frac{dr}{\sqrt{r^2-p_i^2}} = \left[\ln\left[r+\sqrt{r^2-p_i^2}\right]\right]_{\tilde{r}_{0_e}}^{\tilde{r}_{1_e}} \tag{8.68d}$$

$$\mathcal{I}_r(\tilde{r}_{1_e},\tilde{r}_{0_e}) = \int_{\tilde{r}_{0_e}}^{\tilde{r}_{1_e}} \frac{dr}{r\sqrt{r^2-p_i^2}} = \left[\frac{1}{p_i}\text{arcsec}\frac{r}{p_i}\right]_{\tilde{r}_{0_e}}^{\tilde{r}_{1_e}} \tag{8.68e}$$

Using (8.64) and (8.68), (8.62) reduces to

$$\tilde{\mathbf{m}}_{\mathbf{zz}_e}(p_i,z_i) = \mathcal{I}_1(\tilde{r}_{1_e},\tilde{r}_{0_e})\boldsymbol{\chi}_{\mathbf{0}_e}(z_i)+\mathcal{I}_2(\tilde{r}_{1_e},\tilde{r}_{0_e})\boldsymbol{\chi}_{\mathbf{1}_e}(z_i)+\mathcal{I}_3(\tilde{r}_{1_e},\tilde{r}_{0_e})\boldsymbol{\chi}_{\mathbf{2}_e} \tag{8.69a}$$

$$\tilde{\mathbf{m}}_{\mathbf{rz}_e}(p_i,z_i) = p_i\mathcal{I}_0(\tilde{r}_{1_e},\tilde{r}_{0_e})\boldsymbol{\chi}_{\mathbf{0}_e}(z_i)+p_i\mathcal{I}_1(\tilde{r}_{1_e},\tilde{r}_{0_e})\boldsymbol{\chi}_{\mathbf{1}_e}(z_i)+p_i\mathcal{I}_2(\tilde{r}_{1_e},\tilde{r}_{0_e})\boldsymbol{\chi}_{\mathbf{2}_e} \tag{8.69b}$$

$$\tilde{\mathbf{m}}_{\mathbf{rr}_e}(p_i,z_i) = p_i^2\mathcal{I}_r(\tilde{r}_{1_e},\tilde{r}_{0_e})\boldsymbol{\chi}_{\mathbf{0}_e}(z_i)+p_i^2\mathcal{I}_0(\tilde{r}_{1_e},\tilde{r}_{0_e})\boldsymbol{\chi}_{\mathbf{1}_e}(z_i)+p_i^2\mathcal{I}_1(\tilde{r}_{1_e},\tilde{r}_{0_e})\boldsymbol{\chi}_{\mathbf{2}_e} \tag{8.69c}$$

Computations of the right hand side in (8.69) cause no difficulty except for the case $p_i = \tilde{r}_{0_e} = 0$ for which the L'Hopital rule must be used as

$$p_i\,\ln\left[\tilde{r}_{0_e}+\sqrt{\tilde{r}_{0_e}^2-p_i^2}\right]\Bigg|_{\tilde{r}_{0_e}=p_i=0} = 0 \tag{8.70}$$

$$p_i\,\text{arcsec}\frac{\tilde{r}_{0_e}}{p_i}\Bigg|_{\tilde{r}_{0_e}=p_i=0} = 0 \tag{8.71}$$

Also note that when $\tilde{r}_{0_e} \neq 0$, $p_i = 0$ $\text{arcsec}(\tilde{r}_{0_e}/p_i) = \pi/2$ is finite and thus

$$p\,\text{arcsec}\frac{\tilde{r}_{0_e}}{p_i}\Bigg|_{\tilde{r}_{0_e}\neq 0,p_i=0} = 0 \tag{8.72}$$

Using (8.61), (8.59) reduces to

$$k_{c_{ac}}^{(i)} = 2\sum_e \tilde{\boldsymbol{\phi}}_{\mathbf{ac}_e}^{\mathrm{T}}\tilde{\mathbf{M}}_{\mathbf{c}_e}^{(i)}\tilde{\boldsymbol{\phi}}_{\mathbf{ac}_e} \tag{8.73a}$$

$$k_{s_{ac}}^{(i)} = 2\sum_e \tilde{\boldsymbol{\phi}}_{\mathbf{ac}_e}^{\mathrm{T}}\tilde{\mathbf{M}}_{\mathbf{s}_e}^{(i)}\tilde{\boldsymbol{\phi}}_{\mathbf{ac}_e} \tag{8.73b}$$

$$k_{c_{hy}}^{(i)} = 2\sum_e \tilde{\boldsymbol{\phi}}_{\mathbf{ac}_e}^{\mathrm{T}} \tilde{\mathbf{M}}_{\mathbf{c}_e}^{(i)} \tilde{\boldsymbol{\phi}}_{\mathbf{dc}_e} \tag{8.73c}$$

$$k_{s_{hy}}^{(i)} = 2\sum_e \tilde{\boldsymbol{\phi}}_{\mathbf{ac}_e}^{\mathrm{T}} \tilde{\mathbf{M}}_{\mathbf{s}_e}^{(i)} \tilde{\boldsymbol{\phi}}_{\mathbf{dc}_e} \tag{8.73d}$$

where

$$\tilde{\mathbf{M}}_{\mathbf{c}_e}^{(i)} = \tilde{\mathbf{D}}_{\mathbf{z}_e}^{\mathrm{T}} \tilde{\mathbf{m}}_{\mathbf{zz}_e}(p_i, z_i) \tilde{\mathbf{D}}_{\mathbf{z}_e} - \tilde{\mathbf{D}}_{\mathbf{r}_e}^{\mathrm{T}} \tilde{\mathbf{m}}_{\mathbf{rr}_e}(p_i, z_i) \tilde{\mathbf{D}}_{\mathbf{r}_e} \tag{8.74}$$

$$\tilde{\mathbf{M}}_{\mathbf{s}_e}^{(i)} = \tilde{\mathbf{D}}_{\mathbf{z}_e}^{\mathrm{T}} \tilde{\mathbf{m}}_{\mathbf{rz}_e}(p_i, z_i) \tilde{\mathbf{D}}_{\mathbf{r}_e} + \tilde{\mathbf{D}}_{\mathbf{r}_e}^{\mathrm{T}} \tilde{\mathbf{m}}_{\mathbf{zr}_e}(p_i, z_i) \tilde{\mathbf{D}}_{\mathbf{z}_e} \tag{8.75}$$

Equation (8.73) relates the ith Kerr electro-optic measurement to the nodal values of electric potential. Similar to the development of the finite element energy functional, the sum in (8.73) is now expressed as a global matrix equation

$$k_{c_{ac}}^{(i)} = \boldsymbol{\Phi}_{\mathbf{ac}}^{\mathrm{T}} \mathbf{M}_{\mathbf{c}}^{(i)} \boldsymbol{\Phi}_{\mathbf{ac}} \tag{8.76a}$$

$$k_{s_{ac}}^{(i)} = \boldsymbol{\Phi}_{\mathbf{ac}}^{\mathrm{T}} \mathbf{M}_{\mathbf{s}}^{(i)} \boldsymbol{\Phi}_{\mathbf{ac}} \tag{8.76b}$$

$$k_{c_{hy}}^{(i)} = \boldsymbol{\Phi}_{\mathbf{ac}}^{\mathrm{T}} \mathbf{M}_{\mathbf{c}}^{(i)} \boldsymbol{\Phi}_{\mathbf{dc}} \tag{8.76c}$$

$$k_{s_{hy}}^{(i)} = \boldsymbol{\Phi}_{\mathbf{ac}}^{\mathrm{T}} \mathbf{M}_{\mathbf{s}}^{(i)} \boldsymbol{\Phi}_{\mathbf{dc}} \tag{8.76d}$$

where the matrices $\mathbf{M}_{\mathbf{c}}^{(i)}$ and $\mathbf{M}_{\mathbf{s}}^{(i)}$ are assembled from $\tilde{\mathbf{M}}_{\mathbf{c}_e}^{(i)}$ and $\tilde{\mathbf{M}}_{\mathbf{s}_e}^{(i)}$ in (8.74) and (8.75) in correspondence to the sums in (8.73).

Equation (8.76) is an expression for a single measurement. For a set of measurements (8.76) becomes

$$\mathbf{k}_{\mathbf{c_{ac}}} = \boldsymbol{\Phi}_{\mathbf{ac}}^{\mathrm{T}} \mathbf{M}_{\mathbf{c}} \boldsymbol{\Phi}_{\mathbf{ac}} \tag{8.77a}$$

$$\mathbf{k}_{\mathbf{s_{ac}}} = \boldsymbol{\Phi}_{\mathbf{ac}}^{\mathrm{T}} \mathbf{M}_{\mathbf{s}} \boldsymbol{\Phi}_{\mathbf{ac}} \tag{8.77b}$$

$$\mathbf{k}_{\mathbf{c_{hy}}} = \boldsymbol{\Phi}_{\mathbf{ac}}^{\mathrm{T}} \mathbf{M}_{\mathbf{c}} \boldsymbol{\Phi}_{\mathbf{dc}} \tag{8.77c}$$

$$\mathbf{k}_{\mathbf{s_{hy}}} = \boldsymbol{\Phi}_{\mathbf{ac}}^{\mathrm{T}} \mathbf{M}_{\mathbf{s}} \boldsymbol{\Phi}_{\mathbf{dc}} \tag{8.77d}$$

where the vectors $\mathbf{k}_{\mathbf{c_{ac}}}$, $\mathbf{k}_{\mathbf{s_{ac}}}$, $\mathbf{k}_{\mathbf{c_{hy}}}$, $\mathbf{k}_{\mathbf{s_{hy}}}$ respectively contain $k_{c_{ac}}^{(i)}$, $k_{s_{ac}}^{(i)}$ $k_{c_{hy}}^{(i)}$, $k_{s_{hy}}^{(i)}$ and the matrices $\mathbf{M}_{\mathbf{c}}$ and $\mathbf{M}_{\mathbf{s}}$ contain $\mathbf{M}_{\mathbf{c}}^{(i)}$ and $\mathbf{M}_{\mathbf{s}}^{(i)}$. For example, in its explicit form (8.77d)

is

$$\mathbf{k}_{\mathbf{s}_{\mathbf{hy}}} = \begin{bmatrix} k_{s_{hy}}^{(1)} \\ k_{s_{hy}}^{(2)} \\ \vdots \\ k_{s_{hy}}^{(n)} \end{bmatrix} = \mathbf{\Phi}_{\mathbf{ac}}^{\mathrm{T}} \begin{bmatrix} \mathbf{M}_{\mathbf{s}}^{(1)} \\ \mathbf{M}_{\mathbf{s}}^{(2)} \\ \vdots \\ \mathbf{M}_{\mathbf{s}}^{(n)} \end{bmatrix} \mathbf{\Phi}_{\mathbf{dc}} = \mathbf{\Phi}_{\mathbf{ac}}^{\mathrm{T}} \mathbf{M}_{\mathbf{s}} \mathbf{\Phi}_{\mathbf{dc}} \tag{8.78}$$

where n is the number of measurements.

Since $\mathbf{\Phi}_{\mathbf{ac}}$ is available from the finite element method, (8.77a) and (8.77b) do not provide any new information. They can however be used for statistical purposes on the experimental error. Equations (8.77c) and (8.77d) can be combined into a single matrix equation

$$\mathbf{k} = \begin{bmatrix} \mathbf{k}_{\mathbf{c}_{\mathbf{hy}}} \\ \mathbf{k}_{\mathbf{s}_{\mathbf{hy}}} \end{bmatrix} = \begin{bmatrix} \mathbf{\Phi}_{\mathbf{ac}}^{\mathrm{T}} \mathbf{M}_{\mathbf{c}} \\ \mathbf{\Phi}_{\mathbf{ac}}^{\mathrm{T}} \mathbf{M}_{\mathbf{s}} \end{bmatrix} \mathbf{\Phi}_{\mathbf{dc}} \tag{8.79}$$

which relate the measurements $\mathbf{k}$ to the dc potential. Since the potential values on the Dirichlet boundaries are already known we write (8.79) in the form

$$\mathbf{M}\mathbf{\Phi}_{\mathbf{u}_{\mathbf{dc}}} = \mathbf{k} - \mathbf{M}_{\mathbf{d}}\mathbf{\Phi}_{\mathbf{d}_{\mathbf{dc}}} \tag{8.80}$$

Here $\mathbf{M}$ and $\mathbf{M}_{\mathbf{d}}$ are the partitioned parts of the matrix in (8.79) with respect to the nodal potential values on Dirichlet boundaries and unknown potential values

$$\begin{bmatrix} \mathbf{M} & \mathbf{M}_{\mathbf{d}} \end{bmatrix} = \begin{bmatrix} \mathbf{\Phi}_{\mathbf{ac}}^{\mathrm{T}} \mathbf{M}_{\mathbf{c}} \\ \mathbf{\Phi}_{\mathbf{ac}}^{\mathrm{T}} \mathbf{M}_{\mathbf{s}} \end{bmatrix} \tag{8.81}$$

Equation (8.80) is the final result of this section. It relates the unknown dc potential values to the Kerr electro-optic measurements and the dc Dirichlet values. In principle it can be used as a basis for a family of reconstruction algorithms which reconstruct the potential distribution from Kerr electro-optic measurements. The potential distribution can then be used to calculate the electric field and space charge density. However with such an approach, any reconstruction error in reconstructed potential is greatly magnified in the electric field and space charge density values because of the differentiation and equation (8.53), which in essence is the discretized form of Poisson's equation that relates the electric potential and space charge density, is not utilized.

8.5 FEBKER

The equation that FEBKER relies on follows from (8.53) and (8.80)

$$\mathbf{M}\mathbf{P}_{\mathbf{uu}}^{-1}\mathbf{T}\boldsymbol{\rho} - \mathbf{k} - \left[\mathbf{M}\mathbf{P}_{\mathbf{uu}}^{-1}\mathbf{P}_{\mathbf{ud}} - \mathbf{M}_{\mathbf{d}}\right]\boldsymbol{\Phi}_{\mathbf{d_{dc}}} = 0 \tag{8.82}$$

Equation (8.82) is the fundamental result of this chapter. It relates the unknown space charge distribution $\boldsymbol{\rho}$ to the measurements $\mathbf{k}$ and the applied dc voltage $\boldsymbol{\Phi}_{\mathbf{d_{dc}}}$. In principle with enough measurements it is an overdetermined or a square matrix equation and can be solved as a least squares problem for which a number of established methods exist [60].

However solving (8.82) directly for $\boldsymbol{\rho}$ has two potential problems. First $\mathbf{M}\mathbf{P}_{\mathbf{uu}}^{-1}\mathbf{T}$ is a full matrix for which solution of the least squares problem is computationally expensive. The size of the least squares problem is determined by the size of $\boldsymbol{\rho}$ and for a typical finite element mesh with thousands of elements the computational time requirement is generally unacceptable. The second problem stems from the fact that the finite element method, as formulated in this work, minimizes an integrated error criterion. For individual triangular elements there may be great discrepancies between the specified charge density and the charge density found by taking the divergence of the numerical electric field solution. For (8.82) this translates into a considerable number of erroneous elements in $\boldsymbol{\rho}$. Of course one can always refine the mesh to improve $\boldsymbol{\rho}$, however this increases both the size of the problem and the number of measurements to make (8.82) an overdetermined or a square matrix equation.

8.5.1 ρ-Mesh Method

In this work we address the problems stated in the previous paragraph by specifying the space charge density $\boldsymbol{\rho}$ in terms of a less detailed mesh with fewer number of unknowns. In the following, such a mesh is referred to as ρ-mesh and the resulting methodology is referred to as ρ-mesh method. Figure 8.3 (b) illustrates a ρ-mesh on the example geometry. Here ρ-mesh consists of uniform squares imposed on top of the triangular FEM mesh shown in (a). Recall that each unknown entry in $\boldsymbol{\rho}$ corresponds to a triangle in the FEM mesh. If we group triangles in ρ-mesh squares and assume the space charge density is step-wise constant over ρ-mesh (as opposed to over individual triangles) then for the particular case of Figure 8.3 (b) the number of the unknowns is approximately halved since each square contains two triangles.

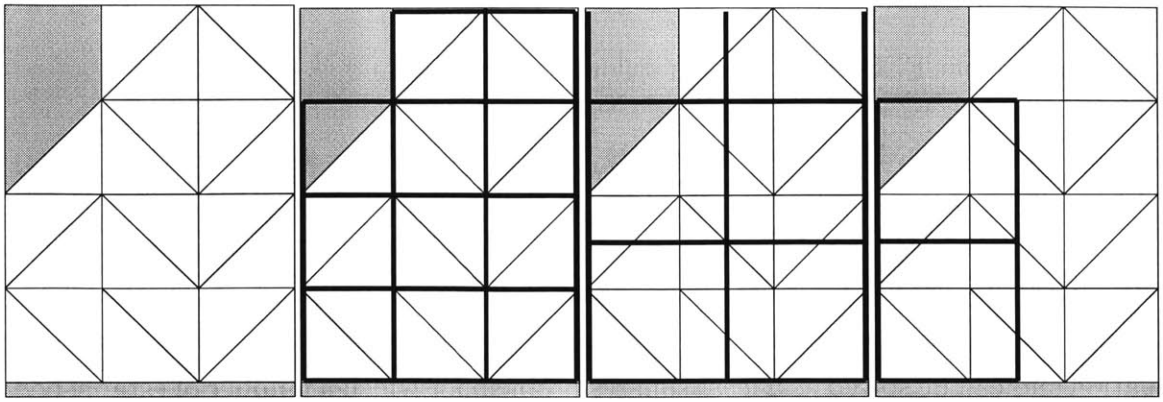

(a) (b) (c) (d)

Figure 8.3: The size of the least squares problem in (8.82) is determined by the size of $\boldsymbol{\rho}$ which is equal to the number of triangles in the FEM mesh. Each entry of $\boldsymbol{\rho}$ corresponds to an unknown value of space charge density in a triangle. In the ρ-mesh approach $\boldsymbol{\rho}$ is expressed in terms of a new set of unknowns which are specified on a less detailed mesh such as those shown in (b), (c) and (d).

For a realistic mesh (see Figure 8.5) each square can contain many more triangles reducing the number of unknowns more dramatically. Gathering a group of triangles in a ρ-mesh square on which the space charge density value is assumed to be constant is in essence averaging unknown space charge density values of individual triangles into a single space charge density value. Thus, the ρ-mesh method also averages out the error in the space charge values.

It is important to note that specifying a ρ-mesh to reduce the number of unknowns in $\boldsymbol{\rho}$ is not equivalent to formulating the FEM equation (8.53) in terms of the ρ-mesh. One extreme situation which clarifies the distinction is the case when the space charge density is constant throughout the geometry. Then the choice of ρ-mesh does not affect the quality of reconstructed elements of $\boldsymbol{\rho}$ from (8.82) since for perfect solution the values of the elements should be identical. However if ρ-mesh is also used to formulate (8.53) then the accuracy of $\mathbf{P_{uu}}$, $\mathbf{P_{ud}}$, $\mathbf{T}$, $\mathbf{M}$, and $\mathbf{M_d}$ will decrease degrading the quality of reconstructed $\boldsymbol{\rho}$ from (8.82).

Clearly the spatial resolution of the reconstructed space charge density does depend on the detail of the ρ-mesh. For example in Figure 8.3 (c) we show another ρ-mesh based on the example geometry. Obviously a reconstruction based on this ρ-mesh will have less spatial resolution than a reconstruction based on the ρ-mesh in (b). Note that the computational load to find the solution with less spatial resolution is also less. Thus the detail of ρ-mesh is a trade-off between the spatial resolution and computational

load. The number of measurements also figure in the decision for the choice of ρ-mesh because if the ρ-mesh is too detailed (8.82) becomes an underdetermined matrix equation. Figure 8.3 (c) also shows the typical situation where the elements of the FEM mesh does not necessarily lie inside of a single element in ρ-mesh. In this work we decide the ρ-mesh element that an individual triangle belongs to by the position of the triangle centroid; each triangle is assumed to belong to the square that contains its centroid. Also we only use uniform square ρ-meshes.

In a ρ-mesh it is not necessary to assume that space charge density is step-wise constant; one can use other assumed solution types. One immediate improvement over the step-wise constant approach is to use local solutions that are linear in r and z and interpolate values on the vertices of squares. For a square with edge length l and lower-left vertex coordinate $(\tilde{r}_{v_1}, \tilde{z}_{v_1})$ such a solution can be expressed by inspection

$$\begin{aligned}\tilde{\rho}(r,z) = \tilde{\rho}_{v_1}\left(1-\frac{r-\tilde{r}_{v_1}}{l}\right)\left(1-\frac{z-\tilde{z}_{v_1}}{l}\right) + \tilde{\rho}_{v_2}\left(\frac{r-\tilde{r}_{v_1}}{l}\right)\left(1-\frac{z-\tilde{z}_{v_1}}{l}\right) \\ + \tilde{\rho}_{v_3}\left(\frac{r-\tilde{r}_{v_1}}{l}\right)\left(\frac{z-\tilde{z}_{v_1}}{l}\right) + \tilde{\rho}_{v_4}\left(1-\frac{r-\tilde{r}_{v_1}}{l}\right)\left(\frac{z-\tilde{z}_{v_1}}{l}\right) \quad (8.83)\end{aligned}$$

where $\tilde{\rho}_{v_1}$, $\tilde{\rho}_{v_2}$, $\tilde{\rho}_{v_3}$, and $\tilde{\rho}_{v_4}$ are respectively the space charge density values on lower-left vertex, lower-right vertex, upper-right vertex and upper-left vertex. Each entry of $\boldsymbol{\rho}$ can then be found in terms of $\tilde{\rho}_{v_i}$ by evaluating (8.83) on the centroid of the corresponding triangle for the square that the triangle belongs to. Note that for the example ρ-mesh in Figure 8.3 (b) this does not decrease the number of unknowns. However this is an extreme case where each square contains only two triangles. When each square contains many triangles the number of unknowns again decrease dramatically. Also notice that although for each square there are now 4 unknowns some of these unknowns are shared with the neighbor squares. For a typical mesh the number of unknowns defined by the step-wise constant approach approximately doubles for the locally linear approach. This increase in the unknowns is justified by the superiority that the local linear functions can represent arbitrary space charge distributions. In this work we use both the step-wise approach and the local linear approach.

We did not use any physical arguments to reduce the number of unknowns. The ρ-mesh method is valid for any electrode geometry. The physical expectations that the electrode geometry imposes on the space charge density can be used to reduce the number of unknowns further. For point/plane electrode geometry, which constitutes the case study in this work, space charge injection is expected to be mostly from the

needle. In fact the wide use of point/plane electrode geometry in high voltage research is due to the localization of space charge injection. Far from the needle axis the space charge density is expected to vanish. Thus one can assume from the outset that the elements of $\boldsymbol{\rho}$ that corresponds to outer triangles are zero. We illustrate the approach in Figure 8.3 (d). Here ρ-mesh consists of just two squares under the needle. On the outer triangles the space charge density values are assumed to be zero. Notice that the number of unknowns reduced from 21 in Figure 8.3 (a) to 2 for(d) when we use the step-wise constant approach and to 6 when we use the locally linear approach.

The ρ-mesh method can be mathematically described by a matrix equation that relates $\boldsymbol{\rho}$ to a new unknown vector which we denote by $\boldsymbol{\varrho}$

$$\boldsymbol{\rho} = \mathbf{U}\boldsymbol{\varrho} \tag{8.84}$$

Here $\mathbf{U}$ is a rectangular matrix. If $\mathbf{U}$'s row number is larger than its column number then the size of the least squares problem reduces. Note that for step-wise constant ρ-method each row of $\mathbf{U}$ is either all zeros (for triangles outside the ρ-mesh that are assumed to have zero space charge density) or contains a single nonzero element which is 1. For locally linear each non-zero row now has 4 non-zero elements whose magnitudes are dictated by (8.83).

8.5.2 Measurement Positions and One Parameter Measurements

In (8.82) the size of the measurement vector $\mathbf{k}$ is two times the number of measurements since each measurement can yield two independent parameters. Since the number of equations is determined by the size of $\mathbf{k}$ and the number of unknowns is determined by the size of $\boldsymbol{\varrho}$ in (8.84), the number of measurements required to make (8.82) square or overdetermined is at least half the size of $\boldsymbol{\varrho}$.

In Figure 8.4 we consider a ρ-mesh of six squares on the example geometry. Assuming the space charge density is step-wise constant over ρ-mesh, $\boldsymbol{\varrho}$ is six dimensional; there are six unknowns. In (a) there are six measurement positions resulting in twelve characteristic parameters; $\mathbf{k}$ is twelve dimensional. Thus for the set-up in (a) (8.82) is a 12×6 overdetermined matrix equation. In (b) there are three measurement positions resulting in six characteristic parameters. Then for the set-up in (b) (8.82) is a 6×6 square matrix equation.

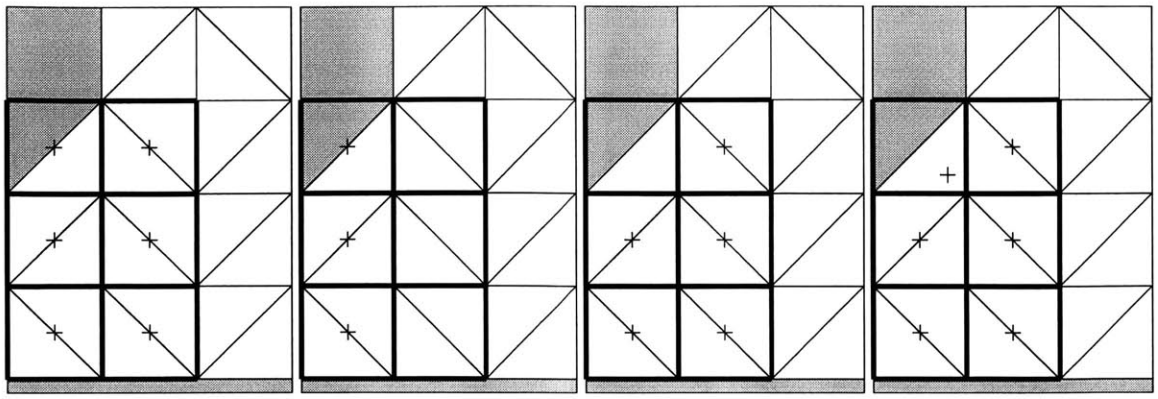

(a) (b) (c) (d)

Figure 8.4: Different measurement combinations which are used for illustrative purposes.

Recall from Section 5.5 and in particular from (5.45) that two parameter Kerr electro-optic measurements requires rotating the analyzer during experiments. Rotating the analyzer is slow making it impractical to investigate time transient charge injection and transport using Kerr electro-optic measurements. As discussed in the previous paragraph for the set-up in Figure 8.4 (a) (8.82) is a 12×6 overdetermined matrix equation. This suggests that if we use one parameter measurements that does not require analyzer rotation we can still obtain a 6×6 square system which can still be solved to determine $\boldsymbol{\varrho}$.

To incorporate single parameter measurements into the formulation in (8.82), we first normalize (5.45) to define a normalized intensity measurement k_ω

$$k_\omega \equiv \frac{1}{4\pi B} I_\omega / I_{dc} = \frac{\gamma_{hy}}{4\pi B} \sin\bigl(2\alpha_{hy} - 2\theta_a\bigr) \tag{8.85}$$

Then it follows from (8.58) that for the ith measurement

$$k_\omega^{(i)} = -\sin 2\theta_a k_{c_{hy}}^{(i)} + \cos 2\theta_a k_{s_{hy}}^{(i)} \tag{8.86}$$

Thus for any fixed analyzer angle, the set of $k_\omega^{(i)}$ follows from (8.79) (also see (8.78))

$$\begin{bmatrix} k_\omega^{(1)} \\ k_\omega^{(2)} \\ \vdots \\ k_\omega^{(n)} \end{bmatrix} = \mathbf{Vk} \tag{8.87}$$

where n is the number of measurements and $\mathbf{V}$ is the $n \times 2n$ matrix given by

$$\mathbf{V} = \begin{bmatrix} -\sin 2\theta_a \mathbf{I} & \cos 2\theta_a \mathbf{I} \end{bmatrix} \tag{8.88}$$

with $\mathbf{I}$ denoting the identity matrix. Then for any particular analyzer angle the one parameter measurement least squares problem is obtained by multiplying (8.82) with $\mathbf{V}$.

Finally we note that beside the number of measurements, the positions of the measurements are also important for the quality of the solutions of (8.82). Consider Figure 8.4 (c) where there are five two parameter measurements for which (8.82) is an overdetermined system. The only difference between (a) and (c) is that for (c) the measurement right under the needle is not used. This has considerable practical significance since it shows that it might be possible to use FEBKER even when there are missing measurements around the needle tip due to blockage and/or extreme noise. However since there are no measurements directly related to this region the reconstructed space charge value for this region can be in great error. This problem can be solved by adding a measurement position as illustrated in Figure 8.4 (d) which is relatively far from the needle but in the region just under the needle.

8.5.3 Summary

With the improvements discussed in (8.5.1) and (8.5.2), (8.82) is modified to

$$\mathbf{VMP}_{\mathbf{uu}}^{-1}\mathbf{TU}\boldsymbol{\varrho} - \mathbf{Vk} - \mathbf{V}\left[\mathbf{MP}_{\mathbf{uu}}^{-1}\mathbf{P}_{\mathbf{ud}} - \mathbf{M}_{\mathbf{d}}\right]\boldsymbol{\Phi}_{\mathbf{d_{dc}}} = 0 \tag{8.89}$$

Here $\mathbf{V}$ is the identity matrix for two parameter measurements and given in (8.88) for one parameter measurements. Similarly $\mathbf{U}$ is the identity matrix if the ρ-mesh method is not being used and assumes various other forms when the ρ-mesh method with step-wise constant approach or locally linear approach is used.

8.6 Application Of FEBKER

In this section, as a case study we apply FEBKER to the finite point/plane electrode geometry in Appendix C. It is assumed that the peak applied ac and dc voltages are the same at 40 kV and the space charge distribution is given as in Figure C.4 with $\tilde{\rho}_0 = 0.12$ C/m^3. Note that the space charge density is non zero only within a 1 mm radius of the axisymmetry axis. The medium is transformer oil.

In Figure 8.5 we show the ρ-mesh that is used to decrease the number of unknown space charge density values as discussed in Section 8.5. We assume that the space charge density is zero outside a 1.25 mm radius of the axisymmetry axis. The value 1.25 mm is chosen as opposed to the actual value of 1 mm to simulate the fact that in an actual measurement the exact radius is not known but can be estimated using the convergence of fundamental and double harmonic light intensity measurements with the ac modulation method. Note that ρ-mesh method decreases the number of unknowns from ~5500 to ~60 for the step-wise constant approach and ~150 for the locally linear approach.

We use uniformly spaced measurements with distance of 0.1 mm both in the p and z directions. Only measurements within the 1.5 mm radius of the axisymmetry axis are used. In this section we only use perfect synthetic data which is obtained from numerical integrations of (8.57) using the finite element solutions of the electric field for the specified charge density. Section 8.7 investigates the impact of error on the reconstructions. The least squares problem in (8.89) is solved using both the method of normal equations and QR factorization. The difference between these two methods were negligible.

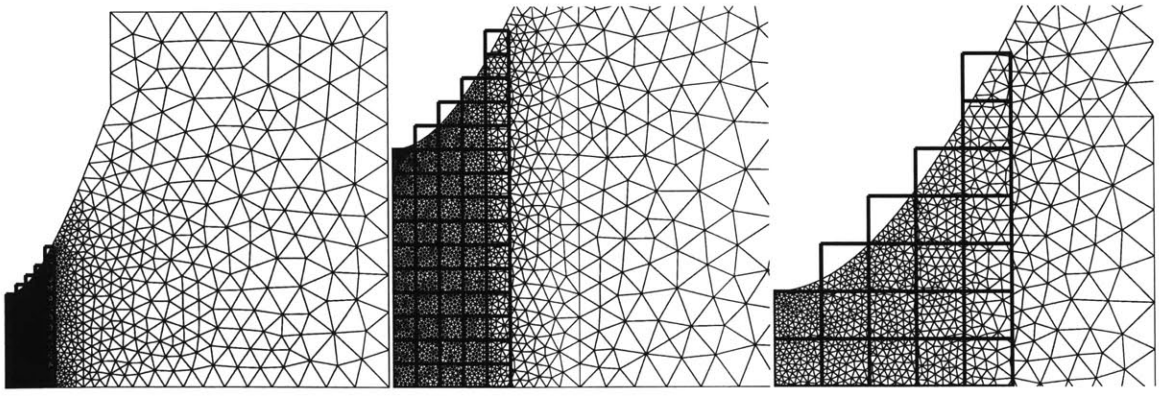

Figure 8.5: The ρ-mesh used for the case study in this section.

Figure 8.6 shows the reconstruction results when the step-wise constant approach is used. For the upper left reconstruction two parameter measurements are used while for the upper right reconstruction single parameter measurements with $\theta_a = \pi/2$ are used. The reconstruction results show that FEBKER reconstructs the space charge density accurately for both cases. The bottom left and bottom right reconstructions are based on one parameter measurements which are not closer than 0.3 mm and 0.5 mm to the needle tip respectively. These results suggests that FEBKER is applicable even when measurements at certain locations are not available. However when there are not enough measurements results at certain positions become undependable.

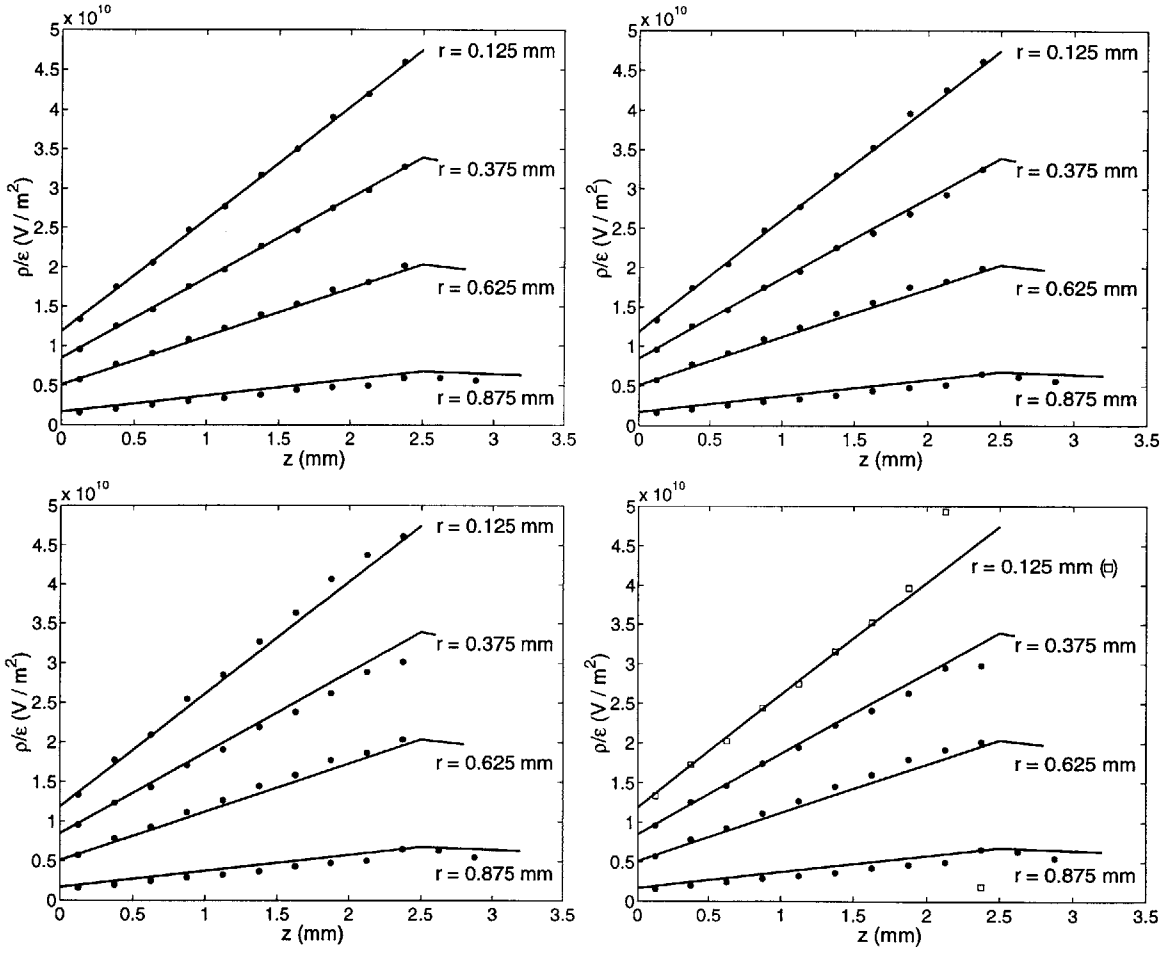

Figure 8.6: Charge density reconstructions using FEBKER with the step-wise constant approach. The upper left reconstruction is based on two parameter measurements, the upper right reconstruction is based on one parameter measurements ($\theta_a = \pi/2$), the lower left reconstruction does not use measurements that are less than 0.3 mm distance to the needle tip and the lower right reconstruction does not use measurements that are less than 0.5 mm distance to the needle tip.

Figure 8.7 shows the reconstruction results when the locally linear approach is used. The upper left reconstruction is based on two parameter measurements while the upper right reconstruction is based on single parameter measurements with $\theta_a = \pi/2$. The results are more accurate than those in Figure 8.6 as expected since the locally linear approach perfectly models the space charge distribution shown in Figure C.4. Similar to those in Figure 8.6, the bottom reconstructions do not use measurements around the needle tip. Note that for the locally linear approach the range of measurements that can be left out without any major impact on the reconstructions (1.3 mm) is much larger than the similar range for the step-wise constant approach (0.5 mm).

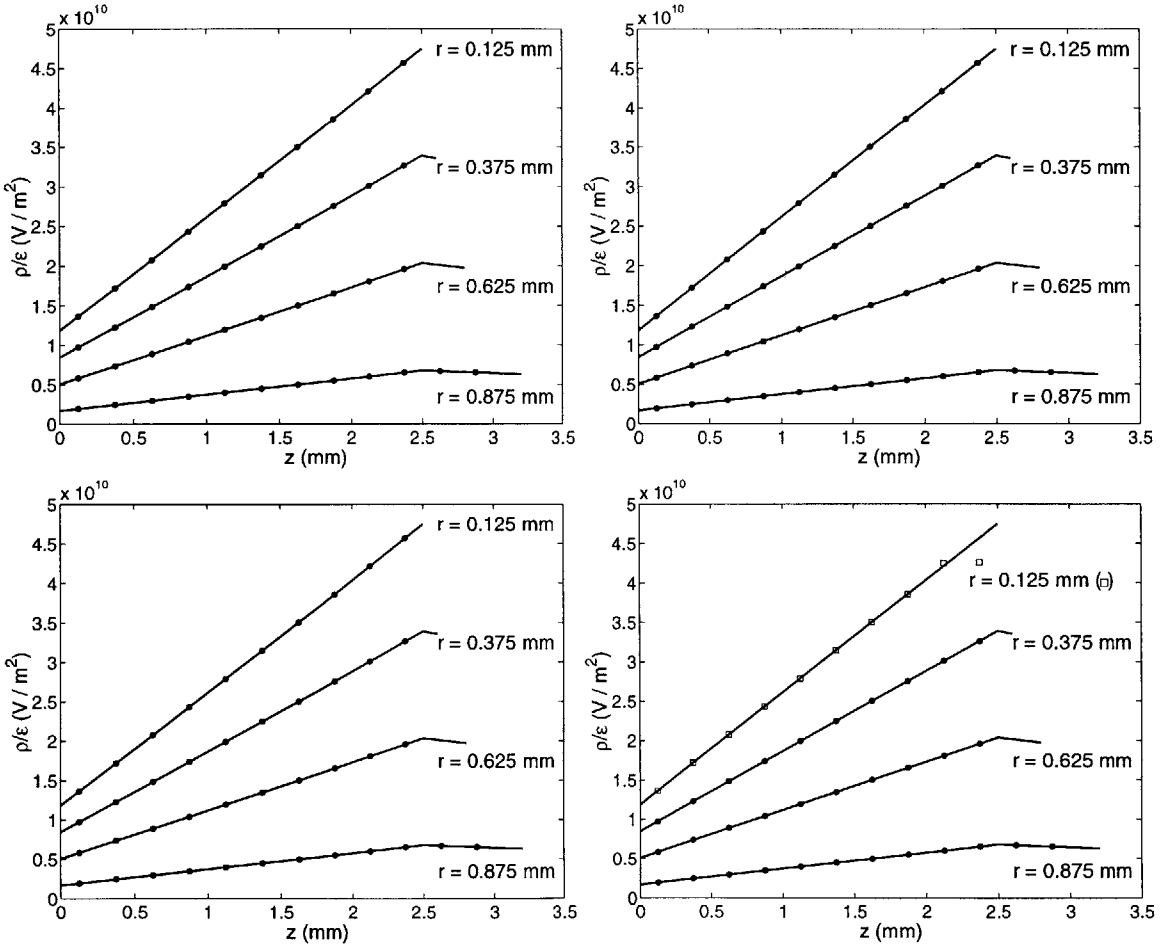

Figure 8.7: Charge density reconstructions using FEBKER with the locally linear approach. The upper left reconstruction is based on two parameter measurements, the upper right reconstruction is based on one parameter measurements ($\theta_a = \pi/2$), the lower left reconstruction does not use measurements that are less than 1 mm distance to the needle tip and the lower right reconstruction does not use measurements that are less than 1.3 mm distance to the needle tip.

8.7 Impact Of Error And Regularization

Reconstructions from line integrals are in general ill-posed. Even small amount of noise can have large effect in the performance of FEBKER. The top reconstructions in Figure 8.8 illustrate the difference between using perfect synthetic data and 5% random noise added synthetic data, both based on one parameter measurements. The results are typical of ill-posed problems; in the presence of noise a direct application of FEBKER results in completely unintelligible results. In this section we use regularization to decrease the impact of the noise.

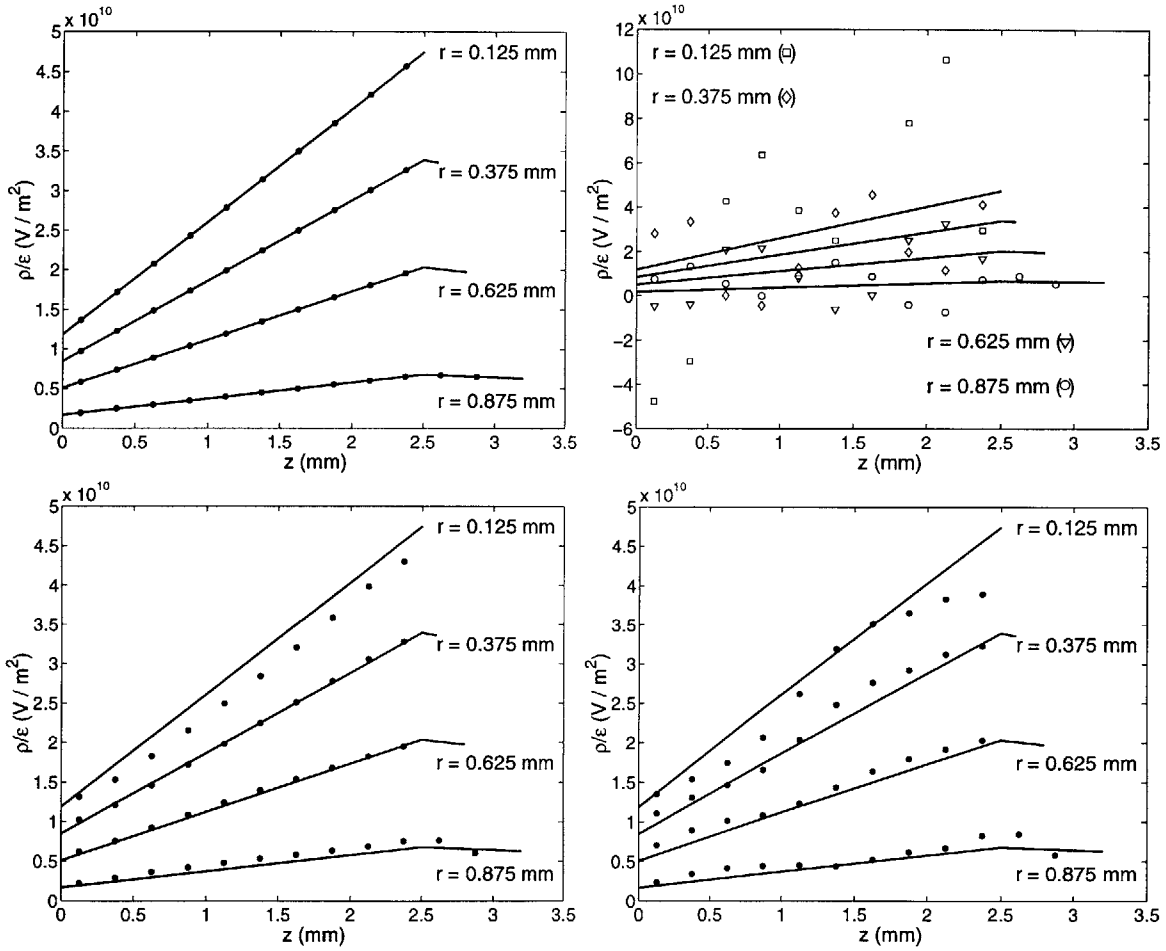

Figure 8.8: Charge density reconstructions using FEBKER using the locally linear approach. All reconstructions are based on one parameter measurements. The upper left and upper right reconstructions are respectively from perfect synthetic data and synthetic data with 5% random noise. The bottom reconstructions use the same data but regularization is incorporated to the reconstruction algorithm.

By regularization we mean using an extra information about the space charge distribution. Here as the extra information we assume that the space charge density distribution is smooth (differentiable). Then one can put a penalty on the variations between neighbor reconstructed values; for reconstructions using the locally linear approach neighbor values are the elements of $\boldsymbol{\rho}$ that corresponds neighbor vertices in the ρ-mesh shown in Figure 8.5. To illustrate regularization mathematically we write (8.89) in the form

$$\mathbf{A}\boldsymbol{\varrho} - \mathbf{b} = \mathbf{0} \tag{8.90}$$

where

$$\mathbf{A} = \mathbf{V}\mathbf{M}\mathbf{P}_{\mathbf{uu}}^{-1}\mathbf{T}\mathbf{U} \tag{8.91}$$

$$\mathbf{b} = \mathbf{V}\mathbf{k} + \mathbf{V}\left[\mathbf{M}\mathbf{P}_{\mathbf{uu}}^{-1}\mathbf{P}_{\mathbf{ud}} - \mathbf{M}_{\mathbf{d}}\right]\boldsymbol{\Phi}_{\mathbf{d_{dc}}} \tag{8.92}$$

The least squares problem in (8.90) is the minimization of the functional

$$\mathcal{A}(\boldsymbol{\varrho}) = \|\mathbf{A}\boldsymbol{\varrho} - \mathbf{b}\|^2 \tag{8.93}$$

where $\|\quad\|$ denotes the two norm of a vector. Instead of (8.93), the regularized least squares problem minimizes a related functional.

$$\mathcal{L}(\boldsymbol{\varrho}) = \mathcal{A}(\boldsymbol{\varrho}) + \lambda\mathcal{B}(\boldsymbol{\varrho}) \tag{8.94}$$

where λ is a nonnegative constant and $\mathcal{B}(\boldsymbol{\varrho})$ is measure for variations between neighbor elements of $\boldsymbol{\varrho}$. $\mathcal{B}(\boldsymbol{\varrho})$ is typically expressed in terms of a matrix $\mathbf{B}$

$$\mathcal{B}(\boldsymbol{\varrho}) = \|\mathbf{B}\boldsymbol{\varrho}\|^2 \tag{8.95}$$

When $\mathcal{L}(\boldsymbol{\varrho})$ is minimized to find $\boldsymbol{\varrho}$ instead of $\mathcal{A}(\boldsymbol{\varrho})$, the added penalty on the variations suppresses the impact of noise.

Clearly the success of the regularization is dependent on the choice of $\mathbf{B}$ and λ. We will not go into detail on how to choose the matrix $\mathbf{B}$ and the constant λ. In fact this is still an active research topic and is very much dependent on the application. Here we choose $\mathbf{B}$ such that minimization of $\mathcal{B}(\boldsymbol{\varrho})$ is equivalent to minimization of the

average difference between the neighbor elements of $\boldsymbol{\varrho}$ and λ is given as

$$\lambda = \frac{\text{Trace}(\mathbf{A}^{\mathrm{T}}\mathbf{A})}{\text{Trace}(\mathbf{B}^{\mathrm{T}}\mathbf{B})} \tag{8.96}$$

as suggested in [45].

Bottom reconstructions in Figure 8.8 we show the effects of regularization. The left reconstruction is based on synthetic data without any added noise. Notice that regularization causes significant distortion at $r = 0.125$ mm. This distortion is due to our assumed form of space charge density in Figure C.4 which is not differentiable at $r = 0$. Regularization smoothes out the space charge density at $r = 0$ causing lower than expected values. The right reconstruction shows the reconstruction when 5% random noise is added to the synthetic data. Remarkably the impact of noise is not very significant which proves that with regularization FEBKER can be used in the presence of noise.

In (8.8) the distortion caused by regularization at $r = 0.125$ mm Figure C.4 is only due to the assumed form of space charge density which is rather unphysical since it is not differentiable at the axisymmetry axis. Note that this piece-wise linear form is chosen for its simplicity. A comparably simple space charge density distribution which is differentiable at $r = 0$ is given in Figure 8.10. The difference between this distribution and the one in Figure 8.10 is the r dependence between 0 and 1 mm.

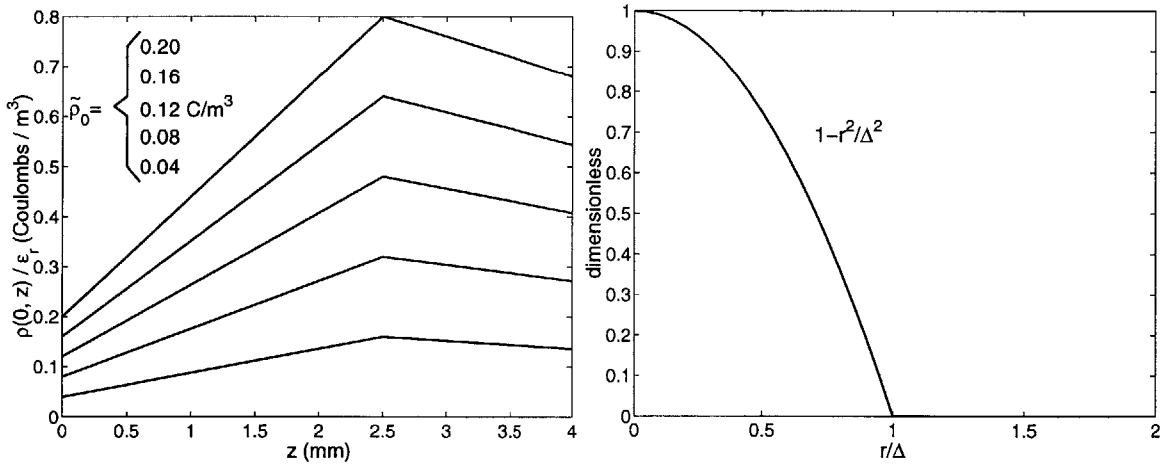

Figure 8.9: Case study space charge density distributions for the geometry shown in Figure C.1. The two dimensional charge density $\rho(r, z)$ can be found by multiplying the z dependence on the left and the r dependence on the right. The relative dielectric constant of the medium is ϵ_r.

In Figure 8.10 we show the reconstruction results when the space charge distribution in Figure 8.9 (with $\tilde{\rho}_0 = 0.12$ C/m^3) is used instead of the one in Figure C.4. As expected the distortion caused by the regularization is considerably less and the impact noise does not diminish the applicability of FEBKER.

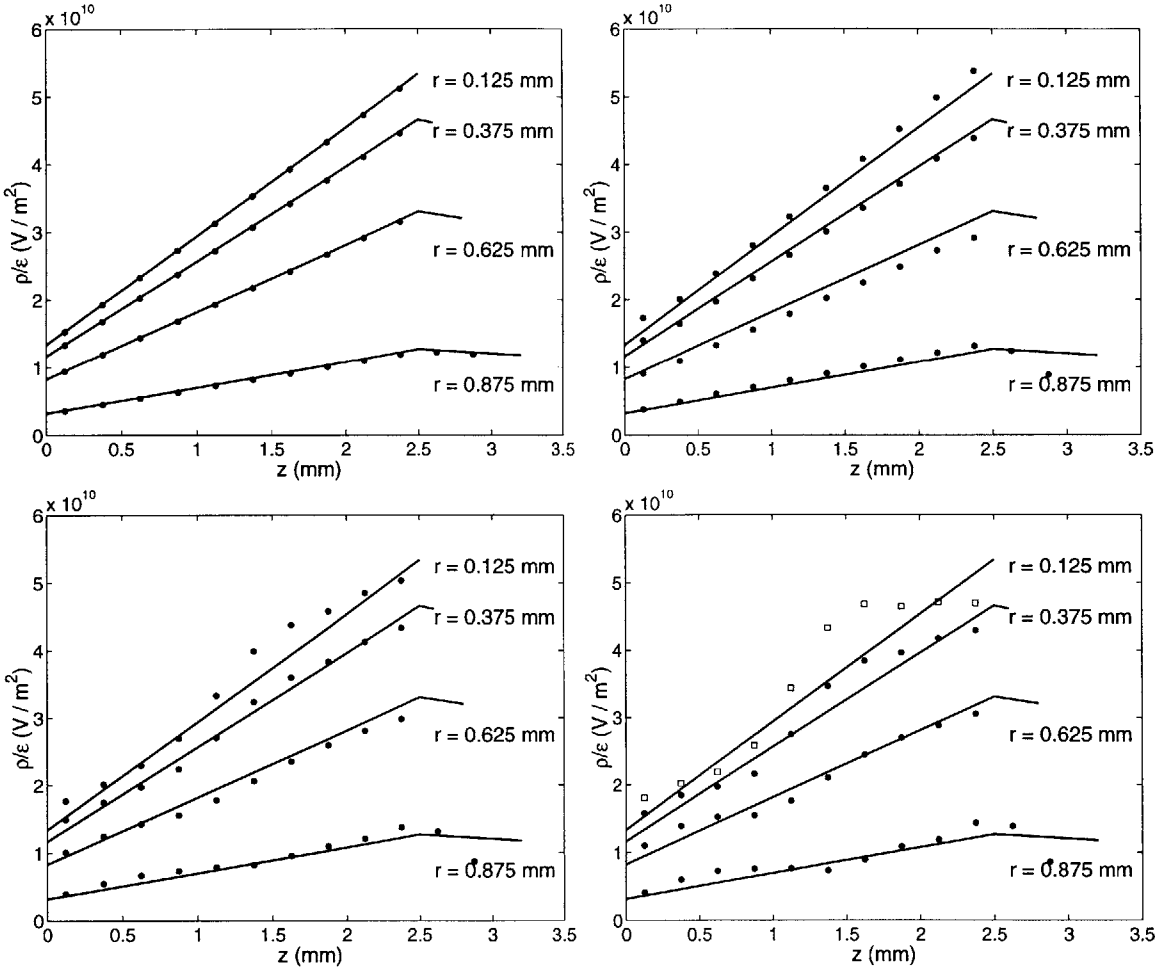

Figure 8.10: Charge density reconstructions using FEBKER using the locally linear approach. All reconstructions are based on one parameter measurements. The upper left and upper right reconstructions are from perfect synthetic data with and without regularization. The bottom regularized reconstructions are from noisy data with 5% and 10% random noise respectively.

Chapter 9

Transform Methods

9.1 Introduction

The reconstruction methods introduced in Chapters 6 to 8 discretize the electric field and/or space charge density distributions in terms of unknown coefficients which are then found by minimizing the difference between the measurements and forward theory based predictions based on the discretized electric field. In scalar tomography similar methods are often called algebraic.

A second family of methods in scalar tomography are called transform methods and are based on mathematical forward and inverse transform relations between the measurables and the quantities to be reconstructed. Especially in medical tomography the transform methods are often preferred over algebraic techniques due to their better performance.

For planes where the electric field direction is constant along the light path, transform methods of scalar tomography can be directly applied to Kerr electro-optic measurements. However generalization of the methods to Kerr media for which the electric field direction changes along the light path is not straight-forward due to the complex dependence of the characteristic parameters on the electric field components. In this chapter we briefly discuss transform methods and the main difficulties faced for their application to Kerr electro-optic measurements.

9.2 Axisymmetric Problem And Abel Transform

When the electric field direction is constant and perpendicular along the light path the characteristic phase retardation γ_c is related to the electric field magnitude by

$$\gamma_c = \pi B \int_{-\infty}^{\infty} E^2(s)\, ds \tag{9.1}$$

where we used subscript c to indicate constant direction. If in addition the electric field magnitude is axisymmetric (9.1) can be reduced to

$$\gamma_c = 2\pi B \int_{p}^{\infty} \frac{E^2(r)\, r\, dr}{\sqrt{r^2 - p^2}} \tag{9.2}$$

where p is the position of the measurement on the radial axis. For example (9.2) can be used to relate the characteristic phase retardation to the electric field magnitude in Kerr electro-optic measurements on the ground planes of point/plane or sphere/plane electrode geometries.

For varying p, (9.2) is one form of the well known Abel integral equations which arise frequently in different disciplines of science and engineering [61]. Its relevance to Kerr electro-optic measurements was first recognized by Zahn [4]. The solution of (9.2) is

$$E^2(r) = \frac{-1}{\pi^2 B r} \frac{d}{dr} \int_{r}^{\infty} \frac{\gamma_c(p)\, p\, dp}{\sqrt{p^2 - r^2}} = \frac{-1}{\pi^2 B} \int_{r}^{\infty} \frac{d\gamma_c(p)}{dp} \frac{dp}{\sqrt{p^2 - r^2}} \tag{9.3}$$

where we used the condition that the electric field magnitude is zero at $p = \infty$.

Equation (9.3) is an explicit formula that gives E^2 in terms of γ_c. Finding E^2 from experimental γ_c is still not a trivial task due to the singularity of the integral at $p = r$ and for evaluating the derivative of γ_c with respect to p. Nevertheless with additional mathematical machinery (9.3) can be used to reconstruct E^2.

Inverse transforms similar to (9.3) provide the basis of transform methods. These methods are profoundly different than methods similar to those in Chapters 6 to 8 in that the problem reduces to evaluating an inverse transform similar to (9.3). This may or may not be the better choice depending on the complexity and error characteristics of the inverse transform.

For general highly birefringent Kerr media, integral transforms that relate the characteristic parameters to the applied electric field do not exist. Thus there is not even

a starting point to develop an inverse transform. For axisymmetric weak Kerr media the situation is more optimistic as the forward transforms do exist as discussed in Section 4.4.4

$$k_c \equiv \gamma \cos 2\alpha = 2\pi B \int_p^\infty \frac{E_z^2(r)\, r\, dr}{\sqrt{r^2 - p^2}} - 2\pi B \int_p^\infty \frac{E_r^2(r)\, p^2\, dr}{r\sqrt{r^2 - p^2}} \tag{9.4}$$

$$k_s \equiv \gamma \sin 2\alpha = 2\pi B \int_p^\infty \frac{E_z(r)\, E_r(r)\, p\, dr}{\sqrt{r^2 - p^2}} \tag{9.5}$$

In analogy to (9.3) the inverse transform of (9.5) yields

$$E_z(r)E_r(r) = \frac{-1}{\pi^2 B}\frac{d}{dr}\int_r^\infty \frac{k_s(p)\, dp}{\sqrt{p^2 - r^2}} \tag{9.6}$$

We define

$$k_{c_z} = 2\pi B \int_p^\infty \frac{E_z^2(r)\, r\, dr}{\sqrt{r^2 - p^2}} \tag{9.7}$$

$$k_{c_r} = 2\pi B \int_p^\infty \frac{E_r^2(r)\, p^2\, dr}{r\sqrt{r^2 - p^2}} \tag{9.8}$$

Again in analogy to (9.3) we get

$$E_z^2(r) = \frac{-1}{\pi^2 B r}\frac{d}{dr}\int_r^\infty \frac{k_{c_z}(p)\, p\, dp}{\sqrt{p^2 - r^2}} \tag{9.9a}$$

$$E_r^2(r) = \frac{-r}{\pi^2 B}\frac{d}{dr}\int_r^\infty \frac{k_{c_r}(p)\, dp}{p\sqrt{p^2 - r^2}} \tag{9.9b}$$

Equation (9.6) shows that it is possible to use transform methods to recover the product of E_z and E_r. Unfortunately it appears from (9.9) that to use the transform methods for k_c is not possible as it requires individual access to parts k_{c_z} and k_{c_r}. Thus at this time we are unable to use transform methods to reconstruct the electric fields. Transforms in (9.4) and (9.5) and inverse transforms in (9.6) and (9.9) have been well studied in the math literature [62,63] and it might be possible to use various properties to combine (9.9) into a single equation. Even if that is achieved however further numerical analysis is necessary to use the inverse transforms to reconstruct the electric field from characteristic parameters as inverse transforms similar to the inverse Abel transform are highly ill-posed. This challenge requires more extensive research which we leave to future work.

For the axisymmetric problem we finally note that if ac modulation is being used, as already stated in (5.50) and (5.51), (9.4) and (9.5) are replaced by

$$k_{c_{hy}} \equiv \gamma_{hy} \cos 2\alpha_{hy} = 8\pi B \int_p^\infty \frac{E_{z_{ac}}(r)\, E_{z_{dc}}(r)\, r\, dr}{\sqrt{r^2 - p^2}} - 8\pi B \int_p^\infty \frac{E_{r_{ac}}(r)\, E_{r_{dc}}(r)\, p^2\, dr}{r\sqrt{r^2 - p^2}} \tag{9.10}$$

$$k_{s_{hy}} \equiv \gamma_{hy} \sin 2\alpha_{hy} = 8\pi B \int_p^\infty \frac{E_{z_{ac}}(r)\, E_{r_{dc}}\, p\, dr}{\sqrt{r^2 - p^2}} + 8\pi B \int_p^\infty \frac{E_{r_{ac}}(r)\, E_{z_{dc}}\, p\, dr}{\sqrt{r^2 - p^2}} \tag{9.11}$$

Again an inverse transform for (9.10) is not readily available since individual terms lead to different inverse transforms. The inverse transform for (9.11) however does exist

$$E_{z_{ac}}(r)E_{r_{dc}}(r) + E_{r_{ac}}(r)E_{z_{dc}}(r) = \frac{-1}{4\pi^2 B}\frac{d}{dr}\int_r^\infty \frac{k_{s_{hy}}(p)\, dp}{\sqrt{p^2 - r^2}} \tag{9.12}$$

Equation (9.12) might be useful to supply additional information for the algorithm Febker developed in Chapter 8. This possibility is also left to future research.

9.3 General Problem And Radon Transform

The Abel transform can be used to reconstruct axisymmetric electric field distributions in planes for which the direction of the transverse electric field is constant. When the field is not axisymmetric but the direction of the electric field along the light path is constant the Abel transform generalizes to the Radon transform.

The Radon transform [64] of a scalar function in a plane is the line integral of the function along lines in the plane. Thus (9.1) shows that γ_c is the Radon transform of $\pi B E^2$. Here (9.1) must be considered for each line on the plane each giving a value for γ_c. To make this dependence clear we define $f \equiv \pi B E^2$ and $\hat{f} \equiv \gamma_c$. $\hat{f}$ is the generally accepted notation for the Radon transfom of f and is most simply expressed as

$$\hat{f}(p,\theta) = \mathcal{R}f = \int_{-\infty}^{\infty} f(p\cos\theta - s\sin\theta, p\sin\theta + s\cos\theta)ds \tag{9.13}$$

Here p and θ describe the line in the xy-plane as shown in Figure 9.1.

A direct inversion for the transform does exist and can be written as

$$f(x,y) = \frac{1}{2\pi^2}\int_0^\pi \int_{-\infty}^{\infty} \frac{1}{x\cos\theta + y\sin\theta - p}\frac{\partial \hat{f}(p,\theta)}{\partial p}\, dp\, d\theta \tag{9.14}$$

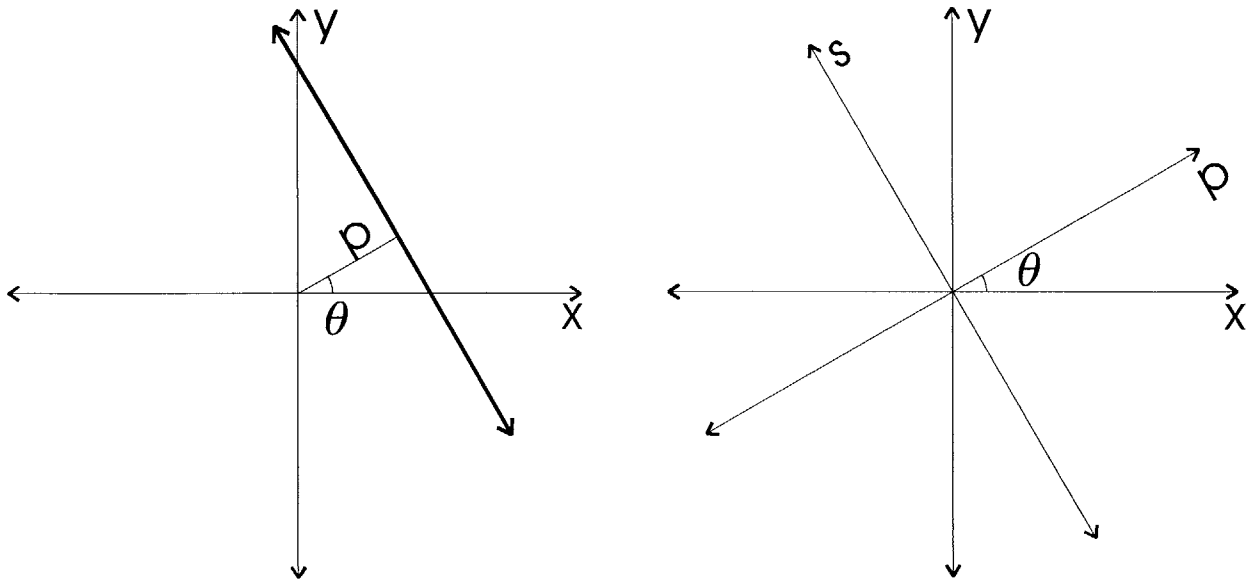

Figure 9.1: (left) Parameters p and θ are used to define a line. p is the distance between the line and the origin and θ is the angle between the normal to the line and the x-axis. (right) ps-coordinate system used to express the line integrals that describe the measurements. z coordinate is out of the page.

This formula however is rarely used in reconstruction primarily because of the numerical problems associated with the partial derivative with respect to p.

A family of algorithms rely on the so called projection slice theorem

$$\psi(m,\theta) = \tilde{f}(m\cos\theta, m\sin\theta) \tag{9.15}$$

Here $\psi(m,\theta)$ is the one dimensional Fourier transform of $\hat{f}$

$$\psi(m,\theta) = \mathcal{R}_1\hat{f} = \int_{-\infty}^{\infty} \hat{f}(p,\theta)e^{-jmp} \tag{9.16}$$

and $\tilde{f}$ is the two dimensional Fourier transform of f.

$$\tilde{f}(k_x,k_y) = \mathcal{R}_2 f = \int_{-\infty}^{\infty}\int_{-\infty}^{\infty} f(x,y)e^{-j(k_x x+k_y y)}dx\,dy \tag{9.17}$$

Equation (9.15) reduces the problem of inversion into problems of finding forward and inverse Fourier transforms.

Most algorithms in scalar tomography use what is known as backprojection. The

backprojection of $\hat{f}(p,\theta)$, denoted here as $g(x,y)$ can be written as

$$g(x,y) = \mathcal{B}\hat{f} = \int_0^{\pi} \hat{f}(x\cos\phi + y\sin\phi, \phi)d\phi \tag{9.18}$$

The important identity regarding the backprojection for practical algorithms is [65]

$$\mathcal{BR}f = f * *\frac{1}{r} \tag{9.19}$$

where $**$ denotes the two dimensional convolution and $r = \sqrt{x^2+y^2}$

$$f * *\frac{1}{r} = \int_{-\infty}^{+\infty}\int_{-\infty}^{+\infty} \frac{f(x',y')dx'dy'}{\sqrt{(x-x')^2+(y-y')^2}} \tag{9.20}$$

Equation (9.19) and the Fourier space equivalent

$$\mathcal{F}_2\mathcal{BR}f = (\mathcal{F}_2 f)(\mathcal{F}_2\frac{1}{r}) \tag{9.21}$$

are the starting point of the very popular filtered backprojection and other most efficient algorithms in scalar field tomography [64]. Here the Fourier transform is understood in distribution (generalized function) sense.

It is important to stress that neither (9.15) nor (9.19) is the end of the scalar tomographic problem. The problems of discretization of these equations, uniqueness and existence of the solutions of the resulting equations, efficiency, ill-conditionness and convergence properties are serious problems to be solved and addressed by scalar field tomography.

Since for highly birefringent media there do not exist direct integral relations between the electric field and the characteristic parameters there is no starting point and the chance of developing a transform pair for characteristic parameters and the applied electric field is slim. For weak Kerr media we have

$$\frac{\gamma(p,\theta)\cos\alpha(p,\theta)}{\pi B} = \int_{-\infty}^{\infty} E_z^2(x,y)ds - \int_{-\infty}^{\infty} E_p^2(x,y)ds \tag{9.22}$$

$$\frac{\gamma(p,\theta)\sin\alpha(p,\theta)}{\pi B} = \int_{-\infty}^{\infty} 2E_z(x,y)E_p(x,y)ds \tag{9.23}$$

in the coordinate frame introduced in Figure 9.1. There are two main difficulties with these transforms. The first is that the argument of the integrals on the right hand side

are also functions of p. Such transformations are called generalized Radon transforms. Although there exists some attempts for inversion of such transforms [66], the results are complicated and the applications are rare. In fact the inverse may not exist [67]. The second problem with this transformation is that they are not linear in terms of the components of the electric field. Most theory on the inversion problems are for linear operators.

The linearization of these equations are implicitly achieved by the ac modulation method for which (9.22) and (9.23) reduce to

$$\frac{\gamma_{hy}(p,\theta)\cos 2\alpha_{hy}(p,\theta)}{4\pi B} = \int_{-\infty}^{\infty} E_{z_{ac}}(x,y)E_{z_{dc}}(x,y)ds - \int_{-\infty}^{\infty} E_{p_{ac}}(x,y)E_{p_{dc}}(x,y)ds \tag{9.24}$$

$$\frac{\gamma_{hy}(p,\theta)\sin 2\alpha_{hy}(p,\theta)}{4\pi B} = \int_{-\infty}^{\infty} E_{z_{ac}}(x,y)E_{p_{dc}}(x,y)ds + \int_{-\infty}^{\infty} E_{p_{ac}}(x,y)E_{z_{dc}}(x,y)ds \tag{9.25}$$

Under the assumption that the ac electric field is known (9.24) and (9.25) are linear in the dc electric field components and seem to be more manageable. In fact recent advances in tomography [68–73] show that the irrotationality of $\mathbf{E_{dc}}$ can be used to reconstruct the electric potential ϕ by the formula

$$\phi(x,y) = \frac{1}{2\pi^2}\int_0^{\pi}\int_{-\infty}^{\infty} \frac{1}{x\cos\theta + y\sin\theta - p} k(p,\theta)\, dp\, d\theta \tag{9.26}$$

when k are measurements of the form

$$k(p,\theta) = \int_{-\infty}^{\infty} E_{p_{dc}}(x,y)\, ds \tag{9.27}$$

Although (9.27) is not exactly the same with the terms in (9.24) and (9.25) the similarities are obvious especially since the ac components of the electric field can be considered known weighting functions and finding an inverse transform for individual terms seem to be achievable. However even when such transforms are found we face the same problem we did for the axisymmetric problem, namely combining the individual transforms into one since only $\gamma_{hy}\cos\alpha_{hy}$ and $\gamma_{hy}\sin\alpha_{hy}$ are available from experiments and not the individual terms on the right hand side of (9.24) and (9.25). Solution of these problems are involved and requires a new line of research which we leave for future work.

Chapter 10

Conclusions And Future Research

10.1 Conclusions

There were two related purposes of this thesis; the mathematical modeling of the forward problem of relating Kerr electro-optic intensity measurements to the applied electric field when the applied electric field magnitude and direction change along the light path; and the mathematical modeling of the inverse problem of reconstructing arbitrary three dimensional applied electric field distributions from sets of Kerr electro-optic light intensity measurements.

The solution to the forward problem is now complete and has already been tested by laboratory measurements in transformer oil. To our knowledge, in the dielectric literature there is no development of the governing equations of light propagation in the form we developed in this work although the equations themselves seem to be well known in other disciplines, most notably photoelasticity. The governing equations are thoroughly investigated. Case studies that allow analytical evaluation are studied. We developed software that is capable of producing synthetic data based on the governing equations.

We adapted the characteristic parameter theory of photoelasticity to the Kerr electro-optic measurements. It is shown that for arbitrary Kerr media each intensity measurement can at most yield three independent characteristic parameters. The number of independent characteristic parameters reduces to two for axisymmetric and/or weakly birefringent media. We related the characteristic parameters to the applied electric field through differential equations and in the case of weakly birefringent media through simple integral relations.

The input/output intensity relations for various polariscope systems are developed in terms of the characteristic parameters. The ac modulation method is generalized to arbitrary three dimensional electric field distributions. We studied the effects of the finite beam size on the Kerr electro-optic measurements. A detailed study on the calculated fringe patterns of highly birefringent axisymmetric Kerr media emphasized the differences between the use of Kerr electro-optic fringe patterns in the case of two dimensional electric fields and analogous axisymmetric electric fields.

We investigated three classes of algorithms for the inverse problem of reconstructing electric field distributions from Kerr electro-optic data. The onion peeling algorithm which is applicable to only axisymmetric electric field distributions is applied to the point/plane electrode geometry. The simulated reconstructions were successful when the data sampling rate was high enough. The algorithm is applied to simulations of both highly birefringent media and weakly birefringent media. A variant of the algorithm is also developed for weakly birefringent media using the integral relations between the characteristic parameters.

Algebraic reconstruction techniques have been developed in Japan in research similar to this one. The present algorithms are limited to weakly birefringent media, weak electric fields, or short path lengths such that the optical phase difference is much less than π. We provided an introduction to these algorithms and applied them to sphere/plane and sphere/sphere electrodes. The results show that these algorithms have no advantage over the onion peeling method for axisymmetric electric field distributions, while for weakly birefringent media we believe that the finite element based reconstruction algorithm that we developed is far superior since it reconstructs the space charge directly, avoiding the numerically troublesome evaluation of the divergence of the electric field and incorporates the continuity and irrotationality of the electric field into the solution process.

The finite element based Kerr electro-optic reconstruction algorithm (FEBKER) is developed for weakly birefringent media when the ac modulation method is used to measure the characteristic parameters. The algorithm reconstructs the space charge directly, avoiding taking the divergence of the electric field to obtain the charge density from Gauss's law. Although the algorithm is only formulated and applied to axisymmetric geometries, its extension to arbitrary three dimensional geometries is straight forward and only complicated due to the complexity of discretization of three dimensional geometries. It can reconstruct the space charge density using a single parameter measurement from each light intensity measurement so that rotating the optical el-

ements during measurements becomes unnecessary. This is important since rotating optical elements are slow, making it impossible to use Kerr electro-optic measurements for transient charge injection and transport phenomena.

When the electric field direction along the light path is constant, even though field magnitude may change along light path, there are direct transform relationships to recover electric field magnitude as a function of position along light path from light intensity measurements. We showed that extension of these transforms to the case when the electric field direction changes along the light path is not trivial and development of transform methods for Kerr electro-optic intensity measurements requires a new line of research.

10.2 Suggestions For Future Research

The most important follow-up to this thesis is the detailed investigation of the impact of error on the onion peeling and FEBKER algorithms. Although simple smoothing techniques seem to work with the onion peeling algorithm, more research is needed to analyze the effects of noise on the quality of the reconstructed electric fields. For FEBKER various regularization techniques have to be investigated incorporating statistical analysis into the solution process. The groupings of the triangles in square regions can be replaced by postulating a global space charge density function with unknown coefficients which can then be found by FEBKER. When this analysis is complete we believe that FEBKER can be used on real world data to investigate the physics of charge injection and transport.

The only remaining open inverse problem from the theoretical point of view is reconstructing the arbitrary three dimensional electric field distributions when the medium is highly birefringent. It appears that the algebraic reconstruction technique can be extended to this case although the exact algorithm needs to be developed after an extensive set of numerical experiments.

When the thesis began, we thought that an extension to the Radon transform, typically used with scalar tomography for medical applications, nondestructive testing and seismology, may be possible for Kerr effect reconstructions of applied electric field magnitude and direction from optical intensity measurements along many light paths. The Radon transform and its axisymmetric version, the Abel transform, can be used when the direction of the transverse applied electric field is constant along the light path. This is typically true along a ground plane. However, when the direction of the

applied electric field varies along the light path, we found that the vector nature of the Kerr effect dependence on the electric field results in integral relationships where the function to be integrated depends on the light path. This makes it impossible to extend the Radon transform based inverse methods which are widely used in scalar tomography. Although there are some attempts to generalize the Radon transform in the literature to allow such cases, the results to date are still restricted and we cannot put the Kerr effect relations in the form required. Extensive research is necessary to find some generalization of the Radon transform which can be used for Kerr effect relations. Such generalizations may not exist as there are results in the literature which claim for certain classes of problems that when the integrand in the forward transform depends on the integral path, the inverse transform does not exist. Even if future work allows such relationships the mathematical complexity requires extensive research to develop practical algorithms competitive with FEBKER.

It is possible to reconstruct the product of the axial and radial components of the axisymmetric electric fields from Kerr electro-optic measurements using an Abel like inverse transform as discussed in Section 9.2. Further research is needed to investigate how this might be used to increase the quality of the reconstructions using FEBKER and the onion peeling algorithms.

For highly birefringent axisymmetric media the complex behavior of Kerr electro-optic data detailed in Section 5.7.2 make otherwise applicable smoothing techniques unusable. Other interpolation techniques have to be developed probably using pre-determined functions which are capable of representing the complex but predictable behavior of Kerr electro-optic data.

Other than these immediate theoretical interests the direction of further research is dependent on the quality of Kerr electro-optic data. It appears that development of a two dimensional measurement system is necessary either using a photo-detector array or a sensitive camera system. When such a system is developed the error characteristic of the measurements is expected to dictate further refinement of the algorithms developed in this work. In particular, statistical analysis needs to be incorporated into the algorithms such that the quality of the reconstructed space charge density distributions can be quantified. Temperature gradients and electrohydrodynamic motion are other disturbance factors expected to have some effect on the measurements. Based on the severity of the effects, it may become necessary either to model these effects in the forward problem or predict and account for the effects in the inverse problem using statistical analysis.

Part III

Appendices

Appendix A

Point/Plane Electrodes Geometry

A.1 Introduction

In this appendix we derive the analytical potential and electric field expressions for the point/plane electrode geometry when the point electrode is a hyperboloid of revolution and both the point and ground electrodes are of infinite extent. Laplace's equation is solved in the prolate spheroidal coordinate system and the solutions are expressed in a cartesian coordinate frame.

A.2 The Prolate Spheroidal Coordinate System

The prolate spheroidal coordinate system can be defined in terms of the cartesian coordinate system as [74, 75] [1]

$$z = a \sin\zeta \cosh\eta \tag{A.1a}$$

$$x = a \cos\zeta \sinh\eta \cos\phi \tag{A.1b}$$

$$y = a \cos\zeta \sinh\eta \sin\phi \tag{A.1c}$$

Here ζ, η and ϕ are the prolate spherical coordinates and a is a positive constant. The angle ϕ is the familiar azimuthal angle of cylindrical coordinates. The point/plane electrode geometry is axisymmetric. Hence instead of working with x and y, it is more convenient to work with the cylindrical coordinate r, the radial distance to the

[1] Equation (A.1) is not identical to the corresponding equation that defines prolate spheroidal coordinates in [74]. One can arrive at that definition with the replacement $\zeta \rightarrow \frac{\pi}{2} - \zeta$.

axisymmetry axis (z-axis)

$$r = \sqrt{x^2 + y^2} \tag{A.2}$$

$$= a \cos\zeta \sinh\eta \tag{A.3}$$

It follows from (A.1a) and (A.3) that the surfaces of constant ζ are hyperboloids of revolution

$$\frac{z^2}{\sin^2\zeta} - \frac{r^2}{\cos^2\zeta} = a^2 \tag{A.4}$$

and a is the focal point of the hyperboloids. The surfaces of constant η are prolate spheroids whose equations also follow from (A.1a) and (A.3)

$$\frac{z^2}{\cosh^2\eta} + \frac{r^2}{\sinh^2\eta} = a^2 \tag{A.5}$$

Of interest are the asymptotic curves to the hyperboloids for large z and r. From (A.4) we get

$$z = \pm r \tan\zeta \quad (x \gg a \text{ and } r \gg a) \tag{A.6}$$

A.3 Solution To Laplace's Equation

To solve Laplace's equation for a point/plane electrode geometry we let the ground plane to be $\zeta = 0$ ($z = 0$) and the point electrode to be $\zeta = \zeta_0$. If the applied voltage is V_0 then the boundary conditions for Laplace's equations are

$$\Phi(\zeta, \eta, \varphi)|_{\zeta=\zeta_0} = V_0 \tag{A.7a}$$

$$\Phi(\zeta, \eta, \varphi)|_{\zeta=0} = 0 \tag{A.7b}$$

Since boundary conditions involve neither ϕ nor η, Laplace's equation simplifies to [74]

$$\frac{d^2\Phi(\zeta)}{d\zeta^2} - \tan\zeta \frac{d\Phi(\zeta)}{d\zeta} = 0 \tag{A.8}$$

whose general solution is

$$\Phi(\zeta) = A \ln \left[\tan \left(\frac{\zeta}{2} + \frac{\pi}{4} \right) \right] + B \tag{A.9}$$

where A and B are arbitrary constants to be found from the boundary conditions of (A.7). Substituting (A.9) into (A.7) yields the analytical expression for the potential

$$\Phi(\zeta) = C \ln \left[\tan \left(\frac{\zeta}{2} + \frac{\pi}{4} \right) \right] \tag{A.10}$$

where

$$C = \frac{V_0}{\ln \left[\tan \left(\frac{\zeta_0}{2} + \frac{\pi}{4} \right) \right]} \tag{A.11}$$

A.4 Tip-Plane Distance And The Radius Of Curvature

The point/plane electrode geometry is often specified by the distance between the tip of the point electrode and the ground plane d and the radius of the curvature of the point electrode R_c. The distance d may be found directly from (A.1a) as

$$\begin{aligned} d &= z|_{\zeta=\zeta_0,\, \eta=0} \\ &= a \sin \zeta_0 \end{aligned} \tag{A.12}$$

while equations (A.1a), (A.3) and (A.12) give the radius of curvature [76] of the point electrode as

$$\begin{aligned} R_c &= \left. \frac{\left[\left(\frac{\partial z}{\partial \eta} \right)^2 + \left(\frac{\partial r}{\partial \eta} \right)^2 \right]^{\frac{3}{2}}}{\left| \frac{\partial z}{\partial \eta} \frac{\partial^2 r}{\partial \eta^2} - \frac{\partial r}{\partial \eta} \frac{\partial^2 z}{\partial \eta^2} \right|} \right|_{\zeta=\zeta_0,\, \eta=0} \\ &= \frac{a^3 \cos^3 \zeta_0}{a^2 \sin \zeta_0 \cos \zeta_0} = a \cos \zeta_0 \cot \zeta_0 \\ &= a \frac{1 - \sin^2 \zeta_0}{\sin \zeta_0} \end{aligned}$$

$$= \frac{a^2}{d} - d \tag{A.13}$$

Equations (A.12) and (A.13) give a and ζ_0 in terms of d and R_c

$$a = \sqrt{d(d + R_c)} \tag{A.14}$$

$$\zeta_0 = \arcsin \frac{d}{a} \tag{A.15}$$

Equation (A.15) together with the identity

$$\ln \tan(\frac{\zeta}{2} + \frac{\pi}{4}) = \frac{1}{2} \ln \frac{1 + \sin \zeta}{1 - \sin \zeta} \quad 0 \leq \zeta < \frac{\pi}{2} \tag{A.16}$$

and equation (A.11) may be used to find C in terms of a and d as

$$C = \frac{2V_0}{\ln \frac{a+d}{a-d}} \tag{A.17}$$

It follows from equation (A.4) that the equation of the point electrode may be written in terms of d and R_c as

$$\frac{z^2}{d^2} - \frac{r^2}{dR_c} = 1 \tag{A.18}$$

which for large r reduces to

$$z = \pm \sqrt{\frac{d}{R_c}} r \tag{A.19}$$

Typically the needle is very sharp and ζ_0 only slightly differs from $\pi/2$. That is

$$\epsilon = \frac{\pi}{2} - \zeta_0 \tag{A.20}$$

where $\epsilon \ll 1$. In terms of ϵ, (A.11) may be written as

$$C = \frac{V_0}{\ln \left[\cot \left(\frac{\epsilon}{2}\right)\right]} \tag{A.21}$$

For a sharp needle it is possible to obtain approximate simpler expressions. In

particular, the radius of curvature is given as

$$R_c \approx a\epsilon^2 \tag{A.22}$$

Since $R_c \ll d$, (A.14) yields

$$d \approx a - \frac{R_c}{2} \tag{A.23}$$

and it directly follows from (A.21) and (A.22) that

$$C \approx \frac{V_0}{\ln \frac{2}{\epsilon}} \approx \frac{V_0}{\ln 2\sqrt{a/R_c}} \tag{A.24}$$

A.5 The Electric Field

The electric field is related to the potential by

$$\mathbf{E}(\vec{r}) = -\nabla\Phi(\vec{r}) \tag{A.25}$$

Since the field is axisymmetric, it can only be in terms of the axial and radial components

$$E_z(r,z) = -\frac{\partial\Phi(r,z)}{\partial z} = -\frac{\partial\Phi(\zeta)}{\partial\zeta}\frac{\partial\zeta}{\partial z} \tag{A.26}$$

$$E_r(r,z) = -\frac{\partial\Phi(r,z)}{\partial r} = -\frac{\partial\Phi(\zeta)}{\partial\zeta}\frac{\partial\zeta}{\partial r} \tag{A.27}$$

$\frac{\partial\Phi(\zeta)}{\partial\zeta}$ follows from (A.10) as

$$\begin{aligned}
\frac{\partial\Phi(\zeta)}{\partial\zeta} &= \frac{C}{\tan\left(\frac{\zeta}{2}+\frac{\pi}{4}\right)}\frac{1+\tan^2\left(\frac{\zeta}{2}+\frac{\pi}{4}\right)}{2} \\
&= \frac{C}{2}\left(\frac{\sin\left(\frac{\zeta}{2}+\frac{\pi}{4}\right)}{\cos\left(\frac{\zeta}{2}+\frac{\pi}{4}\right)} + \frac{\cos\left(\frac{\zeta}{2}+\frac{\pi}{4}\right)}{\sin\left(\frac{\zeta}{2}+\frac{\pi}{4}\right)}\right) \\
&= \frac{C}{\sin\left(\zeta+\frac{\pi}{2}\right)} \\
&= \frac{C}{\cos\left(\zeta\right)}
\end{aligned} \tag{A.28}$$

Taking the partial derivatives of (A.1a) and (A.3) with respect to z and r and solving for $\frac{\partial \zeta}{\partial z}$ and $\frac{\partial \zeta}{\partial r}$ yield

$$\frac{\partial \zeta}{\partial z} = \frac{1}{a}\left(\frac{\cos\zeta \cosh\eta}{\cosh^2\eta - \sin^2\zeta}\right) \tag{A.29}$$

$$\frac{\partial \zeta}{\partial r} = -\frac{1}{a}\left(\frac{\sin\zeta \sinh\eta}{\cosh^2\eta - \sin^2\zeta}\right) \tag{A.30}$$

Equations (A.26), (A.28) and (A.29) yield

$$E_z = -\frac{C}{a}\left(\frac{\cosh\eta}{\cosh^2\eta - \sin^2\zeta}\right) \tag{A.31}$$

In particular, evaluating (A.31) at $\eta = 0$ yields the electric field on the z-axis ($0 \leq z \leq d$)

$$E_z(\zeta,\eta)|_{\eta=0} = -\frac{C}{a}\frac{1}{\cos^2\zeta} \tag{A.32}$$

Of interest are the values on the tip ($\zeta = \zeta_0,\ \eta = 0$) and the ground plane ($\zeta = 0,\ \eta = 0$)

$$E_z(\zeta,\eta)|_{\zeta=\zeta_0,\,\eta=0} = -\frac{C}{a}\frac{1}{\cos^2\zeta_0} = -\frac{C}{R_c\sin\zeta_0} = -\frac{Ca}{dR_c} \tag{A.33}$$

$$E_z(\zeta,\eta)|_{\zeta=0,\,\eta=0} = -\frac{C}{a} \tag{A.34}$$

For a sharp point electrode (A.33) reduces to

$$E_z(\zeta,\eta)|_{\zeta=\zeta_0,\,\eta=0} \approx -\frac{C}{R_c} \tag{A.35}$$

Equation (A.35) is an important identity since it determines the maximum electric field strength in a point/plane geometry with a sharp needle electrode.

Equations (A.27), (A.28) and (A.30) yield

$$E_r(\zeta,\eta) = \frac{C}{a}\left(\frac{\sin\zeta \sinh\eta}{\cos\zeta\left(\cosh^2\eta - \sin^2\zeta\right)}\right) \tag{A.36}$$

Notice that $E_r(\zeta,\eta)$ vanishes both on the ground plane ($\zeta = 0$) and on the $z-$axis ($\eta = 0$)

A.6 Field Quantities In Cartesian Coordinates

Prolate spherical coordinates ζ and η can be found in terms of z and r by solving (A.4) and (A.5) and noting that $z = 0$ implies $\zeta = 0$ and $r = 0$ implies $\eta = 0$. The results are

$$\sin^2\zeta = \frac{(z^2 + r^2 + a^2) - \sqrt{(z^2 + r^2 + a^2)^2 - 4a^2z^2}}{2a^2} \tag{A.37}$$

$$\cosh^2\eta = \frac{(z^2 + r^2 + a^2) + \sqrt{(z^2 + r^2 + a^2)^2 - 4a^2r^2}}{2a^2} \tag{A.38}$$

$$\cos^2\zeta = \frac{(a^2 - z^2 - r^2) + \sqrt{(z^2 + r^2 + a^2)^2 - 4a^2z^2}}{2a^2} \tag{A.39}$$

$$\sinh^2\eta = \frac{(z^2 + r^2 - a^2) + \sqrt{(z^2 + r^2 + a^2)^2 - 4a^2z^2}}{2a^2} \tag{A.40}$$

Equations (A.37) and (A.38) yield

$$\cosh^2\eta - \sin^2\zeta = \frac{\sqrt{(z^2 + r^2 + a^2)^2 - 4a^2z^2}}{a^2} \tag{A.41}$$

while (A.37) and (A.40) yield

$$\sin\zeta \sinh\eta = \left[\frac{z^2 - r^2 - a^2 + \sqrt{(z^2 + r^2 + a^2)^2 - 4a^2z^2}}{2a^2}\right]^{\frac{1}{2}} \tag{A.42}$$

Also from (A.42)

$$\tanh\eta \tan\zeta = \left[\frac{z^2 - r^2 - a^2 + \sqrt{(z^2 + r^2 + a^2)^2 - 4a^2z^2}}{-z^2 + r^2 + a^2 + \sqrt{(z^2 + r^2 + a^2)^2 - 4a^2z^2}}\right]^{\frac{1}{2}} \tag{A.43}$$

It follows from (A.10) and (A.16) that

$$\Phi(\zeta) = \frac{C}{2} \ln \frac{1 + \sin\zeta}{1 - \sin\zeta} \tag{A.44}$$

Substituting (A.37) in (A.44) yields the potential distribution in cartesian coordinates

$$\Phi(r,z) = \frac{C}{2}\ln\left[\frac{\sqrt{2}a + \sqrt{z^2+r^2+a^2-\sqrt{\left(z^2+r^2+a^2\right)^2-4a^2z^2}}}{\sqrt{2}a - \sqrt{z^2+r^2+a^2-\sqrt{\left(z^2+r^2+a^2\right)^2-4a^2z^2}}}\right] \tag{A.45}$$

Equations (A.31), (A.38) and (A.41) yield

$$E_z(r,z) = -\frac{C}{\sqrt{2}}\left[\frac{z^2+r^2+a^2+\sqrt{\left(z^2+r^2+a^2\right)^2-4a^2z^2}}{\left(z^2+r^2+a^2\right)^2-4a^2z^2}\right]^{\frac{1}{2}} \tag{A.46}$$

while (A.36), (A.39), (A.41), and (A.42) yield

$$E_r(r,z) = \frac{Ca}{\sqrt{\left(z^2+r^2+a^2\right)^2-4a^2z^2}}\left[\frac{z^2-r^2-a^2+\sqrt{\left(z^2+r^2+a^2\right)^2-4a^2z^2}}{a^2-z^2-r^2+\sqrt{\left(z^2+r^2+a^2\right)^2-4a^2z^2}}\right]^{\frac{1}{2}} \tag{A.47}$$

Cartesian electric field components E_x and E_y can be found from E_r simply by multiplying by x/r and y/r factors respectively. This form however has a $0/0$ factor at $r = 0$ which may be problematic in computer simulations. This factor may be avoided by multiplying both the denominator and numerator of (A.47) by

$$\sqrt{a^2-r^2-z^2+\sqrt{\left(z^2+r^2+a^2\right)^2-4a^2z^2}} \tag{A.48}$$

This yields a r in the numerator which cancels the denominator of the factors x/r and y/r. The results are

$$E_x(x,y,z) = \frac{\sqrt{2}Cax}{a^2-z^2-r^2+\sqrt{\left(z^2+r^2+a^2\right)^2-4a^2z^2}} \times\left[\frac{z^2+r^2+a^2-\sqrt{\left(z^2+r^2+a^2\right)^2-4a^2z^2}}{\left(z^2+r^2+a^2\right)^2-4a^2z^2}\right]^{\frac{1}{2}} \tag{A.49}$$

and

$$E_y(x,y,z) = \frac{\sqrt{2}Cay}{a^2 - z^2 - r^2 + \sqrt{(z^2+r^2+a^2)^2 - 4a^2z^2}} \times \left[\frac{z^2+r^2+a^2 - \sqrt{(z^2+r^2+a^2)^2 - 4a^2z^2}}{(z^2+r^2+a^2)^2 - 4a^2z^2}\right]^{\frac{1}{2}} \quad \text{(A.50)}$$

On the ground plane ($z = 0$) $E_r(x,y,z)$ vanishes and $E_z(x,y,z)$ is given as

$$E_z(x,y,z)|_{z=0} = -\frac{C}{\sqrt{a^2+r^2}} \quad \text{(A.51)}$$

while on the axisymmetry axis ($r = 0$) $E_z(x,y,z)$ is given as

$$E_z(x,y,z)|_{r=0} = -\frac{Ca}{a^2 - z^2} \quad \text{(A.52)}$$

A.7 Far Field Electric Field Components For $r \gg a, z$

It is of interest to find far field approximate expressions when $r \gg a, z$. The approximation to (A.46) is straight forward and simply found by substituting $a = z = 0$

$$E_z(r,z) = -\frac{C}{r} \quad \text{(A.53)}$$

To find the approximation to (A.47) we first note that by neglecting the terms that are second order in z^2/r^2 and a^2/r^2 we find

$$\sqrt{(z^2+r^2+a^2)^2 - 4a^2z^2} \approx z^2 + r^2 + a^2 \quad \text{(A.54)}$$

which can be substituted in (A.47) to yield

$$E_r(r,z) = \frac{Cz}{r^2} \quad \text{(A.55)}$$

Appendix B

Geometries With Sphere Electrodes

B.1 Introduction

In this appendix we find the potential and electric field distributions for a sphere/plane electrode geometry and a sphere/sphere electrode geometry. Both geometries are axisymmetric. The distributions are found using the method of images for which a detailed description can be found in [29,77].

B.2 Charge Near a Grounded Sphere

We begin by finding the potential distribution when a charge q is placed in the vicinity of a grounded sphere electrode (Figure B.1). To find the distribution, the sphere electrode is replaced by an image charge q_i. Due to the symmetry q_i must be placed on the line that connects q and the center of the sphere electrode. We let b_i be the distance between q_i and the center. The potential distribution (outside the sphere) is

$$\Phi(a,\zeta) = \frac{1}{4\pi\epsilon_0}\left[\frac{q}{d(a,\zeta)} + \frac{q_i}{d_i(a,\zeta)}\right] \tag{B.1}$$

where a, ζ, d and d_i are shown in Figure B.1. Distances $d(a,\zeta)$ and $d_i(a,\zeta)$ follow from the law of cosines

$$d(a,\zeta) = \sqrt{a^2 + D^2 - 2Da\cos\zeta} \tag{B.2a}$$

$$d_i(a,\zeta) = \sqrt{a^2 + b_i^2 - 2b_i a\cos\zeta} \tag{B.2b}$$

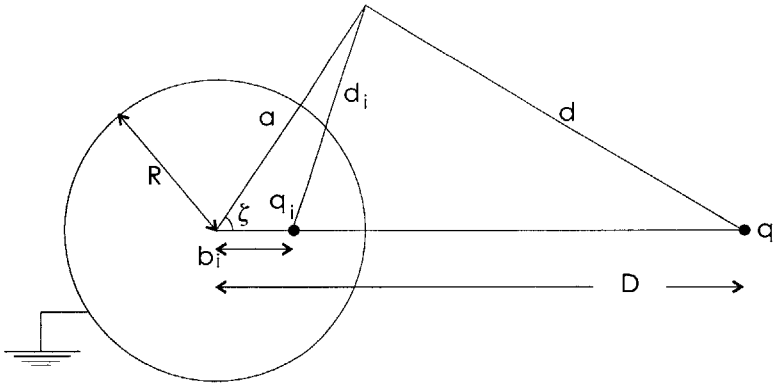

Figure B.1: Point charge q near a grounded sphere electrode. In the method of images the grounded sphere is replaced by an image charge q_i at a distance b_i from the center. The values for q_i and b_i are found such that the boundary condition (vanishing potential at $a = R$) is satisfied.

Here R is the radius of the sphere electrode and D is the distance between q and the center of the spherical electrode.

To find q_i and b_i in terms of D, R and q we let $a = R$. Since $\Phi(R, \zeta) = 0$, (B.1) and (B.2) yield

$$q^2(R^2 + b_i^2) - 2q^2 b_i R\cos\zeta = q_i^2(R^2 + D^2) - 2q_i^2 DR\cos\zeta \tag{B.3}$$

Since (B.3) is valid for all ζ, it yields two equations one of which can be used to eliminate q_i and obtain a quadratic equation for b_i. One solution of this quadratic equation is $b_i = D$ and eliminated since the image charge must be inside the sphere for the method of images to be valid. The other one is the desired solution

$$b_i = \frac{R^2}{D} \tag{B.4}$$

It follows from (B.4) and (B.3) that

$$q_i = -q\frac{R}{D} \tag{B.5}$$

B.3 Image Charges for Sphere/Plane Electrodes

The sphere/plane electrode geometry is shown in Figure B.2. The sphere electrode is at potential V. We begin by replacing the electrodes with an image charge q_{v_1} at the

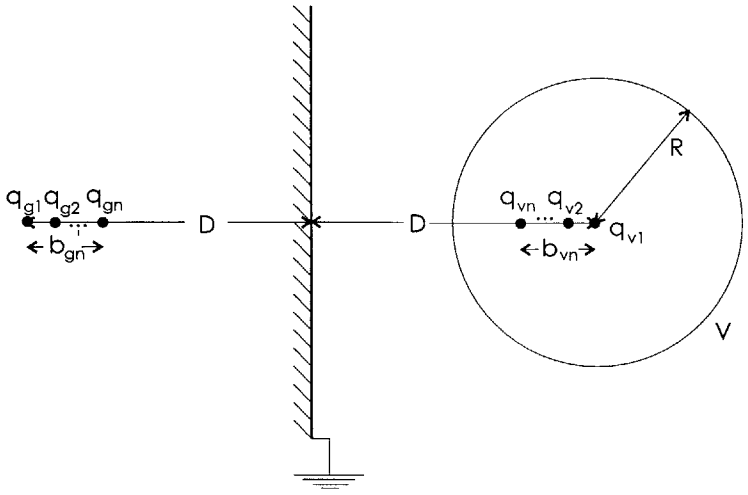

Figure B.2: Sphere/plane electrode geometry. Boundary conditions can be satisfied only by an infinite number of image charges. Image charge q_{v_1} raises the potential on the sphere electrode to V while image charges $q_{g_1}, q_{g_2} \cdots$ are placed to keep the plane at ground potential and $q_{v_2}, q_{v_3} \cdots$ are placed to keep the potential of the sphere electrode at V.

center of the sphere electrode where

$$q_{v_1} = 4\pi\epsilon_0 RV \tag{B.6}$$

With q_{v_1} at the sphere center, the boundary condition on the sphere electrode at $a = R$ of potential V is satisfied. Here a is the distance of a point to the sphere center. To satisfy the boundary condition on the ground plane we place an image charge $q_{g_1} = -q_{v_1}$ symmetrically with respect to the plane. These two charges now satisfy the zero potential boundary condition on the ground plane but the condition on the sphere electrode is now disturbed. To restore the boundary condition on the sphere electrode we place another image charge q_{v_2} inside the sphere electrode so that for a system with q_{g_1} and q_{v_2} the additional potential on the sphere electrode vanishes. The value and the placement of such a charge are found in Section B.2. Using (B.4) and (B.5) and $q_{g_1} = -q_{v_1}$ we obtain

$$q_{v_2} = q_{v_1}\frac{R}{2D} \tag{B.7a}$$

$$b_{v_2} = \frac{R^2}{2D} \tag{B.7b}$$

where we recognize the distance from q_{g_1} to the sphere center is $2D$. With three charges the boundary condition on the sphere electrode is satisfied but now the boundary condition on the ground electrode is disturbed. To restore the condition we again place a charge $q_{g_2} = -q_{v_2}$ symmetrically with respect to the plane. Continuing in this fashion we place an infinite number of charge pairs with

$$q_{v_n} = q_{v_{n-1}} \frac{R}{2D - b_{v_{n-1}}} \tag{B.8a}$$

$$b_{v_n} = \frac{R^2}{2D - b_{v_{n-1}}} \tag{B.8b}$$

$$q_{g_n} = -q_{v_n} \tag{B.8c}$$

$$b_{g_n} = b_{v_n} \tag{B.8d}$$

and q_{v_1} in (B.6) and $b_{v_1} = 0$ are the start-up values for the recursive relations in (B.8).

It is possible to find q_{v_n} and b_{v_n} explicitly as functions of n by obtaining difference equations from the recursive formulas of (B.8). Both obtaining and solving these equations are straightforward but cumbersome. The results are

$$\tilde{q}_{v_n} = \frac{q_{v_n}}{q_{v_1}} = \left[\frac{1}{\lambda} - \lambda\right]\left[\frac{1}{\lambda^n} - \lambda^n\right]^{-1} \tag{B.9a}$$

$$b_{v_n} = 2D - R\left[\frac{1}{\lambda^{n+1}} - \lambda^{n+1}\right]\left[\frac{1}{\lambda^n} - \lambda^n\right]^{-1} \tag{B.9b}$$

where

$$\lambda = \frac{D}{R} - \sqrt{\left(\frac{D}{R}\right)^2 - 1} \tag{B.9c}$$

Figure B.3 shows that for physical values of $D/R > 1$, λ is always less than 1. From (B.9a) we conclude that the decay of q_{v_n} can be slow only if λ is near 1. Figure B.3 shows that even for large λ (≈ 0.9 for $R/D = 0.9$), q_{v_n} are essentially 0 for $n \geq 10$. The values that b_{v_n} converge to follows from (B.9b) as

$$b_{v_\infty} = D - \frac{R}{\lambda} \tag{B.10}$$

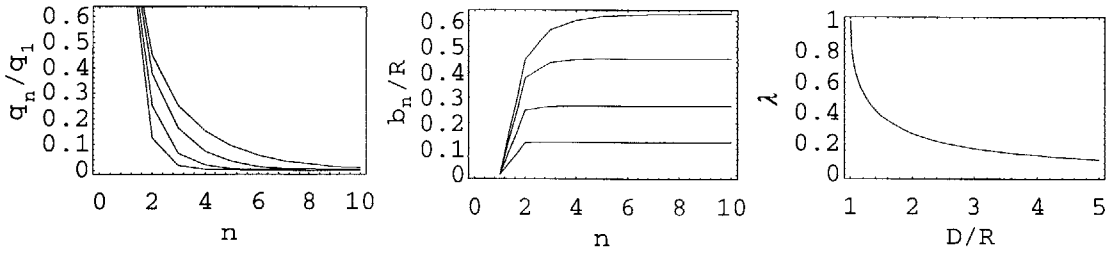

Figure B.3: Convergence of b_{v_n} and q_{v_n} for R/D values of 0.25, 0.5, 0.75 and 0.9 and the dependence of λ on D/R.

B.4 Image Charges for Sphere/Sphere Electrodes

The image charges for sphere/sphere electrodes (Figure B.4), where one of the spheres is grounded and the other is at voltage V, can be found in a similar fashion to sphere/plane electrodes. We first place an image charge q_{v_1} in the center of sphere 1 to satisfy the boundary condition that the sphere potential is V. Then $q_{g_1}, q_{g_2}, \cdots$ are placed inside the grounded sphere electrode to restore the boundary condition that the potential is at ground while $q_{v_2}, q_{v_3}, \cdots$ are placed to restore the boundary condition on sphere 1 that the potential is V. Using (B.4) and (B.5) we obtain the recursive relations

$$q_{v_n} = -q_{g_{n-1}} \frac{R_1}{2D - b_{g_{n-1}}} \tag{B.11a}$$

$$b_{v_n} = \frac{R_1^2}{2D - b_{g_{n-1}}} \tag{B.11b}$$

$$q_{g_n} = -q_{v_n} \frac{R_2}{2D - b_{v_n}} \tag{B.11c}$$

$$b_{g_n} = \frac{R_2^2}{2D - b_{v_n}} \tag{B.11d}$$

where the initial values are

$$q_{v_1} = 4\pi\epsilon_0 R_1 V \tag{B.12}$$

$$b_{v_1} = 0 \tag{B.13}$$

Equation (B.11) can again be used to obtain difference equations for which the

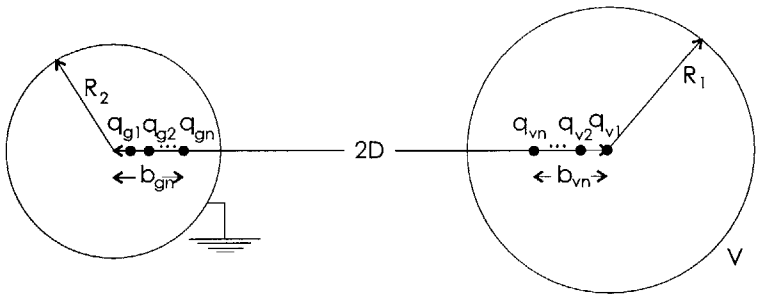

Figure B.4: Sphere/sphere electrode geometry. Boundary conditions can be satisfied only by an infinite number of image charges in each sphere. Image charge q_{v_1} raises the potential on sphere 1 to V. All charges inside the second sphere are placed to keep the left sphere at ground potential while the charges inside the right sphere are placed to keep the surface potential at V.

solutions are

$$\tilde{q}_{v_n} = \frac{q_{v_n}}{q_{v_1}} = \left[\frac{1}{\xi\beta^2} - \xi\beta^2\right]\left[\frac{1}{\xi\beta^{2n}} - \xi\beta^{2n}\right]^{-1} \tag{B.14a}$$

$$b_{v_n} = 2D - \frac{R_1 R_2}{2D}\left[\frac{1}{\xi\beta^{2n+2}} - \xi\beta^{2n+2}\right]\left[\frac{1}{\xi\beta^{2n}} - \xi\beta^{2n}\right]^{-1} - \frac{R_2^2}{2D} \tag{B.14b}$$

$$\tilde{q}_{g_n} = \frac{q_{g_n}}{q_{v_1}} = -\frac{R_2}{2D}\left[\frac{1}{\beta^2} - \beta^2\right]\left[\frac{1}{\beta^{2n}} - \beta^{2n}\right]^{-1} \tag{B.14c}$$

$$b_{g_n} = 2D - \frac{R_1 R_2}{2D}\left[\frac{1}{\beta^{2n+2}} - \beta^{2n+2}\right]\left[\frac{1}{\beta^{2n}} - \beta^{2n}\right]^{-1} - \frac{R_1^2}{2D} \tag{B.14d}$$

where

$$\xi = \frac{R_2}{2D} + \frac{R_1}{2\beta^2 D} \tag{B.15}$$

$$\beta = \left(\gamma - \sqrt{\gamma^2 - 1}\right)^{1/2} \tag{B.16}$$

$$\gamma = 2\left[\frac{D}{\sqrt{R_1 R_2}}\right]^2 - \frac{1}{2}\left[\frac{R_1}{R_2} + \frac{R_2}{R_1}\right] \tag{B.17}$$

A straightforward calculation shows that for $R_1 \approx R_2$ we have $\beta \approx \lambda$ and $\xi \approx 1/\lambda$ hence convergence properties of q_{v_n}, q_{g_n}, b_{v_n} and b_{g_n} are similar to q_{v_n} and b_{v_n} of the sphere/plane electrodes. For either R_1 or R_2 much smaller than the other we have $\beta \approx 0$ and the decrease of q_{v_n} and q_{g_n} is very fast. In fact for $R_1 = 0$ or $R_2 = 0$, q_{v_n} and q_{g_n} are all zero except q_{v_1} and q_{g_1} which is expected since this case is identical to

a point charge near a grounded sphere.

If both of the sphere electrodes are at non-zero potential, say V_1 for the first sphere and V_2 for the second sphere, then two sets of image charges need to be introduced. The first set is identical to the image charges of sphere/sphere electrodes with one electrode grounded and the other is at potential V_1. The second set is identical to the image charges of sphere/sphere electrodes with one electrode grounded and the other is at potential V_2. These two sets constitute the image charges of the sphere/sphere electrodes when one electrode is at V_1 and the other is at V_2. Also these image charges reduce to those of sphere/plane electrodes when $V_1 = V$, $V_2 = -V$ and $R_1 = R_2 = R$ (which also implies $\beta = \lambda$). Another way to get from sphere/sphere electrodes to sphere/plane electrodes is to let R_2 go to infinity such that

$$2D - R_2 = D' \tag{B.18}$$

where D' is a finite number. If $V_1 = V$ and $V_2 = 0$ then the solutions for the sphere/sphere electrodes reduce to those of sphere/plane electrodes with sphere/plane distance of D'.

B.5 Potential Distributions

In the previous sections the equivalent image charge distribution of sphere/plane electrodes and sphere/sphere electrodes are found. The resulting potential distributions assume the form

$$\Phi(r,z) = \sum_{n=1}^{\infty} \frac{q_{v_n}}{4\pi\epsilon_0 d_{v_n}(r,z)} + \sum_{n=1}^{\infty} \frac{q_{g_n}}{4\pi\epsilon_0 d_{g_n}(r,z)} \tag{B.19}$$

where with the aid of Figure B.5

$$d_{v_n}(r,z) = \sqrt{r^2 + (c_{v_n} - z)^2} \tag{B.20a}$$

$$d_{g_n}(r,z) = \sqrt{r^2 + (c_{g_n} + z)^2} \tag{B.20b}$$

with

$$c_{v_n} = D - b_{v_n} \tag{B.21a}$$

$$c_{g_n} = D - b_{g_n} \tag{B.21b}$$

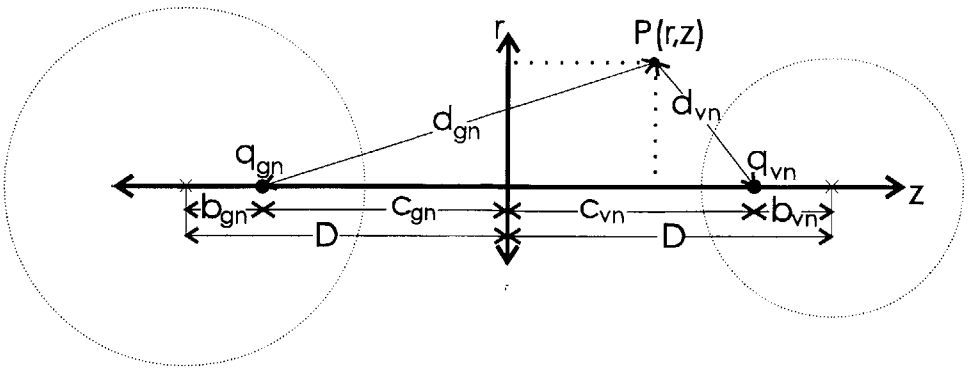

Figure B.5: The coordinate system used for the sphere/plane and sphere/sphere electrodes where r and z are the cylindrical coordinates of point P. Recall that the geometry is axisymmetric around the z-axis line joining image charges.

B.5.1 Sphere/Plane Electrode Geometry

It follows from (B.6), (B.8c), (B.9a) and (B.19) that the potential distribution for sphere/plane electrodes is given as

$$\Phi(r,z) = VR\sum_{n=1}^{\infty}\tilde{q}_{v_n}\left[\frac{1}{d_{v_n}(r,z)} - \frac{1}{d_{g_n}(r,z)}\right] \tag{B.22}$$

Also notice that for sphere/plane electrodes $b_{v_n} = b_{g_n}$ and thus $c_{v_n} = c_{g_n}$.

B.5.2 Sphere/Sphere Electrode Geometry

Using (B.12), (B.14a), (B.14c) and (B.19) the potential distribution of sphere/sphere electrodes is given as

$$\Phi(r,z) = VR_1\sum_{n=1}^{\infty}\left[\frac{\tilde{q}_{v_n}}{d_{v_n}(r,z)} + \frac{\tilde{q}_{g_n}}{d_{g_n}(r,z)}\right] \tag{B.23}$$

B.6 Electric Field Distributions

The electric field distribution for a sphere/plane electrode geometry and sphere/sphere electrode geometry can be found by respectively taking the gradient of the potential distributions in (B.22) and (B.23)

$$\mathbf{E}(r,z) = -\nabla\Phi(r,z) \tag{B.24}$$

The resulting components of the electric field are presented in the next two sections. Recall that for both cases the electric field is axisymmetric along the axis joining all image charges.

B.6.1 Sphere/Plane Electrodes Geometry

$$E_r(r,z) = VRr\sum_{n=1}^{\infty}\tilde{q}_{v_n}\left[\frac{1}{d_{v_n}^3(r,z)} - \frac{1}{d_{g_n}^3(r,z)}\right] \tag{B.25}$$

$$E_z(r,z) = -VR\sum_{n=1}^{\infty}\tilde{q}_{v_n}\left[\frac{(c_{v_n}-z)}{d_{v_n}^3(r,z)} + \frac{(c_{v_n}+z)}{d_{g_n}^3(r,z)}\right] \tag{B.26}$$

B.6.2 Sphere/Sphere Electrodes Geometry

$$E_r(r,z) = VR_1r\sum_{n=1}^{\infty}\left[\frac{\tilde{q}_{v_n}}{d_{v_n}^3(r,z)} + \frac{\tilde{q}_{g_n}}{d_{g_n}^3(r,z)}\right] \tag{B.27}$$

$$E_z(r,z) = -VR_1\sum_{n=1}^{\infty}\left[(c_{v_n}-z)\frac{\tilde{q}_{v_n}}{d_{v_n}^3(r,z)} - (c_{g_n}+z)\frac{\tilde{q}_{g_n}}{d_{g_n}^3(r,z)}\right] \tag{B.28}$$

Appendix C

Finite Point/Plane Electrode Geometry

C.1 Introduction

In this appendix we introduce the finite point/plane electrode geometry that is used as a case study for the forward and inverse theory of Kerr electro-optic measurements in the thesis. Various electric field component plots are presented for different locations and piecewise linear space charge density distributions with varying magnitudes to illustrate the general characteristics of electric field distributions of point/plane electrode geometries.

C.2 The Geometry

The finite point/plane electrode geometry is illustrated in Figure C.1. The needle has 5.4 mm diameter with a tip-plane distance of 2.5 mm and tip radius curvature of 0.5 mm. The tip is a z-translated (-2.5 mm) hyperboloid of revolution whose equation is given in (A.18) with $d = 5$ mm and $R_c = 0.5$ mm. A cylindrical ground electrode of 10 mm in radius bounds the geometry on the sides and the bottom. The dotted line on the top represents an artificial Neuman boundary consistent with the geometry as the upper part of the needle and the surrounding ground form a concentric cylindrical geometry whose electric field distribution is radial.

The radius of the surrounding ground is chosen so that the left and right boundaries are sufficiently larger than the tip-plane distance and thus do not appreciably effect

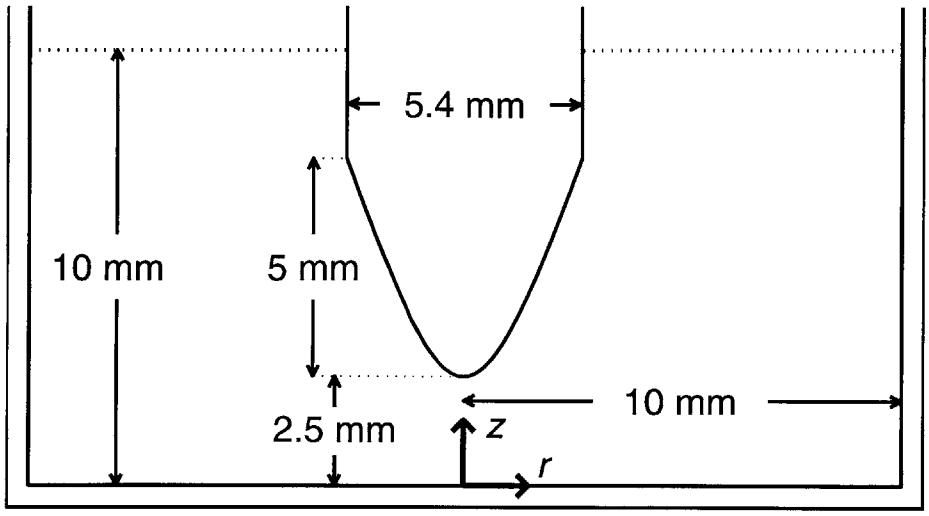

Figure C.1: The finite point/plane electrode geometry used as a case study throughout the thesis.

the electric field between the tip and the plane but small enough so that an excessive number of finite element mesh triangles are not necessary in numerical analysis. A large number of discretizing triangles can then be allocated for the region between the tip and the plane for higher accuracy of finite element solutions and for reasonably continuous optical patterns in Chapter 5. In actual experiments the radius of the surrounding ground (often the chamber itself in Figure 1.1) is often much larger in radius. However, the electric field distributions of such cases do not show any notable characteristic differences from the electric field distribution of the geometry of Figure C.1 except a slower rate of decay for electric field components. Figure C.2 illustrates this fact by comparing the Laplacian (space charge free) electric field componenents of the finite point/plate electrode geometry to those of the infinite extent point/plane electrode geometry with the same radius of curvature $R_c = 0.5$ mm and the tip-plane distance $d = 2.5$ mm. The plots are for $z = 2$ mm and the applied voltage is 40 kV.

One important reason for the extensive use of a point/plane electrode geometry in high voltage research is to localize the charge injection physics near the tip. For the geometry in Figure C.1 which has smaller radial extent and the space charge distributions considered in Section C.3, the plots in Section C.4 show that the electric field components for $r > 5$ mm are essentially equal to the Laplacian (space charge free) electric field distribution when space charge density is non-zero only within a 1 mm radius around the needle tip axis; the radial extent is large enough so that for large r the electric field distribution reduces to the Laplacian one. Thus the geometry

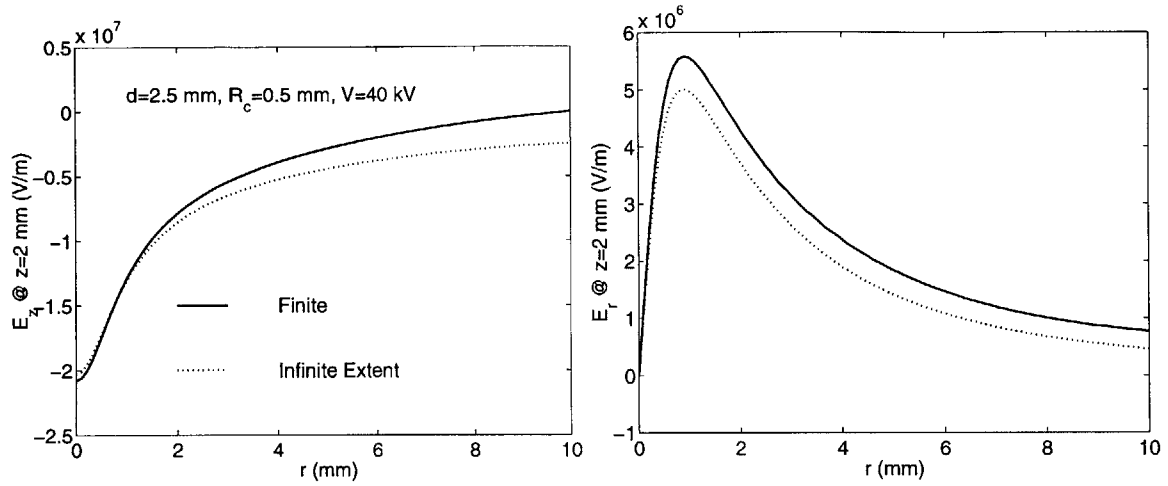

Figure C.2: A comparison between the electric field components at $z = 2mm$ of the finite point/plane electrode geometry of Figure C.1 and infinite point/plane electrode geometry with the same tip-plane distance, tip radius of curvature and applied voltage.

in Figure C.1 is adequate to understand the general characteristics of the electric field distributions of similar geometries with larger plane electrodes and/or large radial extent. The geometry is certainly practical and can be realized by a conductively coated glass as the surrounding ground.

The tip-plane distance is chosen such that the region between the needle and the plane can be discretized with a very fine mesh without exceeding our computing storage capacity yet the geometry can still be considered reasonable for small beam diameter ($w \leq 1$ mm) measurements (Section 1.2.4). The 0.5 mm radius of curvature is indicative of those used at MIT for Kerr electro-optic measurements at the time of this work [28]. It is relatively larger than typical values used in dielectric research and chosen such to smooth the very divergent electric field distributions of smaller radius of curvature needles. This facilitates the development and numerical experiments for the inverse methods. For all plots presented in this chapter the applied voltage is assumed to be 40 kV, a typical value for high voltage research.

The finite element mesh used for the geometry is shown in Figure C.3. We refine the mesh around the needle extensively to minimize the numerical errors from the finite element solutions especially for specified space charge distributions of Figure C.4. Our finite element code approximates the space charge distribution to be triangle wise constant and the average triangle edge length is chosen to be around 0.05 mm between $r = 0$ mm and $r = 1$ mm to approximate the space charge density shown in Figure C.4

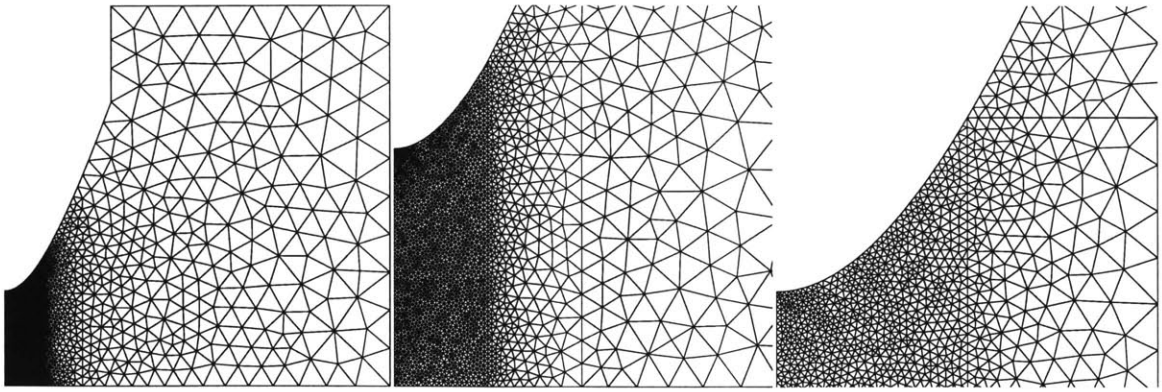

Figure C.3: Views of the mesh used for finite element solutions for the geometry shown in Figure C.1.

adequately. There are around 5500 (second order) triangles in the discretization.

On average, the solution of the problem takes about 10 minutes on a 200 MHz Pentium machine with 64 MB RAM after C++ code is compiled using Visual C++ without any optimization options turned on. The limiting factor was memory as we stopped refining the geometry after the running of the program began to use swap space.

C.3 The Space Charge Distributions

The form of space charge density considered for theoretical case studies is shown in Figure C.4. For constant z the space charge density linearly decreases from its maximum value at $r = 0$ mm to 0 at $r = 1$ mm. For constant r the space charge density linearly increases from its value at ground to a maximum at the needle tip height at $z = 2.5$ mm and then decreases linearly at a slower rate until reaching the needle electrode. A family of distributions are defined by the parameter $\tilde{\rho}_0 = \rho(0,0)/\epsilon_r$ where ϵ_r is the relative dielectric constant of the medium. Then the space charge distributions are

$$\rho(r,z) = \begin{cases} \epsilon_r\tilde{\rho}_0\big[1 - r/\Delta\big]\big[1 + 3z/d\big] & r < \Delta, \;\; z < d \\ \epsilon_r\tilde{\rho}_0\big[1 - r/\Delta\big]\big[5 - z/d\big] & r < \Delta, \;\; z > d, \\ 0 & r > \Delta \text{ or } (r,z) \text{ inside needle} \end{cases} \tag{C.1}$$

where $d = 2.5$ mm is the tip-plane distance and $\Delta = 1$ mm is the radial extent of the space charge distribution. The six values $\tilde{\rho}_0$ considered are 0 (Laplacian), 0.04,

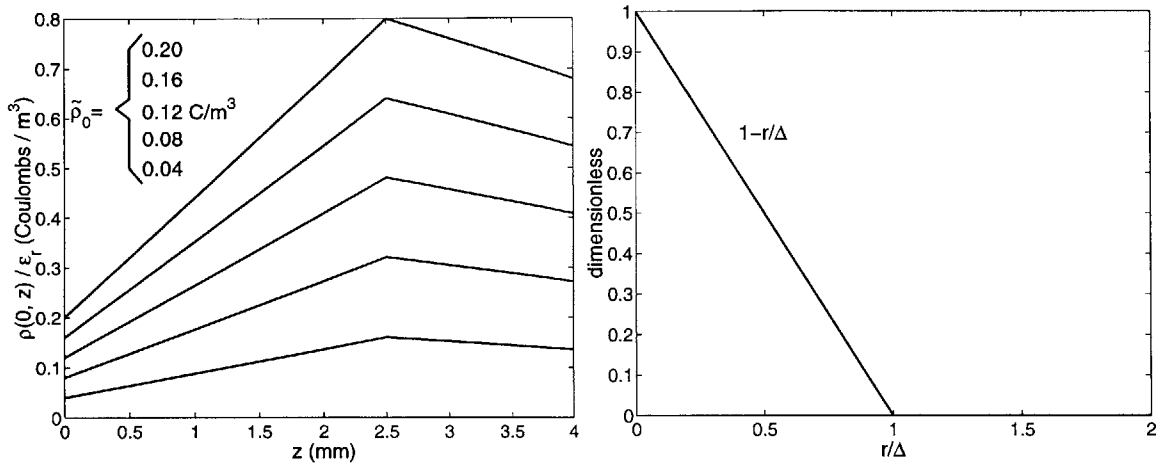

Figure C.4: Case study space charge density distributions for the geometry shown in Figure C.1. The two dimensional charge density $\rho(r, z)$ can be found by multiplying the z dependence on the left and the r dependence on the right. The relative dielectric constant of the medium is ϵ_r.

0.08, 0.12, 0.16 and 0.20 all in C/m^3. This type of space charge density is physically reasonable for phenomena where charge is injected from the needle.

C.4 Electric Field Components

In this section we provide a set of plots of electric field components of the finite point/plane electrode geometry in Figure C.1. The plots use r, z and/or the space charge density distributions in Figure C.4 as parameters.

In Figure C.5 we show the axial component of the electric field on the axisymmetry axis ($r = 0$) and the ground plane ($z = 0$) as the radial component is zero. The plot for $r = 0$ demonstrates the shielding effect of the charge injected from the needle as the electric field at the needle tip decreases with increasing charge density. For the maximum value of $\tilde{\rho}_0$ considered (0.20), $E_z(0, 2.5 \text{ mm})$ approaches the space charge limited condition of 0. Larger values of $\tilde{\rho}_0$ are not considered as they would cause a negative field on the tip inconsistent with positive charge injection. When the electric field magnitude is lowered near the needle, it is increased near the ground plane to keep the average applied field constant at 40 kV / 2.5 mm = 1.6×10^7 V/m. Also note that the change of the axial electric field component near the needle is much larger than the change near ground as expected from the imposed space charge density distributions in (C.1).

The plot for $z = 0$ demonstrates that near the ground plane the space charge density appreciably changes the electric field magnitude only for $r < 5$ mm. For larger r values the effects of the charge density diminishes and the electric field distribution becomes identical to that of the space charge free case. This demonstrates that although the radial extent of the geometry in Figure C.1 is small when compared to typical point/plane electrode systems it is large enough so that for large r the electric field distributions are independent of the space charge distributions localized near the needle-tip axis. In Figure C.6 we show the electric field components as a function of r with the space charge density distributions in Figure C.4 as the parameter. The plots are provided for three z values of 1 mm, 2.25 mm and 2.5 mm. Only the region between $r = 0$ mm and $r = 4$ mm is considered as for larger r the curves in each plot are essentially identical. Notice that for $z = 1$ mm the magnitude of E_z increases with $\tilde{\rho}_0$ as opposed to $z = 2.25$ mm and $z = 2.5$ mm where the magnitude of E_z decreases with $\tilde{\rho}_0$ consistent with the $r = 0$ plot in Figure C.5. Plots for z values above the needle tip ($z > 2.5$ mm) do not provide any additional valuable insight and are not included. The noisy behaviour near $r = 0$ in the $z = 2.5$ mm plots are probably due to the discretization in (C.3) as the $z = 2.5$ mm line goes on edges of the triangles rather than going through them. Finally in Figure C.7 we show the electric field components as a function of r with z as the parameter. The plots are provided for three $\tilde{\rho}_0$ values of 0.2 C/m^3, 0.12 C/m^3 and 0.04 C/m^3. Again only the region between $r = 0$ mm and $r = 4$ mm is considered as for larger r the curves in each plot are essentially identical. Notice that the order of E_z curves on z is different for each $\tilde{\rho}_0$.

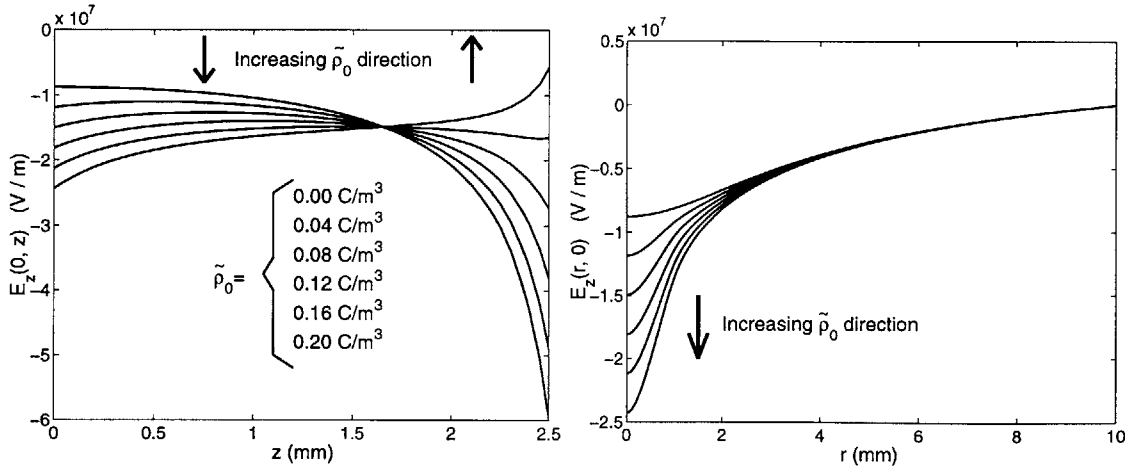

Figure C.5: Axial electric field component at $r = 0$ and at $z = 0$ for the geometry shown in Figure C.1 with the space charge density distributions shown in Figure C.4.

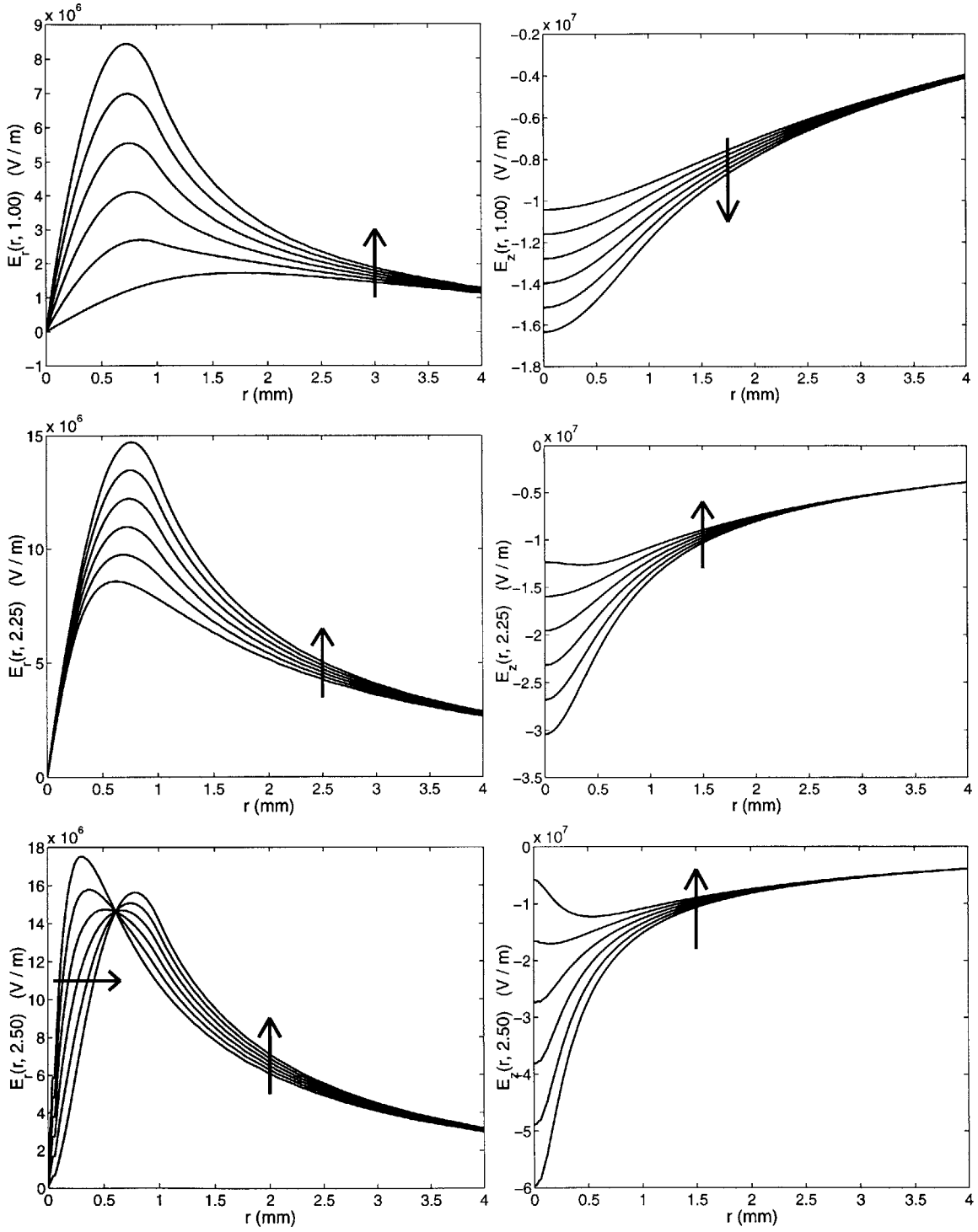

Figure C.6: Electric field component plots above the ground plane for different non-zero z (1, 2.25 and 2.5 mm) with $\tilde{\rho}_0$ values of 0, 0.04, 0.08, 0.12, 0.16 and 0.20 C/m^3 as the parameter. The arrows indicate the direction of increasing $\tilde{\rho}_0$.

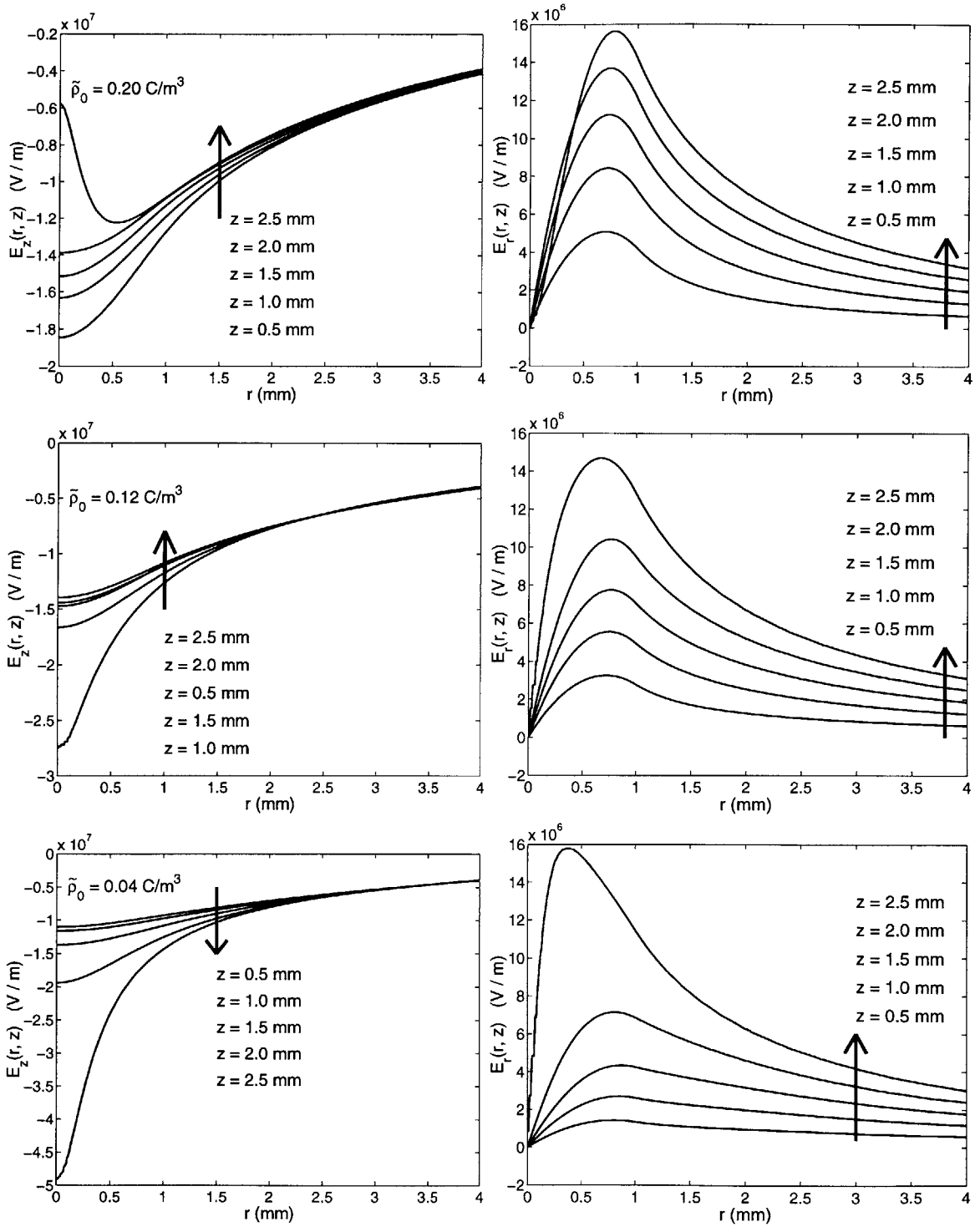

Figure C.7: Electric field component plots for $\tilde{\rho}_0$ values of 0.2, 0.12, 0.04 C/m^3 (top to bottom) with z as the parameter.

Appendix D

Electrostatic Systems With Charge Singularities

D.1 Introduction

In this appendix we provide the electric field distributions of some electrostatic systems with point and/or line charges. These are useful to model the physical distributions and can be used to decrease the end effects of the onion peeling method as described in Section 6.5.2. They also provide case studies for which weak medium characteristic parameters α and γ can be found analytically.

D.2 Semi-Infinite Uniform Line Charge

We first consider the electric field distribution of a semi-infinite uniform line charge λ that extends from the origin to infinity along z-axis. The geometry is axisymmetric and at the position (r, z) infinitesimal electric field components due to the infinitesimal charge at z', $\lambda\, dz'$, are

$$dE_r(r,z) = \frac{\lambda}{4\pi\epsilon}\frac{\sin\theta\, dz'}{(z-z')^2+r^2} = \frac{\lambda}{4\pi\epsilon}\frac{r\, dz'}{\left[(z-z')^2+r^2\right]^{3/2}} \tag{D.1a}$$

$$dE_z(r,z) = \frac{\lambda}{4\pi\epsilon}\frac{\cos\theta\, dz'}{(z-z')^2+r^2} = \frac{\lambda}{4\pi\epsilon}\frac{(z-z')\, dz'}{\left[(z-z')^2+r^2\right]^{3/2}} \tag{D.1b}$$

where θ is the angle with the z-axis and the line joining positions of the infinitesimal charge at z' and the observation point at z, and ϵ is the permittivity of the medium.

Integrating (D.1) along the line charge yields the electric field distribution

$$E_r(r,z) = \int_0^\infty \frac{\lambda}{4\pi\epsilon} \frac{r\,dz'}{\left[(z-z')^2+r^2\right]^{3/2}} = -\frac{\lambda}{4\pi\epsilon_0}\frac{1}{r}\frac{(z-z')}{\left[(z-z')^2+r^2\right]^{1/2}}\Bigg|_0^\infty$$
$$= \frac{\lambda}{4\pi\epsilon_0}\frac{1}{r}\left[1+\frac{z}{\sqrt{z^2+r^2}}\right] \tag{D.2a}$$

$$E_z(r,z) = \int_0^\infty \frac{\lambda}{4\pi\epsilon} \frac{(z-z')\,dz'}{\left[(z-z')^2+r^2\right]^{3/2}} = \frac{\lambda}{4\pi\epsilon_0}\frac{1}{\left[(z-z')^2+r^2\right]^{1/2}}\Bigg|_0^\infty$$
$$= -\frac{\lambda}{4\pi\epsilon_0}\frac{1}{\sqrt{z^2+r^2}} \tag{D.2b}$$

D.3 Semi-Infinite Uniform Line Charge Above A Ground Plane

Let the distance between the tip of the line charge and the ground plane to be d. Without loss of generality we assume that the ground plane is the xy-plane. The ground plane can then be replaced by an image line charge of density $-\lambda$ which extends from $-d$ to minus infinity. The electric field distribution of the line charge above the ground plane follows from (D.2) by translation in z

$$E_r(r,z) = \frac{\lambda}{4\pi\epsilon}\frac{1}{r}\left[1+\frac{z-d}{\sqrt{(z-d)^2+r^2}}\right] \tag{D.3a}$$

$$E_z(r,z) = -\frac{\lambda}{4\pi\epsilon}\frac{1}{\sqrt{(z-d)^2+r^2}} \tag{D.3b}$$

The electric field for the image line charge similarly follows by an inversion and a translation

$$E_r(r,z) = -\frac{\lambda}{4\pi\epsilon}\frac{1}{r}\left[1-\frac{z+d}{\sqrt{(z+d)^2+r^2}}\right] \tag{D.4a}$$

$$E_z(r,z) = -\frac{\lambda}{4\pi\epsilon}\frac{1}{\sqrt{(z+d)^2+r^2}} \tag{D.4b}$$

Superposing the electric field distributions of the line charge and its image yields

$$E_r(r,z) = \frac{\lambda}{4\pi\epsilon}\frac{1}{r}\left[\frac{z-d}{\sqrt{(z-d)^2+r^2}}+\frac{z+d}{\sqrt{(z+d)^2+r^2}}\right] \tag{D.5a}$$

$$E_z(r,z) = -\frac{\lambda}{4\pi\epsilon}\left[\frac{1}{\sqrt{(z+d)^2+r^2}} + \frac{1}{\sqrt{(z-d)^2+r^2}}\right] \tag{D.5b}$$

In the large r limit so that $r \gg |z|$, $|d|$, (D.5) reduces to

$$E_r(r,z) \approx \frac{\lambda}{4\pi\epsilon}\frac{2z}{r^2} \tag{D.6a}$$

$$E_z(r,z) \approx -\frac{\lambda}{4\pi\epsilon}\frac{2}{r} \tag{D.6b}$$

D.4 Dipole At Origin

Let two point charges with equal strength but opposite signs be located at $+d$ and $-d$ on the z-axis. The potential distribution is found by superposing the potential distributions of the individual charges

$$\phi(r,z) = \frac{Q}{4\pi\epsilon}\left[\frac{1}{\sqrt{(d-z)^2+r^2}} - \frac{1}{\sqrt{(d+z)^2+r^2}}\right] \tag{D.7}$$

The electric field components follow from (D.7) as

$$E_z(r,z) = -\frac{Q}{4\pi\epsilon}\left[\frac{d-z}{\left[(d-z)^2+r^2\right]^{3/2}} + \frac{d+z}{\left[(d+z)^2+r^2\right]^{3/2}}\right] \tag{D.8a}$$

$$E_r(r,z) = \frac{Qr}{4\pi\epsilon}\left[\frac{1}{\left[(d-z)^2+r^2\right]^{3/2}} - \frac{1}{\left[(d+z)^2+r^2\right]^{3/2}}\right] \tag{D.8b}$$

In large r limit $r \gg |z|$, $|d|$, the potential and the electric field components respectively reduce to

$$\phi(r,z) \approx \frac{Q}{4\pi\epsilon}\frac{2dz}{r^3} \tag{D.9}$$

and

$$E_z(r,z) = -\frac{Q}{4\pi\epsilon}\frac{2d}{r^3} \tag{D.10a}$$

$$E_r(r,z) = \frac{Q}{4\pi\epsilon}\frac{6dz}{r^4} \tag{D.10b}$$

D.5 Analytical Characteristic Parameters

Both geometries in Section D.3 and Section D.4 are axisymmetric. Their large r limit electric field solutions allow determination of characteristic paramaters analytically for light propagation directions perpendicular to the axisymmetry axis.

For a line charge above a ground plane we have

$$E_z^2(s) - E_p^2(s) = \frac{\tilde{\lambda}^2}{r^2} - \frac{\tilde{\lambda}^2 z^2 p^2}{r^6} \tag{D.11a}$$

$$2E_z(s)E_p(s) = \frac{2\tilde{\lambda}^2 zp}{r^4} \tag{D.11b}$$

where $\tilde{\lambda} = \lambda/2\pi\epsilon$ is a normalized line charge density used to simplify expressions. Using (D.11) the characteristic parameters can be found by evaluating the integrals

$$\gamma \cos\alpha = \pi B \int_{s_{\text{in}}}^{s_{\text{out}}} \left[E_z^2(s) - E_p^2(s)\right] \, ds \tag{D.12a}$$

$$\gamma \sin\alpha = \pi B \int_{s_{\text{in}}}^{s_{\text{out}}} 2E_z(s)E_p(s) \, ds \tag{D.12b}$$

Note that $r^2 = p^2 + s^2$ and s-integrals of reciprocal powers of r are [78]

$$\int \frac{ds}{p^2 + s^2} = \frac{1}{p} \arctan \frac{s}{p} \tag{D.13}$$

$$\int \frac{ds}{(p^2 + s^2)^n} = \frac{1}{2(n-1)p^2} \left[\frac{s}{(p^2 + s^2)^{n-1}} + (2n-3) \int \frac{ds}{(p^2 + s^2)^{n-1}} \right] \tag{D.14}$$

For a dipole on the origin analytical characteristic parameters also follow from (D.12) with

$$E_z^2(s) - E_p^2(s) = \frac{\tilde{Q}^2}{r^6} - \frac{9\tilde{Q}^2 z^2 p^2}{r^{10}} \tag{D.15a}$$

$$2E_z(s)E_p^2(s) = -\frac{6\tilde{Q}^2 zp}{r^8} \tag{D.15b}$$

where $\tilde{Q} = Q/4\pi\epsilon$ is a normalized charge. One can also superpose electric field distributions in Section D.3 and Section D.4 to find the analytical characteristic parameters for a line and point charge combination above a ground plane. For this case (D.12)

must be used with

$$E_z^2(s) - E_p^2(s) = \frac{1}{r^2}\left[\tilde{\lambda}^2 + \frac{2\tilde{Q}\tilde{\lambda}}{r^2} + \frac{\tilde{Q}^2}{r^4}\right] - \frac{z^2p^2}{r^6}\left[\tilde{\lambda}^2 + \frac{6\tilde{Q}\tilde{\lambda}}{r^2} + \frac{9\tilde{Q}^2}{r^4}\right] \tag{D.16a}$$

$$= \frac{\tilde{\lambda}^2}{r^2} + \frac{2\tilde{Q}\tilde{\lambda}}{r^4} + \frac{\tilde{Q}^2 - z^2p^2\tilde{\lambda}^2}{r^6} - \frac{6z^2p^2\tilde{Q}\tilde{\lambda}}{r^8} - \frac{9z^2p^2\tilde{Q}^2}{r^{10}} \tag{D.16b}$$

$$2E_z(s)E_p(s) = -\frac{zp}{r^4}\left[\tilde{\lambda}^2 + \frac{4\tilde{Q}\tilde{\lambda}}{r^2} + \frac{3\tilde{Q}^2}{r^4}\right] \tag{D.16c}$$

$$= -\frac{zp\tilde{\lambda}^2}{r^4} - \frac{4zp\tilde{Q}\tilde{\lambda}}{r^6} - \frac{3zp\tilde{Q}^2}{r^8} \tag{D.16d}$$

Bibliography

[1] H. A. Haus, *Electromagnetic Fields and Energy.* Prentice Hall, 1989.

[2] R. Coelho, *Physics of Dielectrics for the Engineer.* Elsevier, 1979.

[3] M. Zahn, "Space charge effects in dielectric liquids," in *The Liquid State and Its Electrical Properties* (E. E. Kunhardt, L. G. Christophorou, and L. H. Luessen, eds.), pp. 367–430, Plenum Publishing Corporation, 1988.

[4] M. Zahn, "Transform relationships between Kerr-effect optical phase shift and nonuniform electric field distributions," *IEEE Transactions on Dielectrics and Electrical Insulation*, vol. 1, pp. 235–246, April 1994.

[5] R. E. Hebner, R. A. Malewski, and E. C. Cassidy, "Optical methods of electrical measurements at high voltage levels," *Proceedings Of The IEEE*, vol. 65, pp. 1524–1548, November 1977.

[6] M. Zahn and R. Hanaoka, "Kerr electro-optic field mapping measurements using point-plane electrodes," in *Proceedings of the 2nd International Conference on Space Charge in Solid Dielectrics, Antibes-Juan-Les-Pins, France*, pp. 360–372, April 1995.

[7] E. F. Kelley and R. E. Hebner, "Electro-optic measurement of the electric field distribution in transformer oil," *IEEE Transaction on Power Apparatus and Systems*, vol. 102, pp. 2092–2097, July 1983.

[8] H. Maeno, Y. Nonaka, and T. Takada, "Determination of electric field distribution in oil using the Kerr-effect technique after application of dc voltage," *IEEE Transactions on Electrical Insulation*, vol. 25, pp. 475–480, June 1990.

[9] U. Gäfvert, A. Jaksts, C. Tornkvist, and L. Walfridsson, "Electrical field distribution in transformer oil," *IEEE Transaction on Electrical Insulation*, vol. 27, pp. 647–660, June 1992.

[10] M. Hikita, M. Matsuoka, R. Shimizu, K. Kato, N. Hayakawa, M. Hikita, and H. Okubo, "Kerr electro-optic field mapping and charge dynamics in impurity-doped transformer oil," *IEEE Transactions on Dielectrics and Electrical Insulation*, vol. 3, pp. 80–86, February 1996.

[11] H. Okubo, R. Shimizu, A. Sawada, K. Kato, N. Hayakawa, and M. Hikita, "Kerr electro-optic field measurement and charge dynamics in transformer-oil/solid composite insulation systems," *IEEE Transactions on Dielectrics and Electrical Insulation*, vol. 4, pp. 64–70, February 1997.

[12] M. Zahn, T. Takada, and S. Voldman, "Kerr electro-optic field mapping measurements in water using parallel cylindrical electrodes," *Journal Of Applied Physics*, vol. 54, pp. 4749–4761, September 1983.

[13] M. Zahn, Y. Ohki, K. Rhoads, M. LaGasse, and H. Matsuzawa, "Electro-optic charge injection and transport measurements in highly purified water and water/ethylene glycol mixtures," *IEEE Transactions on Electrical Insulation*, vol. 20, pp. 199–212, April 1985.

[14] M. Zahn, Y. Ohki, D. B. Fenneman, R. J. Gripshover, and V. H. Gehman, Jr, "Dielectric properties of water and water/ethylene glycol mixtures for use in pulsed power system design," *Proceedings of IEEE*, vol. 74, pp. 1182–1220, September 1986.

[15] M. Zahn and T. McGuire, "Polarity effect measurements using the Kerr electro-optic effect with coaxial cylindrical electrodes," *IEEE Transactions on Electrical Insulation*, vol. 15, pp. 287–293, June 1980.

[16] E. C. Cassidy, R. E. Hebner, M. Zahn, and R. J. Sojka, "Kerr effect studies of an insulating liquid under varied high-voltage conditions," *IEEE Transactions on Electrical Insulation*, vol. 9, pp. 43–56, June 1974.

[17] E. F. Kelley and R. E. Hebner, Jr, "Electric field distribution associated with prebreakdown in nitrobenzene," *Journal of Applied Physics*, vol. 52, pp. 191–195, January 1981.

[18] M. Zahn, M. Hikita, K. A. Wright, C. M. Cooke, and J. Brennan, "Kerr electro-optic field mapping measurements in electron- beam irradiated polymethylmethacrylate," *IEEE Transactions on Electrical Insulation*, vol. 22, pp. 159–176, April 1987.

[19] M. Hikita, M. Zahn, K. A. Wright, C. M. Cooke, and J. Brennan, "Kerr electro-optic field mapping measurements in electron- beam irradiated polymethylmethacrylate," *IEEE Transactions on Electrical Insulation*, vol. 23, pp. 861–880, October 1988.

[20] A. Törne and U. Gäfvert, "Measurement of the electric field in transformer oil using Kerr technique with optical and electrical modulation," in *Proceedings, ICPADM*, vol. 1, (Xian, China), pp. 61–64, June 1985.

[21] T. Maeno and T. Takada, "Electric field measurement in liquid dielectrics using a combination of ac voltage modulation and small retardation angle," *IEEE Transaction on Electrical Insulation*, vol. 22, pp. 503–508, August 1987.

[22] K. Tanaka and T. Takada, "Measurement of the 2-dimensional electric field vector in dielectric liquids," *IEEE Transaction on Electrical Insulation*, vol. 1, pp. 747–753, 1994.

[23] M. Zahn and T. Takada, "High voltage electric field and space-charge distributions in highly purified water," *Journal Of Applied Physics*, vol. 54, pp. 4762–4775, September 1983.

[24] A. Ustundag and M. Zahn, "Optical tomography of Kerr electro-optic measurements with axisymmetric electric field," in *Conference Record Of The 1996 IEEE International Symposium On Electrical Insulation*, (Montreal, Quebec), pp. 462–465, June 1996.

[25] A. Ustundag, T. J. Gung, and M. Zahn, "Kerr electro-optic measurement technique for determination of nonuniform electric fields," in *Proceedings of The 12th International Conference On Conduction and Breakdown in Dielectric Liquids*, (Rome, Italy), pp. 457–460, July 1996.

[26] T. J. Gung, A. Ustundag, and M. Zahn, "Kerr electro-optic measurements of nonuniform axisymmetric electric field distributions using point-plane electrodes," in *Proceedings of The Conference On Electrical Insulation and Dielectric Phenomena*, (Millbrae, CA), pp. 61–63, 73, October 1996.

[27] A. Ustundag, T. J. Gung, and M. Zahn, "Kerr electro-optic theory and measurements of electric fields with magnitude and direction varying along the light path," *IEEE Transactions on Dielectrics and Electrical Insulation*, vol. 5, pp. 421–442, June 1998.

[28] T. Gung, *Kerr Electro-Optic Measurements and Nonuniform Electric Field Reconstructions.* PhD thesis, MIT, 1999.

[29] M. Zahn, *Electromagnetic Field Theory: A Problem Solving Approach.* John Wiley and Sons, 1979; Krieger, 1987.

[30] H. A. Haus, *Waves and Fields in Optical Electronics.* Prentice Hall, 1984.

[31] J. A. Kong, *Electromagnetic Wave Theory.* John Wiley & Sons, 1990.

[32] R. W. Munn, "Nonlinear optical phenomena," in *Principles and Applications of Nonlinear Optical Materials* (R. W. Munn and C. N. Ironside, eds.), Blackie, 1993.

[33] C. J. F. Böttcher, *Theory Of Electric Polarization*, vol. 1. Elsevier, 1973.

[34] R. W. Boyd, *Nonlinear Optics.* Academic Press, 1992.

[35] N. Davidson, *Statistical Mechanics.* McGraw-Hill, 1962.

[36] C. J. F. Böttcher and P. Bordewijk, *Theory Of Electric Polarization*, vol. 2. Elsevier, 1978.

[37] R. D. Mindlin and L. E. Goodman, "The optical equations of three dimensional photoelasticity," *Journal Of Applied Physics*, vol. 20, pp. 89–95, 1949.

[38] H. Kubo and R. Nagata, "Equations of light propagation in an inhomogeneous crystal," *Optics Communications*, vol. 27, no. 2, pp. 201–206, 1978.

[39] H. Aben, *Integrated Photoelasticity.* McGraw-Hill International Book Company, 1979.

[40] C. M. Bender and S. A. Orszag, *Advanced Mathematical Methods For Scientists And Engineers.* McGraw-Hill, 1978.

[41] M. C. Pease III, *Methods Of Matrix Algebra.* Academic Press, 1965.

[42] A. S. Deif, *Advanced Matrix Theory.* John Wiley & Sons, 1982.

[43] F. R. Gantmacher, *The Theory Of Matrices.* Chelsea Publishing Company, 1959.

[44] G. Strang, *Introduction To Linear Algebra.* Wellesley-Cambridge Press, 1993.

[45] W. H. Press, S. A. Teukolsky, W. T. Vetterling, and B. P. Flannery, *Numerical Recipes in C.* Cambridge University Press, 1992.

[46] M. K. Jain, *Numerical Solution Of Differential Equations.* John Wiley, 1984.

[47] L. S. Srimath, K. Ramesh, and V. Ramamurti, "Determination of characteristic parameters in three-dimensional photoelasticity," *Optical Engineering*, vol. 27, no. 3, pp. 224–230, 1988.

[48] R. C. Jones, "A new calculus for the treatment of optical systems," *Journal Of The Optical Society Of America*, vol. 31, pp. 488–503, 1941.

[49] L. S. Srimath and S. Y. Keshavan, "A fast iterative procedure to determine photoelastic characteristic parameters," *Mechanical Research Communications*, vol. 5, no. 3, pp. 159–165, 1978.

[50] H. K. Aben, "Kerr effect tomography for general axisymmetric field," *Applied Optics*, vol. 26, no. 14, pp. 2921–2924, 1987.

[51] R. Gordon, "A tutorial on ART," *IEEE Transactions on Nuclear Science*, vol. 21, pp. 78–93, June 1974.

[52] H. M. Hertz, "Kerr effect tomography for nonintrusive spatially resolved measurements of asymmetric electric field distributions," *Applied Optics*, vol. 25, pp. 914–921, March 1986.

[53] H. Ihori, M. Fujii, S. Nishimoto, I. Kitani, and K. Arii, "Two-dimensional Kerr electrooptic measurement of nonuniform electric fields by CT method," *Japanese Journal Of Applied Physics*, vol. 31, pp. 1901–1904, June 1992.

[54] S. Uto, Y. Nagata, K. Takechi, , and K. Arii, "A theory for three-dimensional measurement of nonuniform electric field using Kerr effect," *Japanese Journal Of Applied Physics*, vol. 33, pp. 683–685, May 1994.

[55] H. Ihori, S. Uto, K. Takechi, and K. Arii, "Three-dimensional electric field vector measurements in nitrobenzene using Kerr effect," *Japanese Journal Of Applied Physics*, vol. 33, pp. 2066–2071, April 1994.

[56] K. Takechi, K. Arii, S. Udo, and H. Ihori, "Calculation of the three-dimensional field vectors in dielectrics," *Japanese Journal Of Applied Physics*, vol. 34, pp. 336–339, January 1995.

[57] H. Ihori, S. Uto, and K. Arii, "Electrooptic measurement of three-dimensional nonuniform electric field mapping in nitrobenzene," *Japanese Journal Of Applied Physics*, vol. 35, pp. 4550–4555, August 1996.

[58] S. R. H. Hoole, *Computer-Aided Analysis and Design Of Electromagnetic Devices.* Elsevier, 1989.

[59] T. J. R. Hughes, *The Finite Element Method.* Prentice-Hall, 1997.

[60] G. H. Golub and C. F. Van Loan, *Matrix Computations.* The Johns Hopkins University Press, 1996.

[61] R. Gorenflo and S. Vessella, *Abel Integral Equations.* No. 1461 in Lecture Notes In Mathematics, Springer-Verlag, 1980.

[62] A. Dold and B. Eckmann, eds., *Fractional Calculus And Its Applications.* No. 457 in Lecture Notes In Mathematics, Springer-Verlag, 1975.

[63] S. L. Kalla and V. S. Kiryakova, "An H-function generalized fractional calculus based upon composition of Erdelyi-Kober operators in L_p," *Math. Japonica*, vol. 35, no. 6, pp. 1151–1171, 1990.

[64] S. R. Deans, *The Radon Transform and Some of Its Applications.* Krieger Publishing Company, 1993.

[65] G. T. Herman, H. K. Tuy, K. J. Langenberg, and P. C. Sabatier, *Basic Methods of Tomography and Inverse Problems.* Adam Hilger, 1987.

[66] G. Beylkin, "The inversion problem and applications of the generalized radon transform," *Communications on Pure and Applied Mathematics*, vol. 37, pp. 579–599, 1984.

[67] A. G. Ramm and A. I. Katsevich, *The Radon Transform and Local Tomography.* CRC Press, 1996.

[68] H. Braun and A. Hauck, "Tomographic reconstruction of vector fields," *IEEE Transactions on Signal Processing*, vol. 39, pp. 464–471, February 1991.

[69] J. L. Prince, "Tomographic reconstruction of 3-D vector fields using inner product probes," *IEEE Transactions on Image Processing*, vol. 3, pp. 216–219, March 1994.

[70] L. Desbat and A. Wernsdorfer, "Direct algebraic reconstruction and optimal sampling in vector field tomography," *IEEE Transactions on Signal Processing*, vol. 43, pp. 1798–1808, August 1995.

[71] G. Sparr, K. Strahlen, K. Lindstrom, and H. W. Persson, "Doppler tomography for vector fields," *Inverse Problems*, vol. 11, pp. 1051–1061, 1995.

[72] J. L. Prince, "Convolution backprojection formulas for 3-D vector tomography with application to MRI," *IEEE Transactions on Image Processing*, vol. 5, pp. 1462–1472, October 1996.

[73] J. Howard, "Vector tomography applications in plasma diagnostics," *Plasma Physics*, vol. 38, pp. 489–503, 1996.

[74] P. Moon, *Field Theory For Engineers.* D. Van Nostrand, 1961.

[75] R. Coelho and J. Debeau, "Properties of the tip-plane configuration," *Journal Of Physics D: Applied Physics*, vol. 4, pp. 1266–1280, 1971.

[76] J. G. B. Thomas and R. L. Finney, *Calculus and Analytic Geometry.* Addison-Wesley, 1980.

[77] W. R. Smythe, *Static and Dynamic Electricity.* McGraw-Hill, 1968.

[78] W. H. Beyer, *CRC Standard Mathematical Tables and Formulae.* CRC Press, 29 ed., 1991.